

UCLA

UCLA Electronic Theses and Dissertations

Title

Theoretical Investigations of Cycloadditions and Subsequent Transformations Involving Allenes and Arenes to Form Complex Polycycles

Permalink

<https://escholarship.org/uc/item/2f1663fp>

Author

Pham, Hung Viet

Publication Date

2015

Peer reviewed|Thesis/dissertation

UNIVERSITY OF CALIFORNIA

Los Angeles

Theoretical Investigations of Cycloadditions and Subsequent Transformations
Involving Allenes and Arenes to Form Complex Polycycles

A dissertation submitted in partial satisfaction of the
Requirements of the degree
Doctor of Philosophy in Chemistry

by

Hung Viet Pham

2015

© Copyright by

Hung Viet Pham

2015

ABSTRACT OF THE DISSERTATION

Theoretical Investigations of Cycloadditions and Subsequent Transformations
Involving Allenes and Arenes to Form Complex Polycycles

by

Hung Viet Pham

Doctor of Philosophy in Chemistry

University of California, Los Angeles, 2015

Professor Kendall N. Houk, Chair

This dissertation is a culmination of research projects that combine the utility of computational methods with the practicality of experiments in order to investigate a variety of chemical phenomena. The theoretical molecular models and quantum chemical calculations reported herein provide explanations of selectivity, elucidations of mechanisms, and predictions of reactivity that will continually advance the scientific community in future endeavors, especially in the field of organic chemistry and complex polycycle synthesis.

Section I describes investigations centering upon the 4+2 cycloaddition between benzene and allene, a reaction developed by Gerhard Himbert in the 1980s. In collaboration with Chris Vanderwal at UC Irvine, we study the mechanisms of intramolecular Diels–Alder cycloadditions of various N-phenyl-allenamides to uncover the competing concerted and stepwise diradical pathways that bring about intriguing experimental observations. Additionally, the reaction optimization of carbon analogues is aided and explained through computations, providing access to novel cycloadducts. With growing interest in the mechanistic intricacy of the 4+2 reaction, a

theoretical study of the Diels–Alder reaction of allene with butadiene and with benzene elucidates the complexity of each cycloaddition, revealing an ambimodal transition state along the butadiene/allene pathway and the importance of preserving aromaticity in the reaction with benzene. To gain insight into the importance of intramolecularity in the original Himbert systems, we conducted a systematic investigation of various tether moieties and their effects on the thermodynamics of the reaction. Finally, in our quest to efficiently synthesize a library of complex polycyclic scaffolds, we looked into subsequent transformations of the bicyclo[2.2.2]octadiene cycloadducts, namely ring-rearrangement metathesis to form fused tricycles and an interesting dyotropic shift that occurs in a stepwise manner, resulting in isomerized bicyclo[3.2.1]octadiene skeletons.

Section II compiles research pertaining to other pericyclic reactions as well as collaborative projects with different research groups. Intramolecular Diels–Alder reactions with tryptamine-derived Zincke aldehydes and diene-tethered cycloalkenones, in conjunction with Chris Vanderwal and Samuel Danishefsky, respectively, are studied computationally to explain stereoselectivities and influences from external reagents. Collaborative efforts with the Barrio and Petric groups provide a deeper understanding of the noncovalent binding modes of a class of positron emission tomography probes used for diagnosing and treating neurodegenerative conditions. Additionally, the utilization of computations to further synthetic efforts is exemplified in the molecular modeling of Vanderwal’s tetracyclic exiguaquinol core and Jung’s palladium-catalyzed alkene isomerizations. The thermodynamic properties of Rebek’s host–guest systems were examined, using molecular mechanics and implicit solvent to understand the binding of adamantyl guests in resorcinarene-based cavitands. Finally, a review analyzes hydrocarbon-bound protein structures and other properties in order to identify potential *de novo* enzyme templates for the cleavage of C–C single bonds.

The dissertation of Hung Viet Pham is approved.

Jorge R. Barrio

Yves Rubin

Kendall N. Houk, Committee Chair

University of California, Los Angeles

2015

I dedicate my dissertation work to my family, who have always been by my side, regardless of any questionable decisions I have made and will continue to make...

To my parents, Thua and Phuong, who have (almost) always allowed me to find my own way; my father's constant encouragement and my mother's constant nurturing have been, and will always be, inexpressibly appreciated.

To my sister, Katie, and my brother-in-law, Kam, who have kept me grounded and provided continual guidance and support throughout my entire journey.

To my nephew, Riley Connor, and my niece, Evelyn Claire, who motivate me to be the best person—or, at least, the best uncle—I can be.

And to my grandfather, to whom I wish I had been able to present my Ph.D. in person.

TABLE OF CONTENTS

List of Schemes	vii
List of Figures	viii
List of Tables	xii
Acknowledgments	xiv
Vita	xviii

Section I – Arene/Allene Cycloadditions and the Re-Emergence of “Himbert Chemistry”

Chapter 1: Mechanism of the Diels-Alder Reaction of Allene Dienophiles

- 1.1 – Studies on the Himbert Intramolecular Arene/Allene Diels–Alder Cycloaddition. Mechanistic Studies and Expansion of Scope to All-Carbon Tethers 1
- 1.2 – Diels–Alder Reactions of Allene with Benzene and Butadiene: Concerted, Stepwise, and Ambimodal Transition States 26

Chapter 2: Determining Tether Effects in Intramolecular Diels–Alder Reactions of Allenes and Arenes Through an Energy Decomposition Analysis 48

Chapter 3: Subsequent Transformations of Himbert Cycloadducts

- 3.1 – Computation and Experiment Reveal That the Ring-Rearrangement Metathesis of Himbert Cycloadducts Can Be Subject to Kinetic or Thermodynamic Control 60
- 3.2 – Computational and Experimental Investigations of the Formal Dyotropic Rearrangements of Himbert Arene/Allene Cycloadducts 83

Section II – Other Pericyclic Reactions, Computational Investigations and Collaborations

Chapter 4: The Intramolecular Diels–Alder Reaction of Tryptamine-Derived Zincke Aldehydes is a Stepwise Process106

Chapter 5: Intramolecular Diels–Alder Reactions of Cycloalkenones: Stereoselectivity, Lewis Acid Acceleration, and Halogen Substituent Effects 121

Chapter 6: Dicyanovinyl naphthalenes for Neuroimaging of Amyloids and Relationships of Electronic Structures and Geometries to Binding Affinities139

Chapter 7: Synthesis of the Tetracyclic Core of Exiguaquinol 159

Chapter 8: Palladium Hydride Promoted Stereoselective Isomerization of Unactivated Di-(exo)methylenes to Endocyclic Dienes 167

Chapter 9: Thermodynamics of Guest Exchange in Self-Folding Cavitands 177

Chapter 10: Hydrocarbon Binding by Proteins: Structures of Protein Binding Sites for $\geq C_{10}$ Linear Alkanes or Long-Chain Alkyl and Alkenyl Groups 184

LIST OF SCHEMES

Chapter 1.1

Scheme 1.1.1	Ring-rearrangement metathesis of Himbert cycloadducts to access complex polycyclic lactams	2
Scheme 1.1.2	Experiments to test for radical intermediates	11
Scheme 1.1.3	Representative Himbert cycloadditions with all-carbon tethers.....	16

Chapter 3.1

Scheme 3.1.1	Sequential use of the Himbert arene/allene IMDA reaction and ring-rearrangement metathesis to afford fused polycyclic lactams	61
--------------	---	----

Chapter 3.2

Scheme 3.2.1	Formal dyotropic rearrangement of Himbert cycloadducts.....	85
Scheme 3.2.2	Resonance-stabilization in intermediate 15g	98

Chapter 4

Scheme 4.1	Base-mediated IMDA reaction of tryptamine-derived Zincke aldehydes	108
Scheme 4.2	Two reasonable mechanistic possibilities for the intramolecular Diels–Alder cycloaddition of tryptamine-derived Zincke aldehydes	109
Scheme 4.3	Possible mechanisms for cycloreversion and regeneration of Zincke aldehyde 15	117

Chapter 7

Scheme 7.1	Synthesis plan to access tetracycle 2a bearing all of the stereochemical complexity of exiguquinol	160
Scheme 7.2	Synthesis of the tetracyclic “core” of exiguquinol, epimeric at C2	161

Chapter 8

Scheme 8.1	Isomerization of 2a to give 3a and/or 4a	168
Scheme 8.2	Attempts to isomerize 2a	169
Scheme 8.3	Isomerization of 2a to give 3a and other products	170
Scheme 8.4	Isomerization of alkenes 2bc	171
Scheme 8.5	Proposed Mechanism for the Isomerization of 2	172

LIST OF FIGURES

Chapter 1.1

Figure 1.1.1	Calculated energies for the stepwise and direct cycloaddition of arene/allene 13	7
Figure 1.1.2	Experimental results of enantiomerically enriched allene 18	10
Figure 1.1.3	Calculated energies for the stepwise and direct cycloaddition of arene/allene 29	14
Figure 1.1.4	Plausible model for diastereocontrol based on minimization of allylic strain	22

Chapter 1.2

Figure 1.2.1	The Diels–Alder and (2+2) cycloaddition reactions of allene with butadiene and benzene	26
Figure 1.2.2	(4+2), 1,3-dipolar and (2+2) cycloadditions of allenes	27
Figure 1.2.3	Diels–Alder reactions of dimethyl-1,3-allenedicarboxylate 2 with Danishefsky dienes 1	28
Figure 1.2.4	Formation of <i>exo</i> -methylenevinylcyclobutane intermediate prior to rearrangement to Diels–Alder adducts	29
Figure 1.2.5	Intramolecular Diels–Alder reaction of arenes and allenes	30
Figure 1.2.6	Possible mechanisms of butadiene 16 and allene 17	32
Figure 1.2.7	Schematic of the potential energy surface for the reaction between butadiene and allene	33
Figure 1.2.8	Potential energy surface (PES) region of the possible transition states of initial bond formation, generated with CASSCF(8,8)/6-31G(d).....	35
Figure 1.2.9	Optimized structures of the cycloaddition of butadiene 16 and allene 17	37
Figure 1.2.10	Possible mechanisms of cycloadditions of benzene 21 and allene 17	39
Figure 1.2.11	Schematic of the potential energy surface for the reaction between benzene 21 and allene 17	40
Figure 1.2.12	Optimized structures for the cycloaddition of benzene 21 and allene 17	41
Figure 1.2.13	Energetics of the Diels–Alder reaction of benzene and allene (left) and the dimerization of allene (right).....	41
Figure 1.2.14	Table of activation energies for the concerted Diels–Alder reaction of butadiene and benzene with unsaturated dienophiles.....	43

Chapter 2

Figure 2.1	Reaction enthalpies for the IMDA reaction of tethered benzene and allene.....	50
Figure 2.2	Development of the model to study allene substitution effects.....	51

Figure 2.3	Graphical representations of the various enthalpic contributions.....	52
Figure 2.4	The extent of alkene in-plane angle distortion	55
Figure 2.5	The strong correlation between the calculated reaction enthalpy and the compilation of theoretical enthalpic factors	56
Figure 2.6	Reaction enthalpies correlate well with strain enthalpies.....	57

Chapter 3.1

Figure 3.1.1	Important relevant examples of ring-rearrangement metathesis, and the related ring-opening metathesis polymerization (ROMP) process ...	63
Figure 3.1.2	Ring-rearrangement metathesis of achiral tricyclic lactams 18a–c	65
Figure 3.1.3	Unusual stereochemical results in the ring-rearrangement metathesis reactions of chiral tricyclic lactams	66
Figure 3.1.4	Unusual ring-rearrangement metathesis results with benzo-fused substrates	67
Figure 3.1.5	Metathesis experiments on cycloadduct derived from 2,3-dimethyl aniline	68
Figure 3.1.6	Possible mechanisms for the ring-rearrangement metatheses of representative Himbert cycloadducts 18a and 18b	70
Figure 3.1.7	Different types of stationary points in the ROM/RCM mechanism for 18a	71
Figure 3.1.8	Comparison of the RCM/ROM and ROM/RCM pathways for 18a	74
Figure 3.1.9	Comparison of the RCM/ROM and ROM/RCM pathways for 18b	74
Figure 3.1.10	Thermodynamically and kinetically controlled RRM products	76
Figure 3.1.11	Steric strain in intermediates Int2	78
Figure 3.1.12	Thermodynamically controlled reactions.....	79

Chapter 3.2

Figure 3.2.1	The Himbert arene/allene cycloaddition and the ring-rearrangement metathesis (RRM) of select alkene-bearing cycloadducts	83
Figure 3.2.2	Type I and Type II dyotropic rearrangements.....	84
Figure 3.2.3	Reaction coordinate diagram of the formal dyotropic rearrangement of 9a	88
Figure 3.2.4	Charge transfer and ring strain	89
Figure 3.2.5	Graph of the correlation between $\log(k_{\text{rel}})$ and charge difference on oxygen.....	93
Figure 3.2.6	Lewis acid catalysis of the formal dyotropic rearrangement of Himbert cycloadduct 9a	95
Figure 3.2.7	Optimized structures of bridgehead-substituted substrates	99
Figure 3.2.8	Reaction coordinate diagrams and optimized structures for the formal dyotropic shift of heterologues	101

Chapter 4

Figure 4.1	The mechanistic continuum of Diels–Alder cycloadditions.....	107
Figure 4.2	Modeling the intermolecular reaction between indolate and Zincke aldehyde ...	111
Figure 4.3	Energy profiles for the IMDA of the anion and the potassium salt.....	113
Figure 4.4	Energy profile for the IMDA reaction with alpha-methylated Zincke aldehyde .	115
Figure 4.5	Energy profile for various pathways of cycloreversion.....	118

Chapter 5

Figure 5.1	Summary of experimental results for the intramolecular Diels–Alder reaction of cycloalkenones	121
Figure 5.2	Reaction coordinate diagrams for reactions of 3-carbon-tethered cycloalkenones 1–3	124
Figure 5.3	Transition structures for the cycloaddition of cyclobutenone 1	125
Figure 5.4	Proposed mechanism to account for the formation of cycloadducts 7P–9P from cycloalkenones 4–6	127
Figure 5.5	Energy profile comparison of 4-carbon-tethered cycloalkenones 4–6 and possible isomerized intermediates 7–9	128
Figure 5.6	Energy profile comparison of the thermal and BF ₃ -catalyzed reactions of cycloalkenones 1–3	132
Figure 5.7	Computed energy diagrams for the Lewis acid-catalyzed intermolecular reactions of cyclobutenone 11 and cyclopentenone 12	134
Figure 5.8	Computed free energy diagrams for cyclobutenone 1 and halogenated analogue 2-bromocyclobutenone 1Br	135

Chapter 6

Figure 6.1	Structures of synthesized FDDNP analogs	140
Figure 6.2	Competitive binding assays for FDDNP and its analogs	143
Figure 6.3	Syn and anti orientations of the dicyanovinyl group.....	147
Figure 6.4	Computational docking results of FDDNP analogs along the fibril spine.....	150
Figure 6.5	Plot of the K_i vs. the energy to distort ω_{torsion}	152

Chapter 7

Figure 7.1	Exiguaquinol and tetracyclic model system hemiaminal diastereomers	159
Figure 7.2	Computed relative free energies of the hemiaminal epimers of the tetracyclic core and exiguaquinol	163

Chapter 8

Figure 8.1	Structure of rugulosone	167
Figure 8.2	Structures of the C ₂ and C _S dienes	168
Figure 8.3	Monoisomerized and C ₂ and C _S bis-isomerized optimized structures	174

Chapter 9

Figure 9.1	Representation of the reaction coordinate diagram of host–guest complexation.....	177
Figure 9.2	Structure of the resorcinarene-based cavitand and mechanism of the self-exchange process	178
Figure 9.3	Plot of the OPLS binding energies	181

Chapter 10

Figure 10.1	Selection of ligands having linear alkane motifs	186
Figure 10.2	Functional classification and the size distribution of the ligands containing linear alkane motifs	189
Figure 10.3	Structures of the 14-carbon ligands, 16-carbon ligands, and cardiolipin.....	190
Figure 10.4	Statistics of the ligand-binding pockets.....	191
Figure 10.5	Resorcinarene-based cavitand dimers.....	195
Figure 10.6	Frequently observed SCOP folds binding ligands with linear alkane motifs	200

LIST OF TABLES

Chapter 1.1

Table 1.1.1	Computed thermodynamic energies of the Himbert cycloadditions of various substituted carbon-linked arene/allenes	17
Table 1.1.2	Scope of the Himbert arene/allene cycloaddition with all-carbon tethers	19
Table 1.1.3	Sequential Himbert arene/allene cycloaddition and ring-rearrangement metathesis to access all-carbon polycycles	21

Chapter 3.2

Table 3.2.1	Substituent effects on rearrangement rates	86
Table 3.2.2	Calculated free energies, partial atomic charges, and theoretically derived relative rates for stepwise dyotropic rearrangements of a range of Himbert cycloadducts	92
Table 3.2.3	Reaction free energies of the formal dyotropic rearrangements of Himbert cycloadducts substituted on the bicyclo[2.2.2]octadiene	97

Chapter 5

Table 5.1	Computed Reaction and Activation Free Energies and Enthalpies for the Thermal Diels–Alder Cycloaddition of Cycloalkenones 1–9	123
Table 5.2	Computed Reaction and Activation Free Energies of the Lewis Acid-Catalyzed Diels–Alder Cycloaddition of Cycloalkenones 1–9	131

Chapter 6

Table 6.1	Selected structural, spectroscopic, and binding data for synthesized DDNP analogs	144
-----------	---	-----

Chapter 8

Table 8.1	Effect of solvents on conversion of 2a to 3a , 4a , 6a , and 7a	171
Table 8.2	Free Energy Calculations for Isomers	173

Chapter 9

Table 9.1	Calculated binding energies of various adamantane derivatives with 1 in octanol	181
-----------	--	-----

Chapter 10

Table 10.1	Description of the Different Protein–Ligand Complex Datasets	187
Table 10.2	PDB Entries of Soluble Proteins and Their Corresponding Ligands Containing Alkyl and Alkenyl Groups Larger than C ₁₀	187
Table 10.3	SCOP Classification of the Selected PDB Entries Containing Linear Alkane Motifs	196
Table 10.4	Subset of the Selected PDB Entries Having Enzymatic Activity	201

ACKNOWLEDGMENTS

First and foremost, I would like to thank my loved ones, to whom this dissertation is dedicated. I am eternally grateful for their enduring support, for I would not be who I am today without them. Although we all may not always see eye to eye, we will always be in each other's hearts.

I am also thoroughly thankful for the mentorship and guidance of Professor Ken Houk. Not only is he an established authority in the field of chemistry, but his enthusiasm and encouraging nature inspire me to continually strive for the best and follow my passion of teaching. With his support, we have been able to push back the frontiers of science, and I wish him many more years of discovery.

The numerous colleagues who come and go through the Houk Lab doors all deserve recognition, for they all have impacted me in one way or another. In particular, I would like to acknowledge Buck, Jessie, Blanton, Janice, Cyndi, Colin, Gloria and Mareike – our invaluable teamwork and stimulating conversations, both scientific and non-scientific, contributed to the inimitable environment of the lab.

A large portion of my research has been in conjunction with other groups, all of which have contributed immensely to this dissertation. Because of this, I am greatly appreciative of my collaborators: Professors Samuel Danishefsky, Mike Jung, Neil Garg and Jorge Barrio, to name a few. I would especially like to thank Professor Chris Vanderwal and his group at UC Irvine, who have not only been integral to the growth of my research career but have also been extraordinarily cooperative and welcoming throughout the years. Go Houkerwallers!

The entirety of this research and training could not have been possible without the generous funding by a number of institutions. My gratitude goes to the UCLA Graduate Division, which provided me with the Joan Palevsky Fellowship as well as select teaching

assistantships. I am also thankful to be the recipient of the Christopher S. Foote Fellowship and the Collegium of University Teaching Fellowship, and a large portion of my graduate studies was funded by the Chemistry–Biology Interface Training Program, an NIH-funded program that focused on the interplay of chemistry and biology. The UCLA Hoffman² Computing Cluster and the San Diego Supercomputer Center also provided the computational resources that made my research possible.

And lastly, but by no means least, I am forever indebted to the friends that have been supportive of my journey and transformation through graduate school: Lyly and Co.; the LQ crew (including Van and Ernie); and, of course, all the amazing people who volunteer at the Truc Lam Buddhist Youth Organization. The strength of your friendships will continue to propel me towards a brighter future.

Chapter 1.1 is a modified version of the publication “Studies on the Himbert Intramolecular Arene/Allene Diels-Alder Cycloaddition. Mechanistic Studies and Expansion of Scope to All-Carbon Tethers.” Schmidt, Y.; Lam, J. K.; Pham, H. V.; Houk, K. N.; Vanderwal, C. *D. J. Am. Chem. Soc.* **2013**, *135*, 7339. Yvonne Schmidt and Jonathan Lam from the Vanderwal group performed the experiments.

Chapter 1.2 is a modified version of the publication “Diels-Alder Reactions of Allene with Benzene and Butadiene: Concerted, Stepwise, and Ambimodal Transition States.” Pham, H. V.; Houk, K. N. *J. Org. Chem.* **2014**, *79*, 8968. I performed quantum chemical calculations while K. N. Houk supervised the research and edited the manuscript.

Chapter 3.1 is a modified version of the publication “Computation and Experiment Reveal That the Ring-Rearrangement Metathesis of Himbert Cycloadducts Can Be Subject to Kinetic or Thermodynamic Control.” Lam, J. K.; Pham, H. V.; Houk, K. N.; Vanderwal, C. D. *J.*

Am. Chem. Soc. **2013**, *135*, 17585. Jonathan Lam from the Vanderwal group performed the experiments.

Chapter 4 is a modified version of the publication “The intramolecular Diels–Alder reaction of tryptamine-derived Zincke aldehydes is a stepwise process.” Pham, H. V.; Martin, D. B. C.; Vanderwal, C. D.; Houk, K. N. *Chem. Sci.*, **2012**, *3*, 1650. Dave Martin from the Vanderwal group performed the experiments that our calculations were based on.

Chapter 5 is a modified version of the publication “Intramolecular Diels–Alder Reactions of Cycloalkenones: Stereoselectivity, Lewis Acid Acceleration, and Halogen Substituent Effects.” Pham, H. V.; Paton, R. S.; Ross, A. G.; Danishefsky, S. J.; Houk, K. N. *J. Am. Chem. Soc.* **2014**, *136*, 2397. Rob Paton, a former postdoctoral scholar in the Houk group, performed the initial quantum mechanical calculations. I completed subsequent calculations and prepared the manuscript. Audrey Ross from the Danishefsky group conducted the experiments upon which our calculations were based.

Chapter 6 is a modified version of the publication “Dicyanovinyl naphthalenes for neuroimaging of amyloids and relationships of electronic structures and geometries to binding affinities.” Petric, A.; Johnson, S. A.; Pham, H. V.; Li, Y.; Ceh, S.; Golobic, A.; Agdeppa, E. D.; Timbol, G.; Liu, J.; Keum, G.; Satyamurthy, N.; Kepe, V.; Houk, K. N.; Barrio, J. R. *Proc. Acad. Nat. Sci.* **2012**, *109*, 16492. Scott Johnson and Ying Li, former members of the Houk group, performed initial docking investigations and modelling. Scott and I ran quantum chemical calculations and modelling studies as well as prepared the manuscript. The Petric and Barrio groups conducted the syntheses, experiments and *in vivo* testing.

Chapter 7 is a modified version of the publication “Synthesis of the Tetracyclic Core of Exiguaquinol.” Schwarzwald, G. M.; Steinhardt, S. E.; Pham, H. V.; Houk, K. N.; Vanderwal,

C. D. *Org. Lett.* **2013**, *15*, 6014. Gregg Schwarzwald and Sarah Steinhardt in the Vanderwal group conducted the syntheses and characterizations.

Chapter 8 is a modified version of the publication “Palladium Hydride Promoted Stereoselective Isomerization of Unactivated Di(exo)methylenes to Endocyclic Dienes.” Jung, M. E.; Lee, G. S.; Pham, H. V.; Houk, K. N. *Org. Lett.* **2014**, *16*, 2382. Experiments were carried out by Gloria Lee in the Jung Group, while computations were computed by the Houk Group.

Chapter 10 is a modified version of the publication “Hydrocarbon Binding by Proteins: Structures of Protein Binding Sites for $\geq C_{10}$ Linear Alkanes or Long-Chain Alkyl and Alkenyl Groups,” Park, J.; Pham, H. V.; Mogensen, K.; Solling, T. I.; Bennetzen, M. V.; Houk, K. N. *J. Org. Chem.* **2015**, *80*, 997. Kristian Mogensen, Theis Ivan Solling, and Martin Vad Bennetzen supported the research and edited the manuscript. The Houk group performed the literature search.

VITA

2008	B. S., Chemistry University of California, Irvine Irvine, CA
2008	B. S., Mathematics University of California, Irvine Irvine, CA
2008–2009	LARC Tutor Advisor University of California, Irvine Irvine, CA
2011	M. S., Chemistry University of California, Los Angeles Los Angeles, CA
2014	Chemistry Adjunct Instructor Santa Monica College Santa Monica, CA

Honors and Awards

- 2008 – Magna cum laude, UC Irvine
- 2011 – Hanson-Dow Award for Excellence in Teaching
- 2011–2014 – NIH Chemistry-Biology Interface Training Grant
- 2013 – Christopher S. Foote Graduate Fellowship
- 2014 – Collegium of University Teaching Fellowship
- 2014 – UCLA Department of Physical Sciences Joan Palevsky Fellowship
- 2015 – UCLA Excellence in Chemistry Research Fellowship

Teaching Experience

- 2010–2011 – General and Organic Chemistry Lab Teaching Assistant, UCLA
- 2014 – Course Instructor and Designer, “Chemistry in the Home”, UCLA
- 2014–2015 – Chemistry Adjunct Instructor, Santa Monica College

PUBLICATIONS

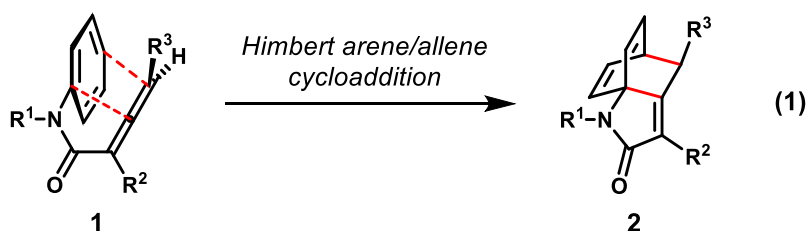
- Pham, H. V.; Karns, A. S.; Vanderwal, C. D.; Houk, K. N. "Computational and Experimental Investigations of the Formal Dyotropic Rearrangements of Himbert Arene/Allene Cycloadducts," *J. Am. Chem. Soc.* **2015**. Just Accepted.
- Park, J.; Pham, H. V.; Mogensen, K.; Solling, T. I.; Bennetzen, M. V.; Houk, K. N. "Hydrocarbon Binding by Proteins: Structures of Protein Binding Sites for $\geq C_{10}$ Linear Alkanes or Long-Chain Alkyl and Alkenyl Groups," *J. Org. Chem.* **2015**, *80*, 997.
- Pham, H. V.; Houk, K. N. "Diels-Alder Reactions of Allene with Benzene and Butadiene: Concerted, Stepwise, and Ambimodal Transition States." *J. Org. Chem.* **2014**, *79*, 8968.
- Jung, M. E.; Lee, G. S.; Pham, H. V.; Houk, K. N. "Palladium Hydride Promoted Stereoselective Isomerization of Unactivated Di(exo)methylenes to Endocyclic Dienes." *Org. Lett.* **2014**, *16*, 2382.
- Pham, H. V.; Paton, R. S.; Ross, A. G.; Danishefsky, S. J.; Houk, K. N. "Intramolecular Diels–Alder Reactions of Cycloalkenones: Stereoselectivity, Lewis Acid Acceleration, and Halogen Substituent Effects," *J. Am. Chem. Soc.* **2014**, *136*, 2397.
- Schwarzwalder, G. M.; Steinhardt, S. E.; Pham, H. V.; Houk, K. N.; Vanderwal, C. D. "Synthesis of the Tetracyclic Core of Exiguaquinol." *Org. Lett.* **2013**, *15*, 6014.
- Lam, J. K.*; Pham, H. V.*; Houk, K. N.; Vanderwal, C. D. "Computation and Experiment Reveal That the Ring-Rearrangement Metathesis of Himbert Cycloadducts Can Be Subject to Kinetic or Thermodynamic Control." *J. Am. Chem. Soc.* **2013**, *135*, 17585.
- Schmidt, Y.*; Lam, J. K.*; Pham, H. V.*; Houk, K. N.; Vanderwal, C. D. "Studies on the Himbert Intramolecular Arene/Allene Diels-Alder Cycloaddition. Mechanistic Studies and Expansion of Scope to All-Carbon Tethers." *J. Am. Chem. Soc.* **2013**, *135*, 7339.
- Pham, H. V.; Martin, D. B. C.; Vanderwal, C. D.; Houk, K. N. "The intramolecular Diels–Alder reaction of tryptamine-derived Zincke aldehydes is a stepwise process." *Chem. Sci.*, **2012**, *3*, 1650.
- Petric, A.; Johnson, S. A.; Pham, H. V.; Li, Y.; Ceh, S.; Golobic, A.; Agdeppa, E. D.; Timbol, G.; Liu, J.; Keum, G.; Satyamurthy, N.; Kepe, V.; Houk, K. N.; Barrio, J. R. "Dicyanovinyl naphthalenes for neuroimaging of amyloids and relationships of electronic structures and geometries to binding affinities." *Proc. Acad. Nat. Sci.* **2012**, *109*, 16492.

*Authors contributed equally

Chapter 1.1. Studies on the Himbert Intramolecular Arene/Allene Diels–Alder Cycloaddition. Mechanistic Studies and Expansion of Scope to All-Carbon Tethers

Introduction

The unusual intramolecular arene/allene cycloaddition reaction reported over 30 years ago by Himbert and Henn^{1,2} (Eq. 1) converts relatively simple reactants into complex bridged polycyclic architectures that are themselves poised for further transformations. In what appears to be the first application of this chemistry, our UC Irvine laboratory used lactam-containing Himbert cycloadducts as the substrates for ring-rearrangement metathesis reactions, resulting in fused polycyclic lactams.³ This chemistry is part of our broader program to take advantage of underutilized processes to convert readily available aromatic systems into complex organic scaffolds.⁴ In past cases when mechanistic details have been difficult to glean from experiment, our UC Irvine and UC Los Angeles laboratories have engaged in fruitful collaborations involving DFT methods to provide useful insights into mechanism.⁵ In this disclosure, we report our joint investigation of some mechanistic aspects of the fascinating dearomatizing cycloaddition first described by the Himbert group, and an expansion of scope to include carbocyclic products that required key computational insights for success.

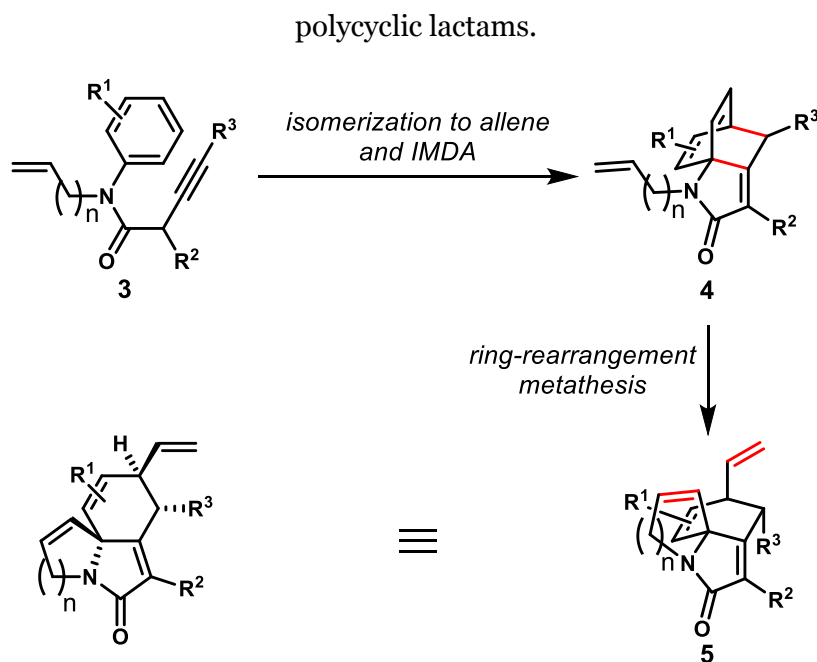


Background

Our recent work on the metathesis rearrangement of Himbert cycloadducts³ (Scheme 1.1.1) points to the utility of this fascinating cycloaddition reaction in strategies to rapidly access complexity from simple substrates. That work represents the first of many applications of this

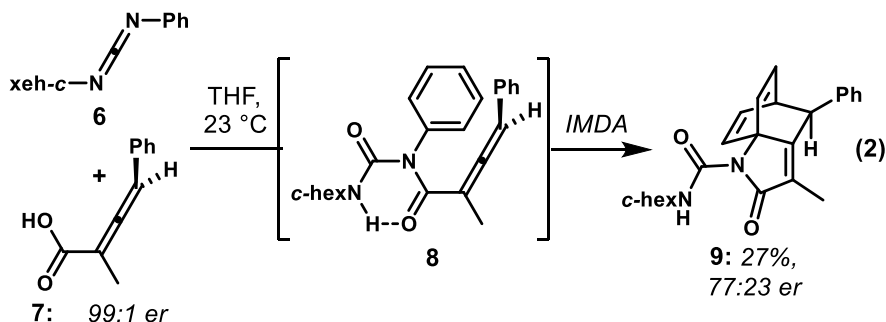
reaction that we are interested in pursuing. As a result, a greater understanding of the mechanism of this dearomatizing intramolecular Diels–Alder (IMDA) cycloaddition, which will provide better predictability in reaction outcome, is critical to our ongoing studies.

Scheme 1.1.1. Ring-rearrangement metathesis of Himbert cycloadducts to access complex.



Himbert and co-workers were the first to discover and study the scope of the intramolecular arene/allene cycloaddition reactions^{1,2} and, on the basis of the relative insensitivity of cycloaddition rates to donor and acceptor groups on the arene in amide-tethered substrates, they were led to favor a concerted cycloaddition mechanism over a polar, stepwise alternative.⁶ Trifonov and Orahovats studied closely related cycloadditions that were set up by the reaction of allenic acids with *N*-arylcarbodiimides (Eq. 2).⁷ After activated ester formation and *O*- to *N*-acyl transfer, a spontaneous cycloaddition of the *in situ*-generated allenecarboximide (**8**) ensued at ambient temperature. In contemplating a possible stepwise mechanism, they began with chiral, non-racemic allenic acid **7**, and subjected it to reaction with a variety of carbodiimides (only one example shown). In all cases, a significant loss of enantiomeric purity

was observed, and reasonable control experiments to ensure that the allenic acid had not racemized prior to reaction were performed. Keeping in mind the results of Himbert that argued against a stepwise *polar* pathway, they suggested that a stepwise radical mechanism would account for all of the data that was available to them (see below).⁷



We posited that a greater comprehension of the reaction mechanism across various substrate types would inform on which, if any, cycloadditions would proceed with high levels of conservation of enantiomeric purity. The ability to transfer allenic axial chirality to point chirality would be critical to some applications of this chemistry in the synthesis of enantiopure complex molecules, including natural products and scaffolds for medicinal chemistry. Furthermore, such an improved mechanistic understanding might facilitate the expansion of scope to systems with different tethers. In the first portion of this disclosure, we present a computational investigation of both the Himbert cycloaddition of allene carboxamides and the Orahovats variant, as well as supporting experimental results. In the second part, we document the previously unknown cycloaddition reactions of benzyl allenyl ketones, and show how computation provides a reliable predictive tool for these reactions.

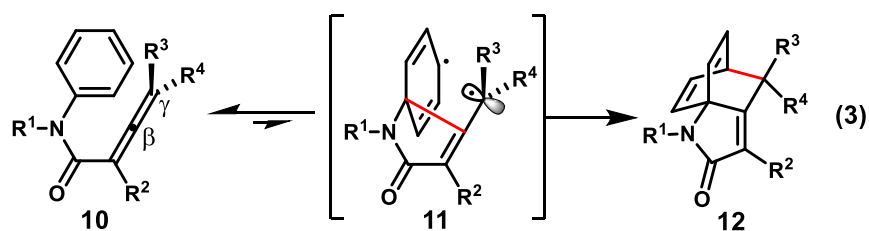
Results and Discussion

Cycloaddition Mechanism

The relatively narrow range of cycloaddition rates noted by Himbert among substrates with a broad range of electronically different arenes⁶ (also observed in our studies) effectively

militates against a polar stepwise mechanism. While there are no reported experimental observations that explicitly reject the notion of a concerted cycloaddition in the reactions studied by Himbert, the experiments of Orahovats do point to the possibility of a stepwise radical pathway. However, it should be noted that this specific system differed from most of the reactions studied by Himbert by the presence of the *N*-acylurea and, more importantly, the γ -phenyl substituent on the allene.

As noted by Orahovats and Trifonov,⁷ molecular models indicate that close proximity and excellent alignment of the *sp*-hybridized allene carbon with the *ipso*-carbon of the arene ring is easy to attain in these cycloaddition substrates; on the other hand, the distal carbons of each reacting π -system are not subject to such a perfect arrangement. This situation lends itself to the idea that five-membered ring formation—leading to a diradical intermediate of type **11** (Eq. 3)—might be a mechanistically relevant first step. Recombination of the pentadienyl radical and the alkyl radical on the γ -carbon of the former allene would complete the formal cycloaddition process. The intermediacy of spiro-fused biradical **11** provides a means for loss of enantioenrichment via rotation about the former allene C β –C γ σ -bond. Certainly, a key consideration for the stepwise radical mechanism is the stability of the partially cyclized biradical intermediate. Appropriate substituents present on the allene γ -carbon can offer significant stabilization to the resulting radical, which does not benefit immediately from allylic stabilization owing to orbital orthogonality.



To learn more about the underlying cycloaddition mechanism in both of the Himbert and Orahovats systems, we studied the energetics of the two likely mechanisms using density function

theory. Furthermore, we investigated the Himbert case experimentally using both stereochemical probes and substrates designed to detect radical behavior.

Cycloaddition of Allene Carboxanilides

Beginning with the Himbert reaction of the type shown in equations 1 and 3, both the concerted and the stepwise radical mechanisms were investigated. All stationary point structures were optimized using the B3LYP⁸ functional and 6-31G(d) basis set in Gaussian09.⁹ Single point calculations on closed-shell species were conducted with M06-2X/6-311+G(d,p) on the B3LYP optimized geometries. In general, B3LYP and M06-2X produce similar optimized geometries.¹⁰ However, activation energies and reaction energies as predicted by the two methods are different; as we have extensively benchmarked for cycloadditions such as those studied here,^{10a} B3LYP is known to overestimate barriers by ~5 kcal/mol for concerted processes but provide sufficiently accurate values for reactions leading to diradicals. Additionally, the energies of cycloaddition reactions are predicted by B3LYP to be ~10 kcal/mol less exothermic than experiment.¹¹ We have found that M06-2X single point calculations with reasonably large basis sets give much better values.

The M06-2X functional has been shown to provide accurate reaction energies and enthalpies for C–C bond formation, but has proven problematic for open-shell species.¹² We consider the M06-2X results to be most reliable for the concerted process; the relative energies of B3LYP open-shell (diradical) and closed-shell species are more reliable. Thus, the difference is used to phase the energetics of diradical species. We refer to the latter as corrected M06-2X energies. All energies by both methods are given in the Supporting Information. Vibrational frequencies were computed to determine the nature of each stationary point; local minima and transition structures showed 0 and 1 imaginary frequency, respectively. The Conductorlike Polarizable Continuum Model (CPCM)¹³ was used to compute solvation energies.

The reaction coordinate diagrams for both the concerted and stepwise mechanisms are shown in Figure 1.1.1. For the reaction **13** → **15**, the transition structures for the concerted reaction, **TS_13-15**, and the formation of the diradical, **TSDi_13-14**, are essentially isoenergetic, suggesting competition of both pathways. The formation of **15** is exergonic by 2.0 kcal/mol (M06-2X). B3LYP calculations suggest that this reaction is endergonic by 9.2 kcal/mol but, as alluded to earlier, this method is known to underestimate the exergonicity of cycloadditions.¹¹ The stepwise pathway initially leads to diradical intermediate **14**, which is 20.4 kcal/mol higher than the starting material. In this intermediate, the pentadienyl radical is extensively stabilized, but the other secondary radical does not initially benefit from allylic stabilization owing to the orthogonality of orbitals. From **14**, radical recombination with the *para*-carbon of the phenyl ring again yields **15**. The transition structure for the second step, **TSDi_14-15**, could not be located on the potential energy surface; all efforts resulted in the concerted transition structure or led directly to ring closure. In order to estimate the free energy value for this process, the C–C bond formed in the previous step was constrained to a value of 1.58 Å, slightly longer than its value of 1.55 Å in intermediate **14**. This process yielded an energy value for “**TS**”**Di_14-15** of about 37.8 kcal/mol, making it the rate-determining step of the stepwise reaction. Reversion of the diradical to reactants and subsequent concerted cycloaddition will be faster than ring closure to the cycloadduct.

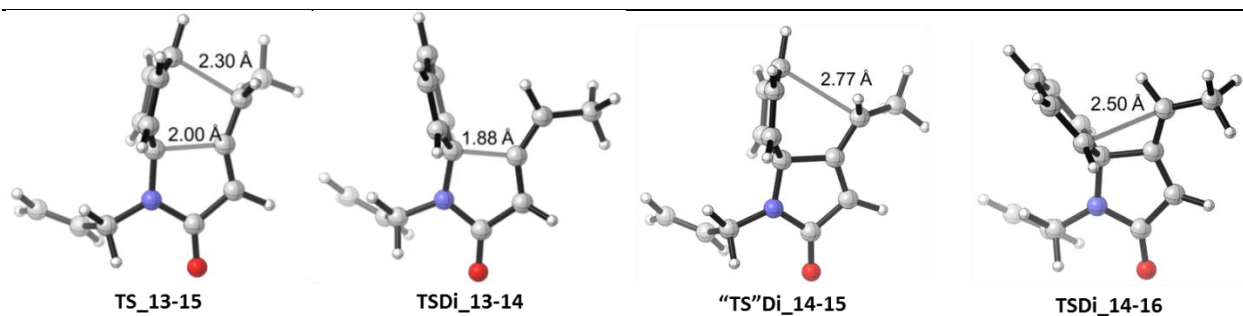
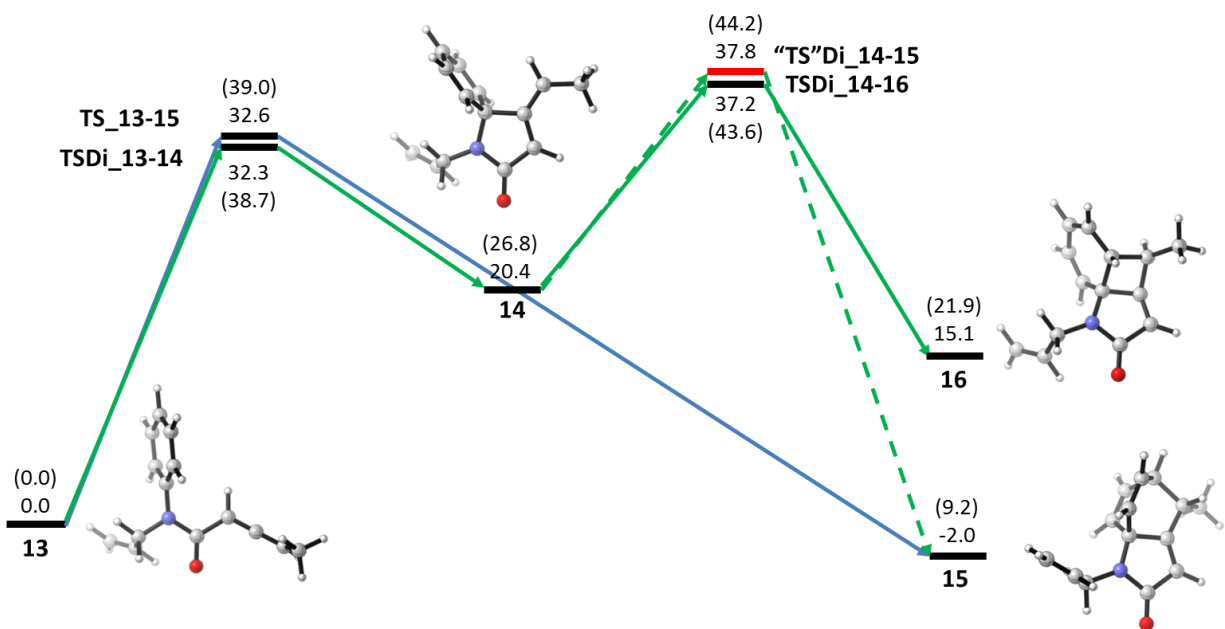
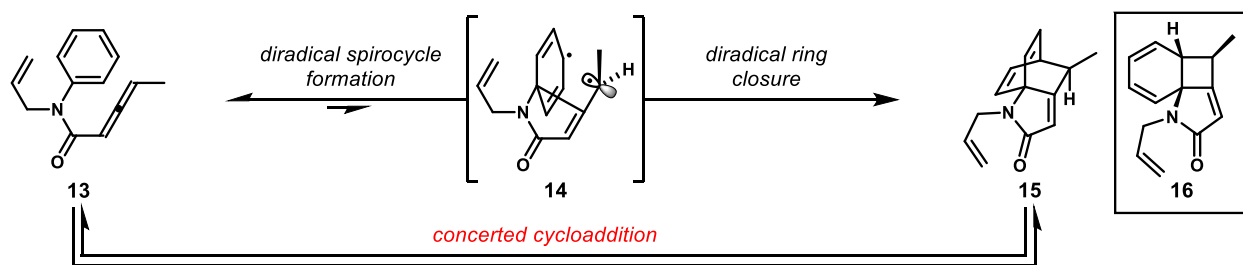


Figure 1.1.1. Calculated energies for the stepwise and direct cycloaddition of arene/allene **13**, with transition structure geometries shown below. All energies shown are in kcal/mol from Mo6-2X/6-311+G(d,p)/CPCM(xylenes) single point calculations on geometries optimized with B3LYP/6-31G(d). **"TS"_{Di_14-15}** (in red) was estimated by constraining the lactam C–C σ bond to 1.58 Å. B3LYP energies are shown in parentheses.

The transition state for the concerted and stepwise pathways have virtually identical energies; conceivably, a single transition state actually leads to both **15** and diradical **14**. This situation would require a bifurcation of the downhill pathway from **TS_13-15**, and related bifurcations have been found in ketene-diene cycloadditions.¹⁴

The energy barrier to cyclization to afford the formal [2+2] cycloaddition product **16** has a ΔG^\ddagger of 37.2 kcal/mol, similar to that for ring closure to observed product **15**. However, **16** is substantially unfavorable thermodynamically and would, if formed at all, reform diradical **14** and proceed either towards initial allene **13** or the more stable product **15**. This conclusion is consistent with the failure to observe product **16** experimentally.

The optimized transition structures for the intramolecular cycloaddition of allenecarboxamide **13** are also shown in Figure 1.1.1. The concerted transition structure **TS_13-15** is slightly asynchronous, with forming-bond lengths of 2.0 Å and 2.3 Å. The diradical transition structure **TSDi_13-14** is relatively late, as indicated by the short C–C forming-bond length of 1.88 Å. By contrast, the two diradical-closing transition structures “**TS**” **Di_14-15** and **TSDi_14-16** are early, demonstrating longer bond lengths typical of radical recombinations.

The reaction is carried out at 170 °C and is nearly thermoneutral. Therefore, the reaction should be reversible and under thermodynamic control. An exergonicity of only 2.0 kcal/mol is consistent with the observed 74% yield of **15**. The computed equilibrium constant, $[\mathbf{15}]/[\mathbf{13}] = 9.7$. By examining the calculated thermodynamic energies of the reactants and products, the outcome of this reaction, as well as those of related analogs, can be predicted (see below).

These results predict that this particular Himbert cycloaddition proceeds via a concerted pathway, but that a single reversible cyclization to form diradical intermediate **14** is competitive with the direct Diels–Alder process. As a result, it might be possible to racemize chiral, enantioenriched allenes via diradicals of type **14**, even while the only productive pathway is via the concerted cycloaddition, a reaction that would be expected to be stereospecific. We have

performed experiments, analogous to those of Orahovats and Trifonov, to test the idea that such a racemization pathway might occur (Figure 1.1.2a). Racemic *N*-methyl allenecarboxanilide **18** was prepared by Wittig reaction of the precursor phosphorane **17** with *in situ*-generated methylketene as described by Himbert,¹⁵ and it was resolved by semi-preparative HPLC using chiral solid supports to obtain (–)-**18** and (+)-**18**, each of greater than 99:1 *e.r.*¹⁶ At this stage, the absolute configuration of these enantiomeric allenes is unknown. Representative experiments shown in the table of Figure 1.1.2 revealed that our hypothesis—that racemization might be competitive with stereospecific cycloaddition—appears to be correct. When enantiomerically enriched **18** was heated to 170 °C, conversion was nearly complete after 4 hours, affording cycloadduct **19** in 80:20 *e.r.* Further experiments revealed a time-dependent decrease in enantiopurity of the product, such that after 24 hours the product was isolated with a 64:36 *e.r.* and in low yield owing to thermal decomposition. However, running the reaction at 140 °C led to product formation with reasonable conservation of enantioselectivity. Therefore, the apparent competition between partial cyclization/allene racemization and direct stereospecific cycloaddition is worthy of concern, but the use of the minimal temperatures needed to promote cycloaddition can lead to products with useful levels of enantioenrichment.

We presumed that loss of enantioenrichment over time occurs in part via reversible cycloaddition with racemization of the allene via radical spirocyclization (also reversible). To test this idea, we investigated the thermal racemization of enantioenriched cycloadduct (Figure 1.1.2b), also obtained by semi-preparative HPLC on chiral solid support. Heating of enantioenriched cycloadduct (+)-**19** to 170 °C for 10 h led to a slight erosion of enantiopurity (from $\geq 99:1$ to 90:10 *e.r.*), whereas heating to 140 °C for the same time led to recovery of enantiopure material. All of this data points to a concerted cycloaddition that is readily reversible given enough thermal energy, and the idea that racemization occurs by reversible spirocyclization via a radical process appears reasonable. Of course, other means of allene racemization cannot be

completely ruled out, but the neutral conditions in this case make racemization via acid-base chemistry or reversible nucleophilic attack to the allene unlikely. Furthermore, in reactions that did not proceed to complete conversion, recovered allene was still highly enantioenriched (96:4 *e.r.* at 140 °C, 88:12 *e.r.* at 170 °C).

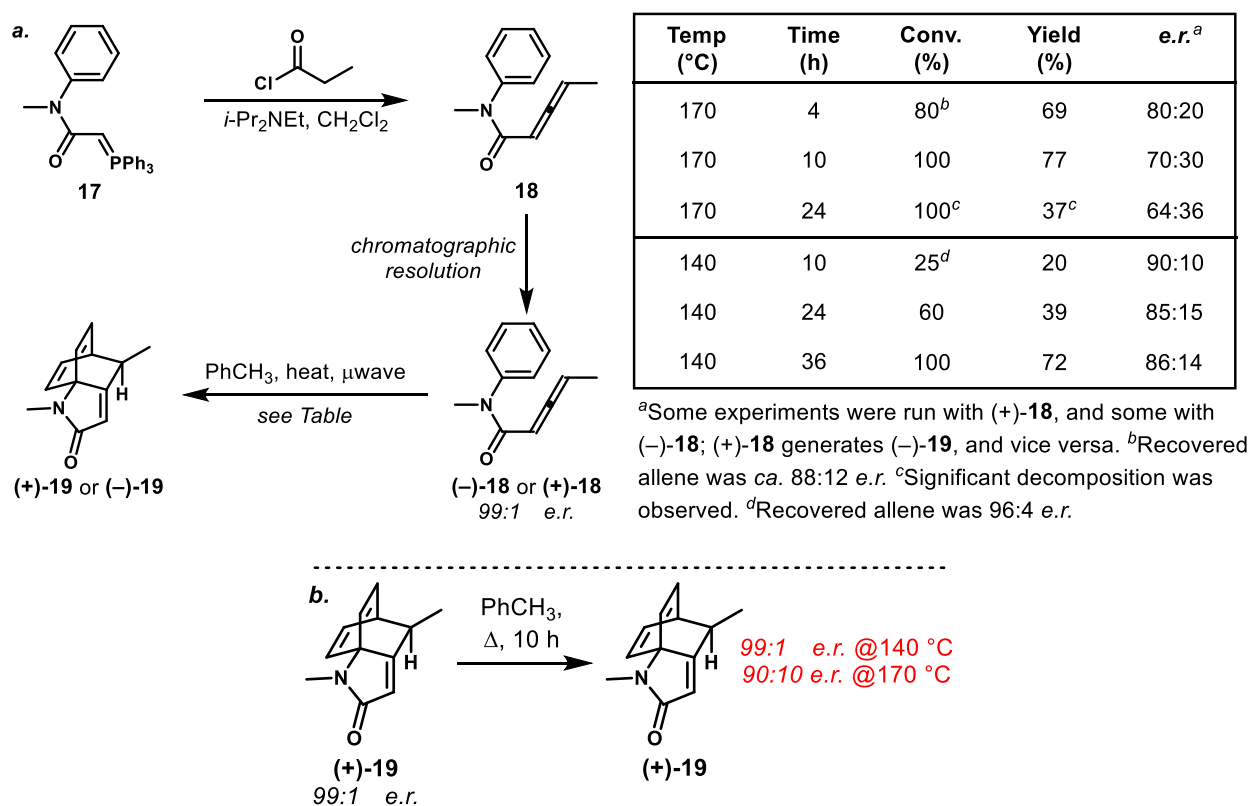
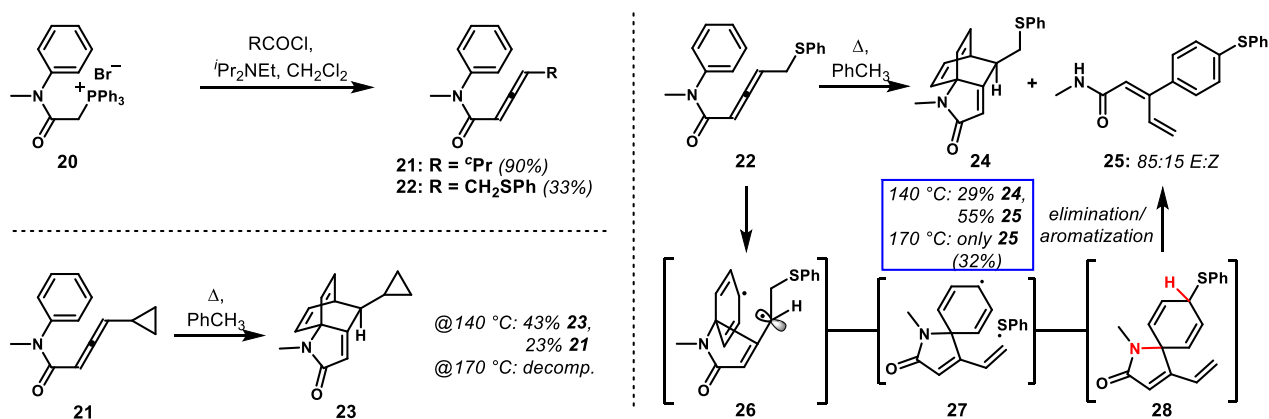


Figure 1.1.2. a. Cycloaddition studies on enantiomerically enriched allene **18**. **b.** Racemization studies on enantiomerically enriched cycloadduct **(+)-19**.

Most importantly, we have shown that there is the possibility of these Himbert cycloadditions proceeding with a significant axial to central chirality transfer. The degree to which enantiopurity is conserved will likely be influenced by the radical stabilizing ability of the allene γ -substituent, and certainly by the reaction temperature.

For probes to detect the intermediacy of radical intermediates, we considered cyclopropane- and phenylthiomethyl-bearing allenes. Generation of γ -cyclopropyl-substituted allene **21** and γ -thiophenylmethyl allene **22** (Scheme 1.1.2) was readily achieved using Wittig chemistry analogous to the method previously described by Himbert.^{15,16} When cyclopropylallene **21** was warmed to 140 °C for 8 h, a relatively clean mixture of unreacted allene and cycloadduct **23** was observed; however, at 170 °C, complete decomposition was observed. This result is consistent with the accessibility of the cycloreversion reaction, which might permit decomposition via radical intermediates related to **14**. In this case, cyclopropylcarbinyl radical ring-opening could lead to a host of different—and difficult to predict—reaction products. In search of a more compelling outcome, we examined thioether **22**. We assumed that the methylene spacer insulating the thioether from the allene in the presumed cycloaddition precursor would reduce any serious steric or electronic impact of this group. We hypothesized that, if the radical mechanism were operative, expulsion of phenylthiyl radical from an intermediate like **26** followed by radical recombination would lead to spirocyclic products related to **28**. When **22** was heated to 140 °C, we obtained a 1:1.7 ratio of cycloadduct **24** to diene **25** (*E:Z* mixture), whose origin is most easily explained by the radical cascade that we had predicted, followed by elimination of the amide to restore aromaticity. At 170 °C, rearranged diene **25** was the only identifiable product.

Scheme 1.1.2. Experiments to test for radical intermediates.



We believe that the outcome of these experiments further supports the potential competition of radical-based reactions in these Himbert cycloadditions, and opens up possibilities to engineer intriguing new reactions based on the relatively facile formation of diradical intermediates of type **26**.

Cycloaddition of Allenic Imides

We have also computationally examined the substrate used by Orahovats.⁷ Urea **8**, formed *in situ* as shown in Equation 2, undergoes cycloaddition to form **9** at ambient temperatures. The key differences present in **9** and the Himbert substrate **13** are the *N*-acylurea group, which is able to engage in intramolecular hydrogen bonding, the methyl group on the allene α -carbon, and the phenyl substituent on the allene γ -carbon (in place of the methyl substituent in **13**). The concerted and stepwise cycloaddition pathways of **29**, a model for imide **8** wherein the cyclohexyl substituent has been replaced with a methyl group, were studied computationally, and are presented in Figure 1.1.3.

The cycloaddition with the Orahovats *N*-acylurea compound shows a greater preference for the stepwise biradical pathway than the Himbert amide case, with **TSDi_29-30** located 1.5 kcal/mol lower than the concerted transition structure **TS_29-31**. Both pathways lead to the energetically favored cycloadduct **31**, with the radical pathway traversing through the diradical intermediate **30**. As expected, the phenyl group on the allene stabilizes the forming diradical; the intermediate is 16.2 kcal/mol higher than the starting material, compared with 20.4 kcal/mol for intermediate **14**. Radical recombination is still the rate-determining step at 24.3 kcal/mol. In short, the computed energetics for this reaction nicely explain the loss of enantioenrichment reported by Orahovats as shown in Equation 2, and in close analogy to our observations with amide **18**.

The overall lowering of the energetics for the Orahovats imide may be attributed in part to the destabilization of reactant **29**; the methyl substituent on the allene prevents adoption of a conformation in which the p-orbitals of the allene are conjugated to the π -system of the amide, thereby preventing stabilization through conjugative effects. The hydrogen-bonding arrangement (shown in Equation 2 and Figure 1.1.3) likely also contributes to the facility of this reaction by biasing in favor of conformations conducive to cycloaddition.¹⁷ As shown earlier, formation of the formal [2+2] cycloadduct is highly thermodynamically unfavorable and was not modeled in this reaction.

Our computational studies strongly suggest that the most favorable cycloaddition mechanism is a concerted pathway, because the second steps of the stepwise diradical mechanisms are highest in energy in both the Himbert and Orahovats systems. Previously described experimental results from Orahovats and new results from our group do corroborate the conclusion reached by computation that the first step of the stepwise diradical mechanism can be competitive with the concerted cycloaddition in both systems; this phenomenon manifests itself in experiment by incomplete conservation of enantiopurity. The preference of one pathway over the other may be influenced by substituents on the benzene or allene components; substituents that stabilize the forming diradical should increase the likelihood of the diradical pathway. The fact that, at lower temperatures, we retained most of the enantioenrichment with substrate **18**—which bears only a methyl group in the γ -position of the allene—but the Orahovats example with the γ -phenyl group suffered greater degradation of enantioenrichment, strongly supports this idea. Most importantly, a mechanism for racemization of chiral, enantioenriched allenes is presented by the relatively low barrier to spirocyclization via a radical manifold, and this potential issue needs to be considered in planning for the use of these types of cycloadditions to access enantioenriched materials. Fortunately, it appears that computation can provide guidance in this regard.

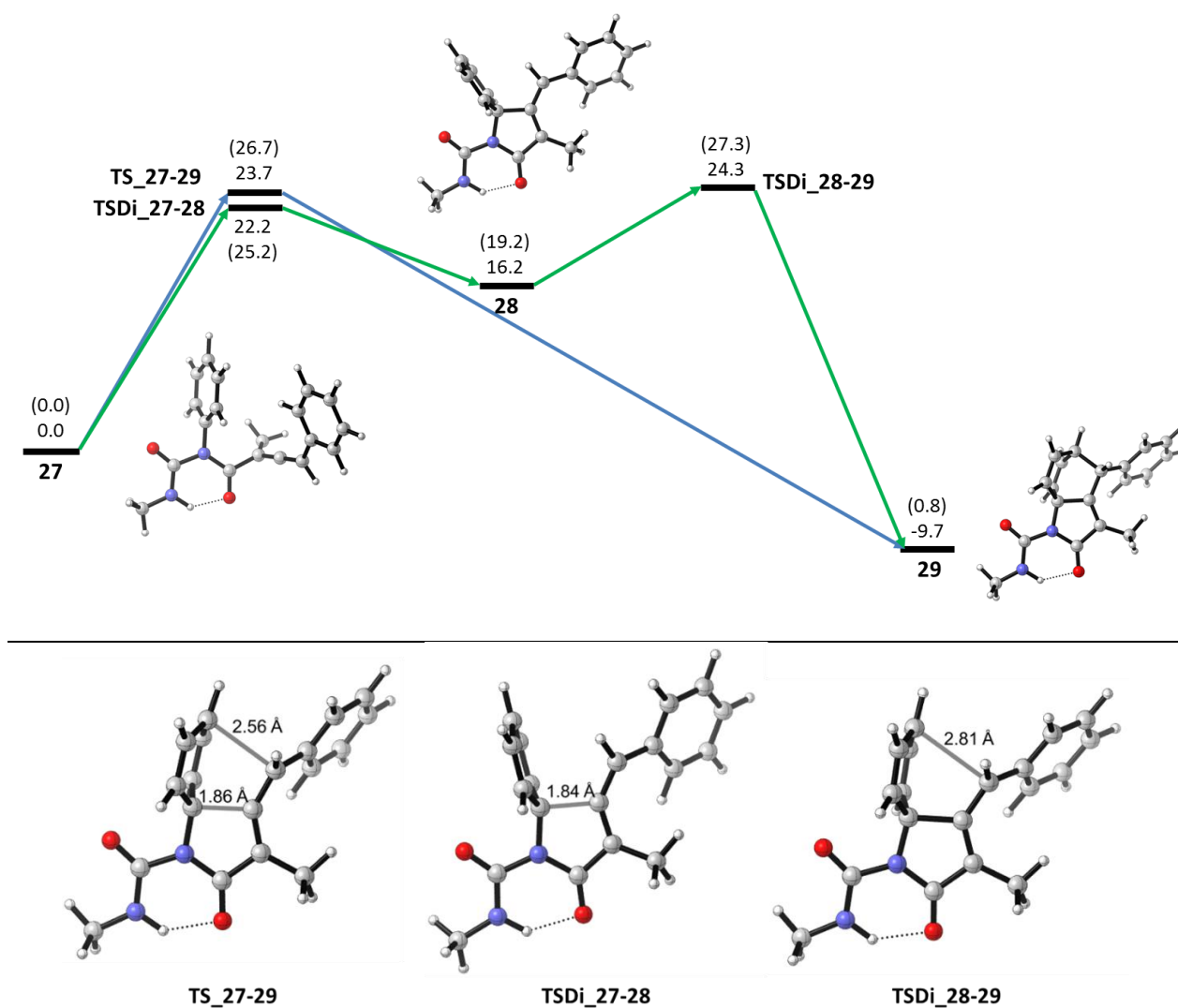
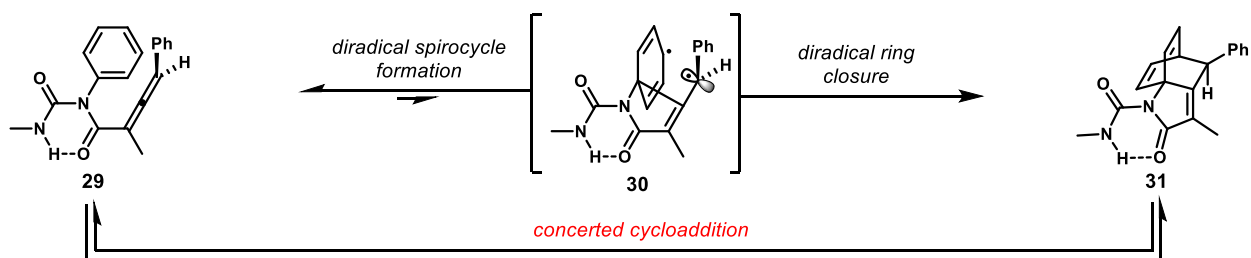


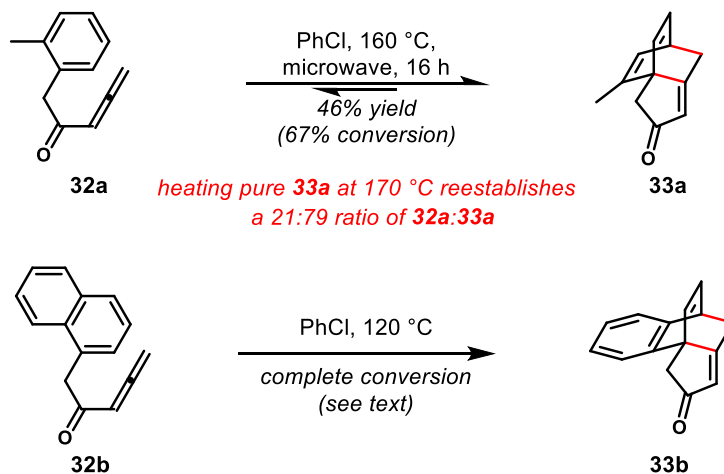
Figure 1.1.3. Calculated energies for the stepwise and direct cycloaddition of arene/allene **29**, with transition structure geometries shown below. All energies shown are in kcal/mol from Mo6-2X/6-311+G(d,p)/CPCM(THF) single point calculations on geometries optimized with B3LYP/6-31G(d). B3LYP energies are shown in parentheses.

Expansion of Substrate Scope to Carbocyclic Systems

In all of the experiments described by the Himbert and Orahovats groups, either carboxylic acid derivatives (amides, esters, thioesters, imides) or phosphorus-based groups (phosphonate esters, phosphinate esters, phosphinic amides) were used as tethers.¹⁸ No examples of benzyl allenyl ketones were ever reported; therefore, as a first extension to different polycyclic architectures, we sought to extend the two-step sequence to carbon-linked systems. The allenyl ketone substrates were, for the most part, made by propargylmetal additions to arylacetaldehydes followed by oxidation.^{16,19}

Our efforts to extend Himbert cycloaddition reactivity to these carbon-linked systems were initially met with mixed results (Scheme 1.1.3). Benzyl allenyl ketone **32a** was partially converted (*ca.* 67%, with slight decomposition) to carbocycle **33a** after heating to 160 °C for 12 hours. Longer reaction times did not improve conversion. Heating isolated cycloadduct **33a** to 170 °C established an equilibrium mixture of allene/cycloadduct, clearly demonstrating that the limited conversion of benzyl allenyl ketone **32a** was a thermodynamic issue. On the other hand, naphthyl system **32b** proceeded with complete conversion—largely to tetracycle **33b**—under milder conditions, pointing to both a more kinetically facile and thermodynamically favorable dearomatization of the fused arene system. Starting allene **32b** could not be purified to homogeneity; from material of only about 75% purity, a 54% yield of cycloadduct was obtained, indicating that the reaction is relatively efficient (*ca.* 70% corrected).

Scheme 1.1.3. Representative Himbert cycloadditions with all-carbon tethers.



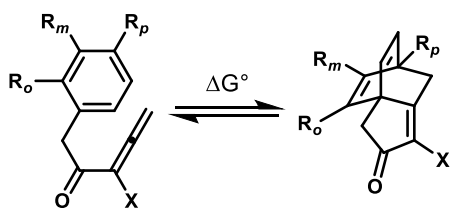
Thermodynamic Considerations and Computational Guidance

In combination with the calculated exergonicity of the cycloaddition of amide **13** of only 2 kcal/mol, the experiments with ketone **32a** suggested that many Himbert-type cycloadditions might be close to thermoneutral. This problem appears to be particularly prevalent for carbon-linked systems bearing monocyclic aromatic dienes. Because calculated energies of reaction for the amide-tethered cases using MO6-2X were quite consistent with experimental results, we used computation as a predictive tool to see what substitution patterns on the benzyl allenyl ketone substrates should perturb the equilibrium toward products (Table 1.1.1).

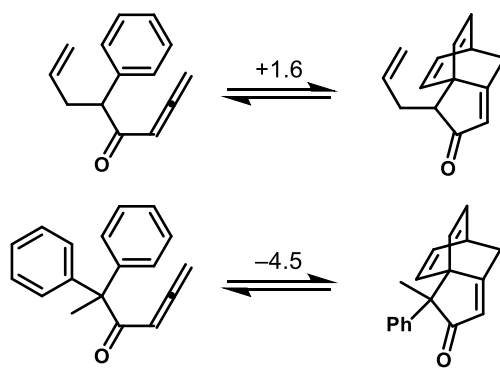
The most important lesson learned from computational analysis of this reaction type was that substitution of most any group at the allene α -position would lead to a favorable reaction outcome. Most exciting was the observation that donor (methoxy) and acceptor (carbomethoxy, carboxamide) groups, alkyl groups (methyl), and a potentially removable substituent (chloride) all led to thermodynamically favored reactions according to computation; the fact that such different groups all led to predicted improvement in reaction outcome strongly suggests that the origin of the effect is steric in nature. Of the substrates evaluated by computation, the only outlier

to this α -substituent effect is trimethylsilyl, which is most unusual. On its own, this result might be explained on the basis of allene stabilization; however, one would expect the α -methoxy group to have a significant stabilizing effect on the allene as well. Attribution to the extreme steric bulk of the group might be reasonable; however, placing a *t*-butyl group at this position still, while overall leading to a thermoneutral reaction, has a net benefit on the thermodynamics of the cycloaddition relative to the unsubstituted case. At this stage, we do not have a clear hypothesis for the trimethylsilyl effect. Because this group is not beneficial to the cycloaddition chemistry, more detailed investigations did not seem warranted.

Table 1.1.1. Computed thermodynamic energies (MO6-2X, in kcal/mol) of the Himbert cycloadditions of various substituted carbon-linked arene/allenes.



X	R	ΔG°	X	R	ΔG°
H	H	+0.4	H	$R_o = \text{OMe}$	-1.9
CO_2Me	H	-4.1	H	$R_m = \text{OMe}$	-1.8
CONHMe	H	-4.6	H	$R_p = \text{OMe}$	+2.0
SO_2Me	H	-3.0	H	$R_o = \text{Me}$	-2.1
Cl	H	-4.0	H	$R_m = \text{Me}$	+3.2
OMe	H	-2.1	H	$R_p = \text{Me}$	+0.8
Me	H	-2.3	H	$R_o = \text{F}$	+2.0
TMS	H	+2.4	H	$R_o = \text{Cl}$	-0.4
<i>t</i> -Bu	H	+0.1	H	$R_o = \text{CF}_3$	-0.8
Me	Me	-5.0	H	$R_o = R_{o'} = \text{Me}$	-2.5



We had posited that placing a donor group on the aromatic ring to mimic the electronic effects of the nitrogen atom in the amide-linked cases might lead to equilibria that favored products. It is evident from the computational data that this hypothesis was too simplistic;

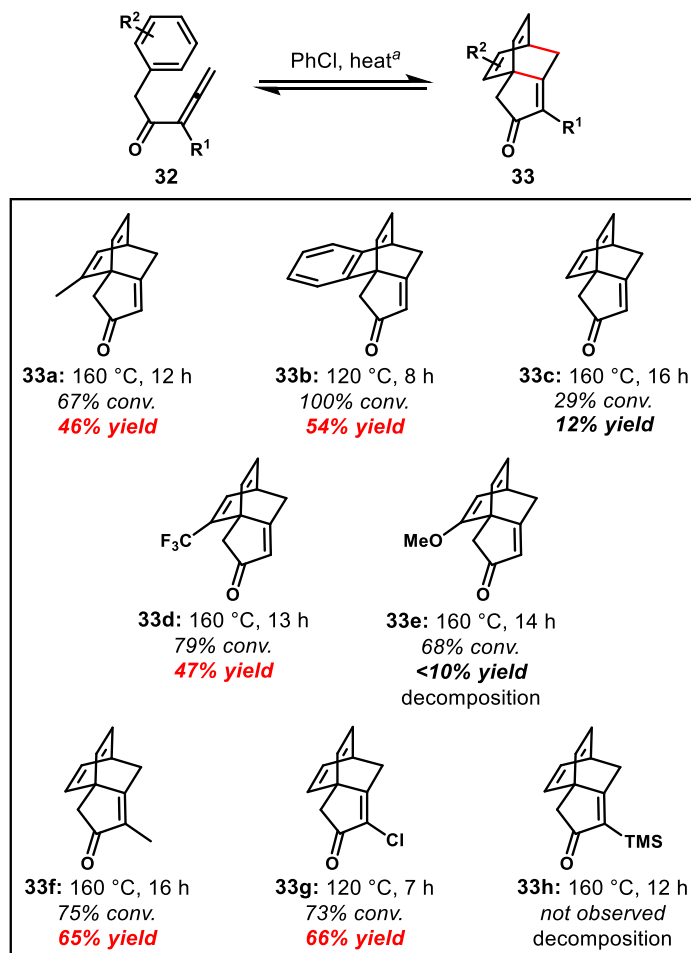
methoxy groups *ortho* and *meta* to the tether lead to favored cycloadditions, whereas placement in the *para* position leads to less favorability. Methyl substitution at the *meta* position appears detrimental. Clearly, the thermodynamic profile of these reactions is affected by both electronic (possible perturbation of either starting material or product ground state energies) and steric factors, and simple trends corresponding with, for example, Hammett parameters,²⁰ did not become obvious. The beneficial effects appear to be somewhat additive in some cases, with a highly favored reaction (5.0 kcal/mol) for the substrate with both allene α -methyl and arene *o*-methyl substituents.

Finally, we note that the presence of a tethered alkene at the ketone α -position (for prospective metathesis rearrangement) makes the cycloaddition less favorable, but a benzylic quaternary center leads to a reaction that is calculated to be highly favored.

Table 1.1.2 shows the outcome of many laboratory experiments that corroborate the computational results. We observed that computational predictions were accurate in all reactions that cleanly proceeded to products; unfortunately, some of the cycloadditions with carbon tethers were more prone to decomposition than the amide-tethered cases, likely owing to facile enol formation and electrocyclic ring-closure, among other possibilities.^{21,22} Certainly, the most important results are those that match the success predicted by computation with the α -methyl and α -chloro groups on the allene (**33f** and **33g**, respectively), simply because they indicate that either an alkyl group *or* a potentially removable/replaceable chloride will favor the formation of cycloadducts.

Although more detailed studies are required, if we assume additivity in the effects of substituents, the dramatic improvement afforded by the inclusion of certain substituents on the allene and the arene offers promise of a relatively general complexity-generating cycloaddition. Some noteworthy examples can be found in the next section.

Table 1.1.2. Scope of the Himbert arene/allene cycloaddition with all-carbon tethers.



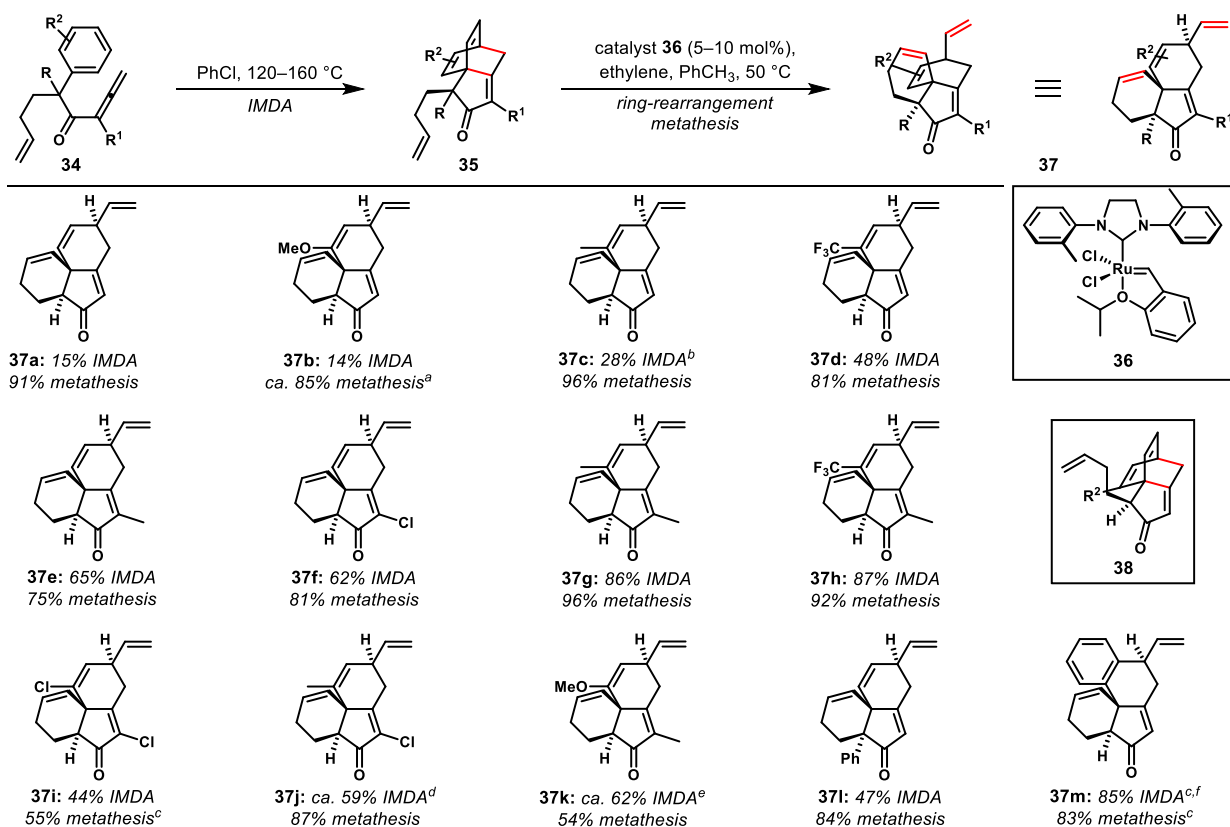
^aConversion values are NMR-based estimates of starting material disappearance, and undesired side products are often observed.

At this stage, we are uncertain why the carbon-linked systems demonstrate different thermodynamic profiles compared with heteroatom-linked substrates; there is significant latitude with respect to linking heteroatom (nitrogen, oxygen, sulfur)^{18a,c,d} in the previous reports, suggesting that the detrimental effect of carbon is more subtle than a simple electronegativity or atomic size argument. However, the synthetically useful yields obtained in many of the cases in Table 1.1.2 clearly demonstrate that an *sp*²-hybridized heteroatom is not absolutely required for successful cycloadditions.

Rapid Generation of Complex Polycycles via Carbocyclic Himerb Cycloaddition and Ring-Rearrangement Metathesis

Because of our desire to access complex all-carbon polycyclic scaffolds using this chemistry, we made several substrates bearing butenyl groups at the benzylic position. Himerb cycloadditions proceeded similarly to the unfunctionalized cases shown in Table 1.1.2. We are pleased to report that metathesis rearrangements of the products that we have generated in this way proceed smoothly to generate the complex carbopolycycles shown in Table 1.1.3. Second-generation Hoveyda–Grubbs-type catalyst **36**²³ performed well in these reactions, as they had in the lactam cases that we had previously reported.³ In several cases, the cycloaddition efficiency is low, as expected on the basis of our computational results. On the other hand, most of the cases are quite efficient, and we note the excellent results when two substituents that predict favorability based on computation are combined (esp. **37g** and **37h**). Finally, the metathesis rearrangement process is efficient in all cases, leading to tri- and tetracyclic compounds that bear natural-product-like scaffolds. Product **37l** is particularly noteworthy, because of its vicinal quaternary stereogenic centers.²⁴

Table 1.1.3. Sequential Himbert arene/allene cycloaddition and ring-rearrangement metathesis to access all-carbon polycycles.



a. While the metathesis reaction was very efficient based on the NMR spectra of the crude reaction mixture, this product decomposed upon attempted purification. b. 17% allene starting material was recovered. c. X-ray structure obtained. d. The allene starting material was unstable, and precluded accurate yield determination. e. 90:10 *d.r.*, 33% yield of the ketone derived from enol ether hydrolysis was also isolated; ^f94:6 *d.r.*

In all cases, the substrates were synthesized in racemic form, and the cycloadducts are therefore also obtained in racemic form. It is noteworthy that the cycloaddition reactions of substrates bearing groups at the *ortho* position of the aromatic ring (those leading to **37b–d**, **37g–k**, and **37m**) are highly diastereoselective, fortuitously providing as the major isomers those that can more easily undergo the subsequent metathesis rearrangement (see **38**) to afford polycyclic ketones **37**. Multiple side products were formed in the cycloadditions leading to **37b** and **37c**, preventing careful analysis of diastereoselectivity; however, the others were all formed in at least 9:1 *d.r.* The high selectivity presumably arises from minimization of A_{1,3}-strain²⁵ in the reactive conformation/transition structure, as shown in Figure 1.1.4.

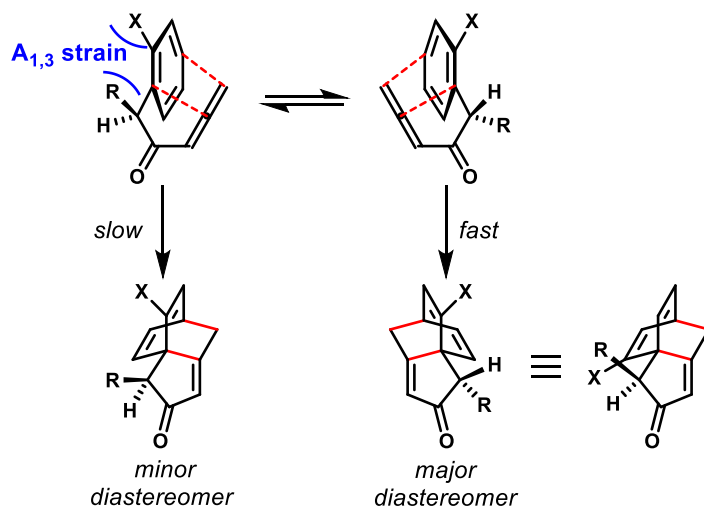
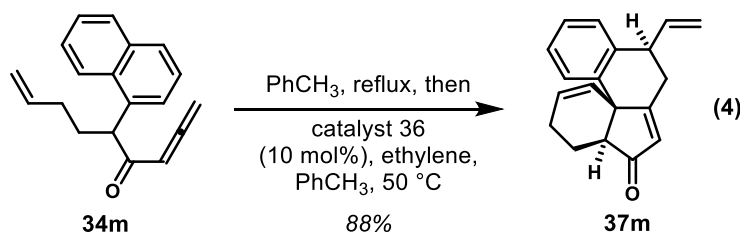


Figure 1.1.4. Plausible model for diastereocontrol based on minimization of allylic strain.

Perhaps not surprisingly, both the cycloaddition and metathesis rearrangement steps can be carried out in a single pot: after consumption of allene **34m**, addition of the ruthenium metathesis catalyst and an atmosphere of ethylene with warming directly provides **37m** in an improved yield as compared with the two-pot process, likely owing to the elimination of one purification step (Equation 4).



Conclusion

Through the combination of experiment and computation, we have learned that the dearomatizing arene/allene cycloaddition first reported by Himbert very likely proceeds by a concerted process rather than the stepwise radical process put forth by Orahovats. However, the first step of the two-step reaction proposed by Orahovats can be competitive, and offers a

mechanism for the racemization of chiral allenes. We have also determined that the carbon-tethered Himer cycloaddition, which had not been reported previously, is feasible in many cases, but can suffer from thermodynamic unfavorability with some substrates. Furthermore, computation provides an excellent predictive tool for these reactions, which will permit the evaluation of specific cycloadditions prior to experiment.

Looking forward, we aim to further improve the scope and efficiency of the carbon-tethered variant, perhaps via catalysis. We will continue to use computation to evaluate new Himer-type systems for feasibility, as we extend to other tether types, including temporary connections of arene diene and allene dienophile. Other, non-metathesis rearrangements of the strained cycloadducts and applications in complex molecule synthesis are also under intense study in our laboratories.

References

1. Himbert, G.; Henn, L. *Angew. Chem. Int. Ed.* **1982**, *21*, 620.
2. The Himbert group published over twenty articles describing this body of work. Please see the Supporting Information for the complete listing of the references.
3. Lam, J. K.; Schmidt, Y.; Vanderwal, C. D. *Org. Lett.* **2012**, *14*, 5566–5569.
4. Vanderwal, C. D. *J. Org. Chem.* **2011**, *76*, 9555–9567.
5. (a) Pham, H. V.; Martin, D. B. C.; Vanderwal, C. D.; Houk, K. N. *Chem. Sci.* **2012**, *3*, 1650–1655. (b) Paton, R. S.; Steinhardt, S. E.; Vanderwal, C. D.; Houk, K. N. *J. Am. Chem. Soc.* **2011**, *133*, 3895–3905.
6. Himbert, G.; Fink, D.; Diehl, K.; Rademacher, P.; Bittner, A. J. *Chem. Ber.* **1989**, *122*, 1161–1173.
7. Trifonov, L. S.; Orahovats, A. S. *Helv. Chim. Acta.* **1989**, *72*, 59–64.
8. (a) Lee, C.; Yang, W.; Parr, R. G. *Phys. Rev. B* **1988**, *37*, 785–789. (b) Becke, A. D. *J. Chem. Phys.* **1993**, *98*, 5648–5652. (c) Parr, R. G. *Annu. Rev. Phys. Chem.* **1995**, *46*, 701–728.
9. Gaussian 09, Revision C.01, Frisch, M. J.; Trucks, G. W.; Schlegel, H. B.; Scuseria, G. E.; Robb, M. A.; Cheeseman, J. R.; Scalmani, G.; Barone, V.; Mennucci, B.; Petersson, G. A.; Nakatsuji, H.; Caricato, M.; Li, X.; Hratchian, H. P.; Izmaylov, A. F.; Bloino, J.; Zheng, G.; Sonnenberg, J. L.; Hada, M.; Ehara, M.; Toyota, K.; Fukuda, R.; Hasegawa, J.; Ishida, M.; Nakajima, T.; Honda, Y.; Kitao, O.; Nakai, H.; Vreven, T.; Montgomery, Jr., J. A.; Peralta, J. E.; Ogliaro, F.; Bearpark, M.; Heyd, J. J.; Brothers, E.; Kudin, K. N.; Staroverov, V. N.; Keith, T.; Kobayashi, R.; Normand, J.; Raghavachari, K.; Rendell, A.; Burant, J. C.; Iyengar, S. S.; Tomasi, J.; Cossi, M.; Rega, N.; Millam, J. M.; Klene, M.; Knox, J. E.; Cross, J. B.; Bakken, V.; Adamo, C.; Jaramillo, J.; Gomperts, R.; Stratmann, R. E.; Yazyev, O.; Austin, A. J.; Cammi, R.; Pomelli, C.; Ochterski, J. W.; Martin, R. L.; Morokuma, K.; Zakrzewski, V. G.; Voth, G. A.; Salvador, P.; Dannenberg, J. J.; Dapprich, S.; Daniels, A. D.; Farkas, O.; Foresman, J. B.; Ortiz, J. V.; Cioslowski, J.; Fox, D. J. Gaussian, Inc., Wallingford CT, 2010.
10. Ess, D. H.; Houk, K. N. *J. Phys. Chem. A* **2005**, *109*, 9542–9553. b) Pieniazek, S. N.; Clemente, F. R.; Houk, K. N. *Angew. Chem., Int. Ed.* **2008**, *47*, 7746–7749.
11. Check, C. E.; Gilbert, T. M.; *J. Org. Chem.* **2005**, *70*, 9828–9834.
12. Zhao, Y.; Truhlar, D. G. *J. Phys. Chem. A* **2008**, *112*, 1095–1099.
13. Cossi, M.; Rega, N.; Scalmani, G.; Barone, V. *J. Comput. Chem.* **2003**, *24*, 669–681.
14. (a) Ussing, B. R.; Hang, C.; Singleton, D. A. *J. Am. Chem. Soc.* **2006**, *128*, 7594–7607. (b) Ess, D. H.; Wheeler, S. E.; Iafe, R. G.; Xu, L.; Celebi-Olcum, N.; Houk, K. N. *Angew. Chem. Int. Ed.* **2008**, *47*, 7592–7601.

15. Himbert, G.; Diehl, K.; Schlindwein, H. *J. Chem. Ber.* **1989**, *122*, 1691–1699.
16. Please see Supporting Information in the original publication for details.
17. Himbert, G.; Diehl, K.; Maas, G.; *J. Chem. Soc., Chem. Commun.* **1984**, 900–901.
18. (a) Himbert, G.; Fink, D. *Tetrahedron Lett.* **1985**, *26*, 4363–4366. (b) Trifonov, L. S.; Simova, S. D.; Orahovats, A. S. *Tetrahedron Lett.* **1987**, *28*, 3391–3392. (c) Himbert, G.; Fink, D. *Z. Naturforsch. B; Chem. Sci.* **1994**, *49*, 542–550. (d) Himbert, G.; Ruppnich, M.; Knöringer, H. *J. Chin. Chem. Soc.* **2003**, *50*, 143–151.
19. (a) Alcaide, B.; Almendros, P.; Martínez del Campo, T.; *Eur. J. Org. Chem.* **2007**, 2844–2849. (b) Marx, V.; Burnell, D. J. *Org. Lett.* **2009**, *11*, 1229–1231.
20. Anslyn, E. V.; Dougherty, D. A. *Modern Physical Organic Chemistry*, University Science Books: Sausalito, CA, 2006, pp 445–453.
21. (a) For an early example of the electrocyclization of a stable enol derivative, see: Woodward, R. B. In *Aromaticity*; Chemical Society Special Publication: London, **1967**; Vol. 21, p 217. See also: (b) Shibuya, M. *Tetrahedron Lett.* **1983**, *24*, 1175–1178. (c) Büchi, G.; Leung, J. C. *J. Org. Chem.* **1986**, *51*, 4813–4818.
22. In the amide-tethered variants studied extensively by Himbert, quinolone formation attributed to electrocyclization was observed in some cases. For an example, see: Diehl, K.; Himbert, G.; Henn, L. *Chem. Ber.* **1986**, *119*, 2430–2443.
23. Stewart, I. C.; Ung, T.; Pletnev, A. A.; Berlin, J. M.; Grubbs, R. H.; Schrodi, Y. *Org. Lett.* **2007**, *9*, 1589–1592.
24. Peterson, E. A.; Overman, L. E. *Proc. Natl. Acad. Sci. U.S.A.* **2004**, *101*, 11943–11948.
25. Hoffmann, R. W. *Chem. Rev.* **1989**, *89*, 1841–1860.

Chapter 1.2. Diels–Alder Reactions of Allene with Benzene and Butadiene: Concerted, Stepwise, and Ambimodal Transition States

Introduction

Allenes readily undergo thermal pericyclic reactions, including Diels–Alder, 1,3-dipolar, and (2+2) cycloadditions.¹ There is some evidence that these reactions are stepwise, although few systematic investigations are available. We report multiconfigurational complete active space (CAS) computational studies of the reactions of allene with butadiene and with benzene, aliphatic and aromatic dienes in Diels–Alder reactions (Figure 1.2.1).^{2,3} For the butadiene–allene reaction, we have discovered that a single ambimodal transition state leads to a path bifurcation to either the (4+2) cycloadduct, via a concerted reaction, or to a diradical intermediate that can subsequently give either Diels–Alder or (2+2) adduct. In contrast, benzene and allene react through a transition state that leads only to a concerted pathway, forming both C–C bonds simultaneously and avoiding the loss of aromaticity in an intermediate. A higher energy transition state leads to a diradical intermediate.

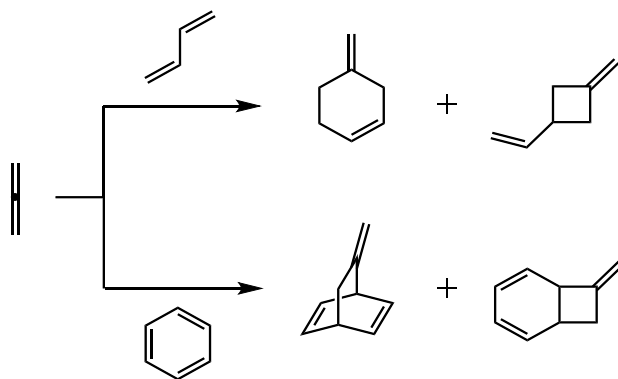


Figure 1.2.1. The Diels–Alder and (2+2) cycloaddition reactions of allene with butadiene and benzene.

Background

Pericyclic reactions involving allenes are known and have been used extensively in the syntheses of natural products.⁴ These reactions include [1,*n*]-, [2,3]-, and [3,3]-sigmatropic shifts⁵ and electrocyclizations.⁶ The relative reactivity of allenes, alkynes and alkenes in these processes have been the subject of some interest. For instance, the Cope rearrangement was found to proceed through similar transition structures, independent of the identity and degree of unsaturation of the π -components.⁷ Allenes also participate in (4+2) cycloadditions, 1,3-dipolar cycloadditions, and (2+2) cycloadditions; examples of each of these studied experimentally are shown in Figure 1.2.2. Maier utilized both cyclopentadiene and Boc-protected pyrrole with monosubstituted allenes to generate bridged bicyclic compounds through the Diels–Alder reaction.⁸ The 1,3-dipolar cycloaddition of C-phenyl-N-methylnitron with electron-deficient allenes produces methyleneisoxazolidines at 40 °C.⁹ Allene dimerization has been known for decades,¹⁰ and Dolbier investigated the preference for formation of 1,2-dimethylenecyclobutane over the 1,3-regioisomer.¹¹

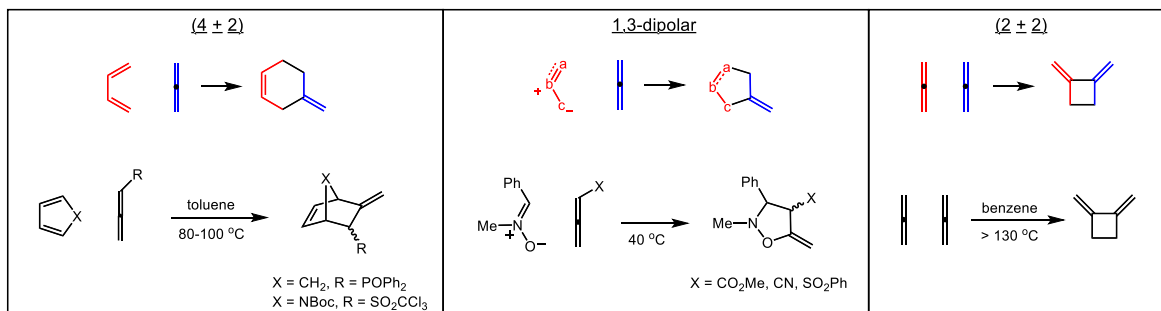


Figure 1.2.2. (4+2), 1,3-dipolar and (2+2) cycloadditions of allenes.

Computational mechanistic studies of allenes as reaction partners in 1,3-dipolar¹² and (2+2) cycloadditions¹³ have been reported. There are, however, limited theoretical investigations of allenes as dienophiles in (4+2) reactions. Venuvanalingam studied the concerted Diels–Alder

cycloadditions of dienes with allenes and fluoroallenes as dienophiles with semi-empirical AM1 and PM3 methods.¹⁴ Gandolfi studied concerted Diels–Alder cycloadditions of allene and fluoroallene with cyclopentadiene and furan with the *ab initio* Hartree–Fock method and MP3 single-point calculations.¹⁵ Houk and co-workers conducted a DFT study of the concerted and stepwise pathways of the parent butadiene–allene cycloaddition as well as some furan cycloadditions with allene but were unable to locate a number of important stationary points.¹⁶ In light of the numerous studies contrasting the Diels–Alder reactions of alkene and alkyne dienophiles,¹⁷ we have undertaken a thorough investigation of the butadiene–allene system.

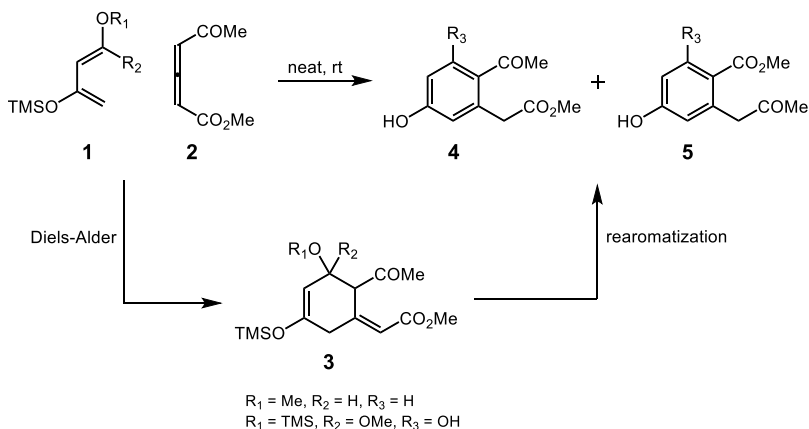


Figure 1.2.3. Diels–Alder reactions of dimethyl-1,3-allenedicarboxylate **2** with Danishefsky dienes **1**.

A variety of substituted dienes undergo Diels–Alder reactions with allenes. As shown in Figure 1.2.3, Danishefsky dienes **1** react with unsymmetrically 1,3-disubstituted allenes **2** to give aromatic products **4** and **5**.¹⁸ These reactions were thought to involve Diels–Alder cycloadditions via intermediate **3**. However, Jung and co-workers have shown for similar cases that (2+2) adducts may precede Diels–Alder adduct formation.¹⁹ Reactions of dienes **6** with allenic ester **7** give *exo*-methylenevinylcyclobutane intermediates **8**, formal (2+2) adducts, when the reaction

time is 5 h (Figure 1.2.4). These adducts undergo formal Cope rearrangements to give the Diels–Alder products **9** and **10** after extended reaction times. The Cope rearrangement of the unsubstituted *exo*-methylenevinylcyclobutane was found in previous computational studies by Houk and co-workers to rearrange to the Diels–Alder adduct in a stepwise fashion through a *bis*-allylic diradical.²⁰ Based on previous studies and experimental results in the literature, it is proposed that (4+2) reactions of this nature are stepwise and proceed first through a formal (2+2) cycloaddition, followed by a formal 1,3- or 3,3-shift to afford the Diels–Alder adduct.

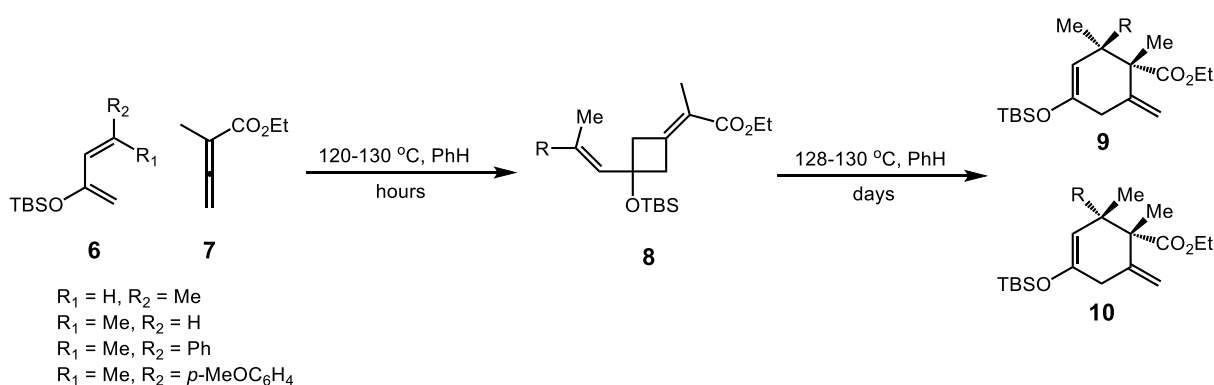


Figure 1.2.4. Formation of *exo*-methylenevinylcyclobutane intermediate prior to rearrangement to Diels–Alder adducts.

Himbert and Henn have shown that intramolecular (4+2) cycloadditions between allenyl amides and tethered aryl groups occur efficiently at elevated temperatures, despite the required disruption of aromaticity (Figure 1.2.5a).²¹ The polar stepwise mechanism was ruled out by the insensitivity of the kinetics of the reaction to varying electron-donating and electron-withdrawing groups on the benzene and allene moieties. However, although a concerted mechanism was initially proposed, a stepwise diradical mechanism could not be ruled out. Vanderwal has recently explored this dearomatizing intramolecular Diels–Alder reaction and has incorporated a subsequent ring-rearranging metathesis to form complex polycyclic scaffolds (Figure 1.2.5b).²²

Together, our groups uncovered important mechanistic insights into these intramolecular cycloadditions of allene to benzene derivatives.²³ In order to understand the energetics of concerted and stepwise pathways in benzene–allene cycloadditions and to make direct comparisons with nonaromatic diene reactions, we have undertaken a systematic investigation of the benzene–allene and butadiene–allene reactions with multiconfigurational CASSCF and CASPT2 methods.

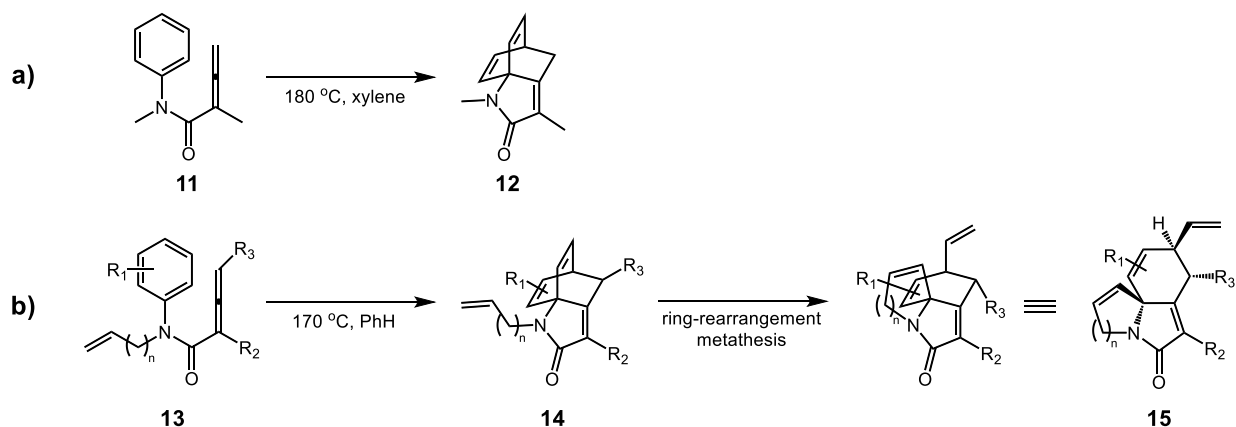


Figure 1.2.5. Intramolecular Diels–Alder reaction of arenes and allenes.

Computational Methodology

We have studied these reactions with complete active space (CAS) multiconfigurational methods. Stationary point structures were optimized using the CASSCF(8,8)/6-31G(d)²⁴ and CASSCF(10,10)/6-31G(d) methods in Gaussian 09²⁵ for the butadiene–allene and benzene–allene systems, respectively. Single-point calculations with second-order perturbation theory CASPT2/6-31G(d)²⁶ were carried out on the optimized structures, using the program MOLCAS²⁷ version 7.4, to account for dynamic electron correlation. CASSCF thermal corrections and zero-point energies are included in the CASPT2 electronic energies. Vibrational frequencies were computed for all optimized structures in order to verify minima and transition states. Intrinsic

reaction coordinate (IRC) calculations were also performed on several transition structures to verify that these transition structures originated from the correct reactants and led to the expected intermediates or products. CASSCF and CASPT2 has been found by Houk and co-workers to provide reasonable energetics for various diradical and pericyclic reactions.²⁸ DFT methods were also employed for optimizations, but we had difficulty locating relevant stationary points.¹⁶ Furthermore, several unrestricted DFT methods gave unrealistically high energy diradicals for the benzene–allene reaction. Consequently, we have used more robust multiconfigurational methods for the entirety of the investigation. A summary of our DFT results can be found in the Supporting Information.

Results/Discussion

Mechanism of the Reaction of Butadiene and Allene

The reaction of butadiene **16** with allene **17** can occur by either a concerted or stepwise radical mechanism (Figure 1.2.6). The concerted pathway has previously been studied using semi-empirical¹⁴ as well as UB3LYP methods.¹⁶ Alternatively, the reaction can give diradical **18** that can subsequently cyclize to Diels–Alder adduct **19** or to (2+2) adduct 3-methylenevinylcyclobutane **20**. The (2+2) adduct can reopen to **18** and then cyclize to yield **19**. This Cope rearrangement to the Diels–Alder adduct of the unsubstituted 3-methylenevinylcyclobutane was found in previous computational studies by Houk and co-workers to occur in stepwise fashion through a *bis*-allylic diradical intermediate.²⁹ The stereoselectivity was postulated to be governed by dynamic effects. Reaction of the diene in the *s-cis* conformation is necessary to permit cyclization to the Diels–Alder adduct; the *transoid* diradical **18(trans)** could be formed and undergo bond rotation around the partial double bond to furnish the *cisoid* diradical **18(cis)**, which can then cyclize to **19**, but this would require rotation around the partial double bond of the allyl radical.

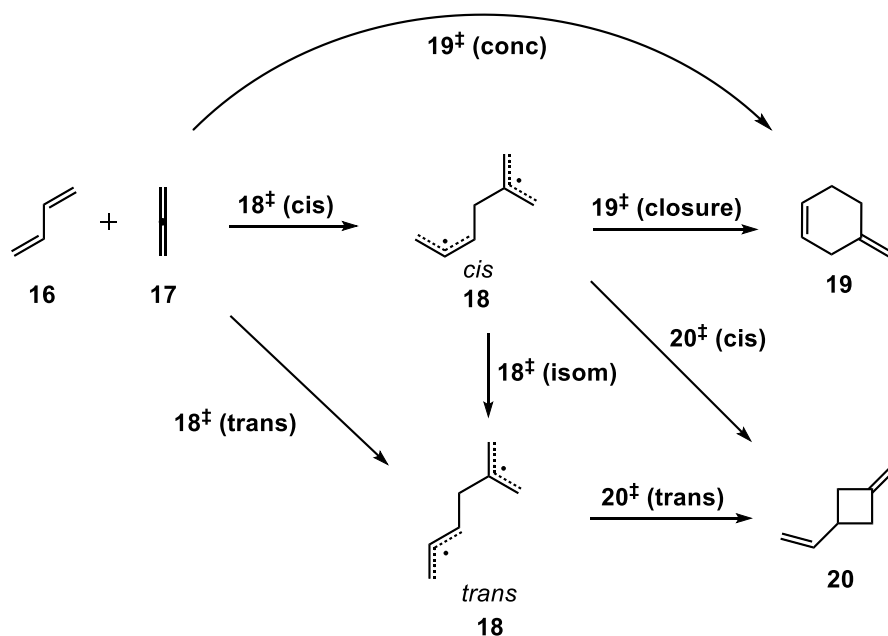


Figure 1.2.6. Possible mechanisms of butadiene **16** and allene **17**.

Four possible reaction pathways were examined using CASSCF(8,8) calculations. The active space was chosen to include the electrons involved in the formation of new bonds, namely the eight π -electrons of butadiene and allene. A schematic of the energy surface was generated from the quantum-chemically calculated values and is shown in Figure 1.2.7. Reported energies are relative to the lowest energy conformations of separated allene and *s-trans* butadiene. At the left of the diagram, the *s-cis* and *s-trans* butadiene reactants are shown. The *s-cis* butadiene is 3.0 kcal/mol higher in energy, consistent with the 2.6–4.0 kcal/mol values for the *gauche* conformation of *s-cis* butadiene found in prior calculations and experiments.³⁰ The barrier to interconversion is approximately 6 kcal/mol to switch from *s-trans* butadiene to *s-cis* butadiene. To the right of the diagram in Figure 1.2.7 are shown the electronic energies of the stationary points. Free energies calculated at room temperature (25 °C) have also been included, since reaction rates are determined from free energies through transition state theory. Because of the entropic penalty ($-T\Delta S$ term in free energy) of bringing two molecules together, ΔG values are

uniformly 11–14 kcal/mol higher than the corresponding ΔE values for all stationary points other than the separated reactants. Consequently, the reaction surfaces generated from both electronic and free energies have similar topologies, and we will proceed by referring to electronic energies for consistency.

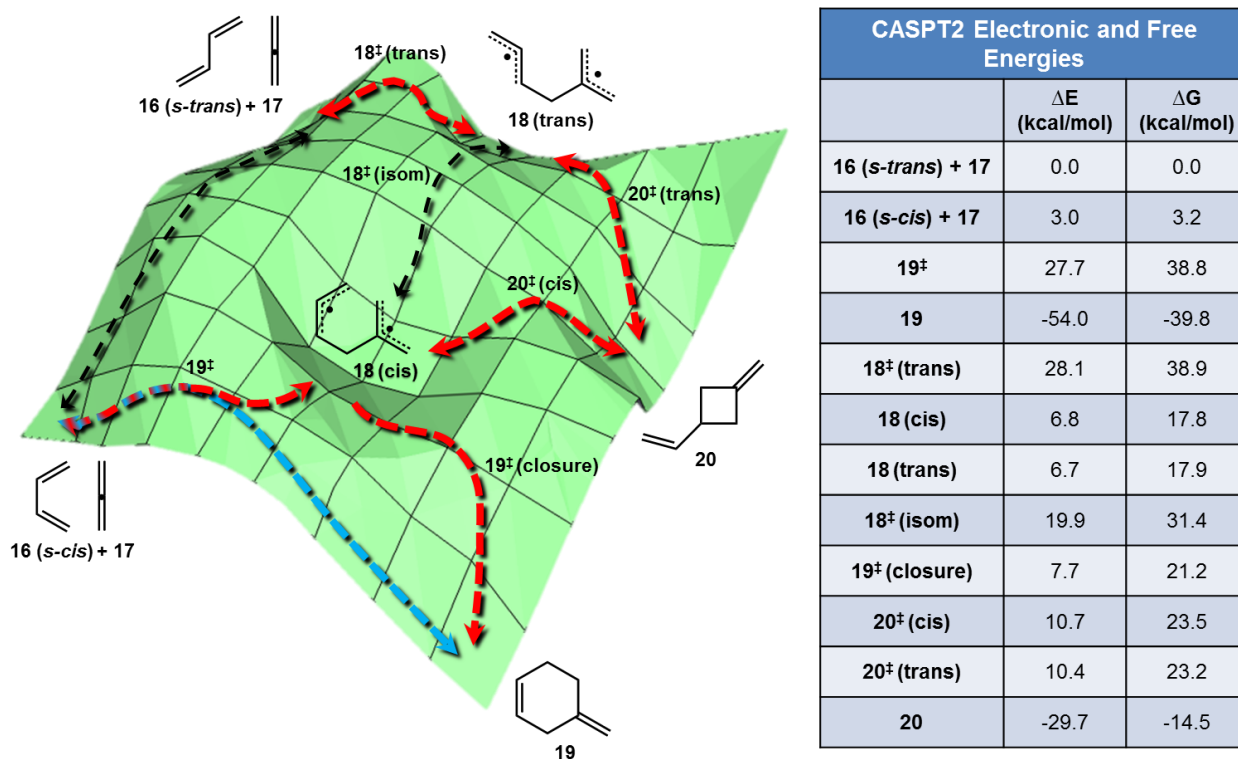


Figure 1.2.7. Schematic of the potential energy surface for the reaction between butadiene and allene. CASPT2//CASSCF(8,8)/6-31G* gas phase energies are shown in kcal/mol. Red arrows refer to the stepwise pathways, the blue arrow is the concerted pathway, and black arrows are for *cis/trans* and *s-cis/s-trans* interconversions.

Along the lower border, the concerted Diels–Alder reaction pathway is shown. **19[‡]** is the concerted transition state at 27.7 kcal/mol but is described in detail in the next section; this is also the transition state leading to the *cis*-diradical **18(cis)**. Several Diels–Alder reactions of two

dienes involving bifurcations are known.³¹ Singleton has also studied a bifurcation that occurs in the Diels–Alder reactions of ketenes with cyclopentadiene which leads to an intermediate or a cycloadduct, as found here.³² At 28.1 kcal/mol, the transition state leading to the *trans*-diradical **18[‡](trans)** will compete with **19[‡]**. Both the *trans* and *cis* diradicals can give the 3-vinylmethylenecyclobutane **20** through transition states of only 10–11 kcal/mol. The transition state for formation of Diels–Alder product, **19[‡](closure)**, is 7.7 kcal/mol with respect to the reactant and only 0.9 kcal/mol higher in energy than the diradical intermediate **18(cis)**. Our calculations predict that Diels–Alder adduct **19** and 3-vinylmethylenecyclobutane **20** should both be formed thermally, with the former being the thermodynamically and kinetically favored major product.

In order to understand the region around **19[‡]**, a detailed potential energy surface was generated (Figure 1.2.8). The energies were calculated by fixing the distance between the internal carbon of the allene and a terminal carbon of butadiene (Bond 1) and varying the distance corresponding to the second forming σ -bond (Bond 2). CASSCF(8,8) single-point calculations were conducted on each structure, and the same protocol was applied to increasing lengths of Bond 1. Examination of the surface shows that only one saddle point exists, corresponding to ambimodal transition state **19[‡]**. An IRC calculation shows that the steepest downhill trajectory leads to formation of diradical **18(cis)**. From this diradical, there is only a small barrier **19[‡](closure)** to radical recombination to form 4-methylenecyclohexene **19** (red arrows). However, an alternative trajectory can lead directly to **19** which, although not the steepest trajectory, bypasses **18** and **19[‡](closure)** (blue arrow). In a study of the allenic Cope rearrangement of 1,2,6-heptatriene, Borden observed a similar phenomenon where both a concerted and a stepwise pathway can emerge after traversing a common transition state.³³ Despite the large preference for reaction at the central carbon of allenes, the allylic stabilization found in the diradical intermediates is not substantial in the transition structures, suggesting the

possibility for direct formation of product without passage through an intermediate. This result is in line with the discovery that the Cope rearrangement involving alkenes, allenes and alkynes are all mechanistically and kinetically similar.⁷

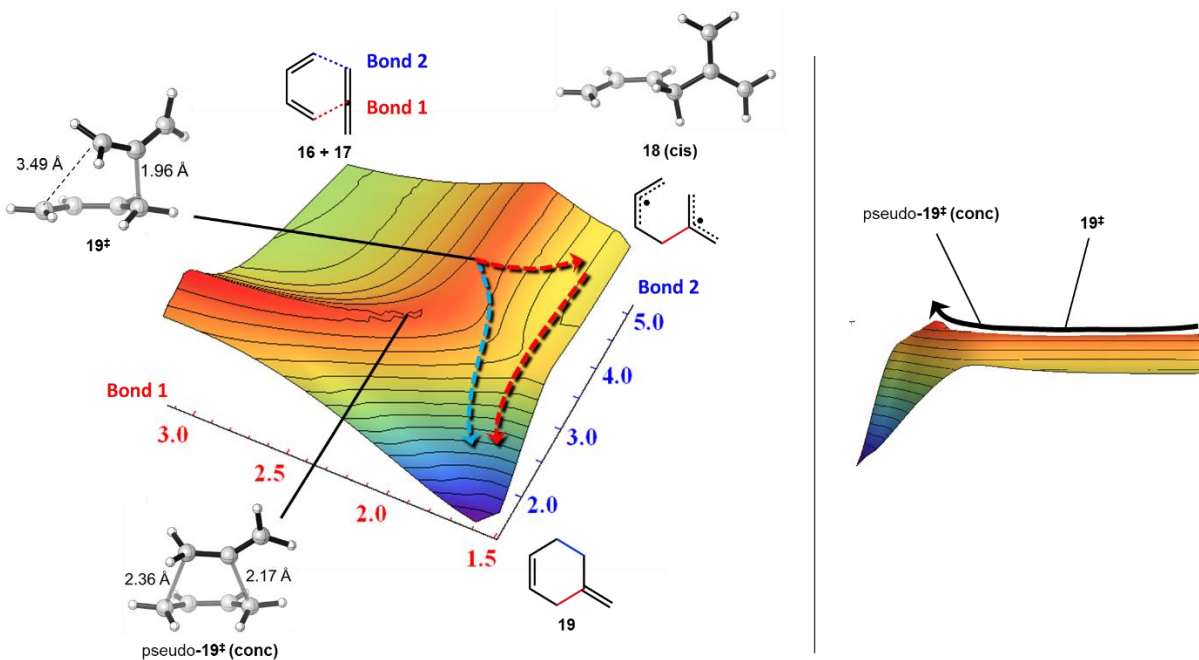


Figure 1.2.8. Left: Potential energy surface (PES) region of the possible transition states of initial bond formation, generated with CASSCF(8,8)/6-31G(d). Energy levels are designated by the following color spectrum: **red** = high energy, **violet** = low energy. The red arrows outline the stepwise pathway from ambimodal transition state 19^\ddagger , while the blue arrow outlines the concerted pathway. **Right:** Side view of the PES, demonstrating the saddle point for 19^\ddagger .

The lengths of the forming σ -bonds in 19^\ddagger differ by 1.5 Å, suggesting significant diradical character. The occupations of the HOMO and LUMO natural orbitals are 1.65 and 0.36, respectively; occupations of 2 and 0 are expected for ideal closed-shell species, while 1 and 1 would represent a pure diradical. To further probe the existence of a distinct concerted transition state, pseudo- $19^\ddagger(\text{conc})$ was optimized with bond-distance restraints of 2.17 Å and 2.36 Å, established

from successful location of the concerted stationary point using the 3-21G basis set; the greater synchronicity of the transition state may be an artifact of the smaller basis set. The potential energy surface connecting **19**[‡] and pseudo-**19**[‡](**conc**) is very flat, requiring only a minor geometric change to interconvert the two structures. Hence, when butadiene is in the *cis* conformation, only a single transition state **19**[‡] leads to diradical **18(cis)** and to Diels–Alder cycloadduct **19**. All optimized structures are shown in Figure 1.2.9.

Although both the blue and red downhill trajectories in Figure 1.2.8 are barrierless on the potential energy surface, Singleton has shown that inclusion of entropic factors can reveal hidden dynamical bottlenecks.^{32a} From **19**[‡], formation of a single C–C bond resulting in diradical **18(cis)** will have a lower entropic penalty than simultaneously establishing the two new σ bonds of **19**. Also, examination of the transition-state region shows that the location of the highly asynchronous transition structure **19**[‡] is skewed toward **18(cis)**. This may cause an entropic bottleneck between **19**[‡] and **19**, establishing a barrier for the blue concerted pathway in Figure 1.2.8 and leading to exclusive formation of intermediate **18(cis)** prior to forming the Diels–Alder adduct **19**. Thus, despite the fact that the potential energy surface contains only one initial bond-forming transition state that can seemingly form either a cycloadduct or a diradical, accounting for entropy would likely lead to preferential diradical formation. Molecular dynamics simulations may be a valuable tool in validating this notion and further probing the surface around the transition state. A similar situation where an IRC predicts a concerted pathway while dynamics suggests a stepwise route has been uncovered in the intramolecular heterolysis of pinacolyl alcohol.³⁴

Formation of the *bis*-allyl diradical can result in either the *cisoid* (**18(cis)**) or the *transoid* (**18(trans)**) intermediate, depending on the orientation of the butadiene prior to bond formation. The intermediates are essentially isoenergetic, but transition state **19**[‡] lies 0.4

kcal/mol lower than **18[‡](trans)**. The *cisoid* and *transoid* intermediates can interconvert only by traversing a 13 kcal/mol barrier due to rotation around the partial double bond of the allyl radical.

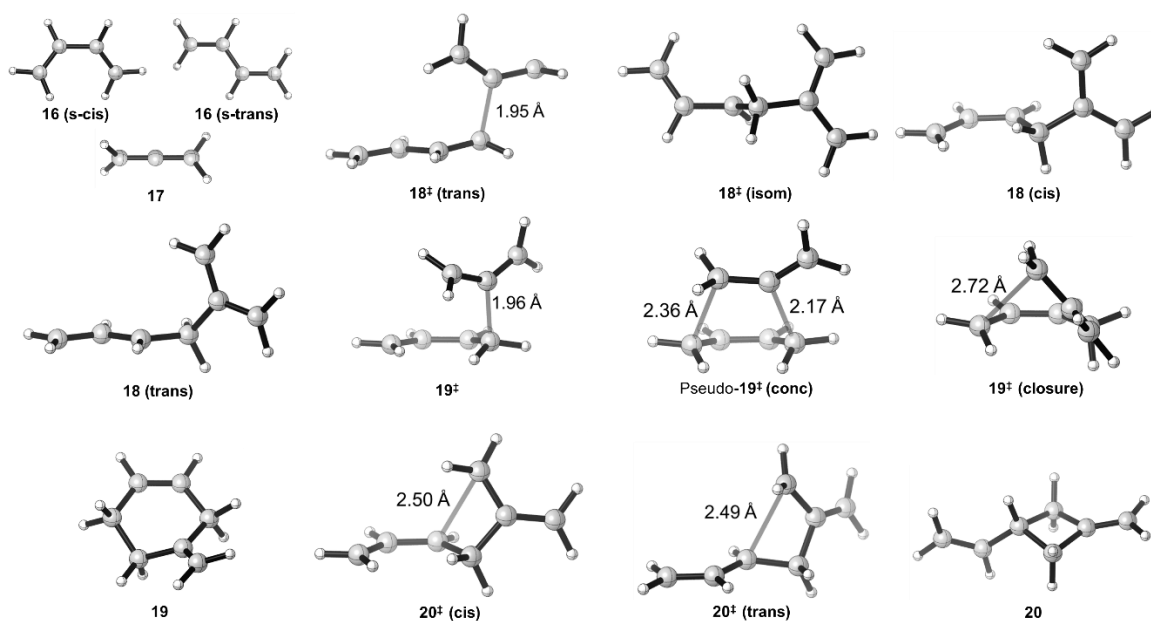


Figure 1.2.9. Optimized structures of the stationary points for the cycloaddition of butadiene **16** and allene **17**.

From the *cisoid* diradical intermediate **18(cis)**, both 3-methylenevinylcyclobutane **20** and 4-methylenecyclohexene **19** can be formed by radical combination through **20[‡](cis)** and **19[‡](closure)**, respectively, while **18(trans)** can only form cyclobutane product **20**. The transition states **20[‡](cis)** and **20[‡](trans)** have the same energy; the structures are identical except for the conformation of the distal double bond. The formation of **20** is exoergic by 29.7 kcal/mol; longer reaction times or higher temperatures result in radical ring-opening back to either stereoisomer of *bis*-allyl diradical **18**. Although the barrier for the ring-opening of **20** is high (~40 kcal/mol) for the unsubstituted system, substituents stabilizing the diradical intermediate will result in a lower barrier for the ring-opening of **20**. The *cisoid* intermediate can

then irreversibly produce the Diels–Alder product **19** through transition state **19[‡](closure)**, which is lower in energy than **20[‡](cis)** and **20[‡](trans)** by 3 kcal/mol.

These results parallel the experimental results reported by Jung on substituted substrates (Figure 1.2.4).¹⁹ After a few hours of heating mixtures containing substituted butadienes and allenyl ester **7**, the formal (2+2) products were isolated. Heating the cyclobutanes over a period of days resulted in rearrangement to the formal Diels–Alder products. This vinylcyclobutane–cyclohexene rearrangement has previously been studied by our group.²⁰

Allene dimerizes readily,^{10,11,35} and the mechanism has been studied theoretically at a coupled-cluster level of theory.¹³ Johnson calculated the dimerization to occur with an energetic barrier $\Delta E^\ddagger = 32.9$ kcal/mol for initial diradical formation, approximately 5 kcal/mol higher than our calculated barrier for reaction with butadiene. Previous successes in (4+2) cycloadditions with substituted butadienes illustrate this preference of Diels–Alder reaction over dimerization.^{18,19}

Mechanism of the Cycloaddition Reaction of Benzene with Allene

The (4+2) reaction of benzene **21** and allene **17** was also explored (Figure 1.2.10). This cycloaddition does not occur in the parent cases because allenes dimerize and oligomerize more rapidly than they react with benzene.^{10,11,35} As mentioned previously, Himbert,²¹ Orahovats,³⁶ and more recently Vanderwal^{22,23} have demonstrated that substituted benzenes and allenes can form intramolecular cycloadducts. The intramolecular cycloadditions of N-aryllallenylamides are known (Figure 1.2.5) and prompted our study of the benzene–allene reaction.

The cycloaddition can occur through a concerted (**23[‡](conc)**) mechanism or through the stabilized pentadienyl radical **22**. Either route can lead to (4+2) cycloadduct **23**, with the latter proceeding through **23[‡](closure)**. The (2+2) product **24** can also be formed.

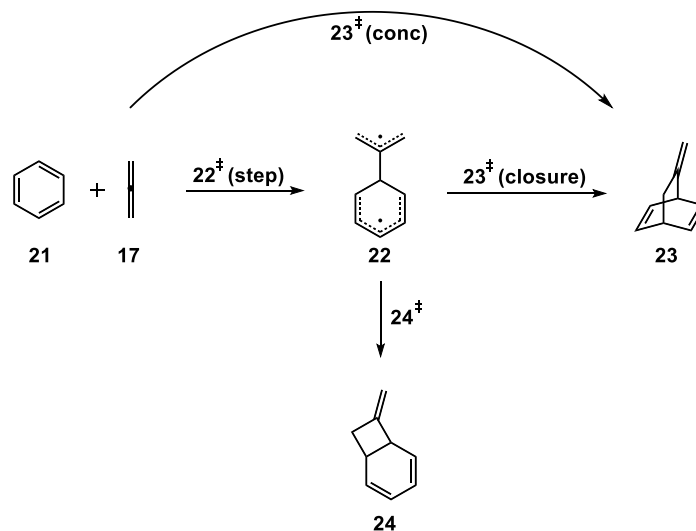


Figure 1.2.10. Possible mechanisms of cycloadditions of benzene **21** and allene **17**.

Optimizations were carried out with CASSCF(10,10) involving an active space of the six π -electrons of benzene and the four π -electrons of allene. A schematic of the reaction profile and energy values are shown in Figure 1.2.11. The concerted transition state **23[‡](conc)** lies 5.0 kcal/mol lower than the stepwise **22[‡](step)**, in contrast to the union of these into a single transition state found with *s-cis* butadiene and ethylene. Formation of the first C–C bond gives intermediate **22**, containing allyl and pentadienyl radicals. Although these radicals are stabilized, loss of aromaticity offsets the favorable conjugation so that **22** is 32.2 kcal/mol higher than the reactants. The allyl radical resulting from the allene does not initially benefit from delocalization; rotations about the C–C bonds are necessary before proper orbital alignment allows for conjugation. Conversely, the concerted **23[‡](conc)** better offsets the loss of aromaticity and maintains most of the benzene stabilization by providing an aromatic transition state.

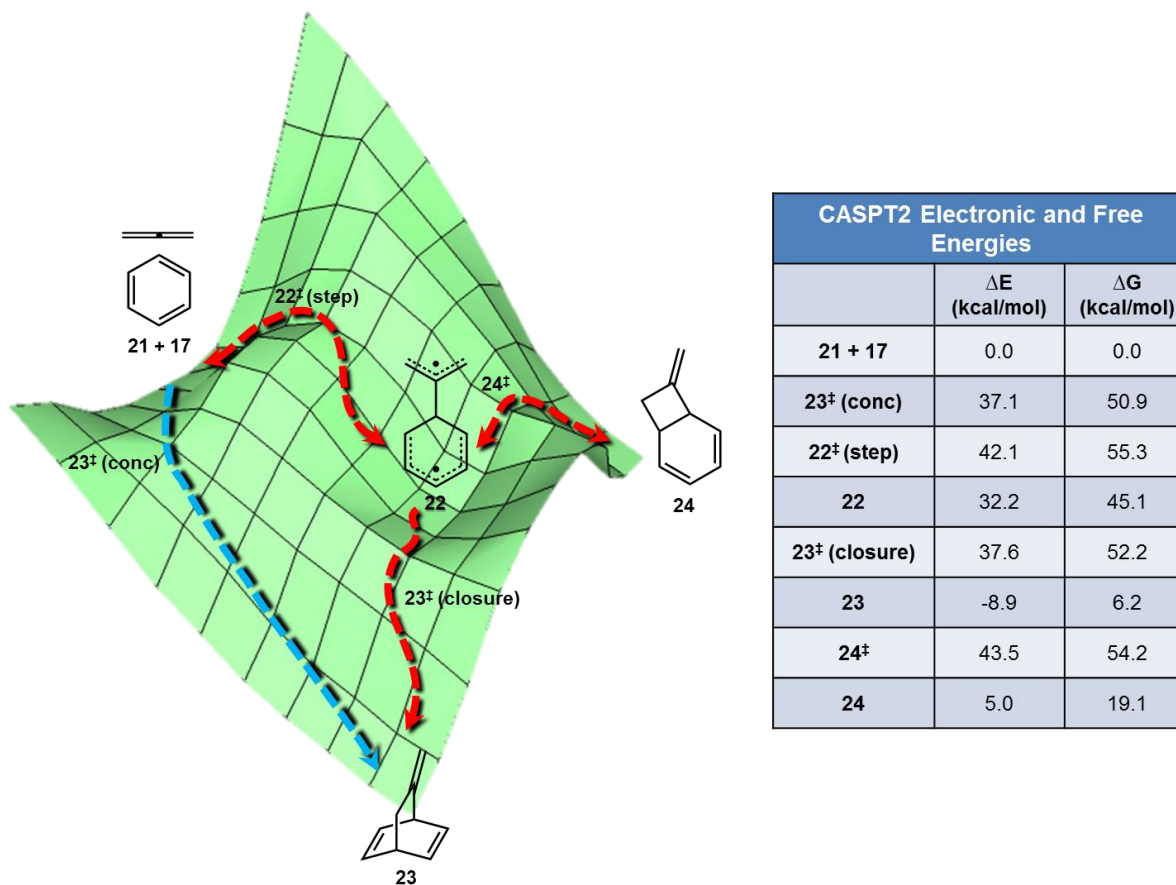


Figure 1.2.11. Schematic of the potential energy surface for the reaction between benzene **21** and allene **17**. CASPT2//CASSCF(10,10)/6-31G(d) gas-phase energies are shown in kcal/mol.

Red arrows refer to the stepwise pathways, **blue** arrow for the concerted pathway.

Ring closure of the diradical to form the (4+2) adduct **23** is favored over formation of the (2+2) adduct **24** by 5.9 kcal/mol. The formation of **24** is endoergic by 5.0 kcal/mol and is reversible. The methylenecyclobutane **24** can ring-open to **22** and ultimately form the thermodynamically favorable product **23**. Optimized structures are shown in Figure 1.2.12.

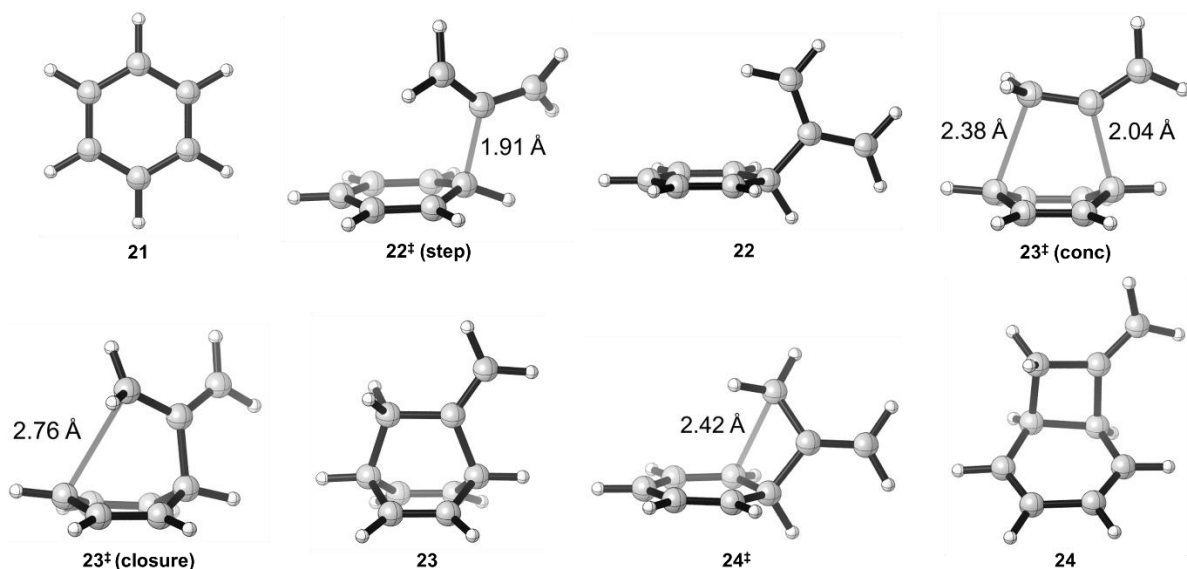


Figure 1.2.12. Optimized structures of the stationary points for the cycloaddition of benzene **21** and allene **17**.

Allene oligomerizes readily in benzene at temperatures of >130 °C. The 37.1 kcal/mol required for the (4+2) cycloaddition of benzene and allene is greater than the 32.9 kcal/mol barrier for dimerization, as calculated by Johnson (Figure 1.2.13).¹⁰ Furthermore, 1,2-dimethylenecyclobutane formation is exoergic by 45.0 kcal/mol, compared to only 8.9 kcal/mol for **23**. The dimerization of allene is thermodynamically and kinetically favored relative to Diels–Alder reaction with benzene, consistent with the lack of formation of **23**.

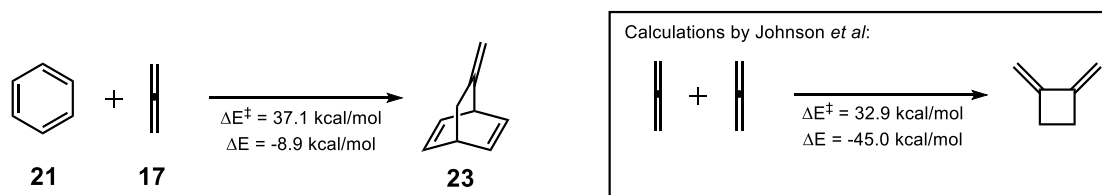


Figure 1.2.13. Energetics of the Diels–Alder reaction of benzene and allene (left) and the dimerization of allene (right). Calculations of the dimerization of allene were conducted by

Johnson *et al.*¹⁰

DFT optimizations using both UB3LYP/6-31G(d) and UMO6-2X/6-31G(d) methods were also utilized for the butadiene–allene and benzene–allene systems; energetics and optimized structures can be found in Supporting Information. For the butadiene–allene system, UMO6-2X predicts energies for all stationary points to within 5 kcal/mol of CASPT2. However, DFT calculations on the benzene–allene system resulted in largely overestimated energies for the open-shell diradical species. The spin-contamination observed with DFT methods,³⁷ which changes over the course of the reaction pathways, may be a large contribution. This outcome has been observed in prior DFT studies of arene–allene cycloadditions.²³ Aside from the unexpectedly high energies for the intermediate in the benzene–allene system, unrestricted MO6-2X computations predict values that are comparable to the CASSCF and CASPT2 methods.

Having established the energetics and mechanism of reactions of allene with butadiene and benzene, we conclude by comparing these results to previously reported studies of the dienes with ethylene and acetylene^{17,38,39} (Figure 1.2.14). The Diels–Alder reactions of allenes, with both butadiene and benzene, have higher activation barriers than their diatomic counterparts. The reactions of ethylene and acetylene with butadiene have a barrier of 22.4 kcal/mol for the concerted cycloaddition, 5.3 kcal/mol lower than that for allene. With benzene, reactions with ethylene and acetylene have reported barriers of 31.9 and 35 kcal/mol, respectively. An allene dienophile raises the activation barrier to 37.1 kcal/mol. Despite the destabilizing cumulated double bonds of allene, computations suggest diminished reactivity towards dienes relative to the (4+2) reaction of ethylene and acetylene.

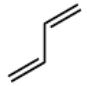
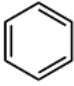



		
	22.4 ^a	31.9 ^b
	22.4 ^a	35 ^c
	27.7	37.1

Figure 1.2.14. Table of activation energies (kcal/mol) for the concerted Diels–Alder reaction of butadiene and benzene with unsaturated dienophiles. ^a Calculated using B3LYP/6-31G(d).³⁸

^b Experimentally derived³⁹ ^c Calculated using MP2/6-31G(d).^{17a}

Conclusions

The cycloaddition reactions of allene with butadiene and with benzene have been elucidated using multiconfigurational CASPT2 calculations. Although the reactions investigated here are not explicitly observed experimentally due to the presence of more favorable processes (allene oligomerization) or decomposition under the required reaction conditions (high temperatures), many substituted analogues have resulted in successful Diels–Alder cycloadditions. Reaction with butadiene occurs through a single ambimodal transition state that can proceed to product along both concerted and stepwise pathways, although inclusion of entropy may ultimately favor the latter. If a diradical intermediate is formed, either the (2+2) or (4+2) cycloadduct can result; the (2+2) adduct can reversibly ring-open to yield the diradical and proceed to the more thermodynamically stable (4+2) product.

Conversely, the loss of aromaticity largely affects the reaction profile of benzene and allene cycloaddition; the propensity of benzene to retain aromaticity prompts the cycloaddition of allene and benzene to occur through a concerted yet asynchronous mechanism, forming both σ -bonds

simultaneously through a pericyclic transition state. The resulting cycloadduct also suffers from the disruption of aromaticity, causing a large decrease in reaction exothermicity relative to the butadiene–allene system. In lieu of computationally intensive CASSCF optimizations, unrestricted DFT methods can be also used to model such systems, but care must be taken when applying them to cycloadditions of aromatic compounds with allenes. Additionally, molecular dynamics simulations on the butadiene–allene Diels–Alder reaction may increase our understanding of possible ambimodal transition states and subsequent bifurcations in allene chemistry.

References

1. Krause, N.; Hashimi, A. S. K. *Modern Allene Chemistry*; Wiley–VCH Verlag: Weinheim, 2004; Vol. 1–2.
2. (a) Diels, O.; Alder, K.; *Justus Liebigs Ann. Chem.* **1926**, 450, 237–254. (b) Fringuelli, F.; Taticchi, A. *Dienes in the Diels–Alder Reaction*; Wiley & Sons: New York, 1990.
3. For select examples with benzene as a diene: (a) Ciganek, E. *Tetrahedron Lett.* **1967**, 8, 3321–3325. (b) Cossu, S.; Garris, F.; DeLucchi, O. *Synlett* **1997**, 12, 1327–1334.
4. Yu, S.; Ma, S. *Angew. Chem. Int. Ed.* **2012**, 51, 3074–3112.
5. (a) Jensen, F. *J. Am. Chem. Soc.* **1995**, 117, 7487–7492. (b) Wentrup, C.; Finnerty, J. J.; Koch, R. *Curr. Org. Chem.* **2010**, 14, 1586–1599.
6. (a) Sakai, S. *J. Phys. Chem. A* **2006**, 110, 9443–9450. (b) Sakai, S. *Theor. Chem. Account.* **2008**, 120, 177–183. (c) Inagaki, F.; Kitagaki, S.; Mukai, C. *Syn. Lett.* **2011**, 5, 594–614.
7. Black, K. A.; Wilsey, S.; Houk, K. N. *J. Am. Chem. Soc.* **1998**, 120, 5622–5627.
8. Scheufler, F.; Maier, M. E. *Eur. J. Org. Chem.* 2000, 3945–3948.
9. (a) Padwa, A.; Kline, D. N.; Koehler, K. F.; Matzinger, M.; Venkatramanan, M. K. *J. Org. Chem.*, **1987**, 52, 3909–3917. (b) For a review on allene dipolarophiles: Pinho e Melo, T. M. V. D. *Curr. Org. Chem.* **2009**, 13, 1406–1431.
10. Lebedev, S. V. *J. Russ. Phys. Chem. Soc.* **1913**, 45, 1357–1372.
11. Dai, S.-H.; Dolbier, W. R., Jr. *J. Org. Chem.* **1972**, 37, 950–955.
12. (a) Kavitha, K.; Venuvanalingam, P. *J. Chem. Soc., Perkin Trans. 2*, **2002**, 2130–2139. (b) Mariappan, M.; Venuvanalingam, *J. Fluor. Chem.*, **1994**, 73, 171–174.
13. Skraba, S. L.; Johnson, R. P. *J. Org. Chem.*, **2012**, 77, 11096–11100.
14. Mariappan, M.; Venuvanalingam, P. *J. Chem. Soc., Perkin Trans. 2*, **1996**, 1423–1427.
15. Rastelli, A.; Bagatti, M.; Gandolfi, R. *J. Am. Chem. Soc.* **1995**, 117, 4965–4975.
16. Nendel, M.; Tolbert, L. M.; Herring, L. E.; Islam, N.; Houk, K. N. *J. Org. Chem.* **1999**, 64, 976–983.
17. (a) R. D. J. Froese, J. M. Coxon, S. C. West K. Morokuma, *J. Org. Chem.* **1997**, 62, 6991 – 6996. (b) Houk, K. N.; Li, Y.; Evanseck, J. D. *Angew. Chem., Int. Ed. Engl.* **1992**, 31, 682–708. (c) Coxon, J. M.; Grice, S. T.; Maclagan, R. G. A. R.; McDonald, D. Q. *J. Org. Chem.* **1990**, 55, 3804. (d) González, J.; Houk, K. N. *J. Org. Chem.* **1992**, 57, 3031 – 3037.
18. Yoshino, T.; Ng, F.; Danishefsky, S. J. *J. Am. Chem. Soc.* **2006**, 128, 14185–14191.

19. (a) Jung, M. E.; Novack, A. R. *Tetrahedron Lett.* **2005**, *46*, 8237–8240. (b) Jung, M. E.; Nishimura, N.; Novack, A. *J. Am. Chem. Soc.* **2005**, *127*, 11206–11207. (c) Jung, M. E.; Nishimura, N. *Org. Lett.* **2001**, *3*, 2113–2116.
20. Zhao, Y.-L.; Suhrada, C. P.; Jung, M. E.; Houk, K. N. *J. Am. Chem. Soc.* **2006**, *128*, 11106–11113.
21. Himbert, G.; Henn, L. *Angew. Chem., Int. Ed.* **1982**, *21*, 620.
22. Lam, J. K.; Schmidt, Y.; Vanderwal, C. D. *Org. Lett.* **2012**, *14*, 5566–5569.
23. Schmidt, Y.; Lam, J. K.; Pham, H. V.; Houk, K. N.; Vanderwal, C. D. *J. Am. Chem. Soc.* **2013**, *135*, 7339–7348.
24. Roos, B. O. In *Advances in Chemical Physics*; John Wiley & Sons, Inc.: 2007, p 399.
25. Frisch, M. J.; *et al.* Gaussian 09, revision C.01; Gaussian, Inc.: Wallingford, CT, 2009.
26. Andersson, K.; Malmqvist, P. A.; Roos, B. O.; Sadlej, A. J.; Wolinski, K. *J. Phys. Chem.* **1990**, *94*, 5483–5488.
27. F. Aquilante, L. De Vico, N. Ferré, G. Ghigo, P.-Å Malmqvist, P. Neogrády, T.B. Pedersen, M. Pitonak, M. Reiher, B.O. Roos, L. Serrano-Andrés, M. Urban, V. Veryazov, R. Lindh, *J. Comp. Chem.* **2010**, *31*, 224–227.
28. (a) Ess, D. H.; Hayden, A. E.; Klärner, F.-G.; Houk, K. N. *J. Org. Chem.* **2008**, *73*, 7586–7592. (b) Li, Y.; Houk, K. N. *J. Am. Chem. Soc.* **1996**, *118*, 880–885. (c) Houk, K. N.; Li, Y.; Storer, J.; Raimondi, L.; Beno, B. *J. Chem. Soc., Faraday Trans.* **1994**, *90*, 1599–1604.
29. (a) Zhao, Y.-L.; Suhrada, C. P.; Jung, M. E.; Houk, K. N. *J. Am. Chem. Soc.* **2006**, *128*, 11106–11113. (b) Northrop, B. H.; Houk, K. N. *J. Org. Chem.* **2005**, *71*, 3–13.
30. Barborini, M.; Guidoni, L. *J. Chem. Phys.* **2012**, *137*, 224309–224309-9 and references therein.
31. (a) Ess, D. H.; Wheeler, S. E.; Iafe, R. G.; Xu, L.; Çelebi-Ölçüm, N.; Houk, K. N. *Angew. Chem. Int. Ed.* **2008**, *47*, 7592–7601. (b) Thomas, J. B.; Waas, J. R.; Harmata, M.; Singleton, D. A. *J. Am. Chem. Soc.* **2008**, *130*, 14544–14555.
32. (a) Gonzalez-James, O. M.; Kwan, E. E.; Singleton, D. A. *J. Am. Chem. Soc.* **2012**, *134*, 1914–1917. (b) Ussing, B. R.; Hang, C.; Singleton, D. A. *J. Am. Chem. Soc.* **2006**, *128*, 7594–7607. (c) Bekele, T.; Christian, C. F.; Lipton, M. A.; Singleton, D. A. *J. Am. Chem. Soc.* **2005**, *127*, 9216–9223.
33. Hrovat, D. A.; Duncan, J. A.; Borden, W. T. *J. Am. Chem. Soc.* **1999**, *121*, 169–175.
34. Ammal, S. C.; Yamataka, H.; Aida, M.; Dupuis, M. *Science*, **2003**, *299*, 1555–1557.
35. Dolbier, W. R.; Dai, S.-H. *J. Am. Chem. Soc.* **1970**, *92*, 1774–1776.

36. Trifonov, L. S.; Orahovats, A. S. *Helv. Chim. Acta* **1989**, *72*, 59–64. (b) Trifonov, L. S.; Orahovats, A. S. *Helv. Chim. Acta* **1987**, *70*, 262–270.
37. Baker, J.; Scheiner, A.; Andzelm, J. *Chem. Phys. Letters* **1993**, *216*, 380–388.
38. Black, K.; Liu, P.; Xu, L.; Doubleday, C.; Houk, K. N. *Proc. Natl. Acad. Sci.* **2012**, *109*, 12860–12865.
39. Doering, W. v. E.; Roth, W. R.; Breuckmann, R.; Figge, L.; Lennartz, H.-W.; Fessner, W.-D.; Prinzbach, H. *Chem. Ber.* **1988**, *121*, 1–9, and references cited therein.

Chapter 2. Determining Tether Effects in Intramolecular Diels–Alder Reactions of Allenes and Arenes Through an Energy Decomposition Analysis

Introduction

The intramolecular Diels–Alder (IMDA) reaction of allenes is a robust technique in organic synthesis, able to form complex polycycles in a single step.¹ In the 1980s, Himbert and Henn developed IMDA reactions of allenyl amides which exhibited the surprising use of an aryl ring as the diene component,² a rare occurrence due to the aromaticity of benzene.³ This transformation to develop aza-tricyclo[6.2.1.0] backbones was extended to oxa-, thia- and phospho- analogues by altering the tether between the aryl and allenyl groups,⁴ but there were no reports of analogous all–carbon tethers. Recently we have collaborated with the Vanderwal group and discovered, through DFT calculations, that successful cycloadditions with heteroatomic tethers are thermodynamically favored while unsuccessful reactions are thermodynamically, not kinetically, disfavored.⁵ The cycloadducts resulting from carbon-tethered substrates are endergonic, consistent with unfavorable experimental ratios. Our previous studies on the allene–aryl Diels–Alder reaction revealed that the intermolecular reaction is energetically favorable by 9 kcal/mol.⁶ Therefore, the composition of the tethers has a considerable effect on the thermodynamics, and consequently the success, of these intramolecular reactions. Prior studies on the effect of tethers on IMDA reactions are known.⁷ We have now performed a systematic investigation to determine the factors that contribute to the large variation of energetics in IMDA reactions of benzene and allene.

Computational Methods

All structures were optimized using the B3LYP functional⁸ and 6-31G(d) basis set in Gaussian09.⁹ Single point calculations were then conducted with MO6-2X/6-311+G(d,p)¹⁰ on the

B3LYP-optimized geometries. In general, B3LYP and Mo6-2X produce similar optimized geometries, although cycloaddition reaction energies are predicted by B3LYP to be ~10 kcal/mol less exothermic than experiment. We have previously shown that Mo6-2X single-point calculations with reasonably large basis sets give much better values.¹¹ Frequency calculations identified the nature of the stationary points, ensuring the location of local minima with no imaginary frequencies. Implicit solvent was simulated using the Conductorlike Polarizable Continuum Model (CPCM) for xylenes.¹²

Results and Discussion

We have considered a variety of different tethers, depicted in blue in Figure 2.1a. Nitrogen, oxygen, sulfur, and both sp²- and sp³-hybridized carbon atoms adjacent to the phenyl group were studied. The allenones, with a carbonyl adjacent to the allene (**Y**: C=O) would best resemble the systems that have been studied experimentally, but we have also incorporated a simple methylene and an exo-methylene at that position to determine the importance of the carbonyl moiety. The ΔH_{rxn} values can be seen in tabular and graphical form in Figure 2.1b and 2.1c. The enthalpy for the intermolecular reaction between benzene and 1,2-propadiene is also included for comparison.

Most of the reactions involving saturated parent linkers (**Y**: CH₂; “Parent”) are endothermic. Only reactant **1_S_CH₂** is exothermic. Incorporation of an exo-methylene group at the **Y**-position lowers the reaction enthalpy for all substrates (**Y**: C=CH₂; “Alkene”), though to varying degrees—from 1.8 kcal/mol for carbon-tethered **1_CH₂_C=CH₂** to 5.9 kcal/mol for nitrogen-tethered **1_NCH₃_C=CH₂**. Further stabilization is achieved when a carbonyl replaces the double bond (**Y**: C=O; “Carbonyl”), again spanning a large range of 2.8–5.0 kcal/mol. These tethers give highly exothermic IMDA reactions, even greater than the –4.9 kcal/mol of the intermolecular case. To elucidate the factors contributing to the difference in reaction enthalpies

and fluctuating stabilization of these tethered substrates, we proceeded to evaluate the effects of substitution of each cycloaddend as well as the strain imparted by the 5-membered ring.

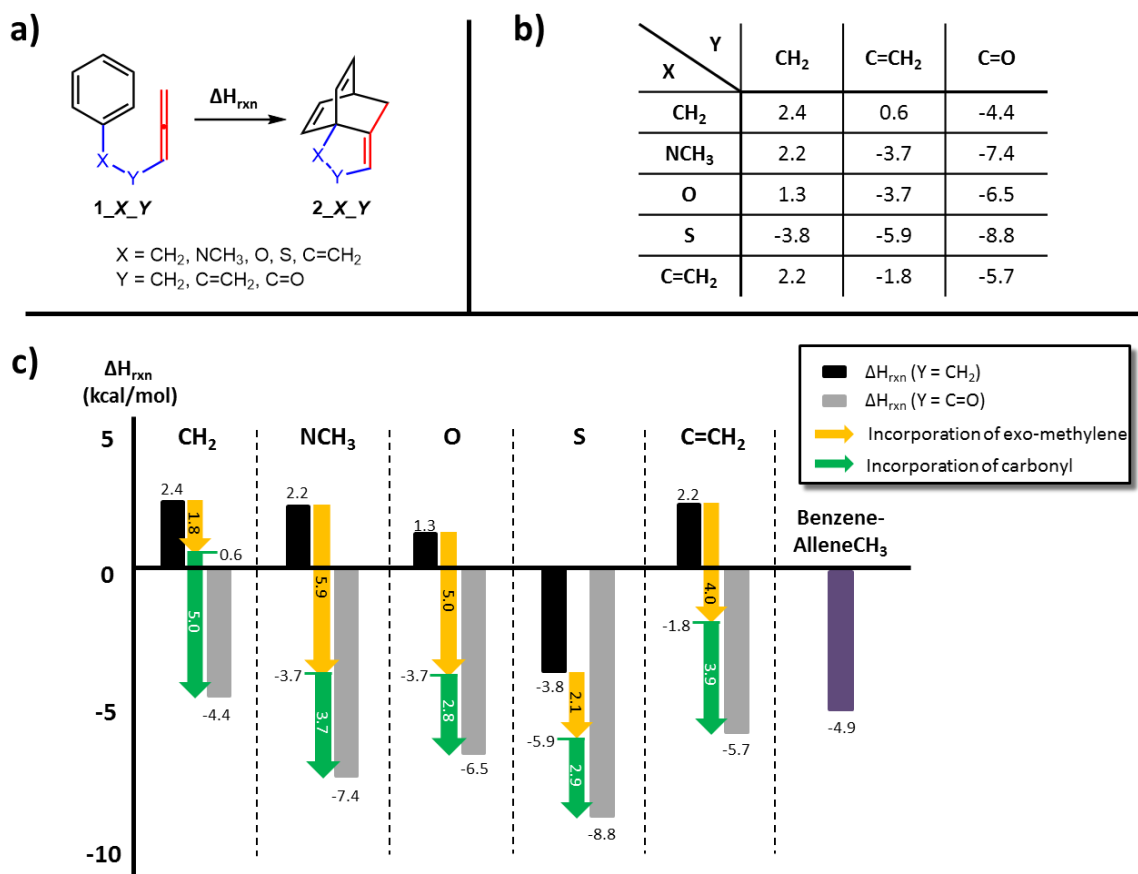


Figure 2.1. **a)** The general IMDA reaction of tethered benzene and allene. **b)** Reaction enthalpies for the reactions involving 15 different tethers. ΔH_{rxn} values are in kcal/mol. **c)** Graphical representation of ΔH_{rxn} values. Both exo-methylene (Y: C=CH₂) and carbonyl (Y: C=O) groups on the tether decrease ΔH_{rxn} . The reaction enthalpy for the intermolecular reaction between benzene and methylallene is also shown in purple.

Allene Substitution

First, we probed the effects of substitution on the allene moiety. As shown in Figure 2.2, we initially computed the enthalpies (ΔH_{allene}) of the intermolecular reactions between benzene and allenes substituted with the various tethers. However, we soon realized that the resulting bicyclic product exhibited steric clashing between the hydrogens on the exo-methylene and the bridgehead carbon, introducing undesired error into our calculated enthalpies. Realizing that the ΔH_{allene} values of interest are, in essence, the enthalpic preference of vinyl substitution compared to substitution of an allene moiety, we subsequently simplified our model to directly measure this energetic difference between vinyl and allenyl substitution (Figure 2.2). A graph of $\Delta\Delta H_{\text{allene}}$ is shown in Figure 2.3a, with values reported relative to the reference transformation where the Y-X substituent is replaced with a hydrogen.

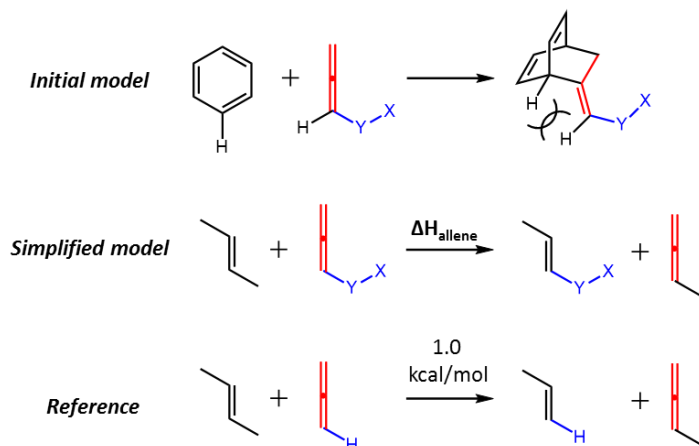
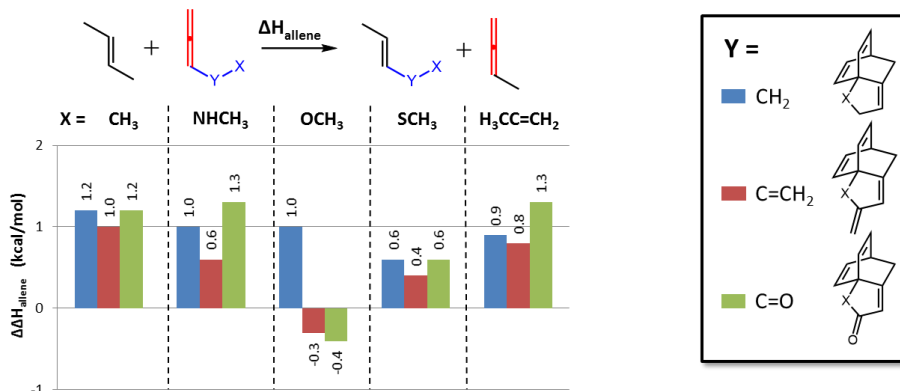


Figure 2.2. Development of the model to study allene substitution effects.

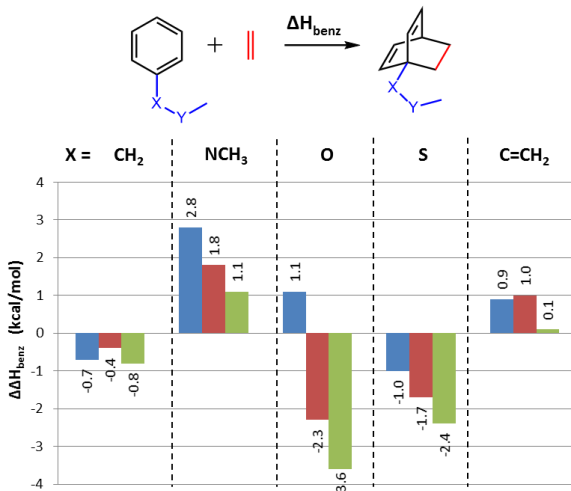
Examination of the $\Delta\Delta H_{\text{allene}}$ values reveals a minimal substituent effect on the allene moiety; relative to hydrogen, all of the substituents studied resulted in similar or marginally higher preference (*ca.* 1 kcal/mol) for allene substitution, regardless of the nature of **X**. Altering **Y** (CH₂, C=CH₂, or C=O) causes little change to $\Delta\Delta H_{\text{allene}}$, with the oxygen-containing tethers showing the largest variance of 1.4 kcal/mol. In general, $\Delta\Delta H_{\text{allene}}$ remains relatively unchanged

despite varying substitution of the allene; therefore, the influence of the tether on the thermodynamics of the IMDA reaction is not largely due to its effect on the allene component.

a) Allene Substitution



b) Benzene Substitution (sp² vs. sp³)



c) Ring Strain

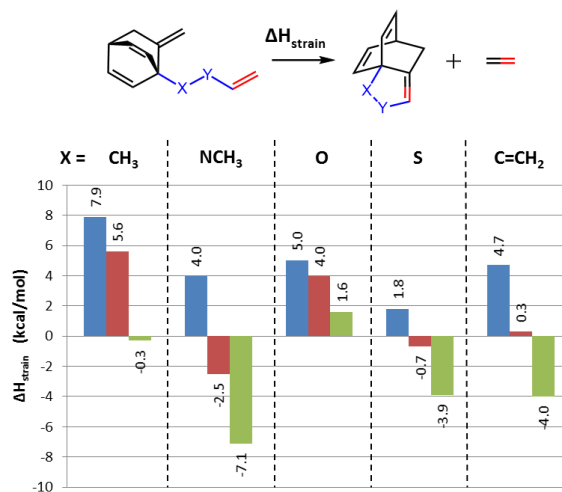


Figure 2.3. Graphical representations of the enthalpic contribution due to **a)** tether substitution on the allene moiety, with respect to the parent unsubstituted allene; **b)** tether substitution on the aryl group, with respect to the benzene/ethylene reaction; and **c)** ring strain.

Benzene Substitution

We then considered the effect of substitution on the phenyl ring by each tether. By examining the intermolecular Diels–Alder reaction between tether-substituted benzene and allene, we can determine the preference of each tether for bonding either to the aromatic sp^2 -hybridized carbon or the bridgehead sp^3 -hybridized carbon. To avoid the issue of errors due to steric hindrance between the exo-methylene and the pendant tether in the bicyclic product, similarly observed in the previous section, ethylene was used as the dienophile. The $\Delta\Delta H_{\text{benz}}$ values in Figure 2.3b are presented relative to the intermolecular reaction of ethylene and benzene, which has a reaction enthalpy of 4.2 kcal/mol.

When $\mathbf{X} = \text{CH}_2$, there is a slight yet consistent preference for substitution at the sp^3 -hybridized carbon over the aromatic ring for the cycloaddition. The sulfur-containing substituents ($\mathbf{X}: \text{S}$) demonstrate a similar tendency, favoring bridgehead substitution more so than their carbon analogues. Alternatively, nitrogen- and alkene-based tethers ($\mathbf{X}: \text{NCH}_3$ and $\text{C}=\text{CH}_2$, respectively) had a preference for attachment to the phenyl ring rather than the tertiary carbon, likely from the lost conjugation in the latter. Conjugation also explains the general decrease in $\Delta\Delta H_{\text{benz}}$ going from methylene to carbonyl tethers ($\mathbf{Y}: \text{CH}_3$ and $\text{C}=\text{O}$) in all the heteroatomic cases; incorporation of the carbonyl allows for continued electron delocalization in the bicyclic product, whereas the Diels–Alder reaction with the saturated methylene tethers results in a complete loss of conjugation. The oxygen-based substituents ($\mathbf{X}: \text{O}$) underwent a more pronounced shift in $\Delta\Delta H_{\text{benz}}$. The methoxy group effectively delocalizes electrons into the phenyl ring; the stereoelectronic nature of the vinyloxy and acetoxy substituents significantly differ from the methoxy analogue, exhibiting decreased resonance with the phenyl ring and increased favorability of bridgehead substitution. Prior studies of phenyl substitution corroborate our ΔH_{benz} values.¹³ Although altering the atom directly connected to the aromatic ring may produce minor enthalpic differences, $\Delta\Delta H_{\text{benz}}$ marginally decreases but remains largely unchanged going from methylene

to exo-methylene to carbonyl tethers. The exception is the oxygen series, where a change in electronics from methoxy to acetoxy causes a 5 kcal/mol switch in preference.

Ring Strain

The most marked difference between the intermolecular and intramolecular Diels–Alder reactions is formation of the additional 5-membered ring by the tether in the latter case. Prior studies of IMDA reactions demonstrate the importance of the tether,⁷ attributing differences in energy to conformationally induced strain. Strain energies of cyclopentenes and heterocyclic analogues have been previously studied computationally through various theoretical schemes, from the long-established group increments¹⁴ to the use of homodesmotic reactions,¹⁵ and more recently with Bader’s theory of ‘atoms-in-molecules.’¹⁶ To determine the importance of strain in the 5-membered ring in our systems, we utilized the homodesmotic reaction shown in Figure 2.3c and calculated ΔH_{strain} for each tether. A direct comparison of the acyclic and cyclic forms of the substrates should provide an appropriate measure of the induced strain in the system.

Regardless of the identity of the **X** atom, the ΔH_{strain} values follow a similar trend when changing **Y** from CH₂ to C=CH₂ to C=O, increasing the preference for the cyclic form. When **Y** = CH₂, strain causes the acyclic form to be favored across the board. The carbon analogue suffers the most, resulting in an endothermicity of 7.9 kcal/mol for the ring-closing transformation. On the other hand, sulfur only disfavors the closed form by 1.8 kcal/mol. The longer C–S bonds allow for less distortion about the trisubstituted double bond of the 5-membered ring (Figure 2.4). By defining ϕ_{diff} as the sum of the change in internal bond angles (ϕ_1 and ϕ_2) between the open and closed forms, we observe that **2_S_CH₂** brings about a ϕ_{diff} value of 16.5° – a 9° smaller angle distortion than **2_CH₂_CH₂**.

Transitioning to the exo-methylene tether (**Y** = C=CH₂) replaces an sp³-hybridized carbon with an sp²-hybridized center, attenuating the angular strain for all instances of **X** but still not

resulting in particularly favorable enthalpies. Proceeding to a carbonyl tether introduces a stronger conjugative effect, increasing the p-character of the neighboring heteroatom and relieving more strain in the 5-membered ring. Comparing ϕ_{diff} of **2**_CH₂_C=O and **2**_S_C=O once again reveals a qualitative correlation between alkene distortion and closed-form favorability; an 8.7 decrease of the in-plane bending angles leads to a 3.6 kcal/mol shift in stability. The nitrogen tether, benefiting the most from conjugation with the carbonyl, favors the closed form by 7.1 kcal/mol.

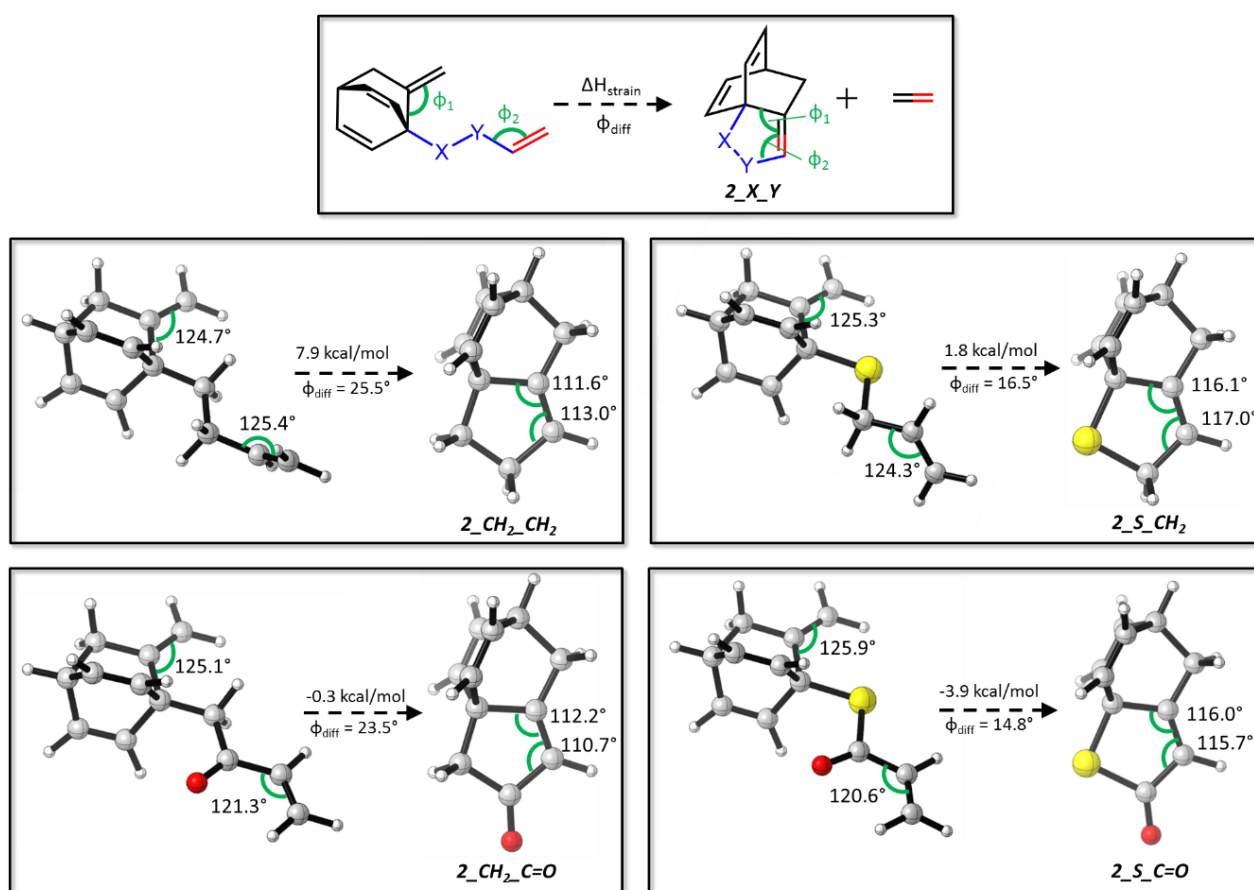


Figure 2.4. The extent of alkene in-plane angle distortion, described by ϕ_{diff} , qualitatively correlates with the enthalpic costs of ring closure. ϕ_{diff} is defined as the combined difference in internal bond angles of the double bond when going from open to closed forms. Carbon and sulfur analogues are shown here.

What Explains the Thermodynamic Differences?

In order to validate our enthalpic decomposition into substituent and strain components, a plot of ΔH_{rxn} against the sum of ΔH_{allene} , ΔH_{benz} , and ΔH_{strain} is shown in Figure 2.5. A strong correlation ($R^2 = 0.98$) was found, certifying the effectiveness of our method in accounting for the differences in reaction enthalpies. Although the -4.1 kcal/mol y-intercept implies that there may be factors we are excluding or over-representing in our analysis, the clear linear relationship suggests that these factors are constant across the various tethers and therefore are inconsequential when contrasting their differences.

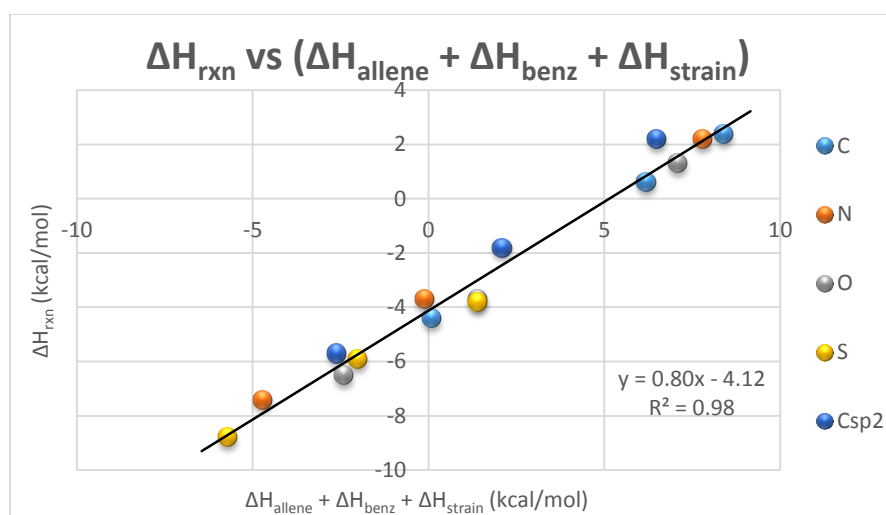


Figure 2.5. The strong correlation between the calculated reaction enthalpy and the compilation of theoretical enthalpic factors validates the energy decomposition analysis.

Ring strain correlates best with and is the principal contributing factor to the computed reaction enthalpies of substrates **1_X_Y**. Examination of a plot of ΔH_{rxn} vs. ΔH_{strain} reveals strong linear correlations within each heteroatomic series when going from methylene to exo-methylene to carbonyl tethers (Figure 2.6). The only series with an $R^2 < 0.99$ is **1_O_Y**, which only has a coefficient of 0.85 and a noticeably different regression line slope. The large difference in

stereoelectronics going from methoxy to acetoxy substituents on the benzene group discussed earlier accounts for this discrepancy. Considerable amounts of strain in the pendant 5-membered ring decrease the thermodynamic favorability of the IMDA products **2_X_Y**; thus, alterations of the tethers which minimize the forming ring strain may lead to potentially successful transformations.

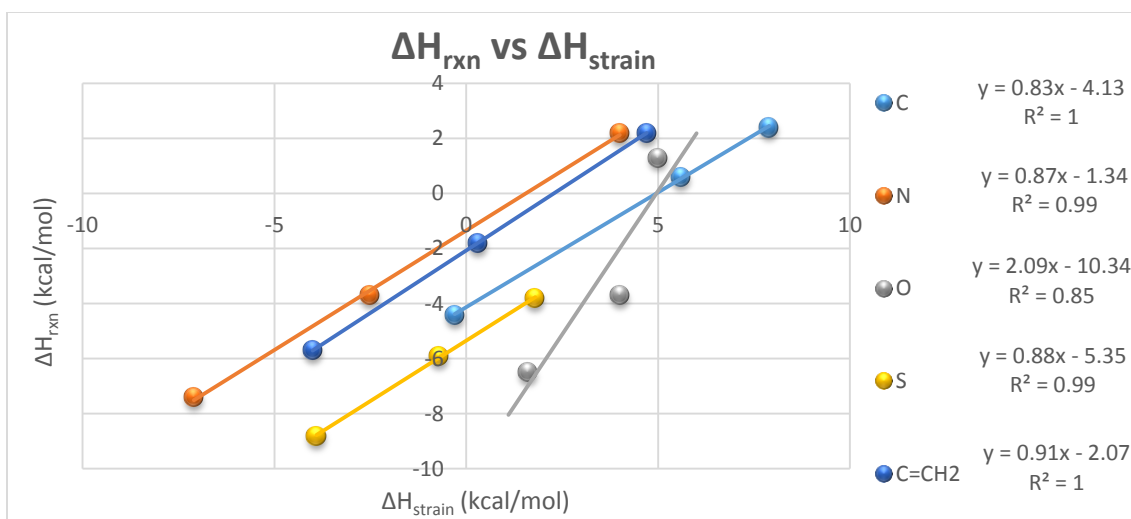


Figure 2.6. Reaction enthalpies correlate well with strain enthalpies.

Conclusion

The success of the IMDA reaction between allene and arene moieties is highly reliant on the nature of the tether linking them together. The thermodynamic variability of the transformation led us to investigate the effects of substitution and strain on the reaction enthalpies. Decomposition of the total enthalpy ΔH_{rxn} into individual components revealed that aryl and allenyl substitution by the tether do not substantially influence the reaction enthalpy. However, strain induced by formation of the 5-membered ring by the tether provides the largest energetic contribution, resulting in a strong correlation between ΔH_{rxn} and ΔH_{strain} . Our analysis reveals that the poor experimental yield⁵ observed for the ketone-tethered substrate

1-CH₂-C=O is due to the strain of the fused cyclopentenone ring of the product, whereas the more successful nitrogen and oxygen analogues, **1-NCH₃-C=O** and **1-O-C=O**, form less-strained lactenam and lactenone scaffolds.

Moreover, replacing the carbonyl moiety with an alkene or a saturated methylene had little effect on benzene and allene substitution but demonstrated significant increases in ring strain in the cyclic products. The introduction of an sp³-hybridized carbon center in lieu of an sp²-center worsens the angle strain as well as decreases conjugation with the heteroatom. Hence, the favorable thermodynamics of IMDA reactions with heteroatomically-tethered substrates are principally attributed to developing ring strain; future substrates looking to successfully employ the benzene/allene cycloaddition should aim to alleviate the strain brought about by the composition of the tether.

References

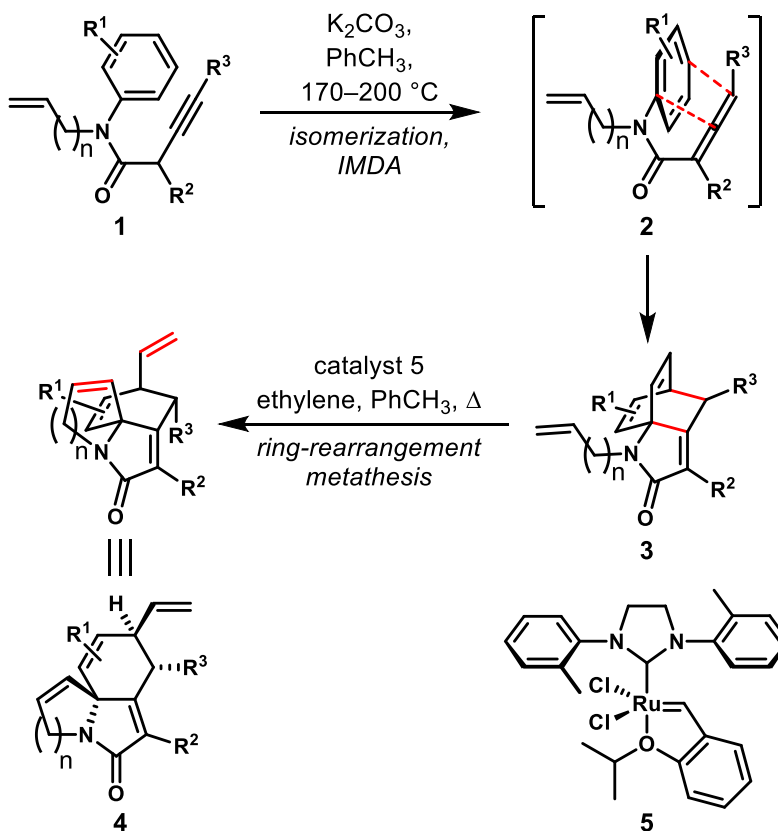
1. Parvatkar, P. T.; Kadamb, H. K.; Tilve, S. G. *Tetrahedron* **2014**, *70*, 2857–2888.
2. Himbert, G.; Henn, L. *Angew. Chem., Int. Ed.* **1982**, *21*, 620.
3. For select examples with benzene as a diene: (a) Ciganek, E. *Tetrahedron Lett.* **1967**, *8*, 3321–3325. (b) Cossu, S.; Garris, F.; DeLucchi, O. *Synlett* **1997**, *12*, 1327–1334.
4. (a) Himbert, G.; Fink, D. *Tetrahedron Lett.* **1985**, *26*, 4363–4366. (b) Himbert, G.; Fink, D.; Diehl, K. *Chem. Ber.* **1988**, *121*, 431–441. (c) Himbert, G.; Fink, D. *J. prakt. Chem.* **1994**, *336*, 654–657. (d) Himbert, G.; Fink, D. *J. prakt. Chem.* **1997**, *338*, 233–242. (e) Himbert, G.; Ruppnich, M.; Knöringer, H. *J. Chin. Chem. Soc.* **2003**, 143–151.
5. Schmidt, Y.; Lam, J. K.; Pham, H. V.; Houk, K. N.; Vanderwal, C. D. *J. Am. Chem. Soc.* **2013**, *135*, 7339–7348.
6. Pham, H. V.; Houk, K. N. *J. Org. Chem.* **2014**, *79*, 8968–8976.
7. (a) Krenske, E. H.; Houk, K. N.; Holmes, A. B.; Thompson, J. *Tetrahedron Lett.* **2011**, *52*, 2181–2184. (b) Krenske, E. H.; Perry, E. W.; Jerome, S. V.; Maimone, T. J.; Baran, P. S.; Houk, K. N. *Org. Lett.* **2012**, *14*, 3016–3019.
8. (a) Lee, C.; Yang, W.; Parr, R. G. *Phys. Rev. B* **1988**, *37*, 785–789. (b) Becke, A. D. *J. Chem. Phys.* **1993**, *98*, 5648–5652. (c) Parr, R. G. *Annu. Rev. Phys. Chem.* **1995**, *46*, 701–728.
9. Frisch, M. J.; et al. *Gaussian 09*, revision D.01; Gaussian, Inc.: Wallingford, CT, 2009.
10. (a) Zhao, Y.; Truhlar, D. G. *Acc. Chem. Res.* **2008**, *41*, 157. (b) Zhao, Y.; Truhlar, D. G. *J. Phys. Chem. A* **2008**, *112*, 1095–1099.
11. (a) Pieniazek, S.; Houk, K. N. *Angew. Chem.* 2006, *118*, 1470; *Angew. Chem., Int. Ed.* 2006, *45*, 1442. (b) Pieniazek, S.; Clemente, F. R.; Houk, K. N. *Angew. Chem.* 2008, *120*, 7860; *Angew. Chem., Int. Ed.* 2008, *47*, 7746.
12. Cossi, M.; Rega, N.; Scalmani, G.; Barone, V. *J. Comput. Chem.* **2003**, *24*, 669–681.
13. Wiberg, K. B.; Rablen, P. R. *J. Org. Chem.* **1998**, *63*, 3722–3730.
14. Schleyer, P. v. R.; Williams, J. E.; Blanchard, K. R. *J. Am. Chem. Soc.* **1970**, *92*, 2377–2386.
15. (a) Wheeler, S. E.; Houk, K. N.; Schleyer, P. v. R.; Allen, W. D. *J. Am. Chem. Soc.* **2009**, *131*, 2547–2560. (b) Houry, P. R.; Goddard, J. D.; Tam, W. *Tetrahedron* **2004**, *60*, 8103–8112.
16. Bauzá, A.; Quiñonero, D.; Deyà, P. M.; Frontera, A. *Chem. Phys. Lett.* **2012**, *536*, 165–169.

Chapter 3.1. Computation and Experiment Reveal that the Ring-Rearrangement Metathesis of Himbert Cycloadducts Can Be Subject to Kinetic or Thermodynamic Control

Introduction

We have recently reported¹ the use of the Himbert arene/allene intramolecular Diels–Alder (IMDA) reaction² to generate strained bridged polycyclic lactams that are, in many cases, excellent substrates for ring-rearrangement metathesis to afford the corresponding fused isomeric polycycles (Scheme 3.1.1). However, upon delving deeper into this chemistry, we have found several substrates that unpredictably did not undergo metathesis rearrangement, some examples of unexpectedly diastereoselective rearrangements, and some interesting qualitative differences in metathesis reaction rates among quite similar substrates. Taken together, these observations suggested some mechanistic subtleties that we felt were worth exploration, given the importance of the bridged-to-fused metathesis rearrangement strategy in complex molecule synthesis.³

Scheme 3.1.1. Sequential use of the Himbert arene/allene intramolecular Diels–Alder (IMDA) reaction and ring-rearrangement metathesis to afford fused polycyclic lactams.



Background

The ring strain in bridged bicycles, especially bicyclo[2.2.1]heptanes, but also bicyclo[2.2.2]octanes, as well as their heterocyclic variants, has long been used as a driving force for rearrangement of these ring systems. Frequently, the substrates are made by cycloaddition chemistry. Starting with the synthesis of capnellene by Stille and Grubbs reported in 1986 (Figure 3.1.1a),⁴ and especially over the past two decades, alkene metathesis has been used extensively to rearrange strained bridged bicyclic structures when a suitable pendant alkene is present;³ in its absence, many of these strained ring systems act as effective monomers for ring-opening

metathesis polymerization (ROMP) (Figure 3.1.1b).⁵ Likely owing to the effectiveness of the ROMP process, it appears that these related ring-rearrangement metathesis processes are often assumed to initiate via ring-opening metathesis driven by relief of ring strain. However, Grubbs clearly demonstrated in 1996 that strain is not a prerequisite for some types of metathesis cascades when his group showed that even cyclopentenes and cyclohexenes bearing two tethered alkenes can undergo productive rearrangements (Figure 3.1.1c);⁶ in this case, the enthalpic benefit of loss of ethylene drives the rearrangement equilibrium. In that paper, the authors reasoned that initiation likely proceeds at the monosubstituted tethered alkene in preference to the disubstituted ring alkene, but that initiation at the ring alkene might well be dominant with sufficient ring strain. Accordingly, both initiation mechanisms might be plausible in many cases, particularly if the ring system is not highly strained. One of many elegant applications of ring-rearrangement metathesis to complex molecule synthesis can be seen in Figure 3.1.1d, wherein the Phillips group rearranged oxanorbornene **14** to fused bicyclic product **15**;⁷ the site of initiation of this key transformation *en route* to kumausyne has apparently not been determined. Finally, and surprisingly, Fallis has recently shown using careful NMR and deuterium labeling studies that the ring-rearrangement metathesis of alkene-tethered norbornenes is not initiated by ring-opening metathesis, but rather by metathesis of the pendant alkene (Figure 3.1.1e).⁸ In all of the examples in Figure 3.1.1 other than the cyclopentene ring-rearrangement (1c), it would appear plausible that there is sufficient ring strain in the starting materials to render these reactions essentially irreversible, and thereby kinetically controlled, although no distribution of related products would be expected in any of these contexts.

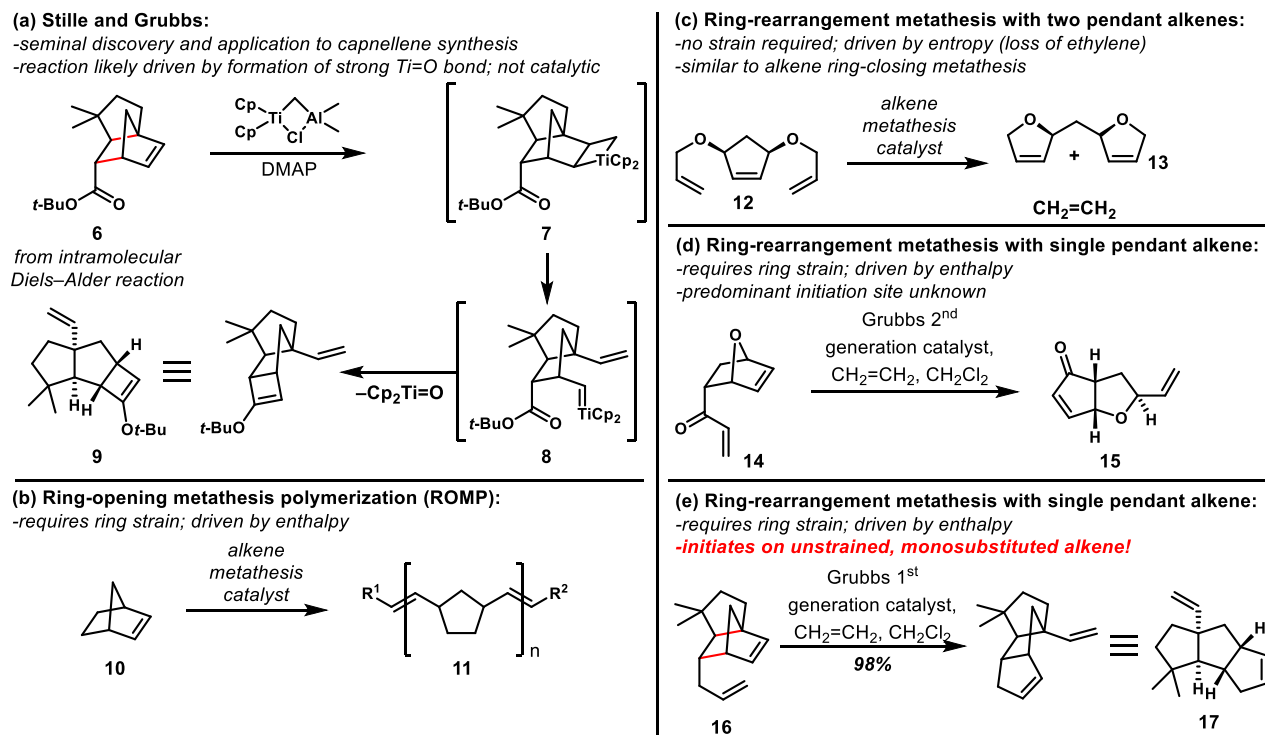


Figure 3.1.1. Important relevant examples of ring-rearrangement metathesis, and the related ring-opening metathesis polymerization (ROMP) process.

In the context of our work on the rearrangement of Himbert cycloadducts, we have found what we believe to be a substrate-dependent change in mechanism for these rearrangement reactions, which we describe in detail in this report. Moreover, some unusual stereochemical results are rationalized on the basis of this mechanistic dichotomy. Some of these unusual findings might be explained by a deviation from the expected kinetic control in strain-driven ring-rearrangement metathesis; experimental and computational results both suggest that many of the rearrangements of Himbert cycloadducts are under thermodynamic control.

Results and Discussion

Ring-Rearrangement Metathesis: Order of Steps

Our first general foray into the ring-rearrangement metathesis of Himbert cycloadducts dealt with achiral tricyclic lactams bearing pendant alkenes on nitrogen (Figure 3.1.2). Substrate **18a** rearranged smoothly under catalysis by 2nd-generation Hoveyda–Grubbs-type catalyst **5**,⁹ although heating in toluene (minimum 50 °C, usually carried out at 100 °C) under an atmosphere of ethylene was required. With this substrate, initiation by metathesis with the pendant alkene is not feasible, because geometric constraints preclude the intermediate ruthenium alkylidene from reacting with the strained alkene of the bicyclo[2.2.2]octadiene system; therefore, productive rearrangement must initiate with ring-opening metathesis. Systems **18b** and **18c**, with homologous tethered alkenes, rearranged under the same conditions to give the rearranged products in high yield, but these reactions were significantly faster than the one with allylic amine **18a**. This observation suggested that initiation was occurring at the unstrained pendant alkene (RCM/ROM pathway) for **18a/b**, because if ROM was initiating, then the subsequent RCM steps might be expected to be slower with increasing ring size, not faster, if the ring closure were the rate-determining step. That supposition assumes that the ROM process would transpire at similar rates regardless of the nature of the tethered alkene. These rather trivial observations and the logical conclusions that followed piqued our interest in the mechanistic subtleties of these reactions.

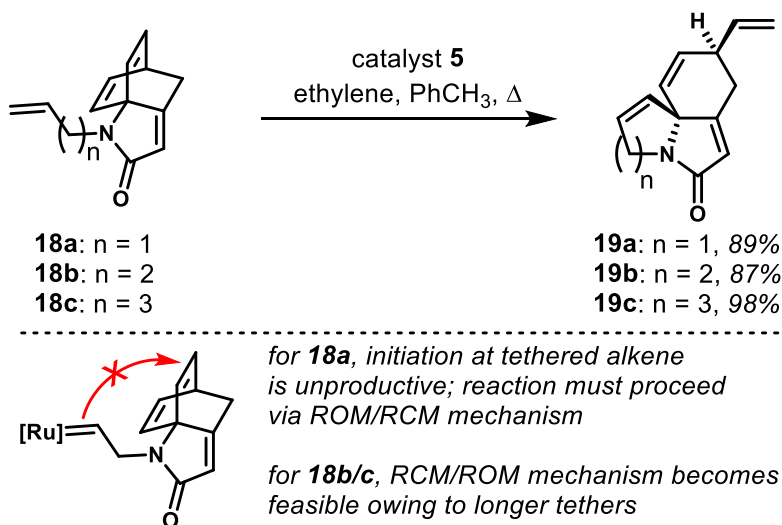


Figure 3.1.2. Ring-rearrangement metathesis of achiral tricyclic lactams **18a–c**.

Much more dramatic results were obtained with the closely related chiral (racemic) tricyclic lactams that were obtained via Himerb cycloaddition of γ -methyl-substituted allene (Figure 3.1.3). These cycloadducts (**20a–c**) each reacted productively under our standard conditions to afford the fused products **21a–c**; however, there was a surprising difference in stereochemical outcome. Whereas *N*-allyl and *N*-pentenyl substrates rearranged to afford single isomers of product to the limits of detection by ¹H NMR, the *N*-butenyl substrate **20b** delivered a 3:1 ratio of diastereomers. As a further data point, the *N*-methyl congener **22** was subjected to the same conditions, and the ring-opened ethenolysis product **23** was obtained as a single diastereomer. When **23** was exposed to metathesis catalyst **5** *without ethylene*, bridged tricyclic compound **22** was regenerated (80% yield, 10% recovered **23**). We also attempted ring-rearrangement metathesis of the *N*-undecenyl substrate **24** and only ring-opened product **25** was obtained. In an attempt to form the 13-membered ring, **25** was exposed to catalyst **5** in dilute solution (no ethylene); tricyclic product **24** was formed in 73% yield. These two examples clearly demonstrate that there is sufficiently little strain in the tricyclic cycloadducts that ring closure can

be effected when coupled to the entropically favored release of ethylene. In the series **20a–c**, only the reaction of **20a** absolutely required ethylene; **20b** and **20c** did not (this dichotomy was also observed with **18a** and **18b**, but **18c** was not tested). These results are consistent with preferential reactivity of the pendant alkene over the cyclic alkene; for *N*-allyl substrates **18a** and **20a**, RCM is not feasible owing to the short tether (see Figure 3.1.2) and ethylene presumably allows for rapid disengagement of the catalyst. For the longer tethers, of course, RCM should be possible and ethylene should play a lesser role in the reaction outcome.

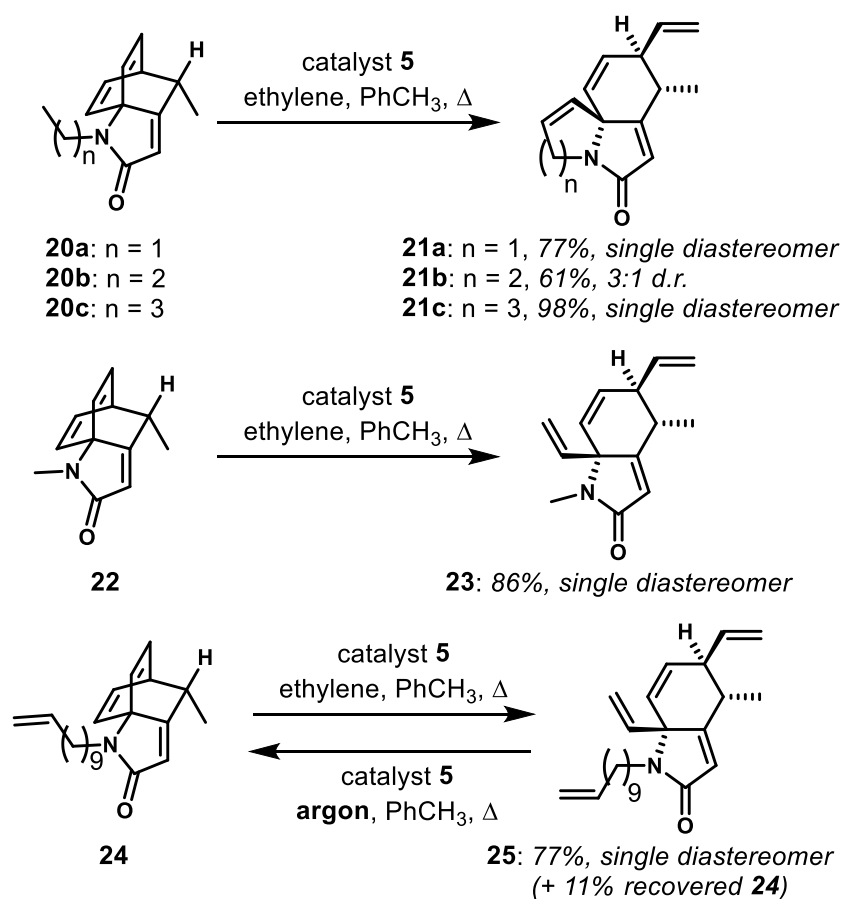


Figure 3.1.3. Unusual stereochemical results in the ring-rearrangement metathesis reactions of chiral tricyclic lactams (starting materials and products are racemic).

Initially, we expected that these metathesis processes would afford a kinetic distribution of products that should be governed by which diastereotopic ring alkene reacted preferentially. Further, we assumed that catalyst approach would be preferred “between” the two alkenes, which didn’t offer obvious possibilities for high levels of diastereocontrol. Therefore, we were surprised to observe high diastereoselectivity in many cases, and even more intrigued by the difference with substrate **20b**. We considered that there might be an unexpected preference for catalyst approach from the other side of the reactive alkenes, which would permit the methyl group on the stereogenic carbon to play a role in determining the regioselectivity of metathesis initiation, ultimately dictating the stereochemical outcome of the reaction. While that idea might reasonably account for the outcome of the reaction of **20a**, in which initiation of rearrangement must occur at the ring alkenes, it does not explain in a clear way why selectivity decreases with **20b**, but the reaction of **20c** is again exquisitely selective.

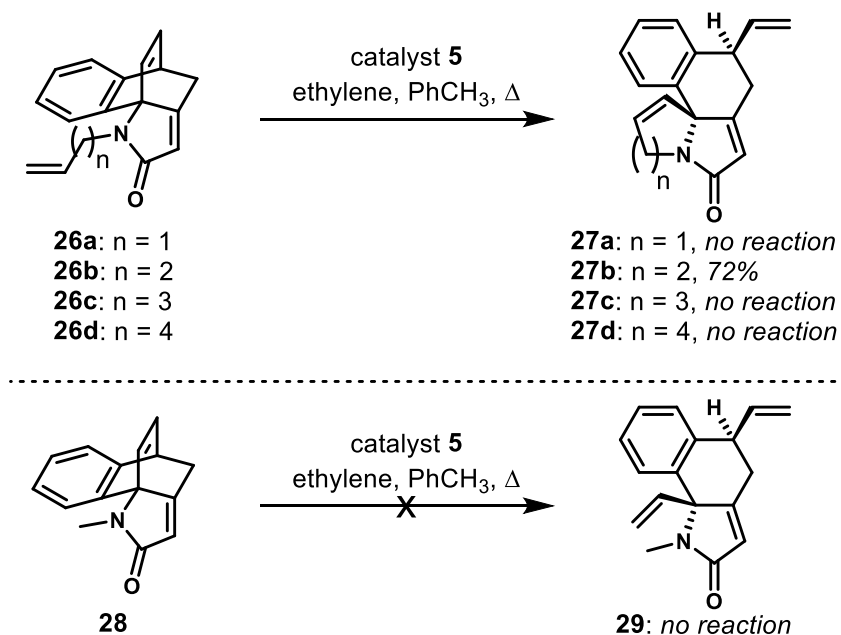


Figure 3.1.4. Unusual ring-rearrangement metathesis results with benzo-fused substrates.

A third striking set of data was obtained from the attempted ring-rearrangement metathesis of the homologous series of benzo-fused cycloadducts shown in Figure 3.1.4. In this particular series, only *N*-butenyl substrate **26b** reacted to afford fused tetracyclic product **27b**; substrates with other tether lengths were recovered unchanged, without ethylenolysis of the bicyclic system. As a control experiment, *N*-methyl substrate **28** was subjected to metathesis conditions and it, too, was recovered unchanged. The differences in reactivity between these benzo-fused systems and the simpler tricycles shown in Figure 3.1.1 were unanticipated. Certainly, a steric impediment to productive ring closure was suspected, but it was not obvious why **26b** would react successfully, and the other substrates were unreactive. Finally, the cycloadducts ultimately derived from 2,3-dimethyl aniline (Figure 3.1.5) led to further confusion, owing to the (moderately) successful rearrangements in all cases examined, but wherein the ring-opening ethylenolysis of **32** failed. We were at a loss to explain differences in reactivity of the series **26a–c** with **30a–c**, given what must be similar steric environments about the relevant alkenes.

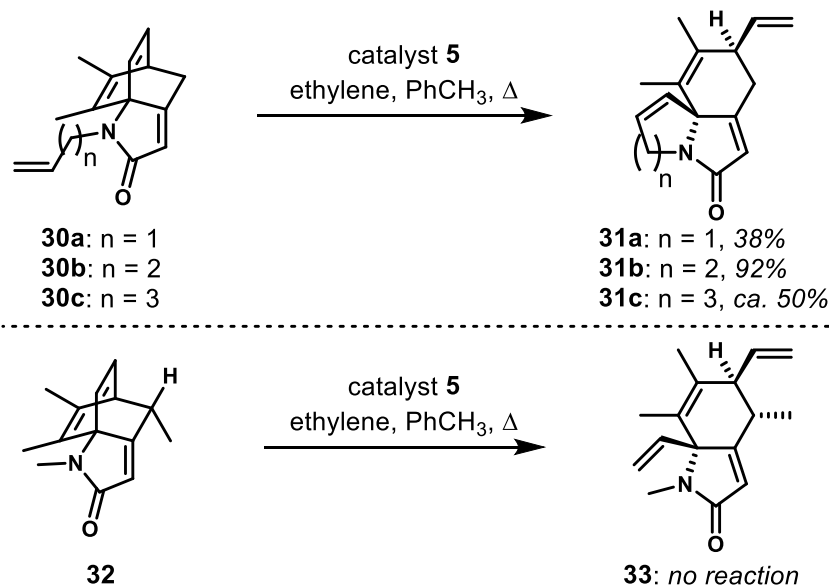


Figure 3.1.5. Metathesis experiments on cycloadduct derived from 2,3-dimethylaniline.

Computation Clarifies Unusual Experimental Results

General Computational Study Design

As a whole, the results shown in Figures 2 through 5 could not be easily reconciled, and it was not clear that further experiments would aid in the development of a working model to understand this family of rearrangement reactions. When faced with situations in which the collection of more experimental data is not likely to increase our understanding of reaction mechanisms or outcomes, our UCI and UCLA groups have engaged in fruitful collaborations, with the latter group providing expertise in DFT calculations of ground-state energies and transition states.^{1b,10} In this section, we will demonstrate how the collection of aberrant/unexpected results described above can in fact be reconciled via careful consideration of both kinetic and thermodynamic reaction parameters; the key data required to shed light on the unusual experimental outcomes could only be obtained by calculation.

The mechanisms of ring-opening and ring-closing metatheses have been studied extensively by computation in recent decades,¹¹ but ring-rearrangement metathesis has received less focus.¹² We began our investigation by determining the chemoselectivity of initiation of the ring-rearrangement metathesis of substrates **18a** and **18b**, which differ by only one carbon in the tether, to determine if tether length influenced whether ROM or RCM would occur first. The two pathways are shown in Figure 3.1.6, with key intermediates shown along each route. In the ROM/RCM manifold, the (somewhat) strained cyclic alkene of the bridged tricyclic system is engaged first, leading to ring-opening; an important consideration here involves the regiochemistry of reaction. Two different ruthenium alkylidenes can be formed, and only one is able to proceed to product by ring-closure onto the tethered alkene. The other regioisomer (not shown) would require ring-closure back to the starting tricyclic system, followed by opening to afford the only productive regioisomer. In the RCM/ROM pathway, the terminal alkene is

engaged first, and the cyclic alkene can only react with the tethered ruthenium alkylidene in one regioisomeric sense, owing to geometrical constraints.

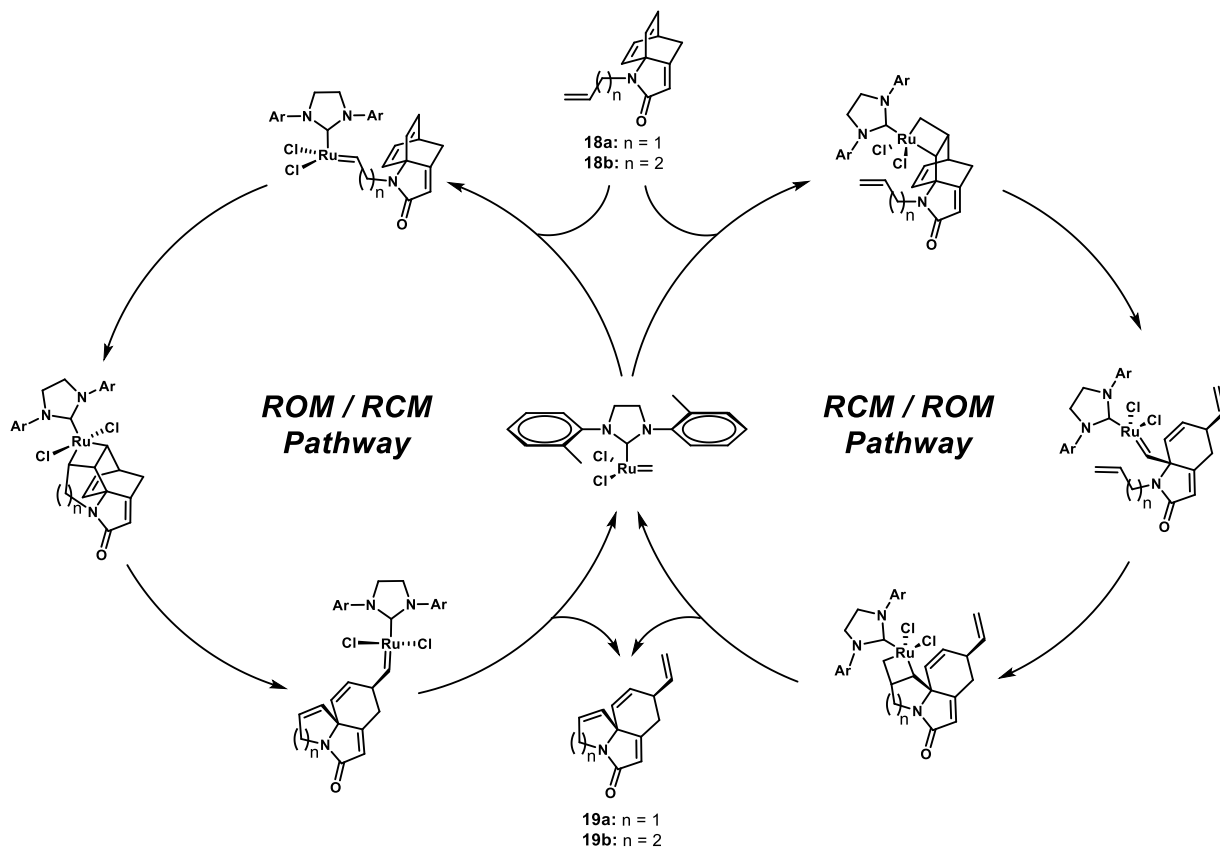


Figure 3.1.6. Two possible orders of events for the ring-rearrangement metatheses of representative Himbert cycloadducts **18a** and **18b**.

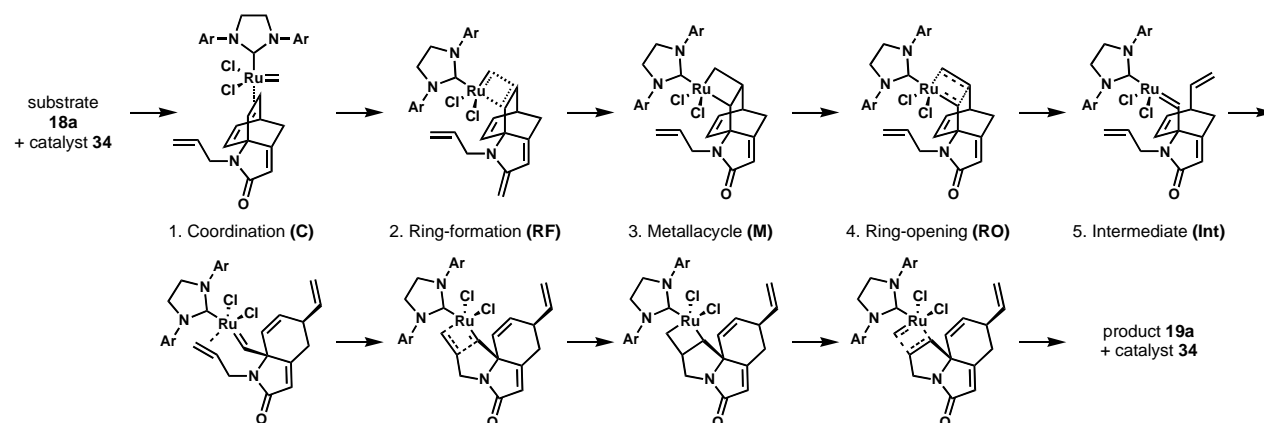


Figure 3.1.7. The five different types of stationary points that will be considered in the computational results described herein, as exemplified in the ROM/RCM mechanism for **18a**.

Note that within each cascade, the first four types stationary points recur in each cycle.

Prior investigations of metathesis cascades have established a Chauvin-type mechanism¹³ that generally consists of five relevant stationary points (Figure 3.1.7, shown for ROM/RCM reaction of **18a**): (1) coordination of the catalyst to the substrate, (2) a transition state for the formation of the metallacycle, (3) a metallacycle intermediate, (4) a transition state for the metallacycle ring-opening, and (5) the newly formed alkylidene intermediate or product. For both the ROM/RCM and the RCM/ROM cascades, there are multiple distinct stationary points of types (1) through (4), as shown in the Figure for the ROM/RCM manifold.

All structures shown in Figure 3.1.7 have been optimized using the B3LYP density functional with a LANL2DZ basis set for the ruthenium atom of the catalyst and a 6-31G(d) basis set for the carbon, oxygen, nitrogen, and hydrogen atoms.¹⁴ Single point energies were calculated with the Mo6 functional, using the mixed basis set of SDD for Ru and 6-311+G(d,p) basis set for the remaining atoms.^{11b,15} This protocol has been successfully applied in prior metathesis investigations.¹⁶ The SMD model for toluene was used for solvation energy corrections.¹⁷

Although the precatalyst **5** consists of a benzylidene ligand and a chelating isopropoxy group, initiation under ethylene atmosphere generates the active species **34** which participates in the catalytic cycle. Initiation of **5** has been studied extensively before, and thus we use **34** as our model catalyst in all calculations.¹⁸

Mechanistic Differences Among Substrates 18a–c

The free energy profiles for the ROM/RCM and RCM/ROM cascades of *N*-allyl substrate **18a** are shown in Figure 3.1.8. Catalyst **34** (derived from precatalyst **5**) initially prefers to react with the pendant alkene, forming **Int1** of the RCM/ROM pathway. However, the short *N*-allyl tether cannot allow formation of **M2** without introducing significant strain into the polycyclic system. This restriction results in transition state **RO2** having an insurmountable free energy 37.1 kcal/mol higher than that of **Int1** and ultimately ruling out the RCM/ROM pathway for **18a**. Conversely, initial ring-opening of the bicyclo[2.2.2]octadiene leads to a more reasonable energy span¹⁹ of 11.5 kcal/mol, calculated from the energy difference between the lowest-lying intermediate (**C2'**) and the highest subsequent barrier (**RO2'**). Because the reaction is only favored by about 5 kcal/mol, and because of the relatively small energy barriers involved, this reaction should be fully reversible (under thermodynamic control).²⁰ Depending on the approach of the ruthenium catalyst, various ring-opening pathways are reasonable. We have computationally studied each reasonable pathways, but the one shown here where ROM and RCM occurs intramolecularly (without dissociation/association of the catalyst with the help of a molecule of ethylene) is the most plausible, containing the lowest energy span. Hence, **18a** follows an ROM/RCM mechanism because of its shorter tether length, a result that one could rationalize without computation in this case, but that nonetheless provides an excellent starting point for this study.

The *N*-butenyl-substituted substrate **18b** exhibits substantially lower strain in the ring-closing and ring-opening steps associated with metallacycle **M2** of the RCM/ROM pathway (Figure 3.1.9). The longer tether allows adoption of a favorable conformation for the intramolecular metathesis reaction to occur, thereby lowering the energy span for the RCM/ROM pathway to 11 kcal/mol. The ROM/RCM cascade, in contrast, is relatively unaffected by the longer tether of **18b**, resulting in a free energy profile similar to that for **18a**. We should note that the initial steps of this pathway (**C1'** to **RO1'**) were not explicitly calculated for **18b**, but rather these energies were taken from **18a** because the tether elongation from **18a** to **18b** is remote from the reaction site and should not appreciably affect the energetics of these stationary points. Although both RCM/ROM and ROM/RCM energy spans are comparable—an 11.0 kcal/mol energy span for RCM/ROM is determined by the energy difference between low-lying intermediate **M3** and extruded product **19b**, while the ROM/RCM energy span of 12.0 kcal/mol from alkylidene **Int1'** to metallocyclobutene formation **RF2'**—the preference for catalyst attack at the less hindered alkene tether points towards RCM/ROM being the dominant pathway. Moreover, the low-lying intermediate **M3** prevents the backward trajectory from occurring, since it would require greater than 20 kcal/mol (back to **RF2**) compared to the 11 kcal/mol needed for the extrusion of product. This large preference for the forward reaction, which is not present in the ROM/RCM cascade for **18a**, also very nicely explains the disparity in diastereoselectivity observed between chiral substrates **20a** and **20b** (see below).

Consequences in the Stereoselectivity of Rearrangement of Chiral Substrates 20a–c

Our computational studies indicate that the favored ROM/RCM pathway for **18a**, and analogously for the methylated **20a**, does not have a strong preference to proceed to product from low-lying intermediate **C2'**; there is only a 2.6 kcal/mol difference between **RO2'** and **RF1'**, the rate-determining steps of the forward and backward reactions, respectively.

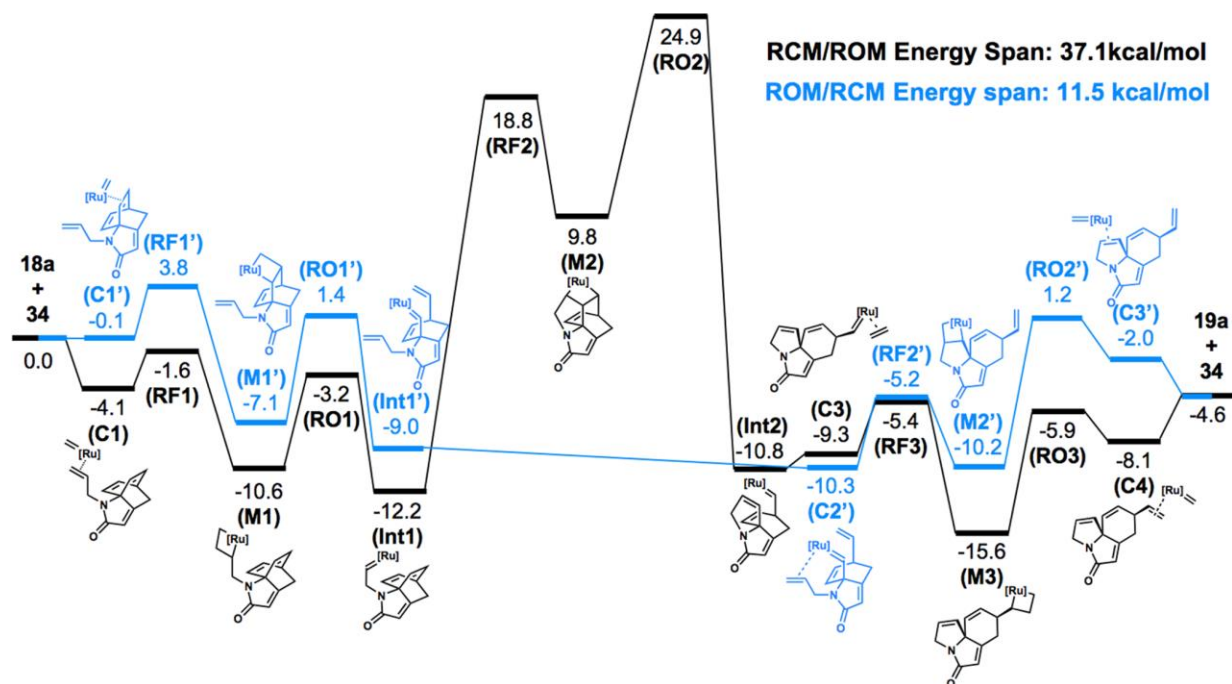


Figure 3.1.8. Computational comparison of the RCM/ROM and ROM/RCM pathways for the metathesis rearrangement of **18a** suggests a strong preference for the ROM/RCM pathway via an equilibrating process. Mo6/6-311+G(d,p)/SDD//B3LYP/6-31G(d)/LANL2DZ, SMD:Toluene.

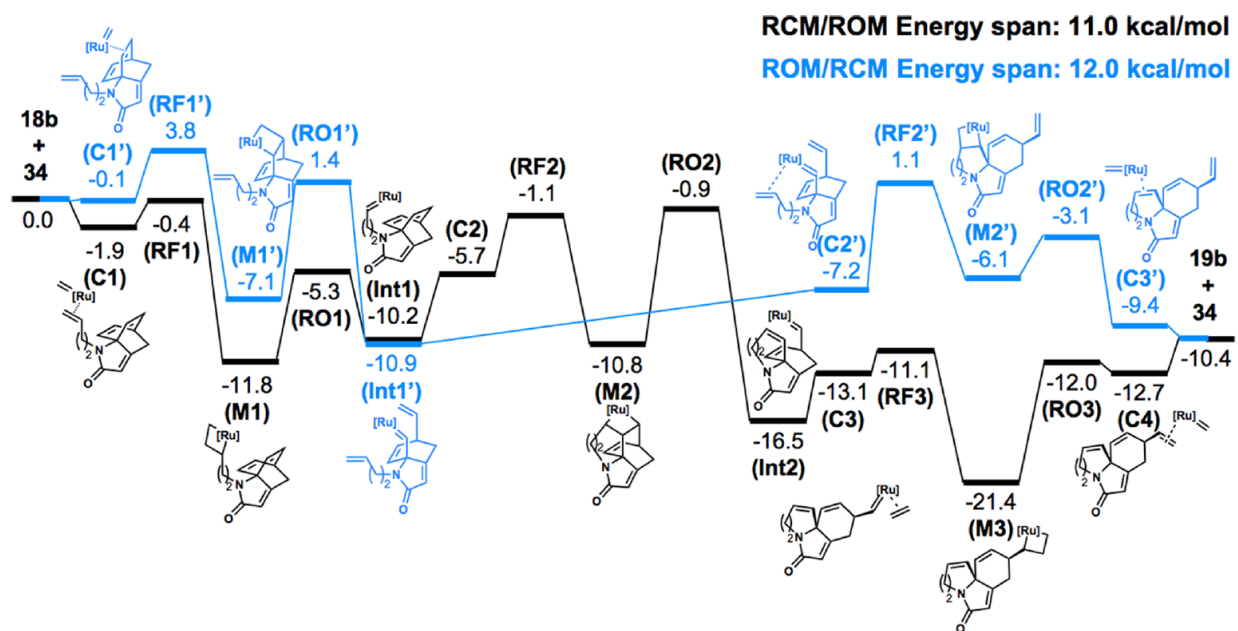


Figure 3.1.9. Computational comparison of the RCM/ROM and ROM/RCM pathways for the metathesis rearrangement of **18b** suggests a preference for the RCM/ROM pathway via a kinetically controlled process. Mo6/6-311+G(d,p)/SDD//B3LYP/6-31G(d)/LANL2DZ, SMD:Toluene.

Consequently, the chiral substrate **20a** will equilibrate between intermediates until product formation and release, and the ratio of diastereomeric products will be governed by reaction thermodynamics. Calculated free energies (DFT) show that **21a_trans** is favored over **21a_cis** by 3.2 kcal/mol, consistent with observing only the trans isomer experimentally (Figure 3.1.10a).

On the other hand, since the reaction profile of **20b** should closely resemble that of **18b**, where formation of **Int2** will exclusively lead to product and equilibration with prior intermediates is not viable, stereoselectivity is determined by the RCM steps **Int1** to **Int2**. Thus, the ratio of **21b_trans** and **21b_cis** is controlled by the energy difference in between barriers **RO2** and **RF2'**, and not the calculated product energies shown. Computations predict a 0.7 kcal/mol preference for major product **21b_trans**, which translates to *ca.* 3:1 dr at 100 °C (Figure 3.1.10b).

Metathesis of the longer pentenyl-substituted **20c** resulted in formation of **21c_trans** exclusively, which is unexpected since **20c** contains a sufficiently long tether to proceed through the RCM/ROM pathway (similar to **20b**) but **RF2** and **RF2'** are virtually degenerate (Figure 3.1.10c). The higher energy of **M3** accounts for this peculiarity; the large propensity for **Int2** to proceed in the forward direction is now diminished because of the facility to revert back to **Int1**. The 5.1 kcal/mol required to recross **RF2** is now comparable to the ~5 kcal/mol needed overcome **RF3** to achieve metallocyclobutane **M3**. Moreover, product **21c_cis** is higher in energy than **RF2**, suggesting that the backwards reaction to form **Int2** is kinetically favored, and eventually only **M3**, and ultimately **21c_trans**, will be formed. Note that the instability of **Int2** and **Int2'** arise from the strain of the newly formed 7-membered ring, as evidenced by the 6 kcal/mol rise in energy on going from **21b** to **21c** for both isomers.

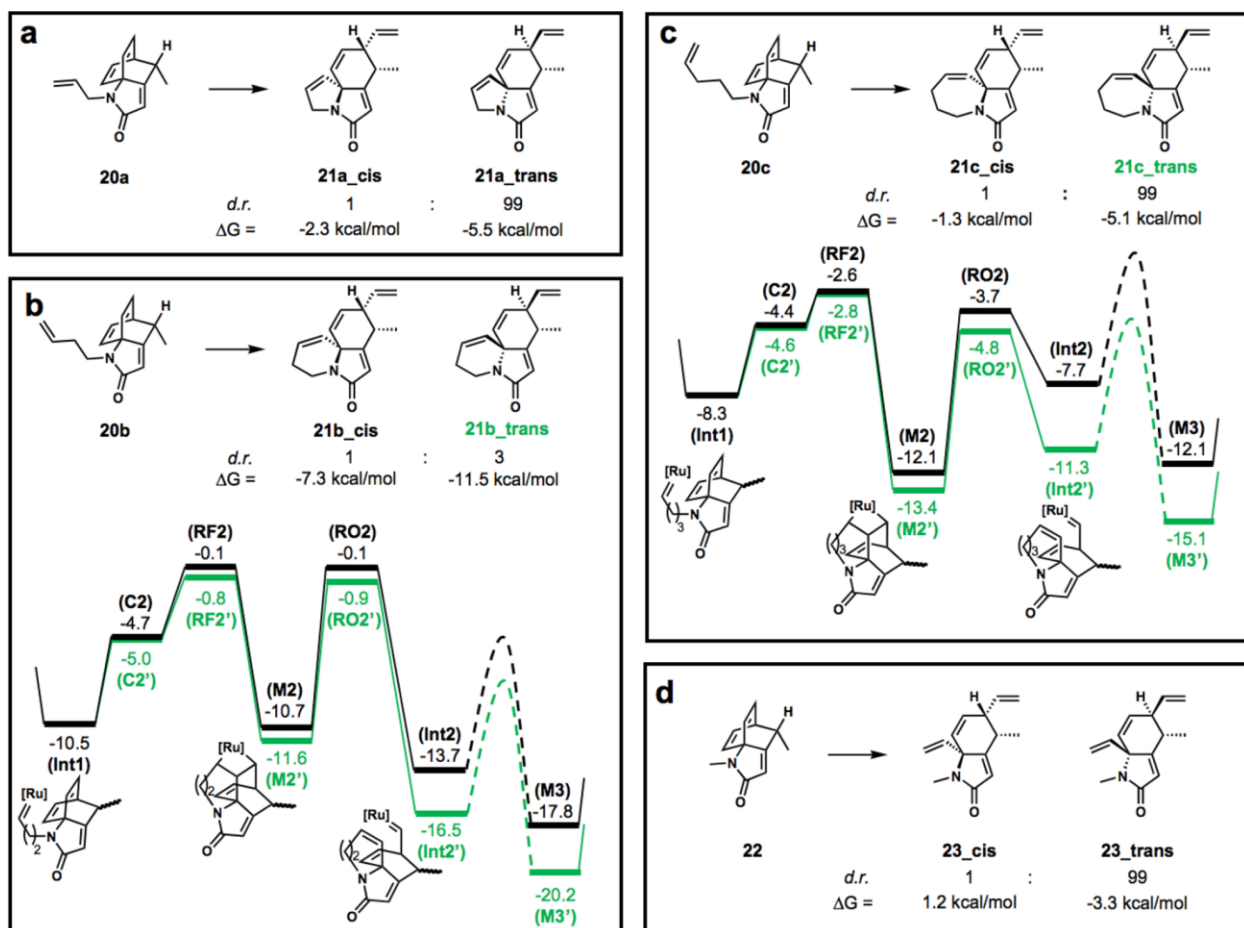


Figure 3.1.10. Concerning the diastereoselectivity of ring-rearrangement metathesis of chiral, methyl-substituted Himbert cycloadducts **20a–c** and **22**. **a.** The rearrangement of **20a** (ROM/RCM) is thermodynamically controlled, and only **21a_trans** is observed. **b.** The rearrangement of **20b** (RCM/ROM) is kinetically controlled, and a 3:1 ratio of products **21b_trans:21b_cis** is observed. **c.** The rearrangement of **20c** (RCM/ROM) is thermodynamically controlled, and only **21a_trans** is observed. **d.** The ring-opening ethenolysis of **22** is thermodynamically controlled, and only **23_trans** is observed. MO6/6-311+G(d,p)/SDD // B3LYP/6-31G(d)/LANL2DZ, SMD:Toluene. *d.r.* values are from experiment, free energies (ΔG) are from DFT and are in kcal/mol.

N-Methyl substrate **22** undergoes clean ethenolysis under standard conditions, affording only the trans product (Figures 3.1. and 3.1.10d), and *N*-undecenyl substrate **24** behaves virtually identically (Figure 3.1.3). The reaction of **22** is thermodynamically controlled, and 4.5 kcal/mol preference calculated for the trans isomer is completely consistent with the observed results. While calculations were not performed on the reaction of **24** to afford ethylenolysis product **25**, it is reasonable to expect the same behavior as **22**, with the kinetics of ring-closure to a 13-membered ring accounting for the lack of tricyclic products observed. Furthermore, under reaction conditions that exclude ethylene, the reverse transformation proceeds to complete conversion.

An Explanation for the Unusual Results with Benzo-Fused and Ring Alkene-Substituted Substrates

A similar explanation can be invoked to explain the reactivity of benzo-fused substrates **26a-d** and alkene substituted reactants **30a-c**. In addition to **26a** and **30a**, which participate in the “quasi-reversible” ROM/RCM mechanism owing to their short tethers, the destabilization of **Int2** provides easier access to the backward reaction for substrates **26b-d** and **30b-c** which undergo RCM/ROM, thereby causing thermodynamics to control the reaction outcomes. Figure 3.1.11 illustrates the steric strain that arises in **Int2** after ring-closing metathesis generates the fused carbocycle. Ring alkene substituents that are in proximity of the nitrogen tether destabilize the fused ring system, and this effect also presents itself in the reaction free energies of the products. Hence, by examining the DFT calculated free energies of reaction in Figure 3.1.12, we can predict whether the reaction will be successful, and a clearer picture can be drawn. Metatheses that result in higher energy products will of course favor the backward reaction, preventing the ring-rearrangement cascade from being productive. The only outlier is the reaction with **26a**, which is predicted to be exergonic but results in no appreciable yield of **27a**. While we do not

completely understand that outcome, we do note that the reaction of **26a** requires traversing one relatively high barrier (compared with the analogous reaction of **18a**, on account of the increased steric strain) that might account for the lack of production of tetracyclic product **27a**.²¹

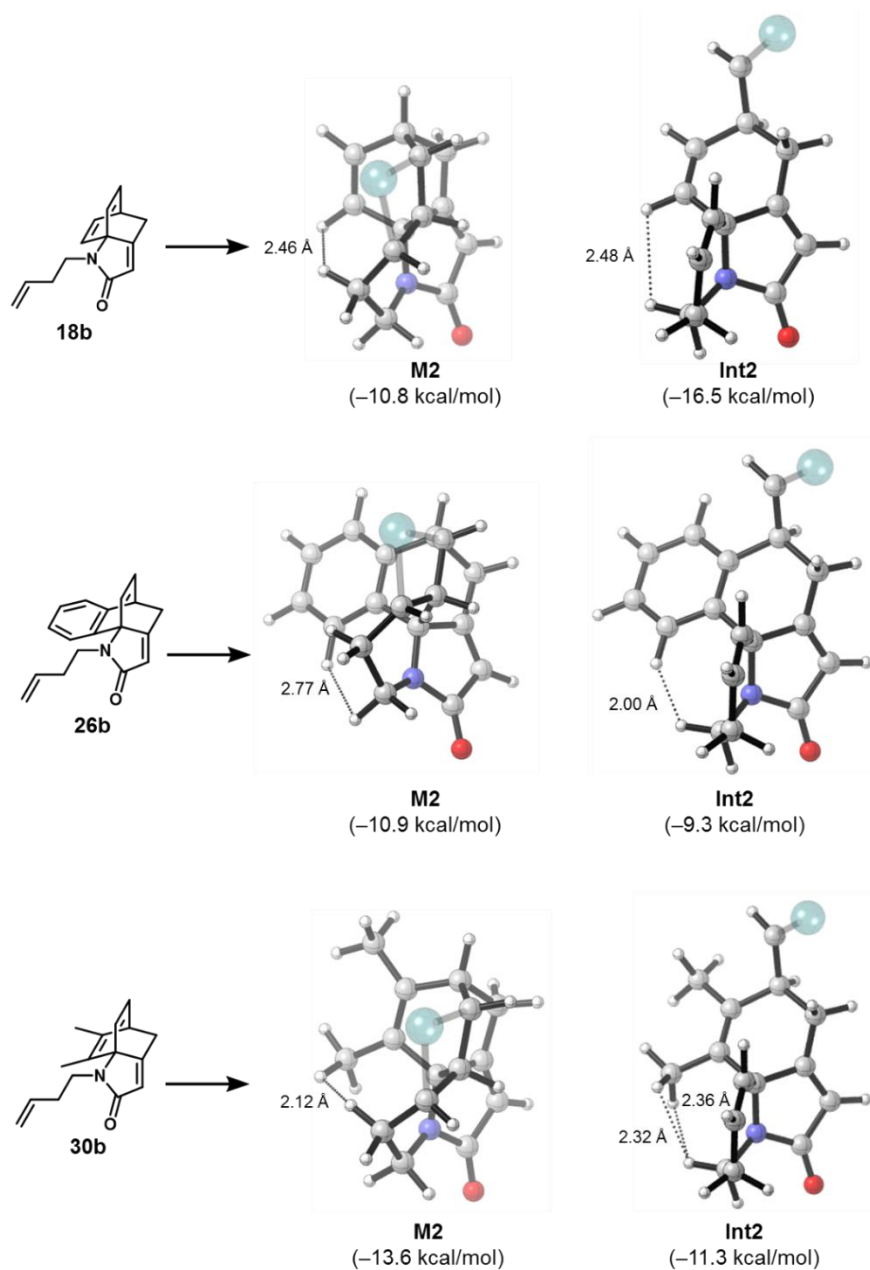


Figure 3.1.11. Steric strain in intermediates **Int2** for substrates of type **26** and **30** bearing ring alkene substituents raises the energy of that intermediate and results in a thermodynamically controlled reaction. Catalyst architecture has been hidden for clarity. Please see the Supporting Information for more details.

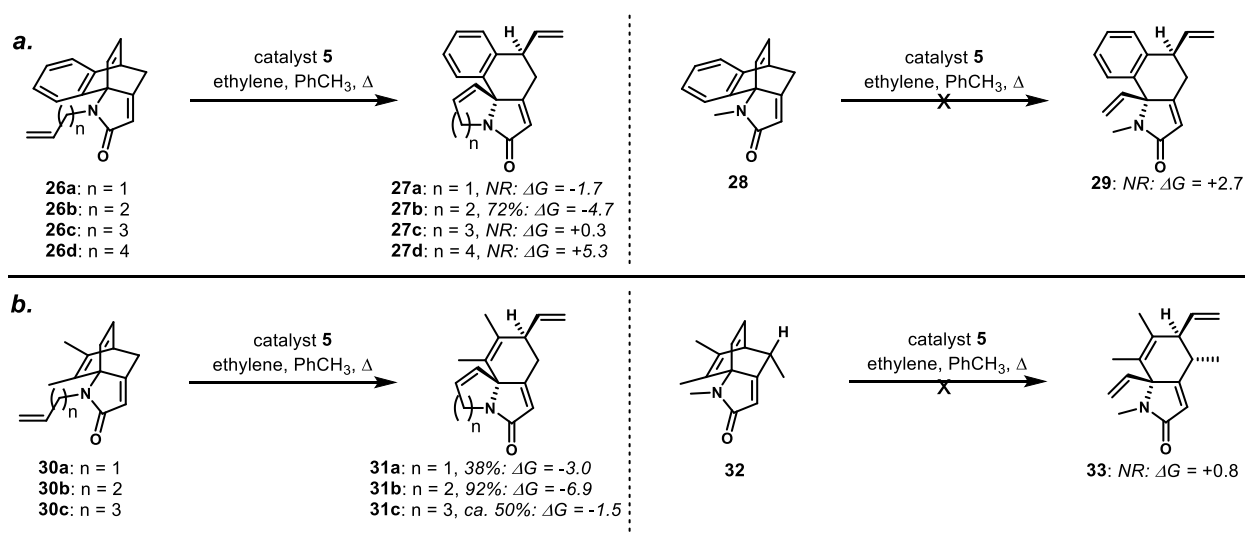


Figure 3.1.12. The reactions of ring alkene-substituted systems are under thermodynamically controlled and can therefore be explained by the free energies of reactions. **a.** Benzo-fused examples **26a–d** and **28**. **b.** Ring alkene-substituted examples **30a–c** and **32**.

Conclusions

Unusual experimental observations in the course of the bridged to fused ring-rearrangement metathesis of Himbert cycloadducts were not readily explained by further experiments. Computational interrogation of these results led to reasonable explanations for the previously irreconcilable results. We now understand that in these systems:

1. Initiation of metathesis by the ruthenium catalysts is favored at the monosubstituted, tethered alkene over the bicyclic alkene, despite the potential for relief of ring strain in the latter. As a result, the RCM/ROM pathway is generally favored.
2. If the tether is not sufficiently long enough to enable an RCM/ROM cascade, then the only productive pathway available is the ROM/RCM, which requires equilibration to ring-opened intermediates.

3. Generally, in the RCM/ROM pathways, the reactions are kinetically controlled owing to the irreversibility of the RCM step; however, in the ROM/RCM cascades, product distribution is thermodynamically controlled because of facile equilibration.

4. In certain substituted cases, sufficient strain can be induced in key metallocyclobutane and ruthenium alkylidene intermediates to raise the energies of these species in such a way as to facilitate equilibration in RCM/ROM systems; in these cases, reaction free energies can explain the success or failure of the metathesis rearrangements.

These general observations allowed for the satisfactory explanation of the experimentally observed changes in reactivity and diastereoselectivity among closely related substrate groups. The message that transcends the current study is that these and related ring-rearrangement metathesis reactions might often be subject to thermodynamic, and not kinetic, control. Naturally, this situation is most likely when the reactants are not highly strained, as in the case of the bridged bicyclo[2.2.2]octadiene substructures in this study.²² Finally, this work serves to reinforce the fact that initiation of ring-rearrangement metathesis cascades is often preferred at a tethered, less substituted alkene,⁸ rather than the strained and “ostensibly more reactive” ring alkene.

References

1. (a) Lam, J. K.; Schmidt, Y.; Vanderwal, C. D. *Org. Lett.* **2012**, *14*, 5566–5569. (b) Schmidt, Y.; Lam, J. K.; Pham, H. V.; Houk, K. N. Vanderwal, C. D. *J. Am. Chem. Soc.* **2013**, *135*, 7339–7348.
2. Himbert, G.; Henn, L. *Angew. Chem. Int. Ed.* **1982**, *21*, 620.
3. For reviews, see: (a) Holub, N.; Blechert, S. *Chem. Asian. J.* **2007**, *2*, 1064–1082. (b) Arjona, O.; Csáky, A. G.; Plumet, J. *Eur. J. Org. Chem.* **2003**, 611–622.
4. Stille, J. R.; Grubbs, R. H. *J. Am. Chem. Soc.* **1986**, *108*, 855–856.
5. Bielawski, C. W.; Grubbs, R. H. *Prog. Polym. Sci.* **2007**, *32*, 1–29.
6. Zuercher, W. J.; Hashimoto, M.; Grubbs, R. H. *J. Am. Chem. Soc.* **1996**, *118*, 6634–6640.
7. Chandler, C. L.; Phillips, A. J. *Org. Lett.* **2005**, *7*, 3493–3495.
8. Nguyen, N. N. M.; Leclère, M.; Stogaitis, N.; Fallis, A. G. *Org. Lett.* **2010**, *12*, 1684–1687.
9. (a) Garber, S. B.; Kingsbury, J. S.; Gray, B. L.; Hoveyda, A. H. *J. Am. Chem. Soc.* **2000**, *122*, 8168–8179. (b) Gessler, S.; Randl, S.; Blechert, S. *Tetrahedron Lett.* **2000**, *41*, 9973–9976.
10. (a) Pham, H. V.; Martin, D. B. C.; Vanderwal, C. D.; Houk, K. N. *Chem. Sci.* **2012**, *3*, 1650–1655. (b) Paton, R. S.; Steinhardt, S. E.; Vanderwal, C. D.; Houk, K. N. *J. Am. Chem. Soc.* **2011**, *133*, 3895–3905.
11. (a) Aagaard, O. M.; Meier, R. J.; Buda, F. *J. Am. Chem. Soc.* **1998**, *120*, 7174–7182. (b) Adlhart, C.; Hinderling, C.; Baumann, H.; Chen, P. *J. Am. Chem. Soc.* **2000**, *122*, 8204–8214. (c) Adlhart, C.; Chen, P. *J. Am. Chem. Soc.* **2004**, *126*, 3496–3510. (d) Torker, S.; Merki, D.; Chen, P. *J. Am. Chem. Soc.* **2008**, *130*, 4808–4814. (e) Bernardi, F.; Bottoni, A.; Miscione, G. P. *Organometallics* **2003**, *22*, 940–947. (f) Cavallo, L. *J. Am. Chem. Soc.* **2002**, *124*, 8965–8973. (g) Cavallo, L.; Correa, A. *J. Am. Chem. Soc.* **2006**, *128*, 13352–13353. (h) Vyboishchikov, S. F.; Bühl, M.; Thiel, W. *Chem.-Eur. J.* **2002**, *8*, 3962–3975. (i) Fomine, S.; Martinez Vargas, S.; Tlenkopatchev, M. A. *Organometallics* **2003**, *22*, 93–99. (j) Suresh, C. H.; Koga, N. *Organometallics* **2004**, *23*, 76–80. (k) Tsipis, A. C.; Orpen, A. G.; Harvey, J. N. *Dalton Trans.* **2005**, 2849–2858. (l) Straub, B. F. *Adv. Synth. Catal.* **2007**, *349*, 204–214. (m) Occhipinti, G.; Bjørsvik, H. R.; Jensen, V. R. *J. Am. Chem. Soc.* **2006**, *128*, 6952–6964. (n) Zhao, Y.; Truhlar, D. G. *Org. Lett.* **2007**, *9*, 1967–1970. (o) du Toit, J. I.; van Sittert, C. G. C. E.; Vosloo, H. C. M. *J. Organomet. Chem.* **2013**, *738*, 76–91.
12. (a) Holub, N.; Blechert, S. *Chem.-Asian J.* **2007**, *2*, 1064–1082. (b) Bose, S.; Ghosh, M.; Ghosh, S. *J. Org. Chem.* **2012**, *77*, 6345–6350. (c) Minger, T. L.; Phillips, A. J. *Tetrahedron Lett.* **2002**, *43*, 5357–5359.
13. Chauvin, Y.; Herisson, J. *Makromol. Chem.* **1971**, *141*, 161–167.

14. a) Becke, A. D. *Phys. Rev. A* **1988**, *38*, 3098–3100. (b) Lee, C.; Yang, W.; Parr, R. G. *Phys. Rev. B* **1988**, *37*, 785–789. (c) Becke, A. D. *J. Chem. Phys.* **1993**, *98*, 5648–5652. (d) Stephens, P. J.; Devlin, F. J.; Chabalowski, C. F.; Frisch, M. J. *J. Phys. Chem.* **1994**, *98*, 11623–11627.
15. Śliwa, P.; Handzlik, J. *Chem. Phys. Lett.* **2010**, *493*, 273–278.
16. a) Liu, P.; Xu, X.; Dong, X.; Keitz, B. K.; Herbert, M. B.; Grubbs, R. H.; Houk, K. N. *J. Am. Chem. Soc.* **2012**, *134*, 1464–1467. (b) Herbert, M. B.; Lan, Y. Keitz, B. K.; Liu, P.; Endo, K.; Day, M. W.; Houk, K. N.; Grubbs, R. H. *J. Am. Chem. Soc.* **2012**, *134*, 7861–7866. (c) Miyazaki, H.; Herbert, M. B.; Liu, P.; Dong, X.; Xu, X.; Keitz, B. K.; Ung, T.; Mkrumyan, G.; Houk, K. N.; Grubbs, R. H. *J. Am. Chem. Soc.* **2013**, *135*, 5848–5858.
17. Marenich, A. V.; Cramer, C. J.; Truhlar, D. G. *J. Phys. Chem. B* **2009**, *113*, 6378–6396.
18. (a) Vorfalt, T.; Wannowius, K. J.; and Plenio, H. *Angew. Chem. Int. Ed.* **2010**, *49*, 5533. (b) Ashworth, I. W.; Hillier, I. H.; Nelson, D. J.; Percy, J. M.; Vincent, M. A. *Chem. Commun.* **2011**, *47*, 5428–5430.
19. For an explanation of "energy span" and its relation to the kinetics of catalytic cycles: Kozuch, S.; Shaik, S. *Acc. Chem. Res.* **2011**, *44*, 101–110.
20. For a review discussing equilibria in ring-closing metathesis reactions, see: Monfette, S.; Fogg, D. E. *Chem. Rev.* **2009**, *109*, 3783–3816.
21. Please see the Supporting Information in the original publication for details.
22. For some representative examples of the metathesis rearrangements of bicyclo[2.2.2]octene systems, see: (a) Minger, T. L.; Phillips, A. J. *Tetrahedron Lett.* **2002**, *43*, 5357. (b) Bose, S.; Ghosh, M.; Ghosh, S. *J. Org. Chem.* **2012**, *77*, 6345–6350.

Chapter 3.2. Computational and Experimental Investigations of the Formal Dyotropic Rearrangements of Himbert Arene/Allene Cycloadducts

Introduction

Over the past several years, our research groups have been collaboratively investigating the mechanistic details¹ and synthetic utility² of a fascinating dearomatizing cycloaddition³ originally discovered by Himbert and Henn.^{3a} The subject reactions convert allenecarboxanilides and closely related arene/allenes into bridged, topologically complex, and relatively strained tricyclic cycloadducts (**1** → **2**, Figure 3.2.1) with great potential for thermodynamically driven rearrangement to other ring systems. For example, we have studied in some detail the ring-rearrangement metathesis of Himbert cycloadducts bearing tethered alkenes (**3** → **4**).^{2,4} In this disclosure, we share the results of our computational and experimental investigations of a formal dyotropic shift that converts Himbert cycloadducts into rearranged tricyclic products.^{3c,5}

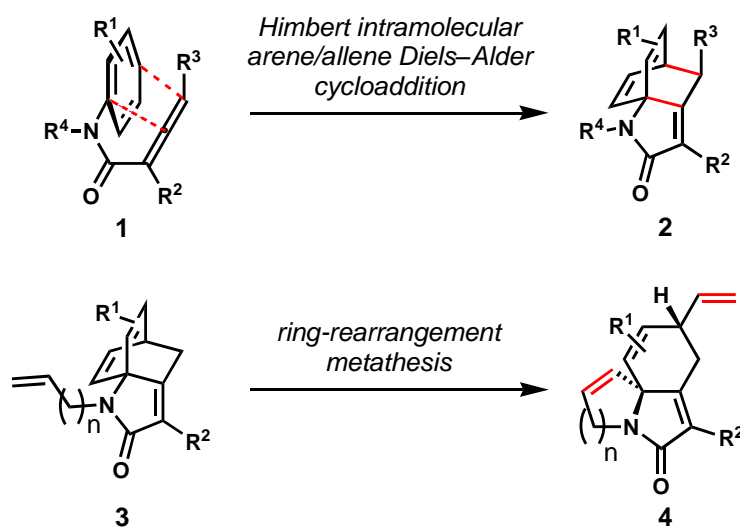


Figure 3.2.1. The Himbert arene/allene cycloaddition and the ring-rearrangement metathesis (RRM) of select alkene-bearing cycloadducts.

Background

Dyotropic Rearrangements

Dyotropic rearrangements are a special type of pericyclic process defined by Reetz in the 1970s^{6,7} that have been leveraged in complex molecule synthesis⁸ and subjected to a range of mechanistic investigations.^{9,10} Reetz distinguished Type I rearrangements,^{6a} where two sigma bonds interchange positions, from Type II rearrangements, where two sigma bonds both move to new bonding sites with a repositioning of a π -bond.^{6b} Mechanistic investigations have shown that the Type I dyotropic shift can occur through either concerted or stepwise pathways. (Figure 3.2.2).^{10a,b,x,y} The stepwise reaction can be described as sequential pinacol-like shifts that cause interconversion of the positions of two groups in a vicinal arrangement.

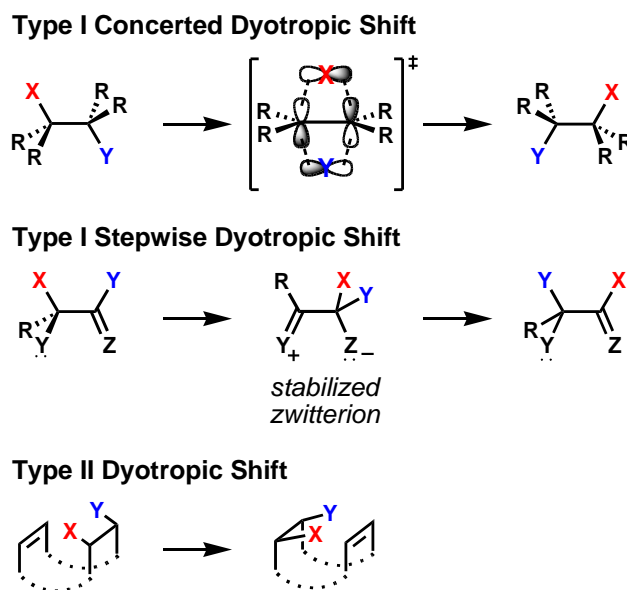


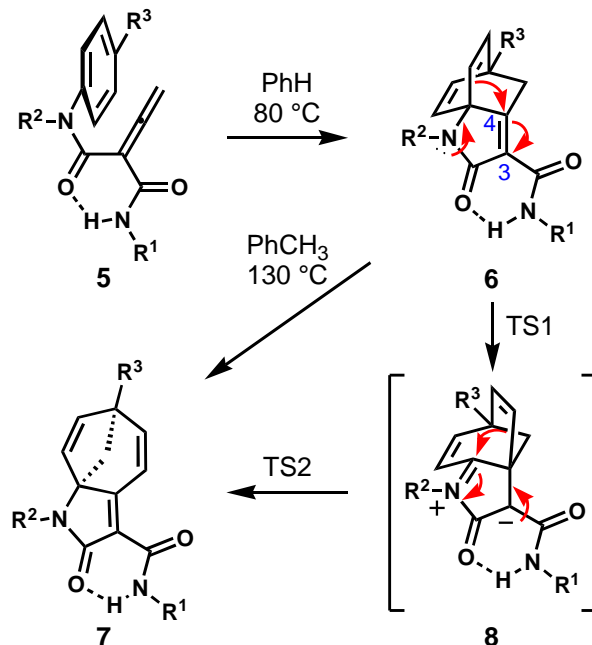
Figure 3.2.2. Type I and Type II dyotropic rearrangements.

Himbert Cycloadditions and the Formal Dyotropic Rearrangement

In certain cases, Himbert observed interesting Type I dyotropic shift products upon heating some of these cycloadducts.^{3c,5} In particular, those substituted with an amide functionality

alpha to the carbonyl of the lactam—cycloadducts that were formed under relatively mild conditions—isomerized efficiently from the bicyclo[2.2.2]octadiene **6** to the bicyclo[3.2.1]octadiene product **7** (Scheme 3.2.1). By changing the substituents at various positions and measuring the kinetics of the rearrangement (see Table 3.2.1), Himbert proposed a stepwise mechanism involving zwitterionic intermediate **8**;¹¹ he reasoned that the experimentally measured half-lives of a number of substrates correlated with the charge-stabilizing ability of the substituents. Trifonov and Orahovats, who also studied the thermal arene/allene cycloaddition,¹² uncovered a photochemical rearrangement closely related to that shown in Scheme 3.2.1; however, success in that reaction was confined to a narrow range of substrates.¹³

Scheme 3.2.1. Formal dyotropic rearrangement of Himbert cycloadducts.



From our perspective, and consistent with Himbert's proposal, a concerted mechanism is unlikely in these systems, owing to the C₃–C₄ alkene disallowing *anti* alignment of the migrating orbitals typically seen in single-step dyotropic rearrangements. We report a computational investigation of the formal dyotropic rearrangement observed in Himbert cycloadducts, including

an elucidation of substituent effects on the rates of these reactions and experimental validation of some of our predictions.

Table 3.2.1. Substituent effects on rearrangement rates.^a

entry	R ¹	R ²	R ³	t _{1/2} (hrs)
1	<i>i</i> -Pr	Me	H	21
2	<i>c</i> -Hex	Me	H	23
3	Ph	Me	H	7
4	1-Naph	Me	H	---
5	<i>t</i> -Bu	Ph	H	230
6	Ph	Ph	H	52
7	Ph	Me	Me	5
8	Ph	Me	Br	1

^aData from reference 11

Results and Discussion

Computational Methods

All stationary point structures were optimized using the B3LYP functional,¹⁴ with a 6-31G(d) basis set in Gaussian09.¹⁵ Single-point calculations were conducted with Mo6-2X/6-311+G(d,p) on the B3LYP optimized geometries. In general, B3LYP and Mo6-2X produce similar optimized geometries.¹⁶ For iodine-containing compounds, split basis sets were necessary: optimizations used the LANL2DZ basis set¹⁷ for iodine and 6-31G(d) for the remaining atoms, while single points used the SDD basis set¹⁸ for iodine and 6-311+G(d,p) for the remaining atoms. Vibrational frequencies were computed to determine the nature of each stationary point; local minima and transition structures showed 0 and 1 imaginary frequency, respectively. Partial atomic charges were calculated using a natural bond orbital (NBO) analysis. The Conductorlike Polarizable Continuum Model (CPCM) simulated implicit xylene solvent for optimizations and single point calculations.¹⁹

Mechanism of the Parent Reaction

We first explored the parent system **9a** (Figure 3.2.3), formed via the intramolecular [4+2] cycloaddition of *N*-phenyl-*N*-methyl allenecarboxamide. Rearrangement of **9a** delivers product **11a**. DFT-optimized structures of substrate **9a** and subsequent rearrangement stationary points are reproduced in this figure. The rearrangement occurs via a stepwise mechanism, passing through a stabilized zwitterionic intermediate **10a**. A concerted transition state could not be located, presumably because of the difficulty of achieving appropriate overlap in a transition state involving this tricyclic system. The lone pair on the nitrogen of the lactam promotes the initial migration of one of the vinyl groups through **TS9a**, which exhibits short bond-forming and bond-breaking lengths of 1.77 Å and 1.94 Å. Although vinyl shifts are not commonly seen, the migratory aptitude of the vinyl group is much larger than that for a methylene group, which explains the lower activation energy for **TS9a**.²⁰ In their kinetic studies of vinyl migrations using the phenanthrenium cation, Bushmelev and co-workers determined that the migration occurs in a 1,2-sigmatropic fashion rather than through mechanisms involving discrete cationic intermediates with completely severed bonds.²¹ Similarly, we did not observe these types of intermediates in the Himbert system. However, it is conceivable that the π -orbital of the migrating vinyl group could be interacting favorably with the π -orbital of the enone, which ultimately forms the new σ -bond in **10a**. We generated and compared the HOMO orbitals of **9a** and **TS9a** using a natural bonding orbital (NBO) analysis; examination of the relevant π -orbitals and inspection of the vinyl dihedral angle along the reaction path validate the significance of these orbital interactions in stabilizing the sigmatropic shift.

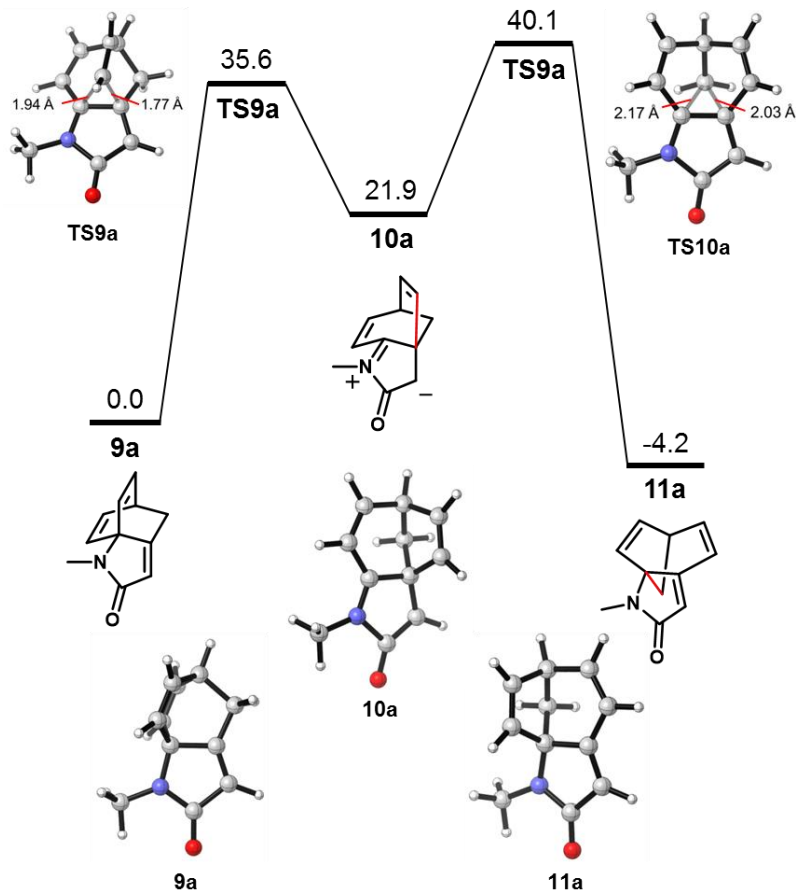


Figure 3.2.3. Reaction coordinate diagram of the formal dyotropic rearrangement of **9a**. Optimized structures and relevant bond-forming and bond-breaking distances are shown.

Energies are in kcal/mol.

Zwitterionic intermediate **10a** is 21.9 kcal/mol less stable than **9a**, despite the stabilization of the cation by the neighboring nitrogen atom and the delocalization of the anion through conjugation with the carbonyl. Moderate charge transfer (defined as the difference in charge per atom relative to starting substrate **9a**) indicates the zwitterionic nature of the intermediate; an unrestricted DFT calculation yields an S^2 value of 0, indicating a closed-shell species. Furthermore, changing the intrinsic solvent from xylenes to the more polar aqueous environment stabilized the intermediate and transition states by 2 kcal/mol, indicative of polarized species, without changing product energy.

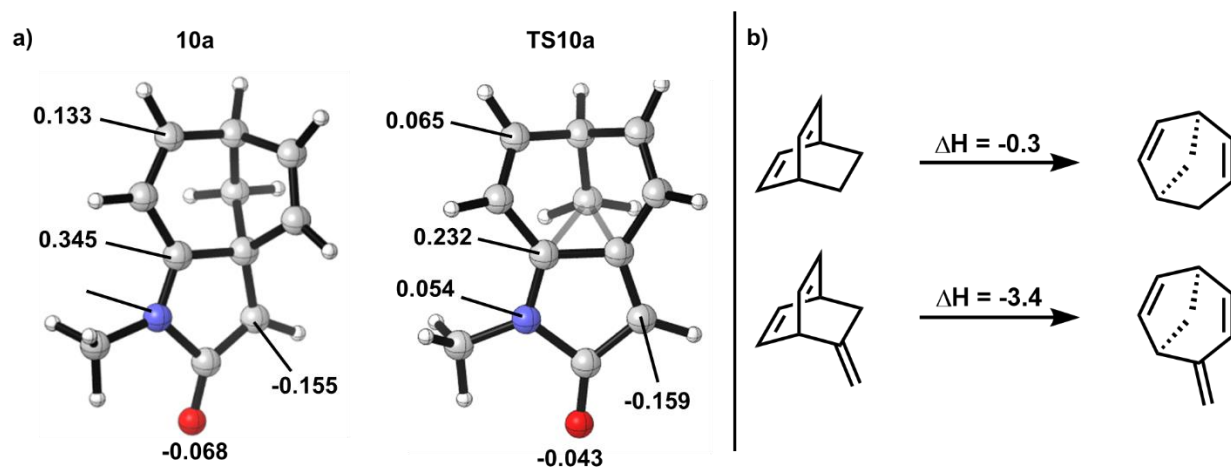


Figure 3.2.4. a) Charge transfer in the zwitterionic intermediate **10a** and transition structure **TS10a**, relative to **9a**. **b)** Contribution of ring strain to reaction energetics.

The subsequent methylene migration **TS10a** alleviates the charge separation and is the rate-determining step of the rearrangement, requiring 18.2 kcal/mol from intermediate **10a** (40.1 kcal/mol from **9a**) to form thermodynamically favored product **11a**; this large barrier is corroborated by the low yield of **11a** observed experimentally (see below), despite the extended conjugation and reduced strain leading to an exergonic reaction. The forming and breaking bond lengths of 2.17 Å and 2.03 Å are longer than those in **TS9a**, an unsurprising result since the methylene sp^3 -orbital holds electrons less tightly than the vinyl sp^2 orbital, owing to the increased s character of the latter. The absence of π -orbital interaction that is observed in **TS9a** explains the higher activation energy of **TS10a**. Stabilization of this transition state would decrease the kinetic barrier and result in a more facile rearrangement.

To determine whether ring strain is important in the transformation of the bicyclo[2.2.2]octadiene to the bicyclo[3.2.1]octadiene moiety, optimizations of the two parent bicyclic molecules were conducted (Figure 3.2.4). The bicyclo[3.2.1]octadiene is minimally more stable than its bicyclo[2.2.2]octadiene precursor, with only a 0.3 kcal/mol energy difference. Addition of an *exo*-methylidene group to better simulate the Himbert cycloadduct substrate

increases the difference to 3.4 kcal/mol in favor of the bicyclo[3.2.1]octadiene isomer, likely owing to the incorporation of another sp^2 -hybridized carbon atom into the bicyclic system along with the added conjugation of the diene. This alleviation of ring strain is also manifested in the exothermicity of the overall rearrangement reaction shown in Figure 3.2.4b and also for the conversion of **9a** into **11a**.

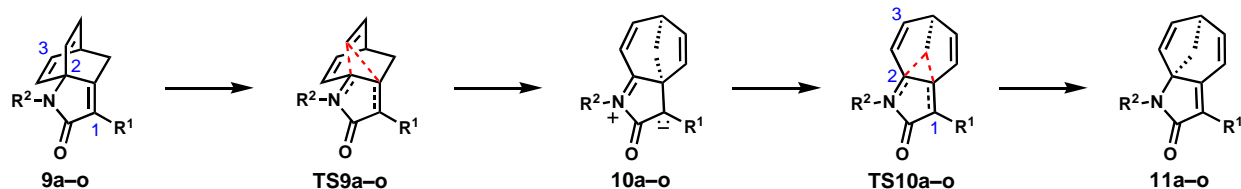
Electronic Activation of the Rearrangement

Owing to the charge separation that develops after the 1,2-vinyl shift, substituents at the α -position of the lactam should have a large effect on the stability of intermediates of type **10a**, and subsequently the rate-determining transition state **TS10a**. Himbert observed that the dyotropic rearrangement occurred only in compounds with an amide functionality α to the carbonyl of the lactam (Scheme 3.2.1);^{3c,5} presumably the anion-stabilizing ability of the electron-withdrawing amide promotes the migration. However, it was unclear to what extent the hydrogen-bonding arrangement shown in structures **6–8** were important to the feasibility of the rearrangements. This question prompted us to probe the effects of various substituents at the α -position of the lactam carbonyl.

In Table 3.2.2, we provide the free energies of the stationary points for the parent unsubstituted cycloadduct (**9a**) as well as the α -substituted analogs (**9b–9k**). The relative rate constants calculated from the Eyring equation using the activation energy of **TS10** are also provided. The exergonicity of the reaction remains relatively consistent across the range of substrates at 2–6 kcal/mol. Substitution with an α -methyl group slightly increases the energies of the intermediate and transition states. When an amide substituent is incorporated (entries c–e), the free energies of the rate-determining **TS10** drop substantially by 6 kcal/mol, consistent with the ability of these substrates to undergo the rearrangement experimentally. The transition state free energies of phenylamide-substituted substrate (**9d**) are stabilized by 1 kcal/mol relative to

the methylamide substrate (**9c**) owing to the better delocalization of the negative charge. The dimethylamido substituent (**9e**) is less electron-withdrawing than its primary amide counterparts, resulting in a higher barrier for rearrangement, although hydrogen-bonding could also be at play. Saalfrank and co-workers observed that a related *N*-methyl-*N*-phenyl amide substrate (not shown, with other substituents on the allene) spontaneously underwent the dyotropic rearrangement under the conditions used to effect cycloaddition; the initial cycloadduct could not be isolated.²² However, the tertiary amide group and allene substitution likely conspire to depress the rate of the IMDA reaction, requiring 150 °C to effect cycloaddition (compared to the 130 °C in prior cases). At this temperature, the dyotropic rearrangement is spontaneous and only isomerized bicyclo[3.2.1]octadiene was isolated. The hydroxymethyl-substituted system (**9f**) has a 40.7 kcal/mol activation barrier, intermediate between the unsubstituted and methyl-substituted substrates; the presence of a potential hydrogen bond donor does not appreciably lower the activation barrier **TS10**. However, replacement with a fluorine atom greatly increases **TS10** to 44.3 kcal/mol (entry g). The large electronegativity of fluorine is overshadowed by its π -donation, causing unfavorable electrostatic repulsion. Electron-withdrawing groups at the α -position lower the activation energies in accord with their known anion stabilization abilities ($\text{NO}_2 > \text{CHO} > \text{CN}$, entries h–j). The zwitterionic intermediates that benefit most from the anionotropy of the α -substituents lie only 7.6–12.5 kcal/mol higher than the starting Himbert cycloadducts, approximately 10 kcal/mol lower than in the unsubstituted case. The trimethylsilyl group shows virtually no change in transition state energy (see entry k); the low-lying vacant orbitals on silicon have only a marginal anion-stabilizing effect.

Table 3.2.2. Calculated free energies, partial atomic charges, and theoretically derived relative rates for stepwise dyotropic rearrangements of a range of Himbert cycloadducts. Highlighted entries are for $k_{\text{rel}} < 1$ (red), $k_{\text{rel}} \cong 1$ (yellow), $k_{\text{rel}} \gg 1$ (green).



Entry	R ¹	R ²	Free Energies				Relative Partial Charge Transfer (TS10)					k _{rel}
			TS9	10	TS10	11	O	C1	N	C2	C3	
a	H	Me	35.6	21.9	40.1	-4.2	0.000	0.000	0.000	0.000	0.000	1
b	Me	Me	36.2	23.7	41.6	-5.9	-0.007	0.019	0.002	-0.003	-0.003	1.5 × 10 ⁻¹
c	CONHMe	Me	31.0	15.6	34.8	-3.3	0.018	0.043	-0.018	0.004	0.000	7.5 × 10 ²
d	CONHPh	Me	30.0	14.4	33.8	-3.2	0.048	0.184	-0.003	0.005	0.000	12.6 × 10 ³
e	CONMe ₂	Me	31.4	15.2	36.1	-3.8	0.015	0.030	-0.013	-0.002	0.000	1.5 × 10 ²
f	CH ₂ OH	Me	35.8	23.6	40.7	-4.3	-0.003	0.026	-0.006	-0.002	-0.003	4.7 × 10 ⁻¹
g	F	Me	39.2	26.5	44.3	-4.5	-0.012	0.024	0.000	-0.012	-0.003	5.3 × 10 ⁻³
h	CHO	Me	27.5	9.7	30.7	-3.3	0.035	0.058	-0.021	0.004	0.001	1.2 × 10 ⁵
i	NO ₂	Me	26.5	7.6	29.7	-2.7	0.042	0.071	-0.022	-0.002	0.001	4.3 × 10 ⁵
j	CN	Me	29.1	12.5	32.6	-4.1	0.023	0.033	-0.015	0.001	0.001	1.2 × 10 ⁴
k	SiMe ₃	Me	34.3	19.9	39.0	-3.6	0.008	-0.008	-0.004	0.005	0.001	3.9
l	H (+BF ₃)	Me	29.8	15.6	34.2	-4.2	0.000	0.080	-0.045	-0.011	-0.006	1.6 × 10 ³
m	CONHMe	Ph	31.1	18.7	36.2	-1.5	0.012	-0.021	-0.039	0.012	-0.007	1.3 × 10 ²
n	CONHMe	<i>p</i> -OMePh	30.3	17.3	35.2	-2.4	0.017	-0.022	-0.010	0.012	-0.008	4.5 × 10 ²
o	CONHMe	SiH ₃	32.2	19.5	36.0	-3.2	-0.001	0.048	-0.004	0.015	0.001	1.7 × 10 ²

To corroborate the notion that charge delocalization is stabilizing the rate-determining transition state, we computed NBO charges to discern the amount of charge transfer from **9** to **TS10**. We focused on the most relevant atoms, i.e. those that possess a substantial formal charge in the resonance hybrid of **10**, namely the oxygen and nitrogen atoms of the lactam and the carbon atoms labeled C1, C2, and C3 (Table 3.2.2). The partial charge transfers are reported relative to the parent unsubstituted case, in which all atoms have been set to 0. The calculated rate constants correlate well with the relative amount of charge developed on the carbonyl oxygen, consistent

with our earlier predictions. Substituents that withdraw electron density away from the carbonyl in the transition state, through either resonance or induction, will lower the activation energy and increase the rate of reaction. A graph of $\log(k_{\text{rel}})$ vs. the extent of charge transfer on oxygen (Figure 3.2.5) shows a definite linear trend, albeit with an R^2 value of only 0.73; the presence of two outliers—the α -phenylamido and the Lewis acid-catalyzed reactions—diminishes the correlation. For the α -phenylamido substituent, a large portion of the negative charge resides on the oxygen of the amide substituent rather than the lactam. Similarly, the coordinated BF_3 molecule inherits the majority of the negative charge. Thus, inclusion of these other atoms in the charge difference calculation should provide a more accurate representation. When these two factors are corrected for, the coefficient of determination increases to 0.98, implying a strong correlation between electron-withdrawing ability of the α -substituent and the predicted reaction rate.

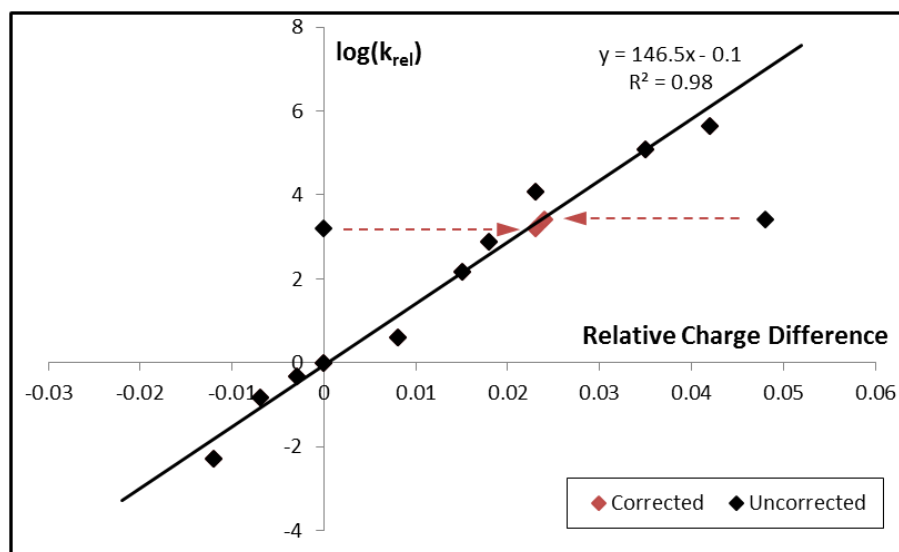
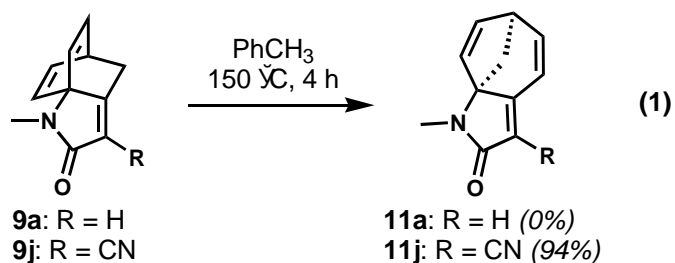


Figure 3.2.5. Graph of the correlation between the calculated reaction rate, $\log(k_{\text{rel}})$, and the charge difference on the carbonyl oxygen when going from **9** to **TS10**, relative to the parent unsubstituted **9a**.

To validate our predictions, we turned to experiment. As suggested by calculations, the introduction of a nitrile substituent in the α -position of the α,β -unsaturated lactam will significantly lower the temperature required for the dyotropic shift (see entry j, Table 3.2.2). Indeed, we found that heating nitrile-substituted cycloadduct **9j** at 150 °C in toluene produced rearranged product **11j** in 94% yield (Eq. 1). When parent cycloadduct **9a** was subjected to identical conditions, we observed no reactivity.

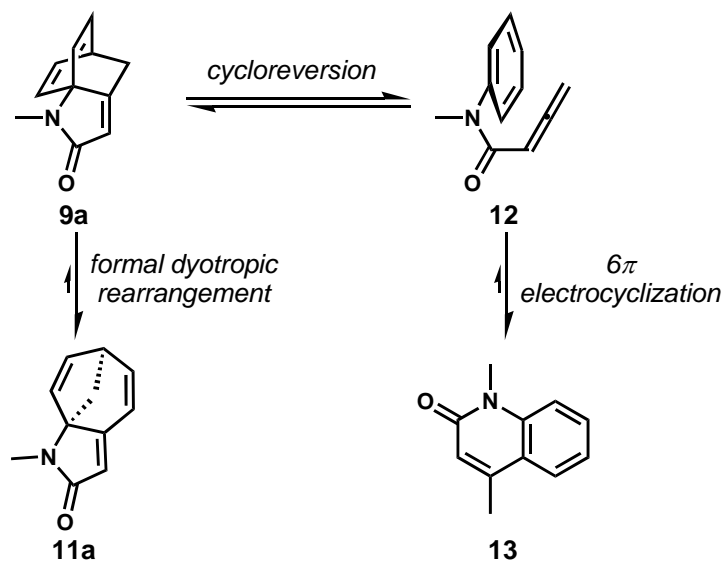


Rate Acceleration by Lewis Acids

With delocalization of the anionic charge contributing most toward decreasing the activation barrier of the rearrangement, we postulated that Lewis acid complexation to the lactam carbonyl could facilitate formal dyotropic shift in substrates that do not rearrange under purely thermal conditions at readily accessible temperatures. As expected, calculations on the parent substrate **9a** in the presence of boron trifluoride (entry l, Table 3.2.2) showed that the free energies for both transition states and the zwitterionic intermediate are each lowered by about 6 kcal/mol, comparable to the successful α -amido-substituted substrates with which Himbert uncovered this reactivity. Therefore, Lewis acid activation should permit these rearrangements to proceed without the presence of a second activation group. That advance would be significant because the synthesis of the doubly activated allene precursors to the Himbert cycloaddition are troublesome, owing to issues of stability.

Our experimental results were consistent with the computational predictions. Attempts to effect rearrangement of the parent compound **9a** without Lewis acid activation resulted in poor

yields, even at 250 °C (Figure 3.2.6). At these temperatures, we observed predominant formation of quinolone **13**, presumably resulting from cycloreversion and subsequent electrocyclicization. Screening of a variety of Lewis acid catalysts (not shown) led to the discovery that TMSOTf, in combination with 2,4-di-*tert*-butylpyridine to scavenge any liberated triflic acid, was optimal. Without the pyridine base and at 200 °C, the formal dyotropic shift product **11a** was produced in 74% yield, accompanied by unidentifiable decomposition products, which were suppressed by inclusion of the base. Furthermore, an excellent yield of **11a** could be obtained at temperatures as low as 100 °C using conventional heating. We note that the use of boron trifluoride (the Lewis acid used in the computations shown in Table 3.2.2), with or without acid scavengers, led to appreciable decomposition.



Conditions	11a
<i>o</i> -DCB, 250 °C, μ wave	12% ^a
TMSOTf (0.5), <i>o</i> -DCB, 200 °C, μ wave	74%
TMSOTf (0.5), DTBP ^b (0.1), <i>o</i> -DCB, 200 °C, μ wave	99%
TMSOTf (0.5), DTBP (0.1), PhMe, 100 °C	92%

^aThe major product was quinolone 13. ^bDTBP: 2,4-di-*tert*-butylpyridine.

Figure 3.2.6. Lewis acid catalysis of the formal dyotropic rearrangement of Himbert cycloadduct **9a**.

Effects of Lactam Nitrogen Substituents

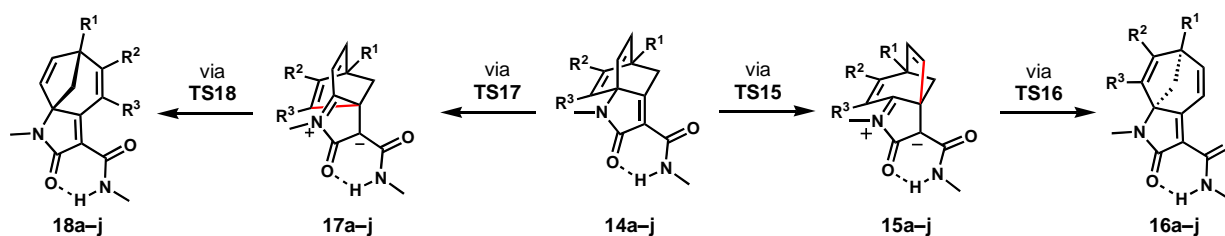
The electronic nature of the *N*-substituent of the lactam should influence stability of the iminium ion portion of the zwitterionic intermediate and should, therefore, impact the energetics of the methylene shift transition state. Table 3.2.2 shows that replacing the methyl group of **9c** with a phenyl group (**9m**) raises the energy of **TS10**, likely owing to the electron-withdrawing nature as well as conjugative properties of the substituent. The more electron-donating *p*-methoxyphenyl substituent mitigates the presumed iminium destabilization (compare **9m** and **9n**). Not surprisingly, a silyl group (**9o**) offers no further stabilization of the neighboring positive charge. *N*-Substitution effects are small, leading to computed changes of *ca.* 2 kcal/mol; the lesser impact of nitrogen substitution relative to α -carbon substitution is likely due to the effects being purely inductive, compared to the electron delocalization offered by the more influential α -substituents.

Effects of the Bicyclo[2.2.2]octadiene Substituents

Given that the dyotropic rearrangement converts the bicyclo[2.2.2]octadiene system to its bicyclo[3.2.1]octadiene isomer, substitution directly on the bridged bicycle should influence the energetics of the reaction. Himbert observed that methyl substitution at the bridgehead carbon (R^1) led to virtually unchanged reaction rates, while bromide at that position resulted in a sevenfold rate increase.⁵ Various positions on the bicyclo[2.2.2]octadiene were considered (Table 3.2.3). Entries a–f show the computed free energies for substrates with different R^1 substituents. Relative to the parent reaction, substitution with a methyl, fluoro, or silyl group does not significantly alter the energy of the rate-determining **TS16** (equivalent to **TS10a** in Figure 3.2.3) migration. However, the incorporation of bromine lowers the activation barrier by 1.4 kcal/mol to 33.4 kcal/mol, consistent with experimental observation. Switching to an iodine further decreases the barrier to 32.4 kcal/mol, providing evidence that the stabilization is due to more

than a simple inductive or steric argument. Examination of the structures of **TS15** reveals increased C–X bond lengths and shorter C–C bonds for the bromo- and iodo-substituted compounds (Figure 3.2.7), indicative of previously studied negative hyperconjugative effects (see **22'**).²³ Donation of electron density from the migrating carbon into the σ^* -orbital of the C–X bond allows delocalization of the negative charge buildup. Optimizations in implicit water supports this notion, demonstrating larger bond-length changes in polar solvent. In other words, better leaving groups at the R¹ position result in the bridgehead carbon developing more sp^2 character, stabilizing the excess negative charge.

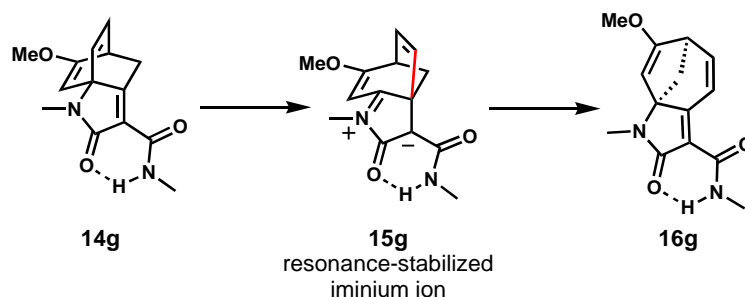
Table 3.2.3. Reaction free energies of the formal dyotropic rearrangements of Himbert cycloadducts substituted on the bicyclo[2.2.2]octadiene. All energies in kcal/mol.



Entry	R ¹	R ²	R ³	TS15	15	TS16	16	TS17	17	TS18	18
a	H	H	H	31.0	15.6	34.8	-3.3	–	–	–	–
b	Me	H	H	31.2	15.7	34.9	-3.9	–	–	–	–
c	F	H	H	31.7	14.8	34.3	-5.0	–	–	–	–
d	Br	H	H	31.8	15.1	33.4	-4.4	–	–	–	–
e	I	H	H	31.0	14.6	32.4	-4.9	–	–	–	–
f	SiH ₃	H	H	31.9	16.5	35.0	-3.0	–	–	–	–
g	H	OMe	H	29.9	8.9	31.9	-4.8	28.7	14.9	33.3	-7.7
h	H	H	OMe	34.6	20.1	38.4	-2.6	32.9	15.8	33.4	6.0
i	H	NO ₂	H	31.8	19.2	36.7	-2.6	34.0	16.0	35.4	-3.4
j	H	H	NO ₂	37.6	23.5	39.6	-1.7	38.3	17.3	34.8	4.3

Substitution on either alkene of the bicyclo[2.2.2]octadiene not only stereoelectronically affects the alkenyl migration but also desymmetrizes the bicycle. Either alkene can participate in the initial migration, which leads to two different products, **16** and **18**. With the electron-donating methoxy group at the R² position (entry g), the zwitterionic intermediate **15g** arising from migration of the unsubstituted alkene is more stable than **17g**, owing to the available resonance stabilization of the iminium ion of **15g** through a push-pull system with the lone pair on oxygen (see Scheme 3.2.2). Despite the favorability of **15g**, **TS18g** is 1.4 kcal/mol lower than **TS16g**, in qualitative agreement with the 7:3 ratio of **18g**:**16g** observed experimentally by Himbert.⁵ The methoxy substituent, regardless of whether the migrating alkene was substituted or unsubstituted, has a similar influence on the methylene shift: both **TS16** and **TS18** are favorable relative to the parent amide.

Scheme 3.3.2. Resonance-stabilization in intermediate **15g**.



When the methoxy substituent is moved to the R³ position (entry h), migration of the substituted vinyl group results in a product that is endergonic by 6.0 kcal/mol, which could revert back to starting material. Steric strain arises from the close proximity of the amide and methoxy groups, preventing **18h** from being favored thermodynamically. On the other hand, migration of the unsubstituted vinyl group and subsequent formation of **16h** requires overcoming a substantial 38.4 kcal/mol barrier, stemming from the general destabilization by the OMe group also present in the intermediate. This is corroborated by the sluggish but exclusive formation of **16h** observed by Himbert.⁵

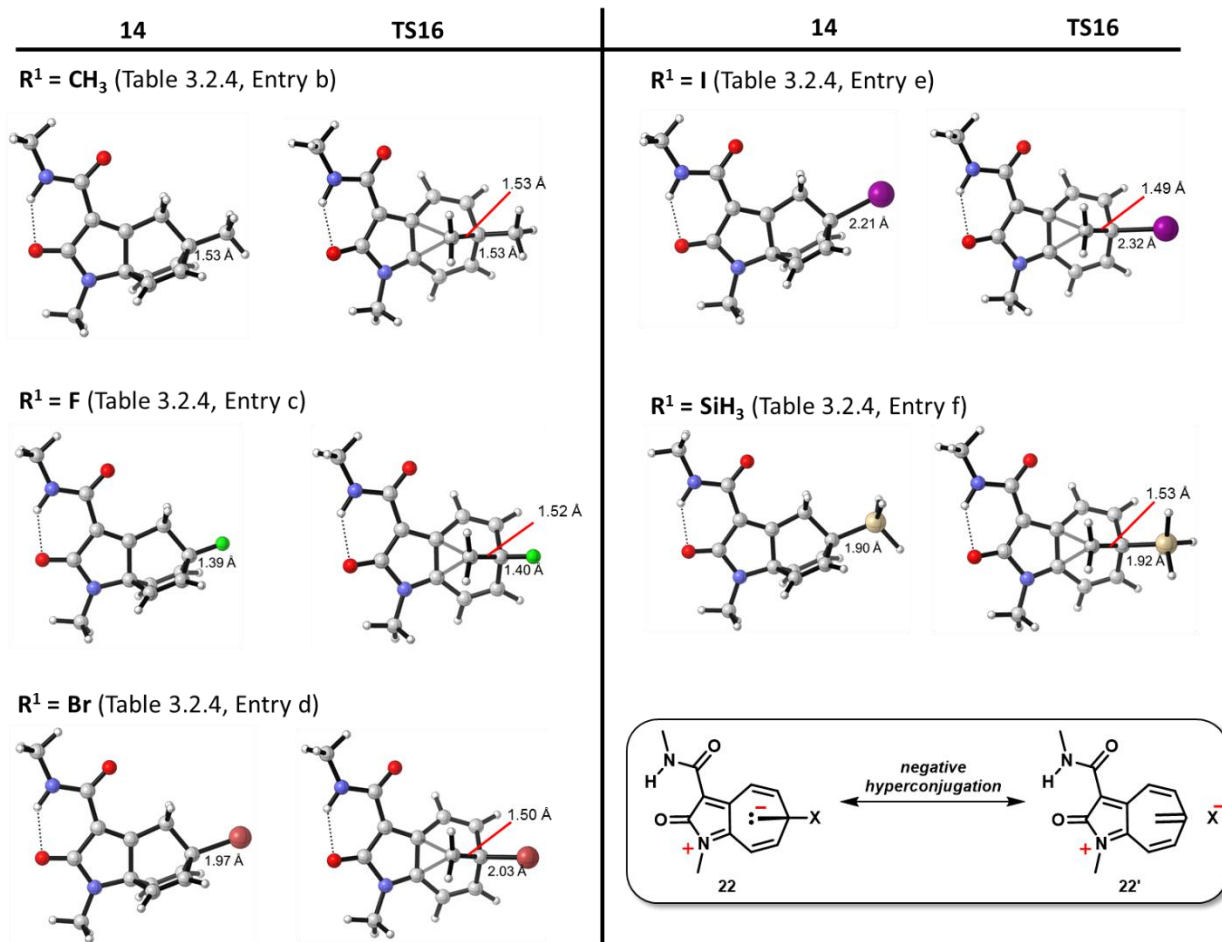
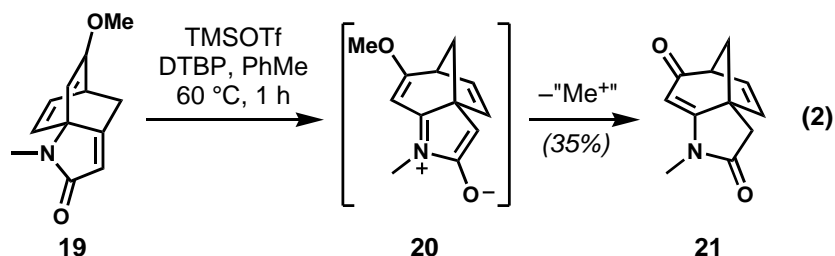


Figure 3.2.7. Optimized structures of bridgehead-substituted substrates. The effects of negative hyperconjugation can be seen in the varying bond lengths.

Replacement of the electron-rich methoxy group with the electron-deficient nitro group at both the R² and R³ causes an increase in activation barrier for all possible dyotropic shifts. For the R² position (entry i), this increase is attributed to the loss of resonance stabilization; the electron-withdrawing NO₂ offers no assistance to the electron-deficient iminium ion and is actually detrimental to the reaction. Placing the nitro group at the R³ position (entry j) causes similar steric strain as seen with the methoxy group in entry h. The higher activation barriers for rearrangement coincide with the observation of decomposition of these nitro-substituted compounds in refluxing xylene.⁵

An Interrupted Dyotropic Rearrangement Supports the Proposed Mechanism

We again looked to experiment for validation of the computational results. Our attempt to experimentally generate the dyotropic shift product from methoxy-substituted cycloadduct **19** (lacking the methyl carboxamide activating group) under Lewis acidic conditions did not afford the expected product at all (Eq. 2); rather, we isolated product **21** in 35% yield. We reasoned that after the initial vinyl shift to form zwitterion intermediate **20**, demethylation and isomerization generates the “trapped intermediate” **21**, which is then unable to undergo the second 1,2-shift. This observation provides further strong circumstantial evidence for the stepwise shifts involved in these formal dyotropic rearrangements.



Dyotropic Rearrangement of Lactone and Ketone Substrates

Curiously, only dyotropic rearrangements of cycloadducts with nitrogen-containing heterocycles have been reported, despite the large amount of successful Diels–Alder reactions of substrates with other heteroatoms by Himbert.^{3c,g} We also computed the rearrangement pathways of unsaturated lactone, unsaturated thiolactone, and cyclopentenone Himbert cycloadducts (Figure 3.2.8). The overall topology of the reaction coordinate diagram is retained across the different substrates; after the initial vinyl migration, formation of the intermediate is followed by the rate-determining methylene shift, resulting in an exergonic reaction. As expected, the carbon analogue offers no stabilization of the intermediate and transition states. Although the oxygen and sulfur atoms significantly lower the activation barriers relative to the all-carbon case, they are not as effective as the nitrogen atom in the lactam substrate. Interestingly, the intermediates of

the sulfur and oxygen analogues were not zwitterionic; rather, the weak C_{sp^2} -X sigma bond breaks to quench the positive charge on the heteroatom, forming a ring-opened ketene intermediate. An intrinsic reaction coordinate calculation and a thorough bond scan each reveals no intermediate between alkenyl migration and ketene formation, suggesting simultaneous occurrence. This unexpected ketene intermediate might be a possible decomposition pathway, which could explain the lack of successful dyotropic shifts reported for these substrates.

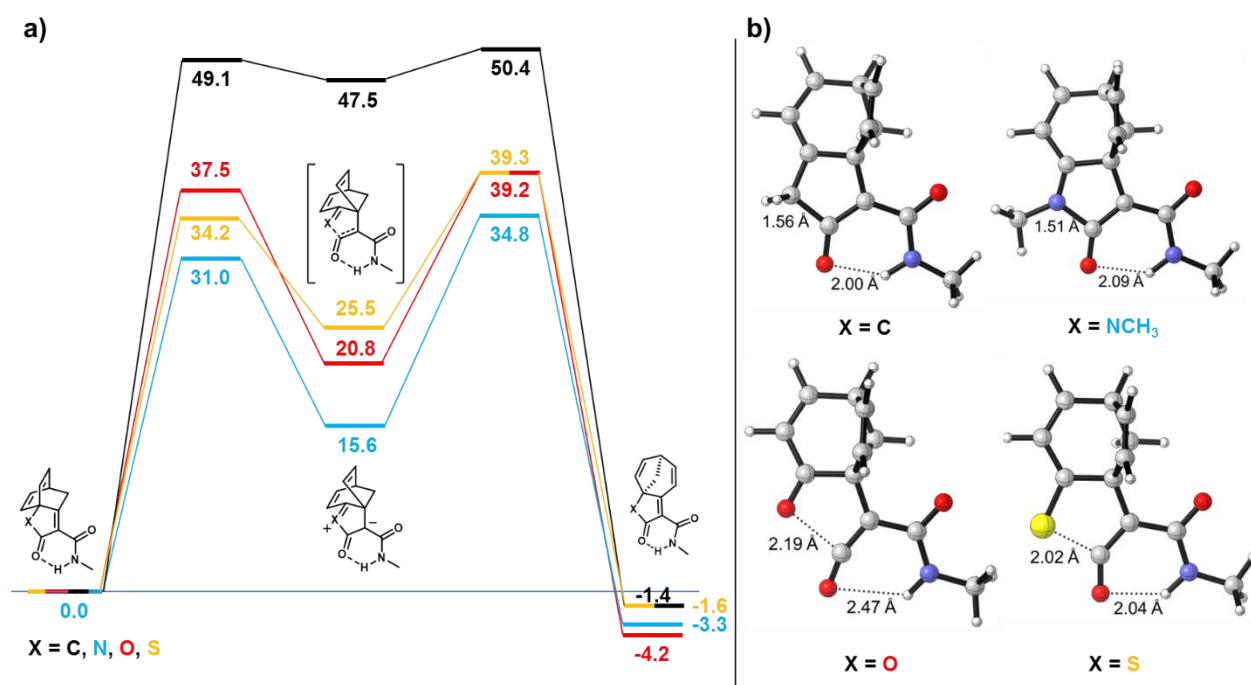


Figure 3.2.8. a) Reaction coordinate diagrams for the formal dyotropic shift of heterologues.

b) Optimized structures of intermediates.

Conclusions

We have investigated the formal dyotropic rearrangements of substituted bicyclo[2.2.2]octadiene moieties to corresponding bicyclo[3.2.1]octadienes discovered by Himbert. The rearrangements are characterized by a stepwise mechanism that proceeds through

a zwitterionic intermediate. Substituents that stabilize the partial charges in the rate-determining methylene shift effectively lower the activation barrier, resulting in more facile transformations. Moreover, substitution at the bridgehead carbon of the bicyclo[2.2.2]octadiene leads to an increase in reaction rate owing to negative hyperconjugative effects. Importantly, many aspects of the computational results have been experimentally validated.

Furthermore, computations suggest that the exclusivity of nitrogen-containing compounds participating in the dyotropic rearrangement may be due to the presence of a cumulenenic intermediate when replacing nitrogen with oxygen or sulfur, which could lead to decomposition pathways or formation of multiple side products. However, it is conceivable that the dyotropic rearrangement might still occur if the methylene shift precedes out-of-plane rotation or nucleophilic attack of the cumulene. The synthesis of these heterologous compounds and their rearrangement reactions could prove useful in the preparation of additional complex heterocyclic compounds.

References

1. Schmidt, Y.; Lam, J. K.; Pham, H. V.; Houk, K. N.; Vanderwal, C. D. *J. Am. Chem. Soc.* 2013, *135*, 7339–7348.
2. Lam, J. K.; Schmidt, Y.; Vanderwal, C. D. *Org. Lett.* 2012, *14*, 5566–5569.
3. Selected, particularly relevant references: (a) Himbert, G.; Henn, L. *Angew. Chem. Int. Ed.* 1982, *21*, 620. (b) Himbert, G.; Diehl, K.; Maas, G. *J. Chem. Soc., Chem. Commun.* 1984, 900–901. (c) Himbert, G.; Fink, D. *Tetrahedron Lett.* 1985, *26*, 4363–4366. (d) Henn, L.; Himbert, G.; Diehl, K.; Kaftory, M. *Chem. Ber.* 1986, *119*, 1953–1963. (e) Himbert, G.; Diehl, K.; Schlindwein, H.-J. *Chem. Ber.* 1986, *119*, 3227–3235. (f) Himbert, G.; Fink, D. *Z. Naturforsch. B; Chem. Sci.* 1994, *49*, 542–550. (g) Himbert, G.; Fink, D. *J. Prakt. Chem.* 1994, *336*, 654–657. (h) Himbert, G.; Fink, D. *J. Prakt. Chem.* 1996, *338*, 355–362.
4. Lam, J. K.; Pham, H. V.; Houk, K. N.; Vanderwal, C. D. *J. Am. Chem. Soc.* 2013, *135*, 17585–17594.
5. Himbert, G.; Diehl, K. *Liebigs Ann./Recueil* 1997, 1255–1260.
6. (a) Reetz, M. T. *Angew. Chem., Int. Ed. Engl.* 1972, *11*, 129–130. (b) Reetz, M. T. *Angew. Chem., Int. Ed. Engl.* 1972, *11*, 130–131.
7. For a review, see: Fernández, I.; Cossío, F. P.; Sierra, M. A. *Chem. Rev.* 2009, *109*, 6687–6711.
8. (a) Stocks, M.; Kocięński, P.; Donald, D. K. *Tetrahedron Lett.* 1990, *31*, 1637–1640. (b) Li, W.; LaCour, T. G.; Fuchs, P. L. *J. Am. Chem. Soc.* 2002, *124*, 4548–4549. (c) Lin, S.; Danishefsky, S. J. *Angew. Chem. Int. Ed.* 2002, *41*, 512. (d) Denmark, S. E.; Montgomery, J. I. *Angew. Chem. Int. Ed.* 2005, *44*, 3732–3736. (e) Denmark, S. E.; Montgomery, J. I.; Kramps, L. A. *J. Am. Chem. Soc.* 2006, *128*, 11620–11630. (f) de Lemos, E.; Porée, F.-H.; Commerçon, A.; Betzer, J.-F.; Pancrazi, A.; Ardisson, J. *Angew. Chem. Int. Ed.* 2007, *46*, 1917–1921. (g) Leverett, C. A.; Purohit, V. C.; Johnson, A. G.; Davis, R. L.; Tantillo, D. J.; Romo, D. *J. Am. Chem. Soc.* 2012, *134*, 13348–13356. (h) Ren, W.; Bian, Y.; Zhang, Z.; Shang, H.; Zhang, P.; Chen, Y.; Yang, Z.; Luo, T.; Tang, Y. *Angew. Chem. Int. Ed.* 2012, *51*, 6984–6988.
9. Reetz, M. T. *Tetrahedron* 1973, *29*, 2189–2194.
10. (a) Grob, C. A.; Winstein, S. *Helv. Chim. Acta.* 1952, *35*, 782–802. (b) Fernández, I.; Sierra, M. A.; Cossío, F. P. *Chem. Eur. J.* 2006, *12*, 6323–6330. (c) Zou, J.-W.; Yu, C.-H. *J. Phys. Chem. A* 2004, *108*, 5649–5654. (d) Kos, A. J.; Jemmis, E. D.; Schleyer, P. v. R.; Gleiter, R.; Fischbach, U.; Pople, J. A. *J. Am. Chem. Soc.* 1981, *103*, 4996–5002. (e)

- Frontiers, A.; Suñer, G. A.; Deyà, P. M. *J. Org. Chem.* 1992, 57, 6731–6735. (f) Mulzer, J.; Hoyer, K.; Müller-Fahrnow, A. *Angew. Chem. Int. Ed. Engl.* 1997, 36, 1476–1478. (g) Buchanan, J. G.; Ruggiero, G. D.; Williams, I. H. *Org. Biomol. Chem.* 2008, 6, 66–72. (h) Fernández, I.; Bickelhaupt, F. M.; Cossío, F. P. *Chem. Eur. J.* 2012, 18, 12395–12403. (i) Gutierrez, O.; Tantillo, D. J. *J. Org. Chem.* 2012, 77, 8845–8850. (j) Davis, R. L.; Tantillo, D. J. *J. Org. Chem.* 2010, 75, 1693–1700. (k) Yu, Y.; Feng, S. *J. Phys. Chem. A.* 2006, 110, 12463–12469. (l) Zhang, X.; Houk, K. N.; Lin, S.; Danishefsky, S. J. *J. Am. Chem. Soc.* 2003, 125, 5111–5114. (m) Davis, R. L.; Leverett, C. A.; Romo, D.; Tantillo, D. J. *J. Org. Chem.* 2011, 76, 7167–7174.
11. Himbert, G.; Diehl, K. *Liebigs Ann./Recueil* 1997, 1255–1260.
12. (a) Trifonov, L. S.; Orahovats, A. S. *Helv. Chim. Acta.* 1986, 69, 1585–1587. (b) Trifonov, L. S.; Orahovats, A. S. *Helv. Chim. Acta.* 1987, 70, 262–270. (c) Trifonov, L. S.; Orahovats, A. S. *Helv. Chim. Acta.* 1987, 70, 1732–1736. (d) Trifonov, L. S.; Simova, S. D.; Orahovats, A. S. *Tetrahedron Lett.* 1987, 28, 3391–3392. (f) Trifonov, L. S.; Orahovats, A. S. *Helv. Chim. Acta.* 1989, 72, 59–64.
13. Trifonov, L. S.; Dimitrov, V. S.; Orahovats, A. S. *Helv. Chim. Acta.* 1989, 72, 502–506.
14. (a) Becke, A. D. *Phys. Rev. A* 1988, 38, 3098–3100. (b) Lee, C.; Yang, W.; Parr, R. G. *Phys. Rev. B* 1988, 37, 785–789. (c) Becke, A. D. *J. Chem. Phys.* 1993, 98, 5648–5652.
15. Gaussian 09, Revision C.01, Frisch, M. J.; Trucks, G. W.; Schlegel, H. B.; Scuseria, G. E.; Robb, M. A.; Cheeseman, J. R.; Scalmani, G.; Barone, V.; Mennucci, B.; Petersson, G. A.; Nakatsuji, H.; Caricato, M.; Li, X.; Hratchian, H. P.; Izmaylov, A. F.; Bloino, J.; Zheng, G.; Sonnenberg, J. L.; Hada, M.; Ehara, M.; Toyota, K.; Fukuda, R.; Hasegawa, J.; Ishida, M.; Nakajima, T.; Honda, Y.; Kitao, O.; Nakai, H.; Vreven, T.; Montgomery, Jr., J. A.; Peralta, J. E.; Ogliaro, F.; Bearpark, M.; Heyd, J. J.; Brothers, E.; Kudin, K. N.; Staroverov, V. N.; Keith, T.; Kobayashi, R.; Normand, J.; Raghavachari, K.; Rendell, A.; Burant, J. C.; Iyengar, S. S.; Tomasi, J.; Cossi, M.; Rega, N.; Millam, J. M.; Klene, M.; Knox, J. E.; Cross, J. B.; Bakken, V.; Adamo, C.; Jaramillo, J.; Gomperts, R.; Stratmann, R. E.; Yazyev, O.; Austin, A. J.; Cammi, R.; Pomelli, C.; Ochterski, J. W.; Martin, R. L.; Morokuma, K.; Zakrzewski, V. G.; Voth, G. A.; Salvador, P.; Dannenberg, J. J.; Dapprich, S.; Daniels, A. D.; Farkas, O.; Foresman, J. B.; Ortiz, J. V.; Cioslowski, J.; Fox, D. J. Gaussian, Inc., Wallingford CT, 2010.
16. (a) Ess, D. H.; Houk, K. N. *J. Phys. Chem. A* 2005, 109, 9542–9553. (b) Pieniazek, S. N.; Clemente, F. R.; Houk, K. N. *Angew. Chem., Int. Ed.* 2008, 47, 7746–7749.
17. Stephens, P. J.; Devlin, F. J.; Chabalowski, C. F.; Frisch, M. J. *J. Phys. Chem.* 1994, 98, 11623–11627.

18. Śliwa, P.; Handzlik, J. *Chem. Phys. Lett.* 2010, 493, 273–278.
19. Cossi, M.; Rega, N.; Scalmani, G.; Barone, V. *J. Comput. Chem.* 2003, 24, 669–681.
20. (a) Marx, J. N.; Hahn, Y.-S. P. *J. Org. Chem.* 1988, 53, 2866–2868. (b) Genaev, A. M.; Shubin, V. G. *Russ. Chem. Bull., Int. Ed.* 2006, 55, 1085–1088.
21. (a) Bushmelev, V. A.; Genaev, A. M.; Shubin, V. G. *Russ. J. Org. Chem.* 2004, 40, 1007–1013. (b) Artamoshkin, V. G.; Bushmelev, V. A.; Genaev, A. M.; Shubin, V. G. *Russ. J. Org. Chem.* 2006, 42, 1279–1285.
22. Saalfrank, R. W.; Hilbig, K.; Schütz, F.; Peters, K.; von Schnering, H. G. *Chem. Ber.* 1988, 121, 1291–1297.
23. Schleyer, P. v. R.; Kos, A. J. *Tetrahedron* 1983, 39, 1141–1150.

Chapter 4. The Intramolecular Diels–Alder Reaction of Tryptamine-Derived Zincke Aldehydes is a Stepwise Process

Introduction

The Diels–Alder cycloaddition is one of the most important ring-forming reactions available to organic chemists.¹ Its impact on natural product synthesis, in both its inter- and intramolecular manifolds, cannot be overstated.² Mechanistically, these reactions must fall along the continuum linking the concerted synchronous pericyclic “ideal”, represented by the parent reaction of 1,3-butadiene with ethylene, and the stepwise Michael addition/aldol addition that is characteristic of processes with highly polarized reaction partners (Figure 4.1).³ Often, a stereochemical test can be used for detection of a stepwise mechanism for cycloaddition; observation of a lack of stereospecificity in a Diels–Alder reaction (correlation of the stereochemistry of the dienophile and/or the diene to that of the product) can be reasonably explained by the operation of a Michael/aldol pathway. For example, Jorgensen and coworkers have found that the purported Diels–Alder reaction in the enzyme-catalyzed reaction of macrophomate synthase is actually a two-step Michael/aldol process.^{3c}

Since the development of relatively accurate density functional methods, computations have become a useful vehicle for the determination of reaction mechanisms.⁴ Here we apply the methods of computational chemistry to establish the mechanisms of a particular class of Diels–Alder reactions that has demonstrated significant value in alkaloid synthesis.

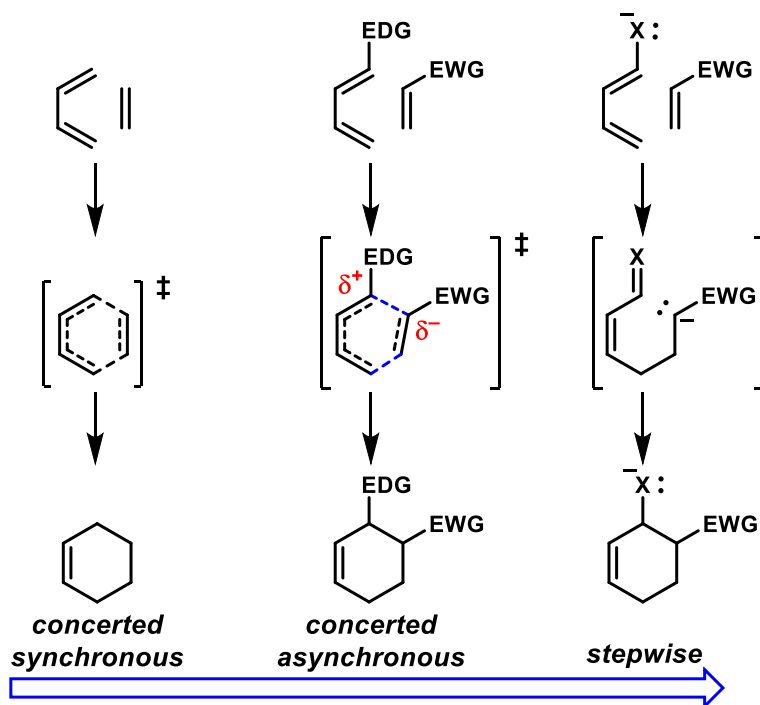
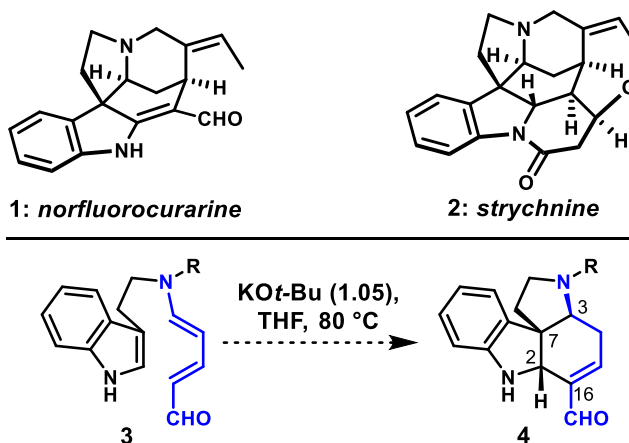


Figure 4.1. The mechanistic continuum of Diels–Alder cycloadditions.

Background

In the course of a project aimed at the synthesis of indole monoterpene alkaloids, including norfluorocurarine (**1**, Scheme 4.1) and the classic target strychnine (**2**), we developed the intramolecular Diels–Alder (IMDA) reaction of tryptamine-derived Zincke aldehydes (**3** → **4**).^{5–7} This complexity-generating transformation was mediated by stoichiometric quantities of base (typically $\text{KO}t\text{-Bu}$) and, in many cases, provided the cycloadducts in high yield. In every successful reaction, the product was formed as a single diastereomer and with conjugation of the unsaturated aldehyde. This conjugation event obscured one of the stereochemical readouts of this Diels–Alder reaction (the relative configuration of C3 and C16). The two dienophile derived stereogenic centers (C2 and C7) can only be *cis*, because the dienophile is part of the five-membered ring of the indole.

Scheme 4.1. Base-mediated IMDA reaction of tryptamine-derived Zincke aldehydes was a key step in norfluorocurarine and strychnine syntheses.



There seemed no obvious experimental way to determine if this cycloaddition reaction of two highly polarized reaction partners proceeded via a stepwise Michael addition/Mannich addition cascade or an asynchronous yet concerted pericyclic process. These two mechanistic possibilities are shown in Scheme 4.2, and knowing which pathway was operative could permit broader application of this powerful reaction type.

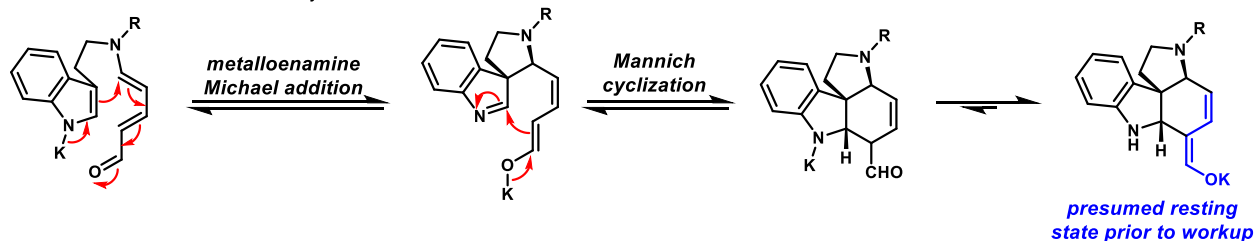
At the outset, the stepwise process seemed entirely reasonable. We presumed that the strong base was metallating the indole. The resulting highly nucleophilic metalloenamine should be competent for intramolecular conjugate addition, even with the donor-acceptor diene, which demonstrates diminished electrophilicity relative to normal conjugate acceptors. A successful bicyclization reaction would require the conjugate addition reaction to engage the *s-cis* conformer of the Zincke aldehyde which, while certainly not its ground state, should be readily accessible. Meeting this requirement allows for the intermediate dienolate to be formed with the *Z* geometry required for the terminal Mannich reaction. We recognized that the conjugate addition reaction might well be reversible, and only when the *s-cis* conformer was participating, would the final tetracyclic product arise. Finally, on the basis of pK_a values, we assumed that the resulting

metallated indoline would equilibrate to the dienolate shown, which should be the resting state of the product prior to acidic workup.

Scheme 4.2. Two reasonable mechanistic possibilities for the intramolecular Diels–Alder cycloaddition of tryptamine-derived Zincke aldehydes.

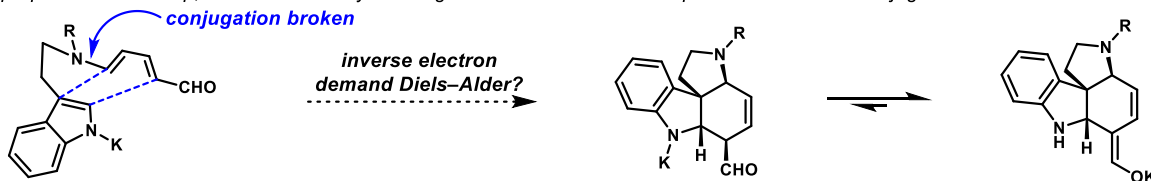
Stepwise:

1. Intermediate dienolate must have a *cis* geometry, arising from an *s-cis* Zincke aldehyde
2. The reaction could be driven by the formation of stable enolate



Concerted:

For proper orbital overlap, the Zincke aldehyde nitrogen's non-bonded electron pair cannot remain conjugated with the rest of the π -system



The concerted (yet certainly asynchronous) cycloaddition possibility also held elements of attractiveness. Zincke aldehydes are known to be poor dienes in intermolecular Diels–Alder cycloadditions, no doubt as a result of their donor-acceptor stabilization.⁸ However, analysis of hand-held molecular models suggested that, for appropriate overlap of the participating π -systems, conjugation of the Zincke aldehyde nitrogen's unshared electron pair with the rest of the system would need to be compromised. In that situation, we surmised that the nitrogen atom would serve predominantly as an inductively electron-withdrawing group toward the $\alpha,\beta,\gamma,\delta$ -unsaturated aldehyde, resulting in a particularly electron-deficient diene. That π -system might well participate in a concerted yet asynchronous Diels–Alder reaction with the metallated indole C2–C3 bond, because the HOMO–LUMO gap might not be too large. We also considered the fact

that the thermal requirements of the reaction (80 °C) might be related to the need to compromise conjugation in the Zincke aldehyde system.

To investigate this notion, HOMO and LUMO energies were calculated for the indole and Zincke aldehyde, respectively. Deprotonation of the indole affords a better electron donor, reflected by the 0.20 eV increase in the energy of the HOMO. In contrast, deconjugation of the nitrogen in the Zincke aldehyde resulted in a lowering of the LUMO energy by only 0.03 eV. Thus, the decrease in the HOMO-LUMO gap is mainly attributed to the indolyl anion and, to a much lesser extent, the amine deconjugation.

Because of the apparent feasibility of the two mechanisms, the importance of the reaction to our efforts in alkaloid synthesis, and the lack of obvious experiments to distinguish between the two possibilities, we looked to computation for a greater understanding of this process. This study ultimately revealed the importance of (1) the counterion of the base used to metallate the indole to the success of the reaction, and (2) the ability to form a stable enolate to drive this reaction forward. Furthermore, we have gained a greater comprehension of a fascinating cycloreversion process that occurs when the cycloadducts are converted to their corresponding iminium ions and heated. We have obtained detailed information about the mechanisms through density functional theory, and the results are consistent with available experimental data.

Results and Discussion

Stepwise versus concerted process?

Our first efforts sought to evaluate the feasibility of the concerted cycloaddition pathway of the *N*-metallated indole. However, a transition state for such a process could not be found; all efforts to locate a concerted transition state resulted in formation of only one of the C–C bonds, strongly suggesting that a stepwise process was at play. We considered the effect of the amine tether on the available conformations of the diene and dienophile. In order to determine if

intramolecularity was preventing favorable orbital overlap for the cycloaddition to occur, an analogous bimolecular reaction was studied where the tether between the indole and Zincke aldehyde was severed. Nevertheless, a concerted transition state could not be attained. As shown in Figure 2, the C3–C7 bond is formed preferentially through a Michael addition. Therefore, the Michael/Mannich reaction sequence of the indole anion was modeled.

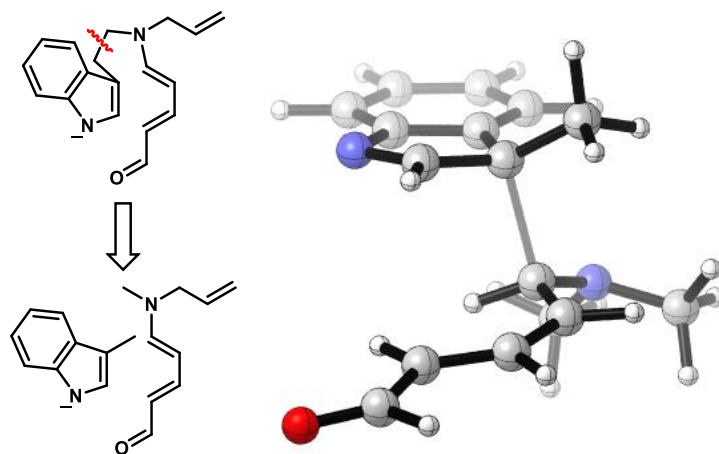


Figure 4.2. Modeling the intermolecular reaction between indolate and Zincke aldehyde. The forming C-C bond is shown in gray. The N-allyl protecting group was modeled by a methyl group.

The reaction coordinate diagram for the step-wise Michael/Mannich reaction sequence is outlined in Figure 4.3. Optimizations were performed with the B3LYP density functional with a 6-31G(d) basis set in the gas phase. Single-point energy calculations were then conducted on the optimized structures with the M06-2X functional, which includes nonlocal effects of electronic dispersion and has been shown to provide good estimates of energies for bond-forming reactions.^{4a} For computational simplicity, the N-allyl protecting group was replaced with a methyl. Using deprotonated indole **5** as our model system, a Michael addition through **TS_5-6** leads to spirocyclic dienolate **6**. The dienolate then undergoes an intramolecular Mannich reaction via **TS_6-7** to form indolate **7**. The tautomer, **8**, is considerably more stable.

Although the Zincke aldehyde of **5** is shown in its lowest energy *s-trans* conformation, it is clear that the double bond in the newly formed cyclohexene ring of **7** must adopt a *cis* configuration. This transformation can happen either through a conformational change of **5** from the *s-trans* to the *s-cis* conformation prior to C3–C7 bond formation, as shown in the energy profile, or by a *cis/trans* isomerization of **6** before proceeding to ring closure. Both transformations are facile under the experimental conditions and thus have energy barriers lower than that of **TS_5-6** and **TS_6-7**, implying that there are *cis/trans* and *s-cis/s-trans* equilibrations throughout the reaction pathway, but only the *cis* configurations of **6** will proceed to product.

The overall reaction has a 33.1 kcal/mol barrier in THF because of the loss of indole aromaticity. This high barrier is consistent with the elevated thermal conditions necessary for the reaction. MO6-2X predicts the reaction to be unfavorable by 3.8 kcal/mol for the free anion, but with the counterion included the reaction becomes favorable, as described in the next section.

In the experimental optimization of this cycloaddition, we found that only potassium bases mediated successful reactions. An extensive survey of bases included: (1) neutral amine and phosphazene bases; (2) lithium, sodium, potassium alkoxides and amides; (3) several metal hydrides; (4) Grignard reagents; and (5) dialkylzincs.^{7,9} The results clearly demonstrated that potassium bases were uniquely effective, with the best outcomes arising from the use of commercially available 1.0 M solutions of KO*t*-Bu in THF; the use of KHMDS and KH did lead to product formation, but with less efficiency. The inclusion of 18-crown-6 or polar solvents known to sequester alkali metal cations (NMP, DMPU, HMPA) completely prevented product formation, pointing to a critical role for this cation, and not simply a preference for more dissociated counterions. The failure of cesium carbonate circumstantially supports this idea. Accordingly, the Michael/Mannich reaction pathway was studied computationally starting from the *N*-potassiated indole.

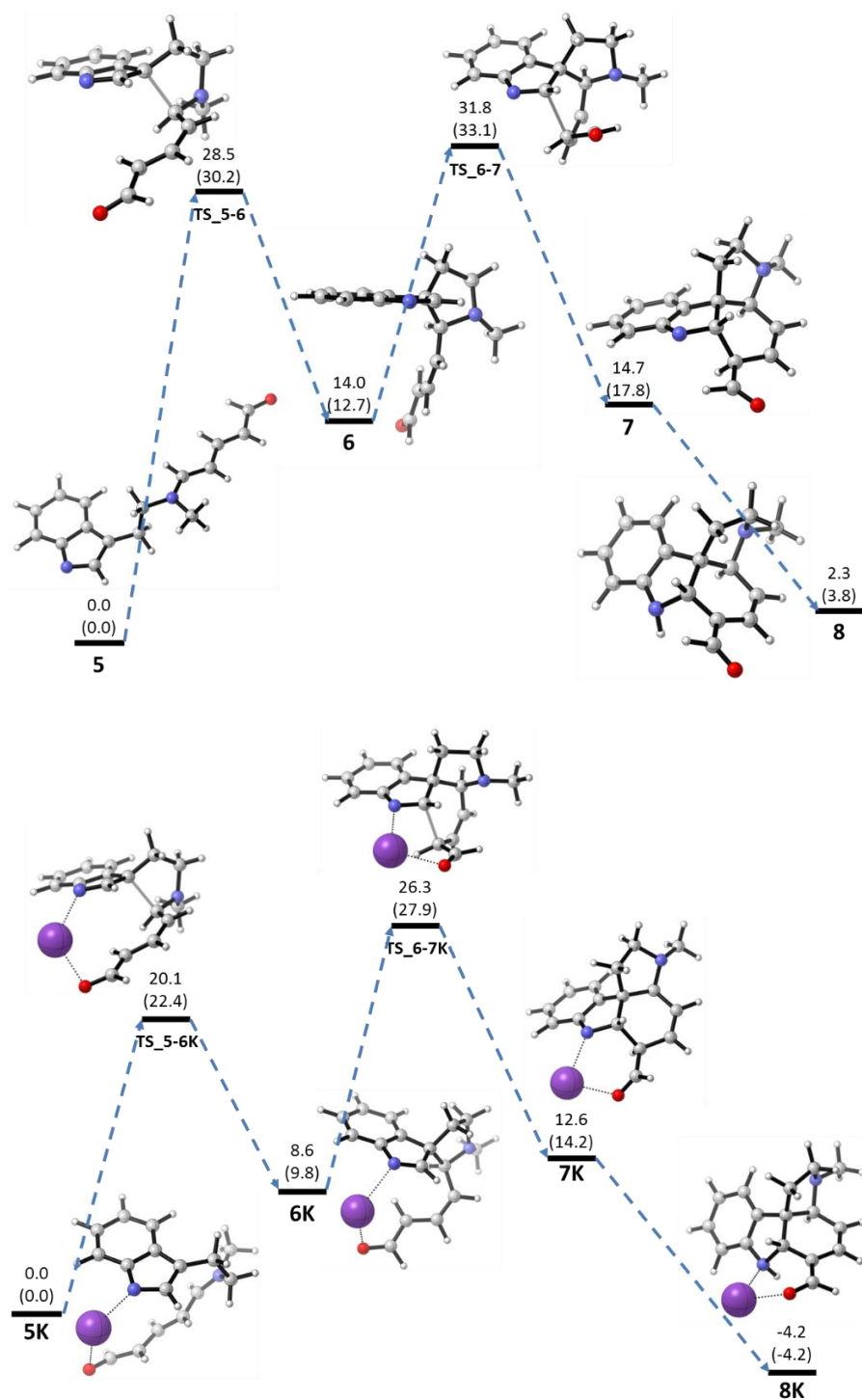


Figure 4.3. Energy profiles for the IMDA of the anion and the potassium salt. ΔG values were calculated using MO6-2X/6-311+G(d,p) single-point energies with B3LYP/6-31G(d) optimized structures in the gas phase. Corrections with the CPCM model of THF solvent are in parentheses.

In an attempt to probe the uniqueness of potassium in this reaction, the IMDA was subsequently modeled with a lithium counterion. The lithiated complexes closely resemble the potassiated ones, and the cyclization is predicted to be favorable by 2.6 kcal/mol.⁹ At this time, we cannot offer any explanation for the lack of success of lithium bases in these laboratory experiments. Because of the subtle differences between potassium and lithium and their propensity to participate in complexation with solvent molecules,¹⁰ a rigorous explicit-solvent model is necessary to explain the success of potassiated bases but not those derived from lithium, which would add a level of complexity to the computations that are outside the scope of this study.

One of the striking features of our results is the apparent “templating” effect of the potassium counterion which, when bound both covalently to the indole nitrogen and datively to the aldehyde oxygen, preorganizes the Zincke aldehyde for successful reaction. Evidently, the chelation of potassium to the substrate favors the adoption of the *s-cis* conformation of Zincke aldehyde, which is a critical requirement for C7–C3 bond formation to lead to the requisite Z-configured dienolate intermediate. As stated above, for geometrical reasons, only the Z-dienolate can engage in the Mannich-type C16–C2 bond formation that generates the *Strychnos* E-ring.

The importance of generating a stable dienolate

One of the features of this reaction that we had long considered to be important was the presumed equilibration of the initial cycloadduct **7K**, with the *N*-potassiated indoline, to the potassium dienolate **8K**. On pK_a grounds, we expected this acid-base reaction to be substantially favored. Certainly, the computational results shown above demonstrate that the cycloaddition reaction is not thermodynamically favored unless this equilibration is taken into account. We performed a simple experiment to further probe the importance of this process. The synthesis of α -methyl Zincke aldehyde **5 α M** was accomplished in two steps from 3-picoline according to our established procedures.⁷ Attempted cycloaddition under the standard conditions led to exclusive

recovery of starting material, and more forcing conditions led to decomposition. These results are nicely supported by the computational results shown in Figure 4.4, which show the very endergonic nature of this reaction.

The IMDA reaction with the α -methyl Zincke aldehyde was modeled using MO6-2X single-point energies. Under the thermal reaction conditions, the ~ 13 kcal/mol barrier for cycloreversion is easy to traverse, resulting in a completely reversible reaction. Without the possibility of a stable enolate as a resting state for the product, the equilibrium strongly favors the starting material by 20.7 kcal/mol, consistent with the recovery of exclusively uncyclized reactant. Similar optimized geometries for the intermediates and transition states compared to the parent reaction suggest that the mechanism is not altered with the introduction of the methyl to the alpha position of the aldehyde. Calculations on the potassiated case present comparable results. Taken together, the computational and experimental results point to a large component of the exergonicity of these anionic cycloaddition reactions arising from the formation of a stable potassium dienolate after the C–C bond forming steps of the sequence is complete.

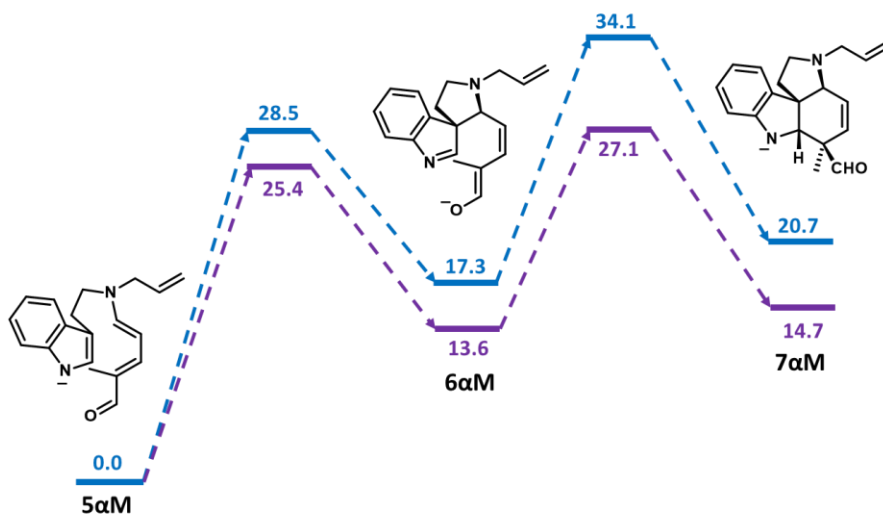


Figure 4.4. Energy profile for the IMDA reaction with alpha-methylated Zincke aldehyde. ΔG values calculated using MO6-2X/6-311+G(d,p) with CPCM THF solvent for the parent reaction (blue) and potassiated reaction (purple).

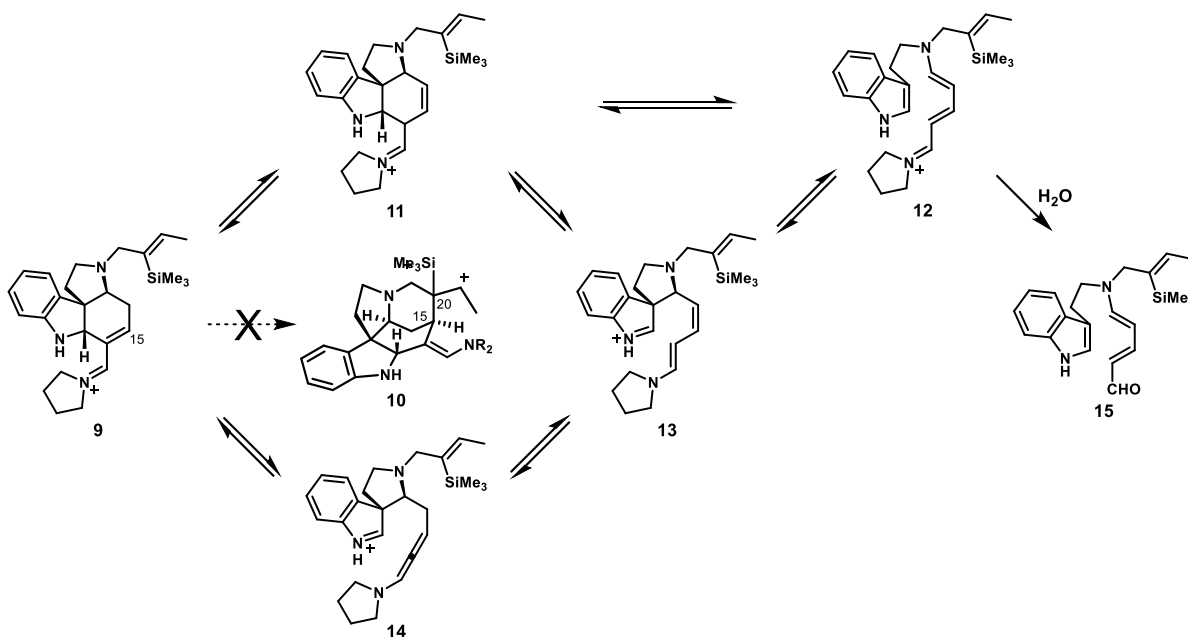
Cycloreversion via iminium intermediates

In the course of an attempt to mediate D-ring formation in a projected route toward strychnine, we tried to induce C15–C20 bond formation by activation of the α,β -unsaturated aldehyde of aldehydes of type **4** ($R=CH_2C(SiMe_3)CHCH_3$) as its corresponding iminium ion (**9**, Scheme 4.3), which we hoped would make it susceptible to nucleophilic attack at the β -position by the tethered vinylsilane, as shown in **10**. Certainly, iminium ions are competent electrophiles in vinylsilane-terminated cyclizations, as pioneered by Overman,¹¹ and the MacMillan group has clearly demonstrated that α,β -unsaturated iminium ions are activated toward nucleophilic attack at the β -position.¹² Upon treatment of aldehyde **4** with pyrrolidine, the corresponding iminium ion **9** was observed by mass spectrometry. Heating the reaction mixture to 150 °C led to clean cycloreversion, and Zincke aldehyde **15** was recovered cleanly after aqueous workup. Some pyrrolidine-derived Zincke aldehyde (not shown) was also observed, from unselective hydrolysis of unsymmetrical iminium ion intermediate **14**. This result clearly demonstrated that the cycloaddition/cycloreversion equilibrium could be perturbed under different conditions. This reaction might also proceed via either a stepwise or a concerted pericyclic process, and we turned to computation to determine its likely course.

Figure 4.5 exhibits the computed energetics for possible ring-opening pathways. Each pathway was calculated using the B3LYP/6-31G(d) basis set, with all optimizations conducted in THF solvent. As before, M06-2X single point energies were then calculated in the gas phase and corrected using the CPCM solvent model. After formation of unsaturated iminium **9**, an alkene isomerization provides intermediate **11** which can then cyclorevert through a concerted retro-Diels–Alder reaction or a stepwise retro-Mannich/retro-Michael sequence via **13** to attain Zincke aldehyde **12**. A third possible pathway involves the retro-Mannich occurring before the isomerization, yielding allenamine **14** before continuing on to intermediate **13** in the previously

mentioned stepwise pathway. A concerted transition state leading to the uncyclized product could not be found.

Scheme 4.3. Possible mechanisms for cycloreversion and regeneration of Zincke aldehyde **15**.



As shown in Figure 4.5, formation of allenamine **14** requires 42.0 kcal/mol, a much higher barrier compared with the pathway involving alkene isomerization. Thus, it is unlikely that this pathway occurs, but rather isomerization to form intermediate **11** takes place initially. The absence of a concerted transition state once again suggests a stepwise mechanism. Imine **11** can proceed to cycloreversion product **12** through intermediate **13**, following a pathway reminiscent of the forward reaction studied earlier.

In short, while the tryptamine-derived Zincke aldehyde cycloaddition is driven forward under basic conditions by the formation of a stable enolate (despite the loss of aromaticity in the indole five-membered ring and the donor-acceptor stabilization of the Zincke aldehyde), the cycloreversion is favored by the formation of the aldiminium ion, which leads to regeneration of

indole aromaticity and the generation of the highly resonance-stabilized donor-acceptor iminium ion. This system provides a rare example of the ability to completely control the Diels–Alder cycloaddition/cycloreversion equilibrium based upon the choice of reaction conditions.

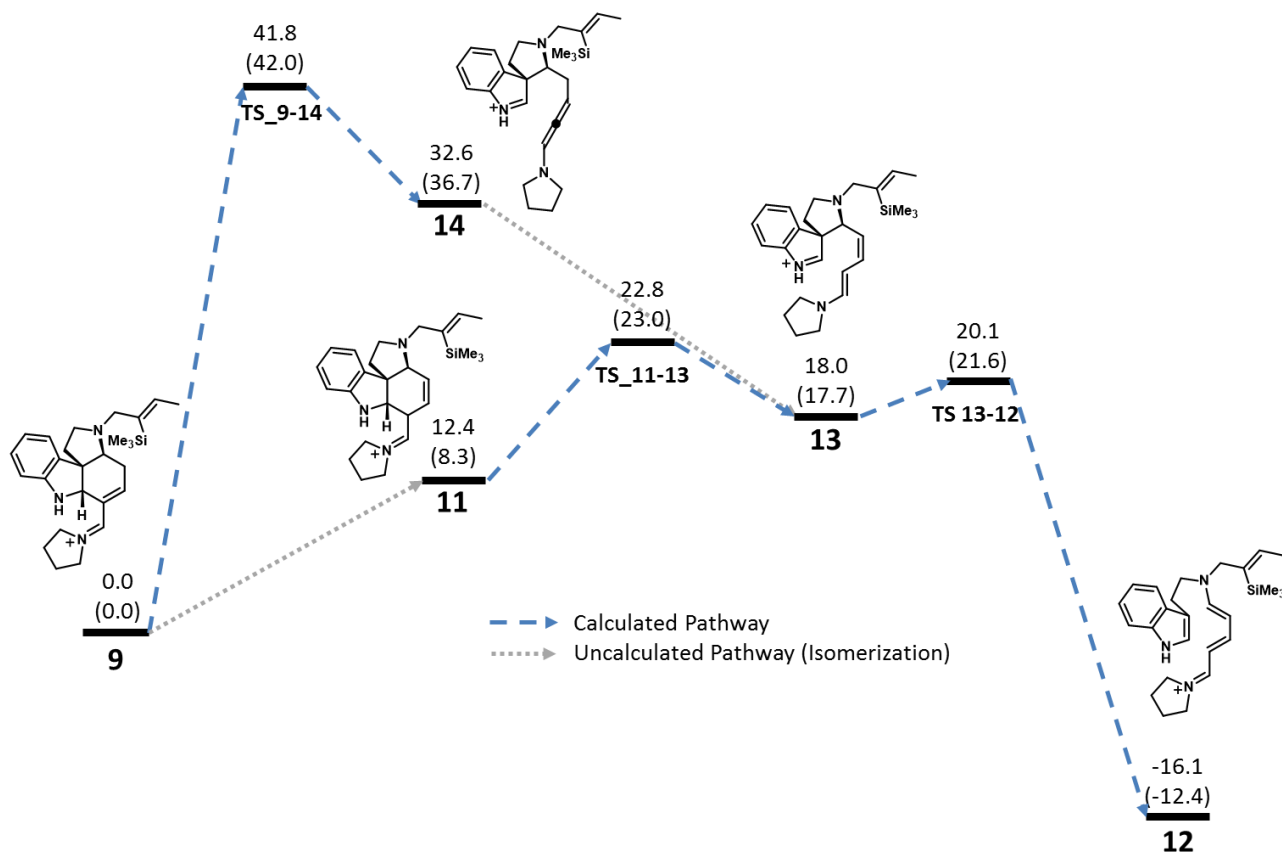


Figure 4.5. Energy profile for various pathways of cycloreversion. ΔG values were calculated using MO6-2X/6-311+G(d,p) single-point energies with B3LYP/6-31G(d) optimized structures in the gas phase. Corrections with the CPCM model of THF solvent are in parentheses.

Isomerizations (gray) were not explicitly calculated.

Conclusion

Through computation, we have developed a much deeper understanding of the key anionic cycloaddition reaction that facilitated concise syntheses of several *Strychnos* alkaloids, including norfluorocurarine and strychnine. This transformation occurs through a stepwise Michael/Mannich cascade rather than a concerted Diels–Alder cycloaddition. This reaction proceeds only when the indole is metalated with potassium bases, and computation has attributed this particularity to potassium's ability to pre-organize the aldehyde in an *s-cis* manner, providing the appropriate conformation for successful reaction. The failure of the cycloaddition reaction when lithium bases were used appears to result from an unfavourable equilibrium in these cases. The driving force for the reaction is the formation of a stable potassium enolate as a resting state for the cyclized product. When the possibility of formation of such a low-energy enolate is removed, the reaction does not proceed because the equilibrium favors starting material.

Formation of an unsaturated iminium ion in attempts to install the D-ring of the *Strychnos* alkaloids caused an unexpected cycloreversion that unravels the B- and C-rings. Ring opening proceeded through a stepwise retro-Mannich/retro-Michael cascade, related to the mechanism of forward cycloaddition. This delicate equilibrium between cycloaddition and cycloreversion allows for manipulation of reaction conditions to achieve either outcome. The greater understanding of the mechanism of this important Diels–Alder-type reaction of Zincke aldehydes will enable broadening of the scope of these complexity generating transformations.

References

1. O. Diels, K. Alder, *Justus Liebigs Ann. Chem.* 1928, **460**, 98.
2. For recent reviews on the application of the Diels-Alder reaction in natural product syntheses: a) K. C. Nicolaou, S. A. Snyder, T. Montagnon, G. Vassilikogiannakis, *Angew. Chem. Int. Ed.* 2002, **41**, 1668–1698; b) M. Juhl, D. Tanner, *Chem. Soc. Rev.* 2009, **38**, 2983–2992.
3. For mechanistic discussions of the Diels-Alder reaction: a) E. Goldstein, B. Beno, K. N. Houk, *J. Am. Chem. Soc.* 1996, **118**, 6036–6043; b) L. R. Domingo, J. A. Sáez, *Org. Biomol. Chem.* 2009, **7**, 3576–3583; c) C. R. W. Guimaraes, M. Udier-Blagovic, W. L. Jorgensen, *J. Am. Chem. Soc.* 2005, **127**, 3577–3588.
4. For the general use of DFT methods: M06-2X: a) Y. Zhao, D. G. Truhlar, *Theor. Chem. Acc.* 2008, **120**, 215–241; B3LYP: b) R. G. Parr, *Annu. Rev. Phys. Chem.* 1995, **46**, 701–728; CPCM solvation method: c) M. Cossi, N. Rega, G. Scalmani, V. Barone, *J. Comp. Chem.* 2003, **24**, 669–681; On Diels–Alder reactions: d) K. S. Khuong, C. M. Beaudry, D. Trauner, K. N. Houk, *J. Am. Chem. Soc.* 2005, **127**, 3688–3689; e) K. N. Houk, B. R. Beno, M. Nendel, K. Black, H. Y. Yoo, S. Wilsey, J. K. Lee, *J. Mol. Struct. (Theochem)* 1997, **398–399**, 169–179; f) B. S. Jursic, Z. Zdravkovski, *J. Chem. Soc., Perkin Trans. 2* 1995, 1223–1226; g) R. S. Paton, S. E. Steinhardt, C. D. Vanderwal, K. N. Houk, *J. Am. Chem. Soc.* 2011, **133**, 3895–3905.
5. D. B. C. Martin, C. D. Vanderwal, *J. Am. Chem. Soc.* 2009, **131**, 3472–3473.
6. D. B. C. Martin, C. D. Vanderwal, *Chem. Sci.* 2011, **2**, 649–651.
7. D. B. C. Martin, L. Q. Nguyen, C. D. Vanderwal, *J. Org. Chem.* published on the web 14 December 2011, doi: 10.1021/jo2020246.
8. J. E. Baldwin, T. D. W. Claridge, A. J. Culshaw, F. A. Heupel, V. Lee, D. R. Spring, R. C. Whitehead, R. C. *Chem. Eur. J.* 1999, **5**, 3154–3161 and references cited therein.
9. See Supporting Information of the original publication for details.
10. B. Eliasson, T. Lejon, U. Edlund, R. L. Mueller, S. W. Staley, *J. Phys. Org. Chem.* 1990, **3**, 9–12.
11. a) L. E. Overman, K. L. Bell, *J. Am. Chem. Soc.* 1981, **103**, 1851–1853; b) T. A. Blumenkopf, L. E. Overman, *Chem. Rev.* 1986, **86**, 857–873.
12. G. Lelais, D. W. C. MacMillan, *Aldrichim. Acta* 2006, **39**, 79–87.

Chapter 5. Intramolecular Diels–Alder Reactions of Cycloalkenones: Stereoselectivity, Lewis Acid Acceleration, and Halogenation Effects

Introduction

Diels–Alder reactions of cycloalkenone dienophiles with a variety of dienes are powerful synthetic tools.¹ Cyclobutenone has been shown to be a potent dienophile^{2,3} with greater reactivity than five- and six-membered cycloalkenones. This has been attributed to the ease of out-of-plane distortion of cyclobutenone, so as to more easily achieve the transition state geometry for cycloaddition.⁴ Intramolecular Diels–Alder reactions of cycloalkenones are reliable methods to generate fused polycycles.⁵ We have performed a computational study to rationalize the high stereoselectivity of the reactions shown in Figure 5.1 as well as describe the positive effect of incorporating a Lewis acid catalyst and an α -bromo substituent. We have also explored an unanticipated diene isomerization that occurs along with cycloaddition, regardless of cycloalkenone ring size.

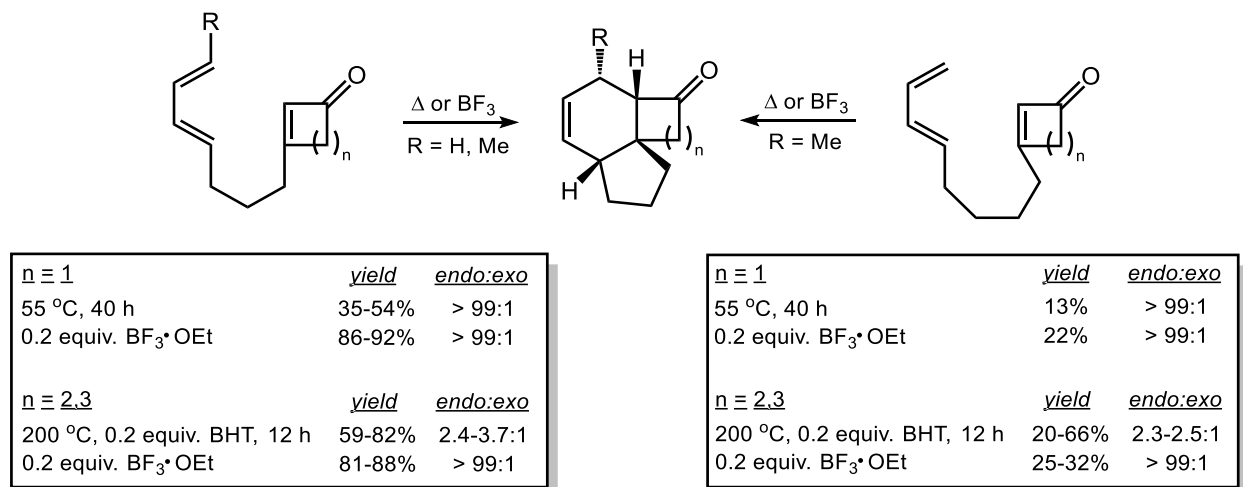


Figure 5.1. Summary of experimental results for the intramolecular Diels–Alder reaction of cycloalkenones.⁵

Computational Methods

Geometry optimizations were conducted in the gas phase using the MO6-2X hybrid meta-GGA density functional.⁶ Through the inclusion of a local spin kinetic energy density term in the exchange-correlation functional and extensive parametrization, MO6-2X has been shown to be effective at modeling kinetics and thermochemistry, particularly where nonlocal dispersion interactions play a non-negligible role.⁷ We have shown previously that it is possible to obtain relatively accurate activation and reaction energies for cycloadditions at the MO6-2X/6-31G(d) level of theory.⁸ Values in the text and figures are for the standard state of the gas phase (1 atm). Brinck has recently shown this level also yields geometries for asynchronous Diels–Alder transition structures in agreement with those obtained at the CCSD/6-31+G(d) level.⁹ Frequency analysis was performed to verify the nature of each stationary point, with transition structures (TSs) and minima possessing a single and zero imaginary frequencies, respectively. Intrinsic reaction coordinate (IRC) scans were conducted when necessary to ensure the TSs led to the correct minima. All calculations were performed using Gaussian 09.¹⁰

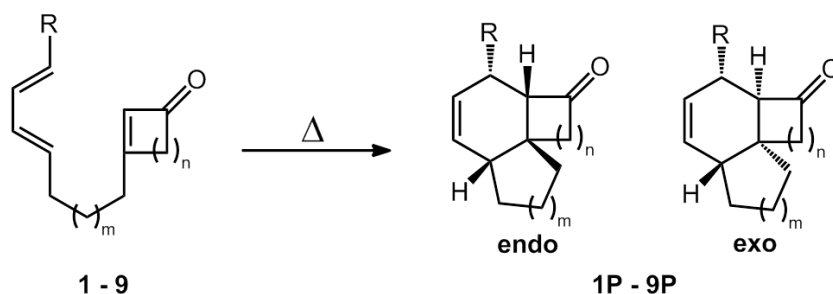
Results and Discussion

Danishefsky and co-workers have recently reported a series of intramolecular Diels–Alder reactions of cycloalkenones.⁵ As shown in Figure 5.1, the *endo:exo* selectivity of the fused tricycles was investigated as a function of cycloalkenone ring size (four-, five- and six-membered rings were considered) and for both thermal and Lewis acid-catalyzed cycloadditions. Here, we initially examine the uncatalyzed, thermal reaction of these cycloalkenones and then consider the influence of BF₃ on the [4+2] cycloaddition.

Endo Selectivity and an Unexpected Isomerization

The computed activation and reaction free energies of the (uncatalyzed) thermal intramolecular Diels–Alder reactions of cycloalkenones **1–3** were calculated and summarized in Table 5.1. These substrates contain a 3-carbon tether between the diene and dienophile, forming a fused cyclopentane ring as a result of the cycloaddition. In all cases (entries 1-3) the *endo* product is kinetically favored, ranging from 0.7 kcal/mol for cyclobutenone **1** and cyclohexenone **3** to 1.1 kcal/mol for cyclopentenone **2**.

Table 5.1. Computed Reaction and Activation Free Energies and Enthalpies (kcal/mol) for the Thermal Diels–Alder Cycloaddition of Cycloalkenones **1–9**.



entry	SM	m	n	R	ΔG^\ddagger endo	ΔG^\ddagger exo	ΔH^\ddagger endo	ΔH^\ddagger exo	ΔG_{rxn} endo	ΔG_{rxn} exo	$k_{\text{endo/exo}}$
1	1	1	1	H	20.8	21.5	15.6	16.4	-32.2	-33.7	3.2
2	2	1	2	H	25.8	26.9	19.7	21.0	-21.8	-28.0	5.8
3	3	1	3	H	27.3	28.0	21.5	22.1	-19.9	-21.9	3.5
4	4	2	1	H	21.7	22.8	16.0	16.7	-40.0	-38.9	6.5
5	5	2	2	H	25.0	26.3	18.4	19.7	-26.9	-32.0	9.0
6	6	2	3	H	26.8	27.3	20.3	20.7	-26.8	-25.1	2.4
7	7	1	1	Me	20.4	21.0	14.3	14.7	-29.0	-31.4	2.5
8	8	1	2	Me	24.4	25.4	18.4	19.7	-17.9	-24.4	5.5
9	9	1	3	Me	25.8	27.0	19.7	21.1	-14.5	-20.5	7.6

As expected, the activation barrier of 20.8 kcal/mol for the Diels–Alder reaction of cyclobutenone is substantially lower than that for its larger-ring counterparts (Figure 5.2). The higher barriers associated with **2** and **3** necessitate higher reaction temperatures. The theoretical preference for the *endo* adduct in each case agrees with experiment, although the preference is underestimated for substrate **1**, where only the *endo* product is observed at 55°C. Temperatures of 200°C were needed for reactions of cycloalkenones **2** and **3**, where an approximately 3:1 *endo:exo* ratio was observed for each.⁵

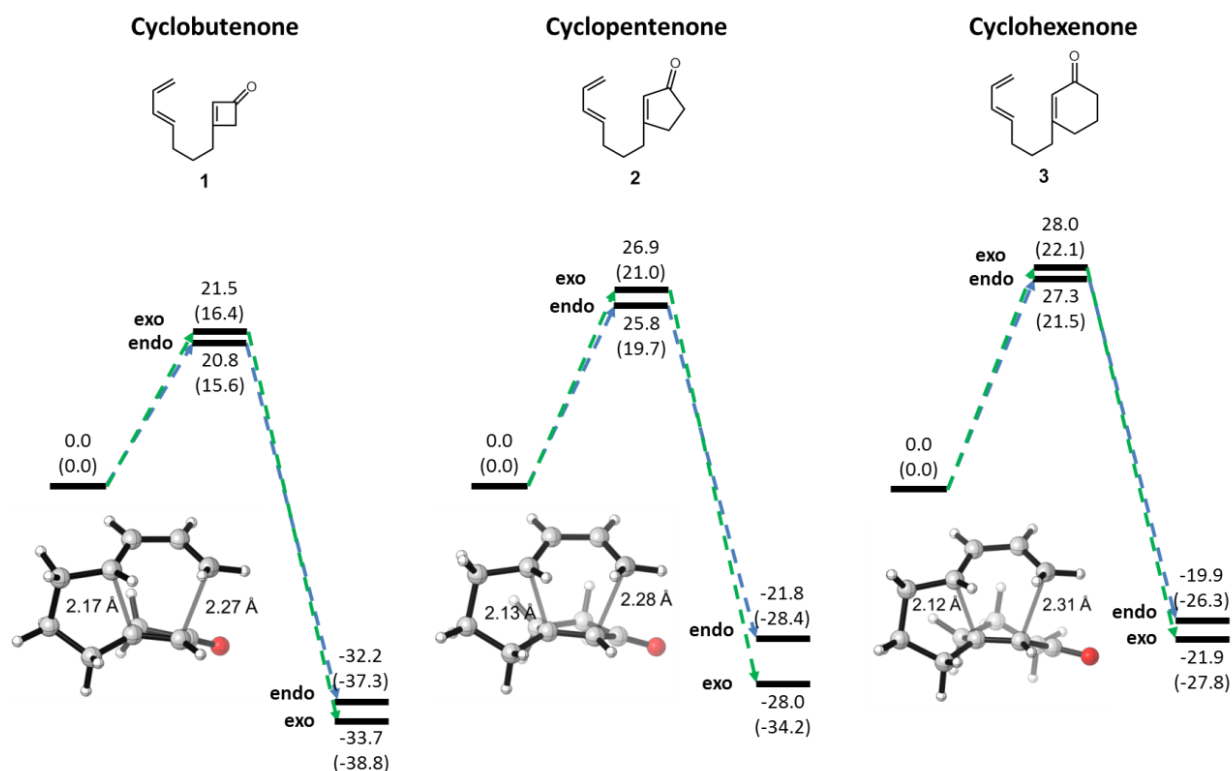


Figure 5.2. Reaction coordinate diagrams for reactions of 3-carbon-tethered cycloalkenones **1–3**. Free energies (enthalpies) are in kcal/mol. *Endo* transition state structures are shown.

Endo selectivity in Diels–Alder reactions has been studied extensively in the past, rationalized through secondary orbital interactions between the π -orbitals of the diene and the carbonyl moieties.¹¹ However, the importance of these interactions has been questioned in recent years.¹² A distortion-interaction model has been used to explain the *endo* preference of the intermolecular cycloaddition between cyclic dienes and cycloalkenones.⁴ Furthermore, the steric clash between the C_{sp^3} –H of the cycloalkenone and the hydrogen of the internal double bond destabilizes the *exo* transition state, as shown for cyclobutenone **1** in Figure 5.3. This steric strain is absent in the *endo* transition state. A similar rationale was used to explain the *cis/trans* selectivity of the parent 1,3,8-nonatriene [4+2] cycloadditions, which were investigated both experimentally and theoretically.¹³

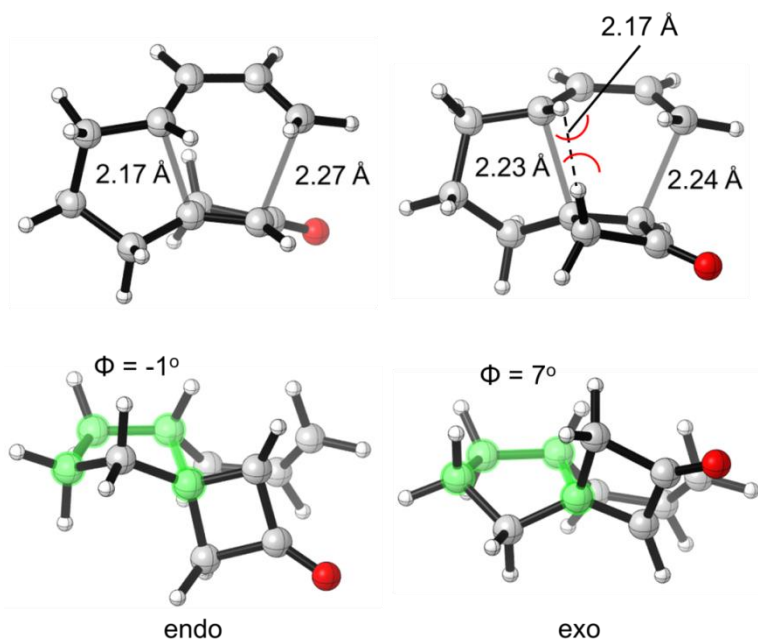


Figure 5.3. Transition structures for the cycloaddition of cyclobutenone **1**. Steric clash between hydrogens is shown in red. Dihedral carbons are highlighted in green.

The tether linking diene and dienophile moieties can play a sizable role in the transition state conformations in intramolecular reactions. Distortion of the carbon tether is a large contributor to the activation energy in previously studied intramolecular Diels–Alder and nitronc cycloadditions.¹⁴ An analogous argument can be used for these cycloalkenone systems. The forming cyclopentane ring in the *endo* transition state of **1** more closely resembles the ideal envelope conformation, with four of the carbons essentially lying in one plane (dihedral angle $\Phi = -1^\circ$). In the *exo* case, the four carbons are slightly distorted out of plane by 7° , causing more strain in the transition state. This deviation along with steric strain provide an explanation of the *endo* selectivity observed.

Adding an extra carbon to the tether does not alter the kinetically favored product (entries 4–6); the *endo* products are still preferred. The *endo* transition states are lower in energy than the corresponding *exo* transition states by 0.5–1.3 kcal/mol and are predicted to yield results similar to those of compounds **4–6**. However, the 6,6-fused cycloadducts were not experimentally observed.⁵ Rather, the products formed were 6,5-fused systems, those in which the initial butadiene had isomerized to methyl-substituted analogues of **1–3** (Figure 5.4). It is interesting to note that early quenching of the reaction revealed no isomerized reactants **7–9**. This is surprising because these compounds, when independently synthesized, seemed to undergo IMDA reactions at rates slower than those governing the cascade-like transformation to products **7P–9P**.^{5,15} Preliminary studies using 1,3-hexadiene suggest that a similar diene migration occurs in intermolecular cases (see below). With this in mind, we also calculated the energetics of the cycloadditions of **7–9** (entries 7–9).

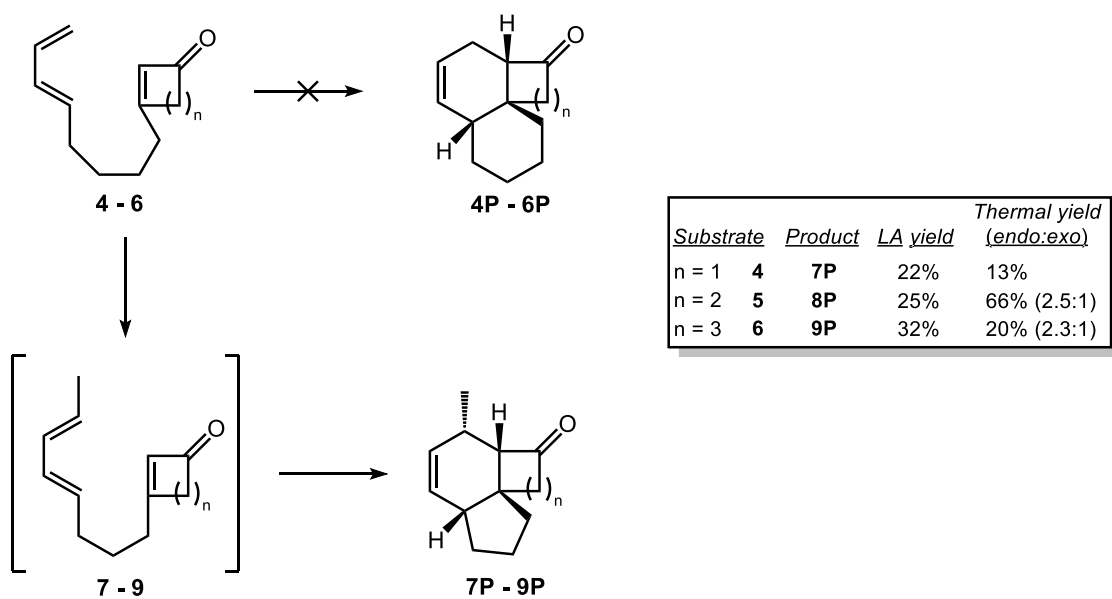


Figure 5.4. Proposed mechanism to account for the formation of cycloadducts **7P–9P** from cycloalkenones **4–6**. Experimental data from the Danishefsky group are shown.⁵

The Diels–Alder reactions of isomerized butadienes **7–9** are predicted to be more facile than those of the corresponding cycloalkenones **4–6** by 0.6–1.3 kcal/mol, translating to about a 10-fold higher reaction rate (Figure 5.5). Additionally, dienes **7–9** are 3.3–3.9 kcal/mol more stable than **4–6**. The free energy difference between TSs in Figure 5.5 of 4.6–5.1 kcal/mol accounts for the absence of product **4P–6P**. Diene isomerization should be independent of cycloalkenone ring size and, according to our results, should rapidly convert substrates **4–6** to the thermodynamically favored internal dienes **7–9** which subsequently react to form the experimentally observed **7P–9P**.

Unanticipated diene isomerizations accompanying the Diels–Alder cycloaddition have been reported in other systems.¹⁶ For example, Grieco observed a similar transformation when performing an IMDA reaction with acyclic enones.^{16a} The presence of 10% camphorsulfonic acid

in highly polar media allowed for a protonation/deprotonation mechanism to be confidently proposed, even without detection of any isomerized diene. Observed isomerizations of octadecatrienoates prior to Diels–Alder cycloaddition had previously been rationalized by Hase through a 1,5-hydrogen shift mechanism to migrated Z,E-dienes.^{16b} Likewise, Gordon observed thermal 1,5-hydrogen shifts in various alkenyl maleates en route to the construction of the decalin core of mniopetals.^{16c}

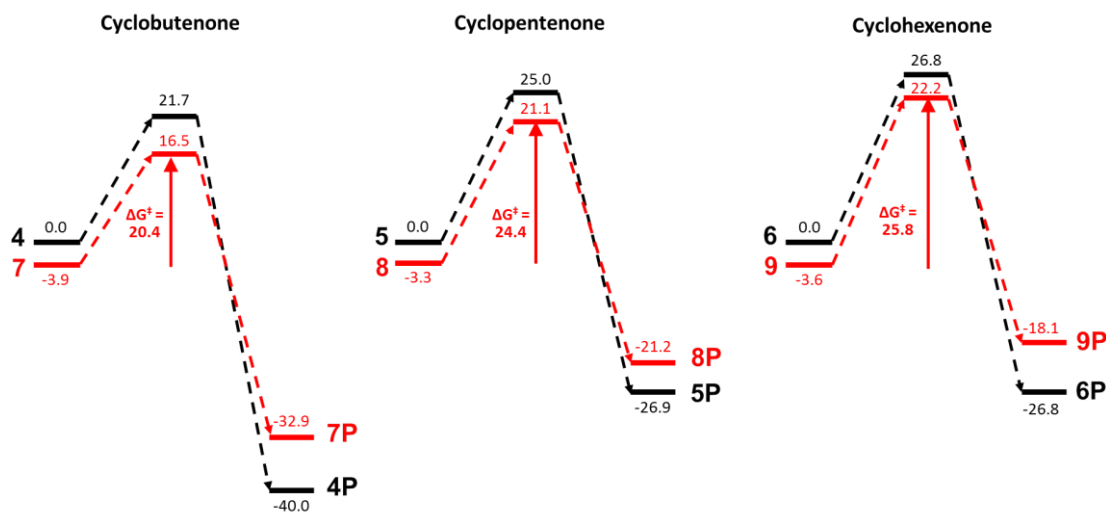
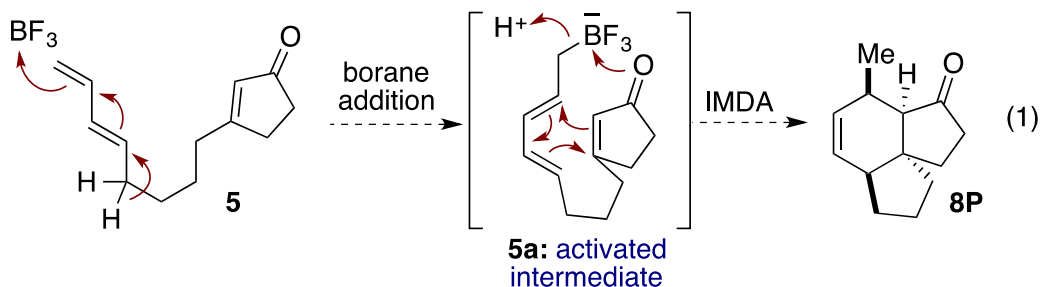


Figure 5.5. Energy profile comparison of 4-carbon-tethered cycloalkenones **4–6** and possible isomerized intermediates **7–9**. Only the *endo* pathways are shown for each substrate. All free energy values are in kcal/mol.

In our cycloalkenone systems, a 1,5-hydrogen shift to account for the isomerization is highly unlikely, since the relative stereochemistry of the observed cycloadducts is consistent with cyclization of E,E-diene precursors, which are not directly accessible via intramolecular 1,5-hydride transfer. Although we are not yet certain as to how the isomerization occurs, it is very likely to be proceeding under catalysis by an acidic agent rather than by thermal means.

Two potential types of mechanistic scenarios warrant consideration: First, it may be that a presently unknown catalytic species, generated exclusively in the course of the isomerization reaction but not in reactions that commence with the preformed methyl diene substrates, is capable of promoting rapid IMDA cyclization. In other words, perhaps when we start with the methyl dienes (**7–9**), we are not duplicating all of the collateral agents present when the methyl dienes are generated via isomerization (cf. **4–6** → **7–9**). For instance, in principle the isomerization of **5** might conceivably lead to the generation of HBF₄ (or HF) in amounts greater than are present when one starts directly with substrate **8**. If such a hypothetical agent accelerated the IMDA cycloaddition, the apparent anomaly could be explained.

Upon further consideration of the problem, an alternative type of solution presented itself (eq 1). While highly conjectural, the notion addresses a broader question than this particular BF₃-driven IMDA curiosity. Applied to the case at hand, perhaps BF₃ reacts with terminal diene **5** to produce, following (or concurrent with) deprotonation at C₅, the *trans*-dienyl methylfluoroborate **5a**; recent studies have shown that Lewis acids are capable of van der Waals interactions with alkenes,¹⁷ with some able to catalyze olefin migrations and *cis/trans* isomerizations.¹⁸ Were that to transpire, the resulting diene substructure would be highly activated to engage the dienophile in an IMDA cycloaddition (perhaps further facilitated by transfer of the boron from C→O), culminating in protonation at carbon to generate the observed **8P**. We must again emphasize the speculative nature of this sort of rationalization of the failure to identify intermediates **7–9** in the conversion of **4–6** to **7P–9P**. It is also well to underscore that the particular progression shown in eq 1 is one of a family of related possibilities which share a common integrating concept: that during the course of BF₃-induced conversion of **4–6** to **7–9**, there is produced a molecular entity that is particularly prone to undergo IMDA.

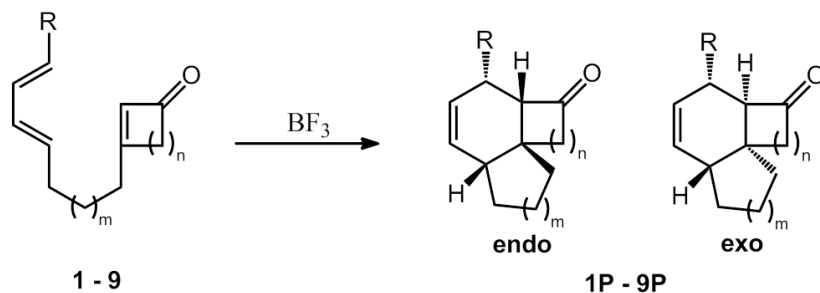


In future research, we hope to explore this question, which may well go to the broader issue of olefin isomerization by apparent Lewis, rather than protic, acids. We also hope to continue our studies into the energetics and new synthetic applications of IMDA reactions to build molecular complexity in a concise fashion.

The Effect of Lewis Acid BF₃

Lewis acids are able to activate enone dienophiles, lowering the activation barrier in the Diels–Alder reactions of enones.¹⁹ The calculated energetics for the Lewis acid-catalyzed reactions of cycloenones **1–9** are shown in Table 5.2. BF₃ was used as the Lewis acid, modeled after the experimental conditions in the Danishefsky lab.⁵ Coordination to each lone pair of the oxygen was considered, and the lowest energy conformations are reported here. The coordination of BF₃ to the cycloalkenone oxygen increases the electrophilic nature of the β-carbon, resulting in a more asynchronous cycloaddition. As shown in Figure 5.6, the difference in length between the forming C–C bonds in the *endo* transition states increases from 0.10–0.19 Å in the thermal reactions to 0.38–0.46 Å in the presence of BF₃. This increase in electrophilicity of the β-carbon consequently enhances the favorable interaction with the nucleophilic carbon of the diene, lowering the activation barriers of all transition states. In contrast, the reaction free energies are largely unaffected, implying that Lewis acids comparably stabilize the reactant enones and product ketones.

Table 5.2. Computed Reaction and Activation Free Energies (kcal/mol) of the Lewis Acid-Catalyzed Diels–Alder Cycloaddition of Cycloalkenones **1–9**.



entry	SM	m	n	R	ΔG^\ddagger endo	ΔG^\ddagger exo	ΔH^\ddagger endo	ΔH^\ddagger exo	ΔG_{rxn} endo	ΔG_{rxn} exo	$k_{\text{endo/exo}}$
1	1	1	1	H	14.5	17.1	8.0	11.0	-32.0	-33.6	83.0
2	2	1	2	H	19.6	23.5	13.1	16.9	-18.4	-23.5	703.2
3	3	1	3	H	19.4	22.2	13.6	16.4	-20.7	-22.4	115.0
4	4	2	1	H	15.9	17.0	9.2	11.1	-40.5	-38.5	7.1
5	5	2	2	H	20.2	22.4	13.2	15.8	-26.1	-27.0	44.6
6	6	2	3	H	22.2	23.3	15.3	16.4	-25.3	-23.5	6.5
7	7	1	1	Me	10.6	14.1	4.3	7.5	-29.9	-31.6	365.7
8	8	1	2	Me	17.2	20.8	9.9	13.4	-15.6	-21.3	414.8
9	9	1	3	Me	17.1	20.9	10.5	14.7	-14.4	-19.8	578.6

The stereoselectivity of the reaction is amplified in the presence of acid, as noted earlier;²⁰ with BF_3 , the *endo* transition state becomes substantially more favorable relative to the *exo* transition state in all cases (~ 2.8 kcal/mol). Because of the asynchronous nature of the Lewis acid-catalyzed reaction, the forming σ -bond that is shared by the fused rings is shorter than under thermal conditions. This intensifies the steric clash between the hydrogens in the *exo* transition state, thus increasing the preference for the *endo* transition state. For instance, the H–H bond distance in the Lewis acid-catalyzed *exo* transition state for cyclobutenone **1** is reduced to 2.08 Å from the 2.17 Å in the thermal *exo* transition state shown earlier. The larger steric strain causes the kinetically favored *endo* product to be formed exclusively, as found in experiment.⁵

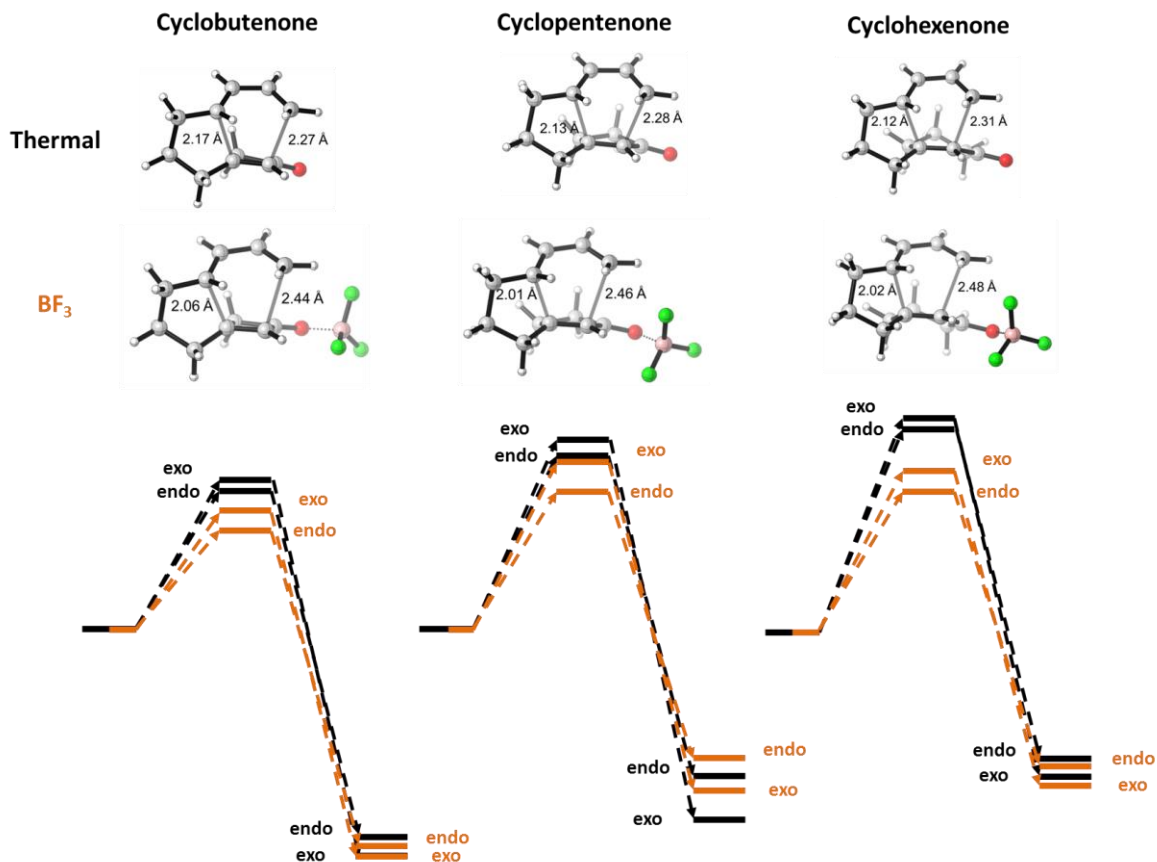


Figure 5.6. Energy profile comparison of the thermal (black) and BF_3 -catalyzed (orange) reactions of cycloalkenones **1–3**. *Endo* transition states are shown.

Respective starting points have been scaled to 0.

Comparing the kinetics of the 4-carbon-tethered substrates (entries 4–6) with their isomerized counterparts (entries 7–9) demonstrates that Lewis acid catalysis now greatly favors the cycloaddition of the latter by upward of 3 kcal/mol for the *endo* transition states. The activation barrier for isomerized cyclobutenone **7** remarkably drops to 10.6 kcal/mol, lower than typically expected for pericyclic reactions. This results from the synergistic contributions of the increase in polarization from BF_3 -coordination and the intrinsic preference of the isomerized internal-diene cycloaddition over terminal-diene cycloaddition, also exhibited in the uncatalyzed reaction.

Does Isomerization Occur in the Intermolecular Case?

Further studies were performed to gain insight into the fine balance of cycloaddition versus diene migration. The BF_3 -catalyzed intermolecular cycloadditions of 1,3-hexadiene **10** and isomeric 2,4-hexadiene **15** with cyclobutenone and cyclopentenone were computed (Figure 5.7). Only the *endo* transition states were considered, because we have previously demonstrated that these are favored over the *exo* counterparts. Cycloaddition with **10** theoretically leads to two regioisomers, with the ethyl substituent on the cyclohexene either proximal (**13a/14a**) or distal (**13b/14b**) to the carbonyl; computations predict that formation of **13a/14a** is preferred by greater than 4 kcal/mol. It is of interest to note that in the intramolecular examples, the tether dictates the regiochemistry of the reaction, forming products with the distal alkyl group analogous to the disfavored **13b/14b**.

Reactions of cycloalkenones with isomerized diene **15** occur with lower barriers with respect to unisomerized diene **10**, implying that any incidence of diene isomerization will lead to cycloaddition and formation of products **16** and **17**. Preliminary experimental results from the Danishefsky lab suggest that the reaction of **10** with cyclobutenone results only in direct Diels–Alder product **13a**, while reaction with cyclopentenone yields a 1.6:1 ratio of **14a** to isomerized **17** (see Supporting Information). Presumably the 13.6 kcal/mol barrier for the cycloaddition of **10** and **11** is lower than that for diene isomerization, which in turn should be lower than the 15.9 kcal/mol barrier seen for the intramolecular Diels–Alder reaction of **4** (Table 5.2, entry 4), because only isomerized product is observed in that case. Hence, the barriers for diene isomerization should be about 15 kcal/mol for isomerization to take place prior to Diels–Alder cycloaddition.

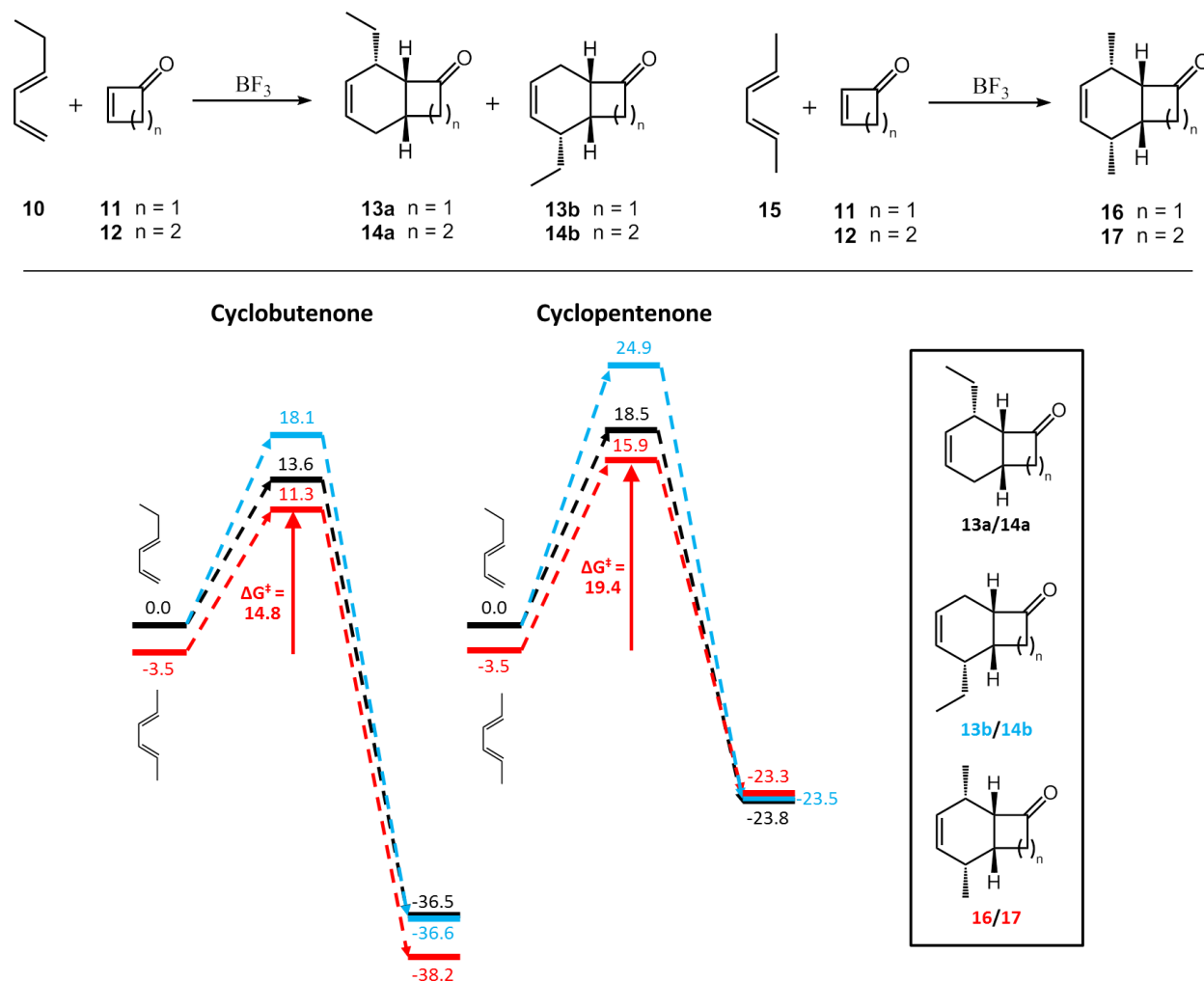


Figure 5.7. Computed energy diagrams for the Lewis acid-catalyzed intermolecular reactions of cyclobutenone **11** and cyclopentenone **12**. Free energies are in kcal/mol. Only *endo* transition states were considered.

The Effect of a Bromine Substituent

The Danishefsky group found that incorporation of a vinyl bromide or chloride at the α -position of the cycloalkenones increases their reactivity in intermolecular Diels–Alder reactions.²¹ This effect should extend to the analogous IMDA reactions, and thus we have modeled the

reaction between 2-bromocyclobutenone and a tethered diene (Figure 5.8). The influence of halogen substituents on dienes in Diels–Alder reactions has been studied by us and other groups,^{8a,22} but the investigations of the effects of α -halogenated enones have been limited to intermolecular cases.²³

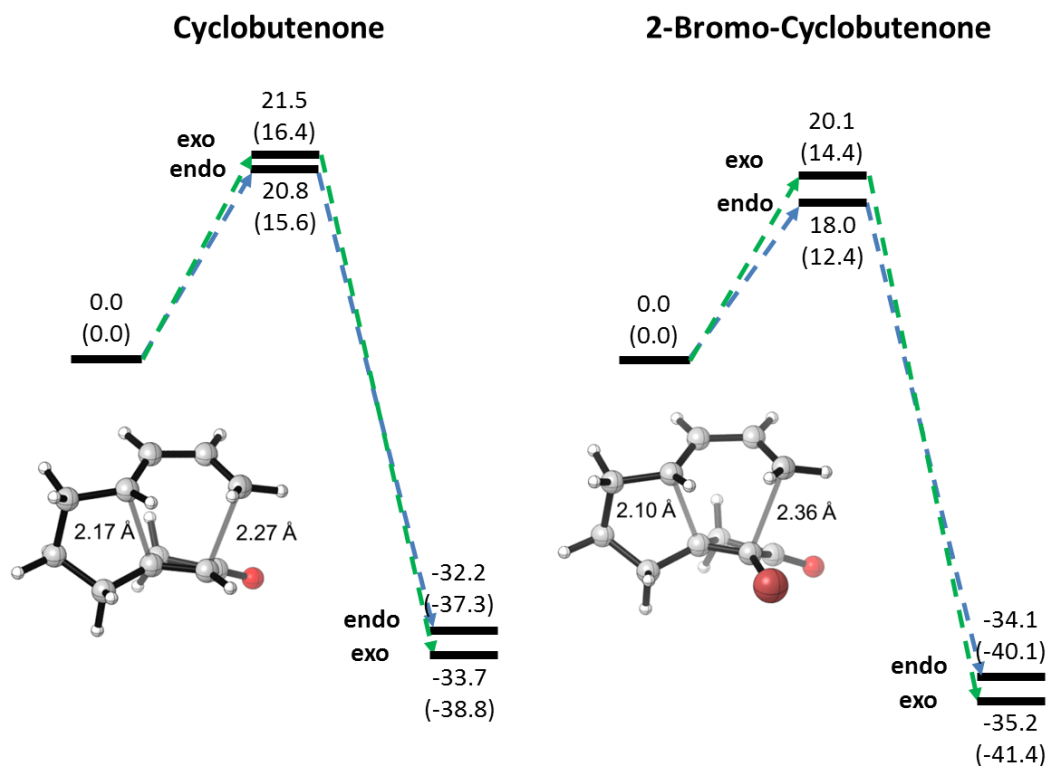


Figure 5.8. Computed free energy diagrams for cyclobutenone **1** and halogenated analogue 2-bromocyclobutenone **1Br**. Free energies (enthalpies) are in kcal/mol. *Endo* transition states are shown.

As compared to the thermal cycloaddition of the parent cyclobutenone, the reaction barriers decrease and the reactions become more exothermic following vinylic halogenation. This “halogen effect” was previously observed in our work on halofuran cycloadditions with Padwa.^{22a} Additionally, the preference of the *endo* transition state is increased from 0.7 to 2.1 kcal/mol.

These changes, along with the larger asynchronicity of the bond formation, are indicative of a more polar transition structure, reminiscent of conducting the reaction in the presence of BF_3 . Both α -halogenation and/or coordination of Lewis acidic BF_3 to the carbonyl oxygen increase the electrophilicity of the β -carbon. The M06-2X-computed LUMO energy of cyclobutenone **1** decreases by 0.4 eV upon incorporation of the α -bromine substituent. Furthermore, the thermodynamic preference for electronegative halogens to be attached to more alkylated sp^3 -carbons explains the larger exergonicity of the halogenated Diels–Alder products.^{8a}

Conclusion

We have investigated the intramolecular Diels–Alder reaction of tethered cycloalkenones and butadienes. The high *endo* selectivity of the reaction observed experimentally arises from strain induced by tether conformation and steric repulsion in the *exo* transition states. Coordination of a Lewis acid increases the rate of reaction as well as the difference in activation energy of the *endo* and *exo* transition states, producing solely the *endo* product. The lack of anticipated 6,6-fused product with a 4-carbon tether is caused by a facile and thermodynamically favorable diene migration prior the Diels–Alder cycloaddition. The addition of a bromine substituent at the α -position of the enone facilitates both the kinetics and the thermodynamics of the reaction and increases the preference for the *endo* transition state.

References

1. a) Fringuelli, F.; Pizzo, F.; Taticchi, A; Halls, T. D. J.; Wenkert, E. *J. Org. Chem.* **1982**, *47*, 5056. b) Karthikeyan, M.; Kamakshi, R.; Sridar, V.; Reddy, B. S. R. *Synth. Commun.* **2003**, *33*, 4199.
2. a) Bienfait, B.; Coppe-Motte, G.; Merényi, R.; Viehe, H. G. *Tetrahedron* **1991**, *47*, 8167. b) Kelly, T. R.; McNutt, R. W. *Tetrahedron Lett.* **1975**, *16*, 285.
3. Li, X.; Danishefsky, S. J. *J. Am. Chem. Soc.* **2010**, *132*, 11004.
4. Paton, R. S.; Kim, S.; Ross, A. G.; Danishefsky, S. J.; Houk, K. N. *Angew. Chem., Int. Ed.* **2011**, *50*, 10366.
5. Ross, A. G.; Li, X.; Danishefsky, S. J. *J. Am. Chem. Soc.* **2012**, *134*, 16080.
6. Zhao, Y.; Truhlar, D. G. *Acc. Chem. Res.*, **2008**, *41*, 157.
7. Zhao, Y.; Truhlar, D. G. *J. Phys. Chem. A*, **2008**, *112*, 1095-1099.
8. a) Pieniazek, S.; Houk, K. N. *Angew. Chem.* **2006**, *118*, 1470; *Angew. Chem. Int. Ed.* **2006**, *45*, 1442. b) Pieniazek, S.; Clemente, F. R.; Houk, K. N. *Angew. Chem.* **2008**, *120*, 7860; *Angew. Chem. Int. Ed.* **2008**, *47*, 7746. c) Paton, R. S.; Mackey, J. L.; Kim, W. H.; Lee, J. H.; Danishefsky, S. J.; Houk, K. N. *J. Am. Chem. Soc.* **2010**, *132*, 9335.
9. Linder, M.; Brinck, T. *Phys. Chem. Chem. Phys.*, **2013**, *15*, 5108.
10. Frisch, M. J.; et al. *Gaussian 09*, revision C.01; Gaussian, Inc.: Wallingford, CT, 2009. The complete reference for Gaussian 09 can be found in the Supporting Information.
11. a) Hoffmann, R.; Woodward, R. B. *J. Am. Chem. Soc.*, **1965**, *87*, 4388. b) Houk, K. N. *Tetrahedron Lett.* **1970**, *30*, 2621. c) Paddon-Row, M. N.; Moran, D.; Jones, G. A.; Sherburn, M. S. *J. Org. Chem.* **2005**, *70*, 10841. d) Wannere, C. S.; Paul, A.; Herges, R.; Houk, K. N.; Schaefer, H. F., III; Schleyer, P. *J. Comput. Chem.* **2007**, *28*, 344.
12. a) Fernández, I.; Bickelhaupt, F. M. *J. Comput. Chem.* **2013**, DOI: 10.1002/jcc.23500. b) García, J. I.; Mayoral, J. A.; Salvatella, L. *Acc. Chem. Res.* **2000**, *33*, 658.
13. a) Lin, Y.-T.; Houk, K. N. *Tetrahedron Lett.* **1985**, *26*, 2269. b) Brown, F. K.; Houk, K. N. *Tetrahedron Lett.* **1985**, *26*, 2297. c) Raimondi, L.; Brown, F. K.; Gonzalez, J.; Houk, K. N. *J. Am. Chem. Soc.* **1992**, *114*, 4796.
14. a) Krenske, E. H.; Houk, K. N.; Holmes, A. B.; Thompson, J. *Tetrahedron Lett.* **2011**, *52*, 2181. b) Krenske, E. H.; Perry, E. W.; Jerome, S. V.; Maimone, T. J.; Baran, P. S.; Houk, K. N. *Org. Lett.* **2012**, *14*, 3016.
15. Ross, A. G. The Development of Cyclobutenone, and Other Work. Ph.D. Dissertation, Columbia University, New York, NY, 2013.

16. a) Grieco, P. A.; Beck, J. P.; Handy, S. T.; Saito, N.; Daeuble, J. F. *Tetrahedron Lett.* **1994**, *35*, 6783. b) Matikainen, J.; Kaltia, S.; Hämäläinen, M.; Hase, T. *Tetrahedron* **1997**, *53*, 4531. c) Allen, A.; Gordon, D. M. *Indian J. Chem.* **1999**, *38B*, 269. d) Humphrey, J. M.; Liao, Y.; Ali, A.; Rein, T.; Wong, Y.-L.; Chen, H.-J.; Courtney, A. K.; Martin, S. F. *J. Am. Chem. Soc.* **2002**, *124*, 8584.
17. a) Zhao, X. X.; Stephan, D. W. *Chem. Sci.* **2012**, *3*, 2123. b) Zhao, X. X.; Stephan, D. W. *J. Am. Chem. Soc.* **2011**, *133*, 12448.
18. Pérez, M.; Hounjet, L. J.; Caputo, C. B.; Dobrovetsky, R.; Stephan, D. W. *J. Am. Chem. Soc.* **2013**, Article ASAP, DOI: 10.1021/ja410379x.
19. Select papers: a) Yates, P.; Eaton, P. *J. Am. Chem. Soc.* **1960**, *82*, 4436. b) Rogers, C.; Keay, B. A. *Synlett* **1991**, 353. c) Yakelis, N. A.; Roush, W. R. *Org. Lett.* **2001**, *3*, 957. d) Taguchi, T.; Saito, A.; Yanai, H. *Chem. Rec.* **2007**, *7*, 167.
20. a) Alonso, I.; Carretero, J. C.; Garcia Ruano, J. L. *Tetrahedron Lett.* **1989**, *30*, 3853. b) Ge, M.; Stoltz, B. M.; Corey, E. J. *Org. Lett.* **2000**, *2*, 1927.
21. Ross, A. G.; Townsend, S. D.; Danishefsky, S. J. *J. Org. Chem.* **2013**, *78*, 204.
22. a) Padwa, A.; Crawford, K. R.; Straub, C. S.; Pieniazek, S. N.; Houk, K. N. *J. Org. Chem.* **2006**, *71*, 5432. b) Crawford, K. R.; Bur, S. K.; Straub, C. S.; Padwa, A. *Org. Lett.* **2003**, *5*, 3337. c) Klepo, Z.; Jakopcic, K. *J. Heterocycl. Chem.* **1987**, *24*, 1787.
23. Sarotti, A. M.; Spanevello, R. A.; Suárez, A. G. *Tetrahedron Lett.* **2011**, *52*, 4145.

Chapter 6. Dicyanovinyl naphthalenes for Neuroimaging of Amyloids and Relationships of Electronic Structures and Geometries to Binding Affinities.

Introduction

Extracellular amyloid- β (A β) senile plaques (SPs) and neurofibrillary tangles (NFTs) of intraneuronal hyperphosphorylated tau peptide aggregates are a characteristic pathology found in the brains of patients with Alzheimer's disease (AD) and other neurodegenerative diseases.¹ Accurate detection of these aggregates in the brains of living AD patients allows early diagnosis and potential treatments to reverse or retard disease progression. The fluorescent thioflavin T and Congo red dyes are traditionally used to label protein aggregates in brain slices for *postmortem* diagnosis of AD. Unlike these charged molecules, the uncharged fluorescent naphthalene derivative 1,1-dicyano-2-[6-(dimethylamino)naphthalen-2-yl]propene (DDNP) (Figure 6.1), also an excellent staining dye *in vitro*, is capable of crossing the blood–brain barrier. The fluorinated DDNP analog, 2-(1-[6-[(2-fluoroethyl)(methyl)amino]-2-naphthyl]ethylidene) (FDDNP), can be synthesized with the ¹⁸F positron emitter and was used as the first molecular imaging probe for the regional assessment of A β and tau deposition in the brains of living AD patients.^{2–5}

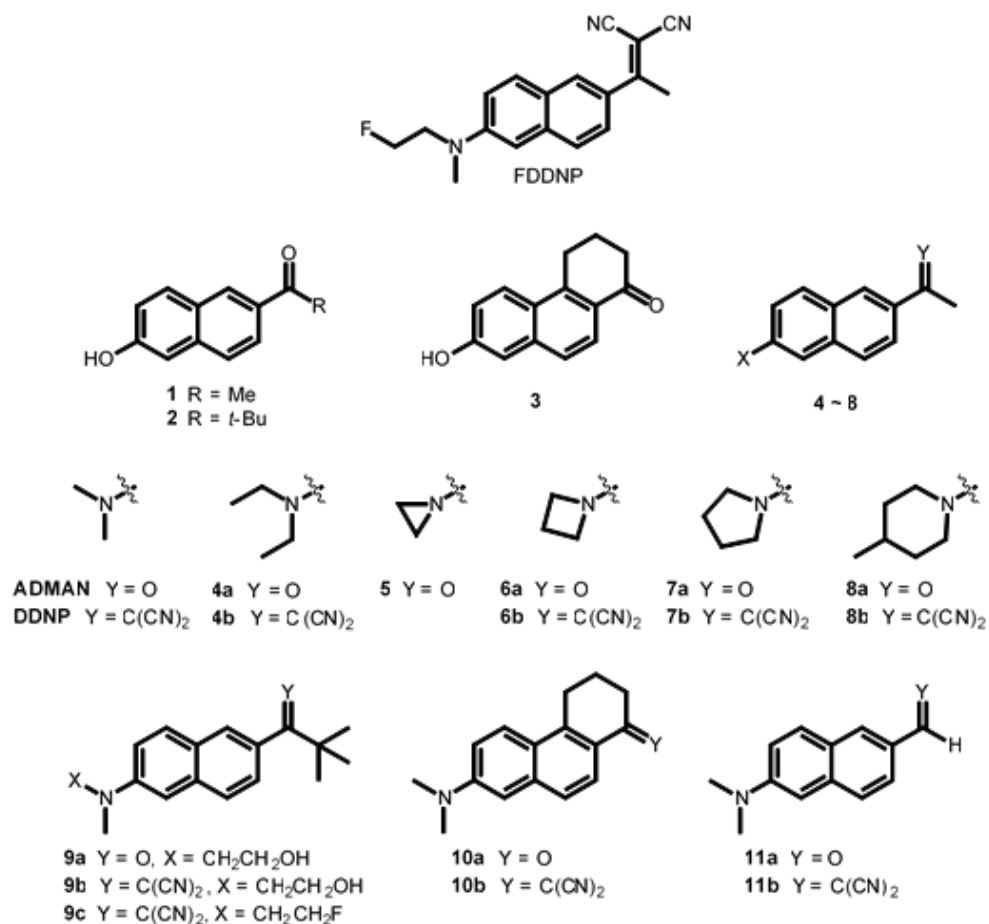


Figure 6.1. Structures of synthesized FDDNP analogs.

Previous studies have shown that it is the neutral and hydrophobic properties of DDNP and its analogs that enable it to recognize the β -sheet domains in amyloid-like aggregates, making it an effective *in vitro* and *in vivo* imaging probe.^{6,7} Recently, DDNP and other amyloid-imaging probes have been co-crystallized with short amyloid-forming segments of the A β and tau polypeptides that form fibrils similar to those formed with the full protein.⁸ These truncated systems contain stacks of self-complementary β -sheets tightly bound to each other in a motif called a steric zipper. The fibrils formed by the steric zippers are similar to those formed by the full-length parent sequence in morphology, diameter, helical pitch, cross- β diffraction pattern,

fibril seeding capacity, stability and dye binding.⁸⁻¹⁰ Numerous investigations have shown that although the steric zippers do not contain all the elements of complexity contained in the parent systems, they serve as excellent models for full-length fibrils.^{8,11} Recently, the VQIVYK steric zipper model from tau has been used to develop a small polypeptide inhibitor of not only truncated peptide aggregation but also aggregation of two tau constructs as well.¹² The X-ray structures solved with DDNP bound to the VQIVYK steric zipper suggested transient binding of DDNP along a hydrophobic channel that runs the length of the longitudinal fibril axis (or fibril spine). The presence of a “smear” of electron density along the binding channel indicated that there may be multiple sites that DDNP binds, unlike the more discrete binding sites associated with charged molecular probes that preferred highly localized sites near complementary charged residues. Molecular docking was used in the crystallographic study to identify the preferred binding modes and sites of DDNP along the fibril channel, while also managing to recapitulate the experimentally observed transient docking phenomenon.

We have synthesized a number of new FDDNP analogs (Figure 6.1) that differ in size both at the electron-donating amine and electron-withdrawing dicyanovinyl moieties. Herein, we report the effects of chemical modifications on the molecular geometries, spectroscopic properties, and binding to A β fibrils. We then use molecular docking to study the binding modes of these molecules to the established tau steric zipper model. The binding information is used to rationalize the effects of chemical substitutions and changes in molecular geometry on the binding affinity.

Experimental Results and Discussion

New Naphthalene Derivatives

Fluorescent compounds **4–11** (Figure 6.1) were prepared based on an established synthetic methodology (for details see Materials and Methods).^{3,13,14} FDDNP and its analogs are environmentally sensitive fluorophores that undergo a significant change in absorption/emission wavelength upon binding to SPs or NFTs.^{3,7,15} Fluorescence microscopy revealed an intense fluorescence of SPs and NFTs with minimal background fluorescence in *post mortem* AD brain specimens stained with FDDNP analogs. The binding affinity of each FDDNP analog was measured using radioactive competitive binding assays with [¹⁸F]FDDNP. Addition of nonradioactive **4b**, **6b**, **7b**, **8b**, **9c**, **10b** or **11b** displaces [¹⁸F]FDDNP from the A β fibril-binding site. This indicates that the analogs share the same [¹⁸F]FDDNP-binding site on the A β aggregates (Figure 6.2, top). All compounds, except **9c**, exhibit rather similar nanomolar binding affinity to A β fibrils (K_i , Table 6.1). Compound **9c** has only weak binding to A β fibrils, also reflected in its poor ability to label A β aggregates in human brain specimens (Figure 6.2, bottom).

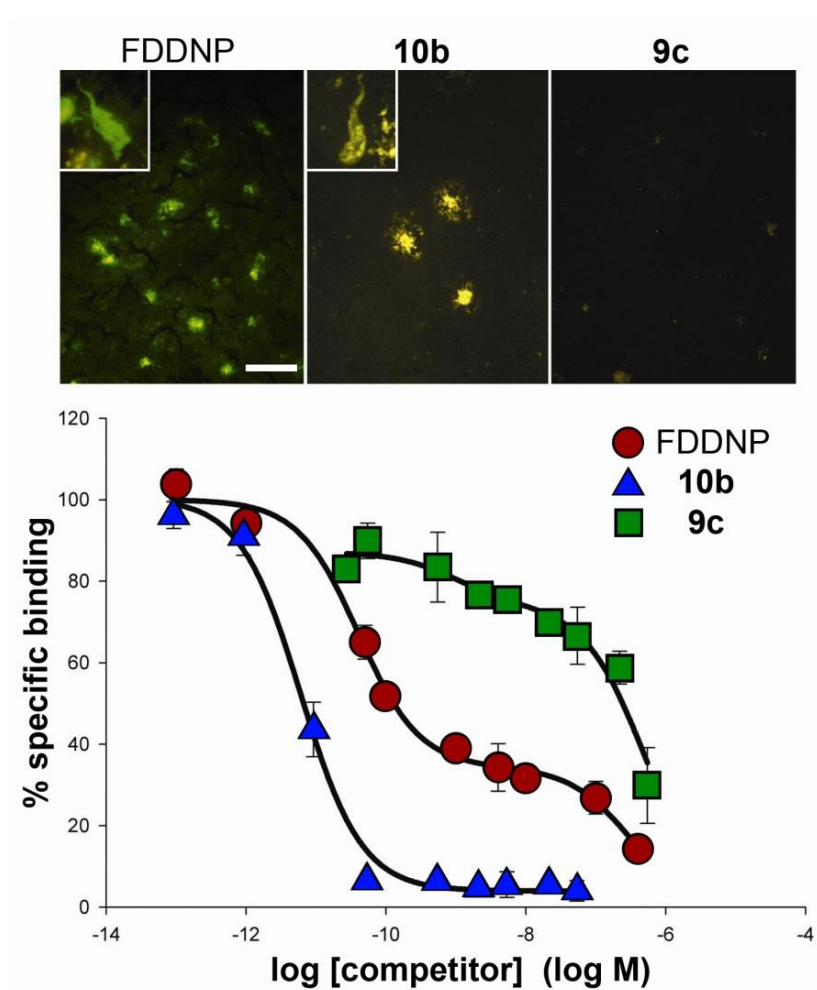


Figure 6.2. (top) Confocal fluorescence micrograph of a neurofibrillary tangle and senile plaque labeled with 10 μ M FDDNP vs. constrained DDNP (**10b**) and *t*-butyl DDNP (**9c**). Digitally captured image produced by laser-scanning Leica TCS SP MP inverted confocal microscope with an argon laser (excitation wavelength = 488 nm). Scale bar: 50 μ m. Note the poor labeling ability of the *t*-butyl analog **9c**, as opposed to the more planar FDDNP and **10b**. (Bottom) Radioactive competitive binding curves of [18 F]FDDNP vs. nonradioactive FDDNP (red circles), **10b** (blue triangles) and **9c** (green squares) in the presence of A β (1-40) fibrils. Each symbol represents the mean value of three determinations per each concentration of competitor. Error bars indicate \pm SD.

Table 6.1. Selected structural, spectroscopic, and binding data for synthesized DDNP analogs.

Compound	NMR		Spectroscopic		Binding			X-ray			Calculated		
	δ (H-5)	δ (H-7)	λ_{\max} (abs*)	λ_{\max} (em)	ϕ^{\dagger}	$\Delta\nu$ (cm ⁻¹)	K_i (nM) [¶]	NC_{ar}^{\ddagger} (Å)	$\Sigma\omega_i^{\S}$ (°)	$\omega_{torsion}$ (°)	NC_{ar} (Å)	$\omega_{torsion}$ (°)	rms (Å)
DDNP	6.85	7.18	438	560	0.030	4,970	10	1.362 1.375	359.9 360.0	31.0 143.7	1.375 1.374	37.1 143.8	0.10 0.11
FDDNP	6.95	7.20	431	553	0.016	5,065	0.20	n/d	n/d	n/d	1.388 1.388	37.7 143.2	—
4b	6.82	7.12	455	564	0.021	4,250	0.46	n/d	n/d	n/d	1.372 1.372	36.2 145.1	—
6b	6.58	6.81	434	567	0.018	5,400	0.43	1.369 1.374	359.8 348.4	33.3 152.6	1.375 1.374	37.3 143.8	0.25 0.10
7b	6.71	7.03	455	566	0.020	4,310	0.19	n/o 1.369	n/o 359.9	n/o 148.8	1.364 1.364	36.3 145.1	— 0.09
8b	7.07	7.33	428	569	0.014	5,790	0.30	n/o 1.411	n/o 347.8	n/o 146.0	1.401 1.402	37.9 143.1	— 0.25
9c	6.91	7.04	374	595	0.013	9,930	520	n/d	n/d	n/d	1.390 1.390	75.4 110.6	—
10b**	6.84	7.18	443	541	0.006	4,090	0.01	1.377	360.0	35.6	1.377	31.9	0.15
††								1.366	359.2	-10.3	1.373	-29.0	0.28
11b	6.83	7.16	470	566	0.137	3,610	0.12	1.360	360.0	2.9	1.369	0.0	0.06
								n/o	n/o	n/o	1.369	180.0	—

n/d, not determined; n/o, not observed; —, uncalculated value.

*Absorption (abs) and emission (em) measured in CH₂Cl₂ (nm), a solvent that mimics the microenvironment of the A β fibril-binding site.

[†]Quantum yields determined relative to DDNP.

[‡]Distance between amine nitrogen and aromatic naphthalene carbon.

[§]Sum of bond angles about amino nitrogen.

[¶]High binding affinity to A β fibrils. Binding affinities were determined in PBS (pH 7.4) containing up to 1% ethanol.

^{||}Heavy atom rmsd with respect to the X-ray structure.

**Orange crystal.

††Red crystal.

The ketone intermediates did have good affinities for amyloid fibrils *in vitro*.¹⁶ We tested the [¹⁸F]fluoroethyl (1-{6-[(2-fluoroethyl)(methyl)amino]naphthalen-2-yl}ethanone) (ADMAN) derivative *in vivo* in humans, which showed significant nonspecific (nonamyloid) binding, consistent with the membrane-intercalating properties of the 2-(dialkylamino)-6-acylnaphthalenes.¹⁷ This reduces ketone effectiveness for *in vivo* use in humans, and this report concentrates on the binding affinities and properties of the amyloid-specific dicyanovinyl compounds.

NMR Spectra

¹H NMR spectra reflect the structural changes upon formal substitution of the acetyl group for the dicyanovinyl acceptor group, most notably through a decrease in chemical shift of proton H-1 from approximately 8.3 to 8.0 ppm attributable to modified magnetic anisotropy of the side

chain (see Supporting Information). The ^1H NMR spectra also provide insights into the ground-state molecular geometry in solution, particularly around the nitrogen atom. Planar geometries support efficient delocalization of the nitrogen electron pair into the aromatic ring and result in increased shielding and smaller chemical shifts for protons H-5 and H-7 (δ , Table 6.1). In compounds with nonplanar arrangement of the substituents around the donor nitrogen (**5**, **8a**, **8b**), chemical shifts of the corresponding protons are substantially larger. The distinct coupling pattern in solution ^1H NMR spectra of compound **8b** and related piperidine and piperazine derivatives shows that at room temperature, the six-membered ring is fixed in a chair conformation.¹⁸ This is in agreement with the ground-state calculations for **8b**, in which the heavy atom angles in the six-membered rings are shown to be between 108° and 112° (see *Structure and Modeling*). Similar NMR spectral results were obtained for compounds with analogous electron-donating groups, which were concluded to contain nonplanar amines.^{13,14} For compound **6b**, which exists both in planar and nonplanar forms in the solid state, ^1H chemical shifts for protons H-5 and H-7 were found to be relatively small in solution. This indicates a greater propensity toward the planar arrangement about the nitrogen, allowing for efficient conjugation with the naphthalene ring system.

Absorption and Emission Spectra

For all compounds except **9c**, replacement of the acetyl acceptor group by the dicyanovinyl side chain resulted in considerable bathochromic shifts of the absorption maxima from 350–380 nm to 400–470 nm (λ_{max} , Table 6.1). This observation is consistent with previous studies that demonstrated a propensity for the dicyanovinyl to be planar and conjugated with the donor group.¹⁹ The lack of red shift in **9c** is the result of the acceptor being forced out of the plane of conjugation due to the bulky *t*-butyl substituent. The absorption maxima are also dependent on the extent of conjugation of the donor group, although the effect is less pronounced.

The emission maxima of these compounds are independent of the geometry about the amine but occur at a higher wavelength for analog **9c**, in which the acceptor group is highly non-planar. Emission maxima are also red-shifted with increasing solvent polarity (see Supporting Information). Large red shifts indicate an increased dipole moment in the excited state compared with that of the ground state, consistent with the formation of an intramolecular charge-transfer excited state (ICT, see Supporting Information).^{20,21} It should be noted that for strongly solvatochromatic compounds, an anomalous blue shift in water is observed because of interactions with the solvent cage. This blue-shifting phenomenon has been long established in the literature.³

Fluorescence-emission intensities depend on the rate of ICT excited-state depopulation. In viscous microenvironments or upon binding to amyloid aggregates, double-bond isomerization or rotational relaxation is restricted and becomes much slower, leading to approximately 10-times enhanced fluorescence yields over in bulk solution (ϕ , Table 6.1).¹⁶

Structure and Modeling

Single crystal X-ray diffraction provided solid-state structures of DDNP, **5**, **6b**, **7b**, **8b**, **10b**, and **11b**. In the case of **6b**, two conformers were present in the crystal. The distinct conformations are attributable to the orientation of the dicyanovinyl, which can be rotated syn or anti with respect to the C6-C7 aromatic bond (Figure 6.3). We have defined the torsion angle responsible for the orientation of the dicyanovinyl as ω_{torsion} . Analog **10b** crystallized into two distinct crystal polymorphs, colored red and orange, which arises due to cyclohexenyl-ring conformations that orient the dicyanovinyl either above or below the plane of the naphthalene ring.

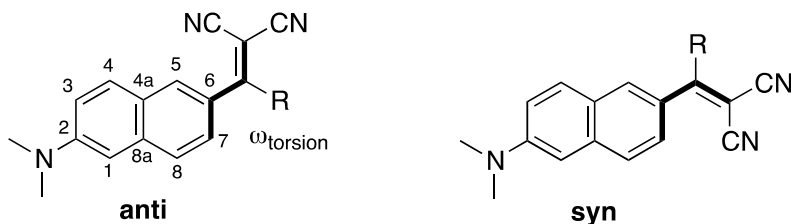


Figure 6.3. Syn and anti orientations of the dicyanovinyl group with respect to the C7-C6 aromatic bond. The syn conformation is defined as $0^\circ \leq |\omega_{\text{torsion}}| < 90^\circ$, and the anti conformation as $90^\circ \leq |\omega_{\text{torsion}}| \leq 180^\circ$.

The X-ray structures exhibit an sp^2 -like planar arrangement of the substituents around the naphthalene ring providing maximal conjugation of the nitrogen lone pair with the aromatic system. The X-ray structures revealed the syn conformation of **6b** to be planar and the anti to be slightly puckered. Azetidine rings, such as the one in **6b**, are nonplanar, with a slight 1.3 kcal/mol nitrogen inversion barrier.²² However, planar azetidine rings have been previously reported in other crystal structures in which the azetidine nitrogen is conjugated with a π system.²³ The pyrrolidine ring in **7b** adopts an envelope conformation. The other cyclic analogs do not allow planarization about the amine nitrogen without a higher energetic penalty. For these analogs, distortion from planarity at the amine results in a slight loss of conjugation, which causes a lengthening of the bond distance between the amine nitrogen and aromatic carbon of the naphthalene ring ($N-C_{\text{ar}}$, Table 6.1). The mean $N-C_{\text{ar}}$ X-ray distances for the planar amines listed in Table 6.1 are 1.368 Å and 1.393 Å for the nonplanar amines. This difference in bond distances for the planar and nonplanar compounds has been observed in a related set of DDNP analogs with structures determined by neutron diffraction.¹³ These molecules demonstrated $N-C_{\text{ar}}$ distances of 1.371 Å for the planar amines and 1.426 Å for the nonplanar amines.

Quantum mechanical (QM) geometry optimizations were performed at the Mo6-2X/6-311+G(d,p) level in the gas phase (details in *Materials and Methods*). The compounds were all

modeled in both the syn and anti orientations of the dicyanovinyl group. The optimized structures agreed well with the geometries of the available X-ray structures (Table 6.1 and Supporting Information), yielding an average heavy atom RMSD of 0.15 Å. The QM geometry optimizations showed that the syn and anti orientations are nearly isoenergetic, with an average difference of 0.4 kcal/mol (see Supporting Information). It has been previously proposed that the dipole moment of DDNP is related to binding affinity.^{2,24} We analyzed the charge distribution of these molecules by mapping the electrostatic potential (ESP) to the molecular surface of each analog (see Supporting Information). The ESP surfaces of all the analogs are very similar, the primary difference between them being their shapes. This is most prominently highlighted by comparing the two most planar analogs with the highest binding affinities, **10b** and **11b**, to the least planar analog with the lowest binding affinity, **9c**.

Amyloid Binding Model

A steric zipper pseudofibril of the VQIVYK tau sequence was built as a model in which to rationalize the relative binding affinities of the analogs in Figure 6.1 (see *Materials and Methods*). Two unique channels run along the fibril spine, which we have denoted as the tyrosine and lysine channels, named for the prominent amino acids characterizing the respective channels (see Supporting Information). Eisenberg and coworkers⁸ observed that the negatively charged fluorescence probe Orange-G preferentially bound the electrostatically positive lysine channel, whereas the neutral probes, DDNP and curcumin, preferred the tyrosine channel. The binding preferences were revealed by a registration shift in β -sheet mating in the steric zipper, enlarging either the tyrosine channel, as in the case of DDNP and curcumin, or the lysine channel, as in the case of Orange-G, to facilitate binding. We have only considered binding to the tyrosine channel. The program AutoDock Vina²⁵ was used to flexibly dock all of the molecules in Figure 6.1 to the rigid VQIVYK pseudofibril model. Side chains were kept rigid during the docking in the same

fashion as for Eisenberg and coworkers, because several computational tests showed that the tightly packed environment of the fibril channel does not provide room for side-chain reorganization upon ligand binding. This greatly diminishes the effect that an induced fit would have on ligand binding.

The docking results for each analog recapitulated the multiple binding modes along the fibril spine observed in the X-ray crystallographic density (Figure 6.4A). It is likely that DDNP and its analogs bind to localized sites along the fibril spine, which is suggested by the ability of the nonsteroidal anti-inflammatories (NSAIDs) naproxen and ibuprofen to displace FDDNP from fibrils at low concentrations (5.7 nM and 11 μ M, respectively).²⁶ However, due to the absence of well-resolved crystallographic density in the fibril channel and the lack of easily identifiable anchors on FDDNP and its analogs (such as the negative charges of Orange-G that clearly place it proximal to the lysine residues⁸), it is difficult to exactly delineate the preferred binding mode. Analysis of the binding modes of each analog immediately justifies the little effect that drastic changes at the amine position have on binding affinity. The amine points directly along the spine of the binding channel, so changes in size along this axis can easily be accommodated without introducing steric clashes with the sides of the binding channel (Figure 6.4B). This is most prominently demonstrated by the similarity in binding affinity between **11b**, containing a dimethyl-substituted amine, and **8b**, containing a methylpiperidine ring. It was noted earlier that the large dipole moments of DDNP and its analogs (computed range of 8-12 Debye) could be important in binding. The polar contacts present between the bound probe, tyrosine oxygen atoms (Figure 6.4D and F), and valine N-termini and stabilization of the negative (dicyanovinyl) and positive (amine) ends of the molecule could be significant factors in binding.

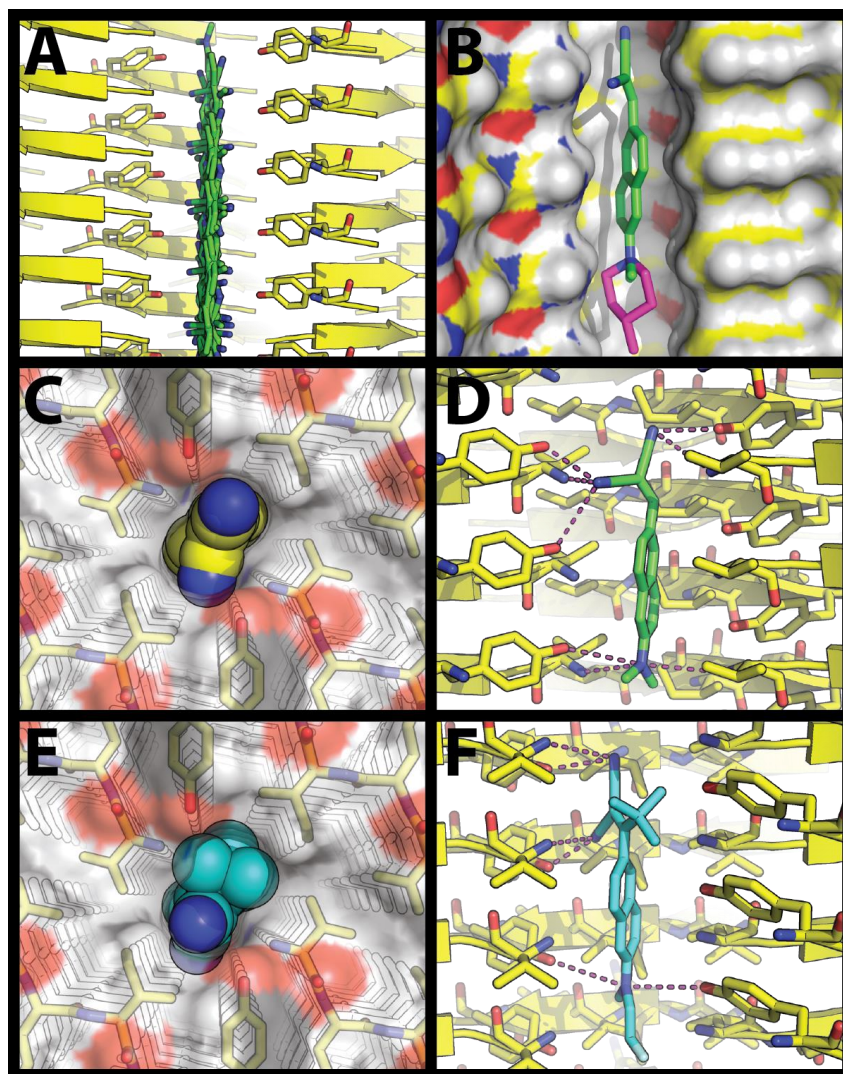


Figure 6.4. (A) Docking of each dicyanovinyl analog from Figure 6.1 yielded a “smear” of poses down the binding channel. (B) The channel accommodates planar molecules of different sizes at the amine position, as shown by the substitution of a methylpiperidine in **8b** for the dimethylamino group in **11b**, which have similar affinities. Differences in binding affinity can be rationalized by the ability of the smaller and more planar analogs, such as **11b** (C and D), to fit within the channel with minimal distortion. Larger and less planar molecules, such as **9c** (E and F), require greater distortion to fit within the pocket. In panels C and E, solid spheres show the atomic radii of the ligand and the transparent surface represents the molecular surface of the protein. Dashed lines represent polar contacts within 3.0 Å between the ligand and pseudofibril.

Analysis of the top ranking poses of each molecule showed that the smaller and more planar molecules (e.g. **11c**, Figure 6.4C and D) better fit the binding channel than the larger molecules (e.g. **9c**, Figure 6.4E and F). Molecules with larger substitutions at the dicyanovinyl position prefer greater degrees of nonplanarity in the free global minimum conformation and, therefore, required more distortion of the ω_{torsion} dihedral to prevent steric clashes of the C6 side chain with the binding channel upon binding. We further examined the magnitude of the ω_{torsion} distortion by performing quantum mechanical/molecular mechanical (QM/MM) optimizations of the docked poses at the M06-2X/6-311+G(d,p):UFF level of theory. The QM region was defined as the ligand, whereas the MM system was defined as the rest of the system and held rigid during the calculation. During the QM/MM optimizations, noticeable differences in the potential energy surfaces between the docking force field and QM/MM were observed. For example, the lowest-energy docked pose of **11b** in the tyrosine channel had a ω_{torsion} value -37.3° and an out-of-plane twisting of the amine group on the naphthalene, whereas after QM/MM optimization, ω_{torsion} decreased to 1.5° and was also accompanied by a planarization of the amine group. The planarization of ω_{torsion} after the QM/MM optimization corresponds to a lower distortion energy on the M06-2X/6-311+G(d,p) potential energy surface (see Supporting Information).

Upon examination of all of the QM/MM optimized complexes, a qualitative trend was found between the energy required to distort ω_{torsion} and the binding affinity of the molecule (Figure 6.5). The constrained DDNP analog **10b** is locked into a near-planar conformation and has the highest binding affinity. Analog **11b**, which has a hydrogen substitution at the dicyanovinyl position, prefers a planar conformation and, correspondingly, also has a high binding affinity. The molecules with a methyl substitution at the dicyanovinyl position, **4b**, **6b**, **8b**, FDDNP, and DDNP, fall within a similar region of the graph. DDNP has 50-fold lower affinity than FDDNP and the other methyl-substituted analogs (10 vs. ~ 0.2 nM). The program QikProp (version 3.0.001w; Schrodinger) was used to compare the molecular properties of these

compounds. DDNP has notably less hydrophobic surface area and thus a lower predicted water/octanol partition coefficient. Similar analysis can also be applied to distinguish the difference in binding affinity between **10b** and **11b**. Both of these molecules require little distortion to fit the binding pocket, yet **11b** has both a lower predicted log(P) value and less hydrophobic contact surface area (SI Appendix). Analog **9c** had the lowest binding affinity but also required significantly more distortion energy to fit the fibril channel than any of the other analogs.

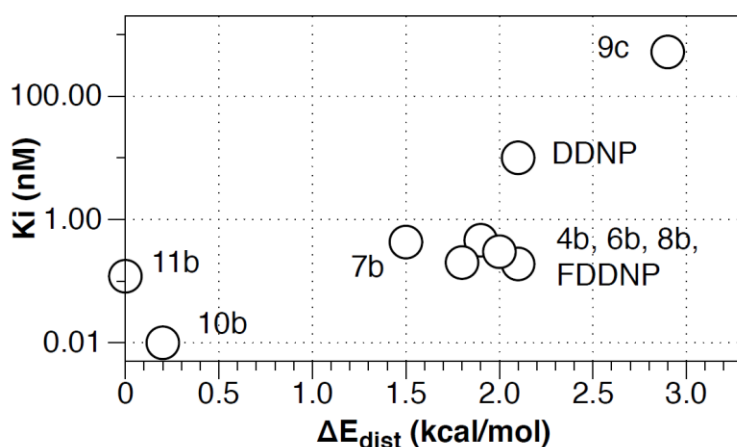


Figure 6.5. Plot of the K_i vs. the energy to distort ω_{torsion} from the global minimum gas-phase conformation to the value in the QM/MM optimized structure.

Conclusions

A series of new FDDNP analogs have been synthesized (Figure 6.1) and characterized using NMR, spectroscopic and computational methods. Two of these molecules, **10b** and **11b**, showed improved affinity to amyloid fibrils over the parent molecule FDDNP. Improved binding affinities are essential for imaging probes to visualize and appropriately quantify amyloid aggregation within the tissue target. Through the use of the steric zipper-binding model for DDNP bound to the VQIVYK segment of tau,⁸ the differences in relative binding affinities of these imaging probes has been attributed to the distortion required for the molecules to fit within the

binding channels that run along the fibril spine. Molecules with larger substitutions at the dicyanovinyl position, such as **9c**, preferred highly nonplanar conformations in solution and required the largest magnitude of distortion to fit within the binding channel. Efforts are underway to (1) modify (lower or increase) the binding affinities to some amyloids (e.g. A β) and (2) provide a differential binding modification between amyloids (e.g. A β and tau aggregates). These modifications could produce imaging probes with selective sensitivity and specificity for different imaging agents. This approach offers a framework for fine-tuning the binding properties of neurofibrillary tau-specific (or A β -specific) imaging probes in parallel with X-ray microcrystallography at atomic resolution in cocrystallization experiments.

Materials and Methods

Syntheses of New Naphthalene Derivatives

In preparing fluorescent compounds **4-11** (Figure 6.1), the 6-acyl-2-naphthols **1-3** were subjected to the Bucherer reaction with open-chain and cyclic amines that are not sensitive to slightly acidic aqueous environment. Aziridine and azetidine rings are too reactive under the Bucherer reaction conditions, and, therefore, the ketones **5** and **6a** were prepared by direct nucleophilic substitution of the methoxy group in (6-methoxy-2-naphthyl)methyl ketone with the respective aziridine and azetidine lithium salts. In the last step of the synthesis, the ketones were subjected to the Knoevenagel reaction with malononitrile to yield the dicyanovinyl naphthalene analogs. Because of high reactivity of the aziridine ring, ketone **5** could not be transformed into the expected product, and decomposition occurred. Naphthaldehyde **11a**, prepared by a modification of a known procedure,²⁷ gave its Knoevenagel product in good yield. Full experimental details for the synthesis and characterization of each molecule are described in the Supporting Information.

QM Structure Calculations

FDDNP analogs from Figure 6.1 with X-ray structures in either the syn or anti conformation were directly optimized to the nearest ground-state minimum using MO6-2X/6-311+G(d,p) in Gaussian09²⁸ with tight convergence. For analogs with a crystal structure of only the syn or anti conformation, the relationship $\omega_{\text{syn}} \approx 180 - \omega_{\text{anti}}$ was used to estimate the starting structure. This relationship held quite well for the optimized structures ($R^2 = 0.99$). For analogs without X-ray structural data, the global minimum conformation was located using a 5,000-step Monte Carlo Multiple Minimum (MCMM) gas-phase conformational search with OPLS2005 performed in MacroModel was used as the starting point. Geometries of the QM-calculated and X-ray structures were superimposed using Maestro giving an average heavy atom RMSD of 0.15 Å (see Supporting Information).

Amyloid Binding Model Construction

The biological unit of the VQIVYK steric zipper was obtained from ref. 8 without DDNP explicitly modeled. The biological unit was duplicated into a 4 x 3 x 8 steric zipper with PyMOL using the crystallographic symmetry information included with the model. This was done in an identical manner as that of Eisenberg and coworkers,⁸ and a superposition of our model to theirs shows they are nearly identical, with corresponding atom–atom deviations of ≤ 0.5 Å. We constructed a larger model to more comprehensively include long-range electrostatics in both the docking and QM/MM simulations.

Molecular Docking and QM/MM Calculations

AutoDock Vina was used to perform the docking simulations²⁵ with the QM-optimized analogs serving as the input ligands. The receptor was prepared for docking using the PyMOL AutoDock plugin.²⁹ Tyrosine and lysine channels located toward the center of the model were

chosen for docking, each with a 12 x 39 x 21 Å rectangular docking region, more than large enough to encompass each entire channel separately. The pseudofibril was held rigid during both docking and QM/MM optimization, because the close packing of the amino acid residues within the channel prevents the side chains from reorganizing upon ligand binding. Individual docking simulations were performed for each channel. Default docking parameters were used for AutoDock Vina, and the top-ranked/lowest-energy docked conformation was used as the best pose. We confirmed that the best pose for each analog was located towards the center of each channel. This pose served as the input to the QM/MM calculations performed in Gaussian09²⁸ at the Mo6-2X/6-311+G(d,p):UFF level of theory.

References

1. Goedert, M.; Spillantini, M. G. A century of Alzheimer's disease. *Science* **2006**, 314, 777-81.
2. Bresjanac, M.; Smid, L. M.; Vovko, T. D.; Petric, A.; Barrio, J. R.; Popovic, M. Molecular-imaging probe 2-(1-[6-[(2-fluoroethyl)(methyl) amino]-2-naphthyl]ethylidene) malonitrile labels prion plaques in vitro. *J Neurosci* **2003**, 23, 8029-33.
3. Jacobson, A.; Petric, A.; Hogenkamp, D.; Sinur, A.; Barrio, J. R. 1,1-dicyano-2-[6-(dimethylamino)naphthalen-2-yl]propene (DDNP): A solvent polarity and viscosity sensitive fluorophore for fluorescence microscopy. *J Am Chem Soc* **1996**, 118, 5572-5579.
4. Liu, J.; Kepe, V.; Zabjek, A.; Petric, A.; Padgett, H. C.; Satyamurthy, N.; Barrio, J. R. High-yield, automated radiosynthesis of 2-(1-{6-[(2-[¹⁸F]fluoroethyl)(methyl)amino]-2-naphthyl}ethylidene)malonitrile ([¹⁸F]FDDNP) ready for animal or human administration. *Mol Imaging Biol* **2007**, 9, 6-16.
5. Small, G. W.; Kepe, V.; Ercoli, L. M.; Siddarth, P.; Bookheimer, S. Y.; Miller, K. J.; Lavretsky, H.; Burggren, A. C.; Cole, G. M.; Vinters, H. V.; Thompson, P. M.; Huang, S. C.; Satyamurthy, N.; Phelps, M. E.; Barrio, J. R. PET of brain amyloid and tau in mild cognitive impairment. *N Engl J Med* **2006**, 355, 2652-63.
6. Shoghi-Jadid, K.; Small, G. W.; Agdeppa, E. D.; Kepe, V.; Ercoli, L. M.; Siddarth, P.; Read, S.; Satyamurthy, N.; Petric, A.; Huang, S. C.; Barrio, J. R. Localization of neurofibrillary tangles and beta-amyloid plaques in the brains of living patients with Alzheimer disease. *Am J Geriatr Psychiatry* **2002**, 10, 24-35.
7. Teplow, D. B. Structural and kinetic features of amyloid beta-protein fibrillogenesis. *Amyloid* **1998**, 5, 121-42.
8. Landau, M.; Sawaya, M. R.; Faull, K. F.; Laganowsky, A.; Jiang, L.; Sievers, S. A.; Liu, J.; Barrio, J. R.; Eisenberg, D. Towards a pharmacophore for amyloid. *PLoS Biol* **2011**, 9, e1001080.
9. Ivanova, M. I.; Thompson, M. J.; Eisenberg, D. A systematic screen of beta(2)-microglobulin and insulin for amyloid-like segments. *Proc. Natl. Acad. Sci.* **2006**, 103, 4079-4082.
10. Gazit, E. Mechanisms of amyloid fibril self-assembly and inhibition. Model short peptides as a key research tool. *FEBS J.* **2005**, 272, 5971-5978.
11. Gazit, E. Mechanistic studies of the process of amyloid fibrils formation by the use of peptide fragments and analogues: Implications for the design of fibrillization inhibitors. *Curr Med Chem* **2002**, 9, 1725-1735.
12. Sievers, S. A.; Karanicolas, J.; Chang, H. W.; Zhao, A.; Jiang, L.; Zirafi, O.; Stevens, J. T.; Münch, J.; Baker, D.; Eisenberg, D. Structure-based design of non-natural amino-acid inhibitors of amyloid fibril formation. *Nature* **2011**, 475, 96-100.

13. Petric, A.; Spes, T.; Barrio, J. R. Novel fluorescent reactive dyes as intermediates for the preparation of UV and Vis wavelength fluorescent probes. *Monatshefte Fur Chemie* **1998**, *129*, 777-786.
14. Petric, A.; Jacobson, A. F.; Barrio, J. R. Functionalization of a viscosity-sensitive fluorophore for probing of biological systems. *Bioorg Med Chem Lett* **1998**, *8*, 1455-60.
15. Selkoe, D. J. Cell Biology of the Amyloid Beta-Protein Precursor and the Mechanism of Alzheimers-Disease. *Annual Review of Cell Biology* **1994**, *10*, 373-403.
16. Agdeppa, E. D.; Kepe, V.; Liu, J.; Flores-Torres, S.; Satyamurthy, N.; Petric, A.; Cole, G. M.; Small, G. W.; Huang, S. C.; Barrio, J. R. Binding Characteristics of Radiofluorinated 6-Dialkylamino-2-Naphthylidenelidene Derivatives as Positron Emission Tomography Imaging Probes for Beta-Amyloid Plaques in Alzheimer's Disease. *J Neurosci* **2001**, *21*.
17. Krasnowska, E.; E, G.; Parasassi, T. Prodan as a membrane surface fluorescence probe: partitioning between water and phospholipid phases. *Biophys J* **1998**, *74*, 1984-93.
18. Petric, A.; Barrio, J. R. Synthesis and NMR Characterization of 4-[(2-Tetrahydrophyranyloxy)-methyl]piperidine and Intermediates. *J Hetero Chem* **1994**, *31*, 545-548.
19. Bures, F.; Schweizer, W. B.; May, J. C.; Boudon, C.; Gisselbrecht, J.-P.; Gross, M.; Biaggio, I.; Diederich, F. Property Tuning in Charge-Transfer Chromophores by Systematic Modulation of the Spacer between Donor and Acceptor. *Chem Eur J* **2007**, *13*, 5378-5387.
20. Reichardt, C. 3rd ed.; Wiley-VCH Verlag GmbH & Co: Weinheim, 2003.
21. Volchkov, V.; Uzhinov, B. Structural relaxation of excited molecules of heteroaromatic compounds. *High Energy Chemistry* **2008**, *42*, 153-169.
22. Bansal, R. K. *Heterocyclic Chemistry*. New Age International: New Delhi, 1999.
23. Bartnik, R.; Faure, R.; Gebicki, K. Synthesis and crystal structure of 1-acetyl-3-bromo-3-phenylazetidene and 1-phenyl-2-(N-acetyl-N-formyl)-aminoethanone. *Journal of Chemical Crystallography* **1998**, *28*, 119-123.
24. Skofic, P.; Dambrot, C.; Kozelj, M.; Golobic, A.; Barrio, J. R.; Petric, A. Syntheses of 4-(2-Naphthyl)pyridine Derivatives from DDNP. *Acta Chim Slov* **2005**, *52*, 391-97.
25. Trott, O.; Olson, A. J. AutoDock Vina: improving the speed and accuracy of docking with a new scoring function, efficient optimization, and multithreading. *J Comput Chem* **2010**, *31*, 455-61.
26. Agdeppa, E. D.; Kepe, V.; Petric, A.; Satyamurthy, N.; Liu, J.; Huang, S. C.; Small, G. W.; Cole, G. M.; Barrio, J. R. In vitro detection of (S)-naproxen and ibuprofen binding to plaques in the Alzheimer's brain using the positron emission tomography molecular imaging probe 2-(1-{6-[(2-[¹⁸F]fluoroethyl)(methyl)amino]-2-naphthyl}ethylidene)-malononitrile. *Neuroscience* **2003**, *117*, 723-30.

27. Umezawa, H.; Tsuji, K.; Duan, X.; Okada, S.; Oikawa, H.; Matsuda, H.; Nakanishi, H. Synthesis of Stilbazolium Derivatives Having 2-(6-Dimethyl amino)naphthyl Group for Nonlinear optics. *MCLC S&T, Section B: Nonlinear Optics* **2000**, *22*, 251-254.
28. Frisch, M. J., et al. Gaussian 09 Revision B.01, Gaussian, Wallingford CT, 2009.
29. Seeliger, D.; de Groot, B. L. Ligand docking and binding site analysis with PyMOL and Autodock/Vina. *J Comput Aided Mol Des* **2010**, *24*, 417-422.

Chapter 7. Synthesis of the Tetracyclic Core of Exiguaquinol

The structurally novel pentacyclic compound exiguaquinol (**1**) was isolated by Quinn *et al.* from the Australian sponge *Neopetrosia exigua* and reported in 2008.¹ High-throughput screening of natural product extracts against the *Helicobacter pylori* MurI enzyme—a glutamate racemase enzyme that is essential for bacterial cell wall biosynthesis—led to the identification of **1** as the first natural product inhibitor of this enzyme. As a result, exiguaquinol might serve as an excellent lead compound for the development of more potent inhibitors of MurI and ultimately selective antibiotics against *H. pylori*.¹ With its complex and congested structure, the important link of *H. pylori*-induced gastritis to stomach cancer,² and the more general implications of MurI as a potential target for the development of new antibiotics, a research program aimed at the synthesis of this complex natural product was warranted on both chemical and biological grounds.

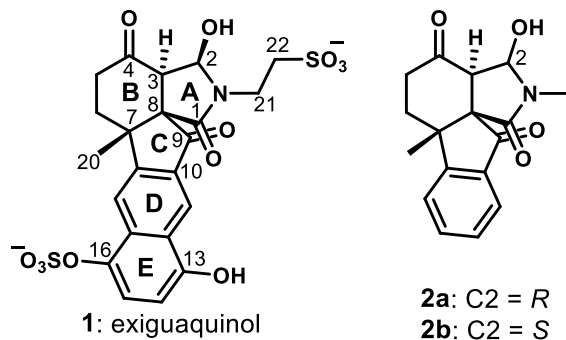
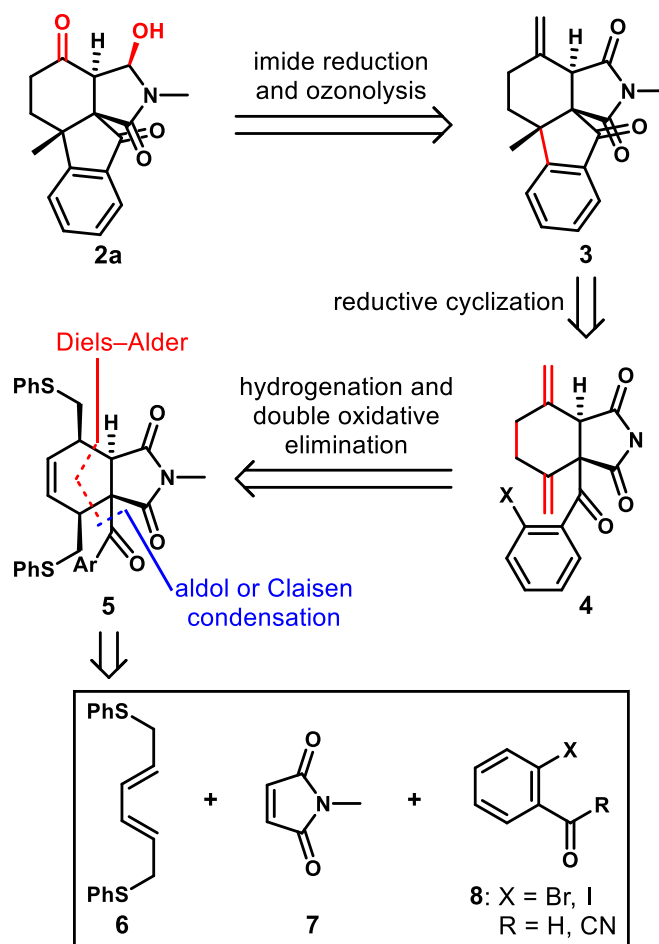


Figure 7.1. Exiguaquinol and tetracyclic model system hemiaminal diastereomers.

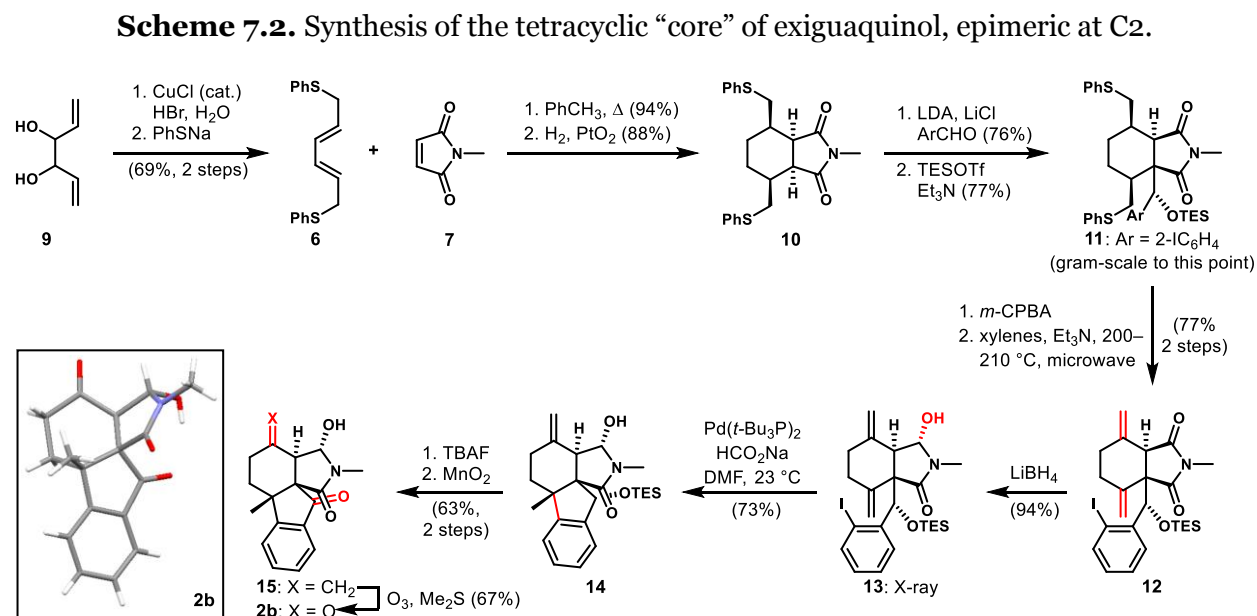
In addition to its biological activity, exiguaquinol (**1**) bears complex structural features that make it a worthwhile synthetic target. With five fused rings, four contiguous stereogenic centers (two vicinal quaternary), an aryl sulfate, and a pendant sulfonate, a laboratory synthesis of this compound presents significant difficulty. To address the stereochemical challenges, we aimed to develop a synthesis of the tetracyclic core (**2**) as a model system, with the stipulation

that any such strategy be amenable to a synthesis of the natural product and structural analogs. Our retrosynthetic plan is illustrated in Scheme 7.1, wherein the exiguquinol core (**2a**) is derived from tetracycle **3** via simple functional group manipulations. The C ring, with its vicinal quaternary stereogenic centers,³ would be forged through a reductive 5-*exo* cyclization of aryl halide **4**. Key fused bicyclic intermediate **5** might be formed from three simple starting materials via a Diels–Alder reaction of **6** and **7** followed by an aldol addition or Claisen condensation, depending on the oxidation state of **8** used.

Scheme 7.1. Synthesis plan to access tetracycle **2a** bearing all of the stereochemical complexity of exiguquinol.



Diene **6** was synthesized on a multi-gram scale in two steps from divinyl glycol **9**, the commercially available pinacol coupling product of acrolein⁴ (Scheme 7.2). Bromination of **9** with allylic transposition⁵ afforded a dienyl dibromide intermediate, which underwent smooth nucleophilic displacement with sodium thiophenolate to afford **6**.⁶ Thermal [4+2] cycloaddition between diene **6** and *N*-methylmaleimide afforded the Diels–Alder adduct in high yield and subsequent reduction with PtO₂ under H₂ pressure led to bicyclic compound **10**. Desymmetrizing aldol addition with *ortho*-iodobenzaldehyde led to a single diastereomer of the benzylic alcohol product, which was silylated to afford **11** in good yield. The inclusion of LiCl⁷ during enolate formation was critical to reproducible reactions, especially on multi-gram scale. Oxidation of the sulfides followed by thermal sulfoxide elimination generated desired diene **12** without complication.



The completion of the synthesis of the tetracyclic model system required a careful orchestration of the final steps. Selective mono-reduction of succinimide **12** with LiBH₄ yielded

hemiaminal **13** as a single diastereomer in high yield. X-ray crystal structure analysis indicated that the hemiaminal was epimeric to that found in the natural product. Reductive Heck cyclization⁸ of **13** provided tetracyclic product **14** in good yield, demonstrating the power (and functional group compatibility) of this catalytic alternative to reductive, tin-based radical cyclizations in complex settings. Deprotection with TBAF and selective oxidation of the benzylic alcohol in the presence of the hemiaminal afforded indanone **15**. Ozonolysis delivered tetracyclic diketone **2b**, which remained epimeric at C2 as confirmed by X-ray crystal structure. Attempts to epimerize the hemiaminal to the “natural” *R*-configuration under acidic or basic conditions proved unsuccessful.⁹

Tetracycle **2b**, with its close structural relationship to exiguaquinol, does not offer any obvious rationale for the difference in configuration at a center that seemed certain to be under thermodynamic control. This quandary led to consideration of a number of hypotheses, including the remote possibility of a misassignment of relative configuration in the natural product. However, the spectroscopic data were fully consistent with the proposed structure; therefore, we considered the possibility that the absence of the sulfonate in simplified system **2b** might lead it to adopt a different thermodynamic hemiaminal configuration. It seemed prudent to computationally model all of the different hydrogen-bonding options in both the model system and the natural product.

Gas-phase ground-state calculations on both epimeric forms of tetracycle **2** (Figure 7.2) revealed that the observed *S*-epimer of the core **2b** is thermodynamically more stable by 4.6 kcal/mol than that with the configuration corresponding to the natural product (**2a**). The lowest energy conformation of the experimentally observed *S*-configured epimer **2b** benefits from hydrogen bonding of the hemiaminal hydroxyl group with the C9 indanone carbonyl; a conformation wherein it is hydrogen bonded to the C4 ketone (not shown) is of significantly

higher energy. The lowest energy conformation of *R*-configured epimer **2a** is also shown; in this configuration, the hemiaminal hydroxyl group is only able to hydrogen bond to the C4 ketone.

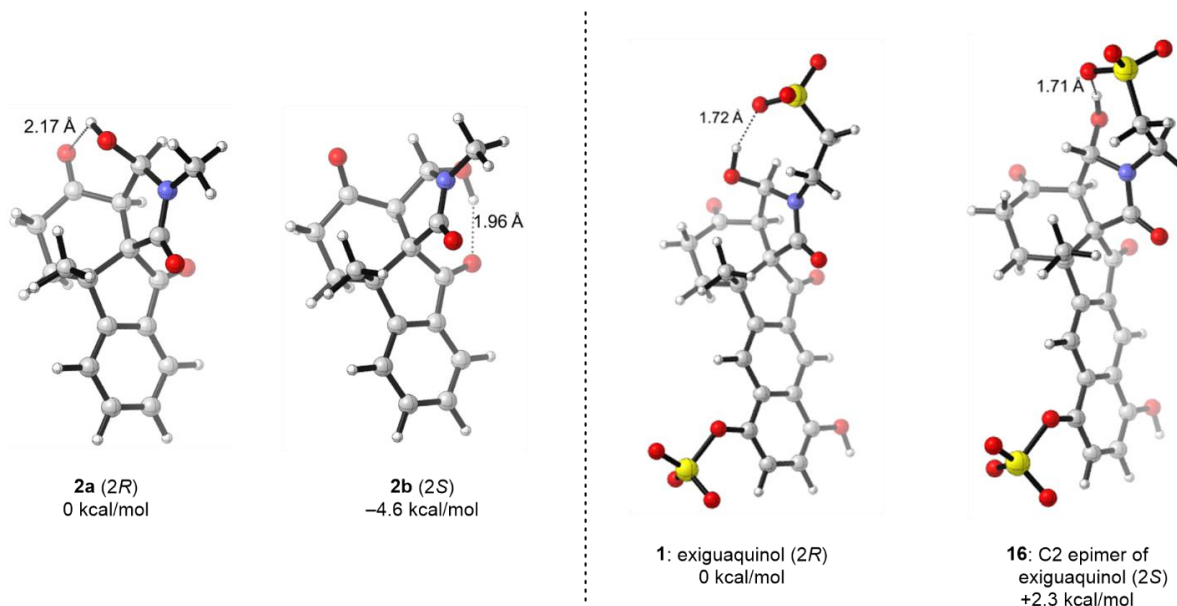


Figure 7.2. Computed relative free energies of the hemiaminal epimers of the tetracyclic “core” (**2a** and **2b**) and exiguaquinol (**1** and **16**). Calculations performed at the B3LYP/6-31G(d) level of theory in the gas phase.

Not surprisingly, calculations of the exiguaquinol hemiaminal epimers suggest that the lowest energy conformation of the natural *R*-epimer (**1**) is thermodynamically preferred by 2.3 kcal/mol over the most stable conformer of the *S*-isomer (**16**). As we had predicted, the sulfonate appears to be the root cause of the difference between **2** and exiguaquinol, because it is apparently involved in hydrogen-bonding with the hemiaminal in the lowest energy conformations of both epimers, with the natural configuration’s conformation preferred by 2.3 kcal/mol. It is plausible that anomeric stabilization (good overlap of amide π system with C–O σ^* orbital) contributes to the preference for the natural configuration; this arrangement is not observed in **16**. For both epimers of exiguaquinol, the other hydrogen-bonded possibilities were also evaluated (for the *R*-

epimer with the C4 carbonyl and for the *S*-epimer with both the C4 and C9 carbonyls); each of these was at least 7.5 kcal/mol higher in energy than the sulfonate–hemiaminal hydrogen-bonded conformer of the natural product.¹⁰ That all of the calculations were performed in the gas phase does leave the possibility that solvation could lead to a different outcome; however, X-ray crystallography, solution NMR (CDCl₃), and computation all demonstrate that the *S*-configuration of the tetracyclic core is preferred, with the crystal structure revealing the same hydrogen bond to the indanone carbonyl. Also, in NMR studies of exiguaquinol performed in DMSO by the Quinn group, the *R*-configured hemiaminal was the only one observed.¹

We did not anticipate the stability of conformations involving hydrogen-bonding between the hemiaminal and the sulfonate via eight-membered rings, particularly relative to the six-membered arrangement involving the C4 ketone favored by **2b**. This phenomenon likely results from the ability of the hydrogen bond to partially offset some of the discrete charge of the sulfonate. Regardless of its physical basis, this bonding pattern might play a key role in determining the active configuration and conformation of exiguaquinol.

Via a short sequence of 13 steps, we have accessed a tetracycle bearing many of the features of exiguaquinol. In particular, this approach addresses the stereocontrolled introduction of three contiguous stereogenic centers, including two adjacent quaternary centers. The fourth asymmetric center—the hemiaminal C2—is generated with the unnatural *S*-configuration; however, computation strongly suggests that our synthesis plan will deliver the desired *R*-configured hemiaminal when applied to fully elaborated substrates. Interesting hydrogen-bonding effects between the two epimers in the model series as well as the natural product appear to define the thermodynamic preference at this center, and point to the complexity of potential interactions of exiguaquinol's array of polar groups.

A triply convergent approach featuring a Diels–Alder cycloaddition and an aldol reaction, followed by a reductive Heck cyclization, rapidly assembles the tetracyclic core with high

diastereocontrol, but in a racemic manner. This modular strategy will allow for the convenient introduction of the extended aromatic and taurine moieties of the natural product, and chiral base technology^{11,12} will facilitate access to optically active material by enantioselective desymmetrizing aldol additions. Efforts to apply this route to enantioenriched exiguaquinol and analogs are underway to permit identification of a more potent inhibitor of the *H. pylori* MurI enzyme.

References

1. Almeida Leone, P.; Carroll, A. R.; Towerzey, L.; King, G.; McArdle, B. M.; Kern, G.; Fisher, S.; Hooper, N. A.; Quinn, R. J. *Org. Lett.* **2008**, *10*, 2585–2588.
2. Polk, D. B.; Peek, R. M. Jr. *Nature Rev. Cancer* **2010**, *10*, 403–414.
3. Peterson, E. A.; Overman, L. E. *Proc. Natl. Acad. U.S.A.* **2004**, *101*, 11943–11948.
4. For a modern procedure, see: Trost, B. M.; Aponick, A. *J. Am. Chem. Soc.* **2006**, *128*, 3931–3933.
5. Schneider, G.; Horvath, T.; Sohár, P. *Carbohydrate Res.* **1977**, *56*, 43–52.
6. Kauffmann, T.; Gaydoul, K.-R. *Tetrahedron Lett.* **1985**, *26*, 4067–4070.
7. For a review on lithium enolate structure and reactivity, including discussions on the remarkable effects of additives such as LiCl, see: (a) Seebach, D. *Angew. Chem. Int. Ed.* **1988**, *27*, 1624–1654. See also (b) Henderson, K. W.; Dorigo, A. E.; Liu, Q.-Y.; Williard, P. G.; von Ragué Schleyer, P.; Bernstein, P. R. *J. Am. Chem. Soc.* **1996**, *118*, 1339–1347.
8. Link, J. T. *Org. React.* **2002**, *60*, 157–534.
9. *O*-Silylation of the hemiaminal in **2b** did not change the configuration at C2, in spite of the elimination of the proposed stabilizing hydrogen bond; however, silylation is likely to be kinetically controlled.
10. Please see the Supporting Information in the original publication for details.
11. O'Brien, P. *J. Chem. Soc., Perkin Trans. 1* **1998**, 1439–1457.
12. For a particularly relevant desymmetrization employing chiral amide bases, see: Simpkins, N. S.; Gill, C. D. *Org. Lett.* **2003**, *5*, 535–537.

Chapter 8. Palladium Hydride-Promoted Stereoselective Isomerization of Unactivated Di(exo)methylenes to Endocyclic Dienes

The isomerization of alkenes using catalytic amounts of transition metals and their complexes has been widely studied.¹ For example, allyl units bearing heteroatoms, e.g., allylic amines, alcohols, and ethers, can be easily converted to their propenyl isomers.² Allyl arenes can likewise be transformed into the alkylstyrene isomers.³ One can also effect an equilibration between *E* and *Z* alkene isomers.⁴ However, there has been little research on the isomerization of unfunctionalized alkenes. Of the few accounts reported, many use large transition metal complexes, numerous additives, high temperatures and long reaction times.⁵ For the synthesis of rugulosone, **1** (Figure 8.1),⁶ we required a simple protocol to prepare the bicyclo[3.3.1]nonadiene core and investigated the isomerization of a symmetric di(exo)methylene to the endocyclic diene. We tested this process on the simple analogue, 1,5-dimethyl-3,7-dimethylenebicyclo[3.3.1]nonan-9-one **2a**. The required dienone **2a** was prepared in one step by the tetraalkylation of 3-pentanone with 1-chloro-2-(chloromethyl)-2-propene. We report here the successful isomerization of this diene **2a** to the desired C₂-symmetric bicyclo[3.3.1]nonadienone **3a** and the isomerization of related analogues.

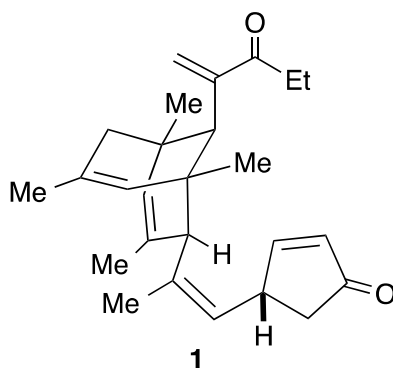
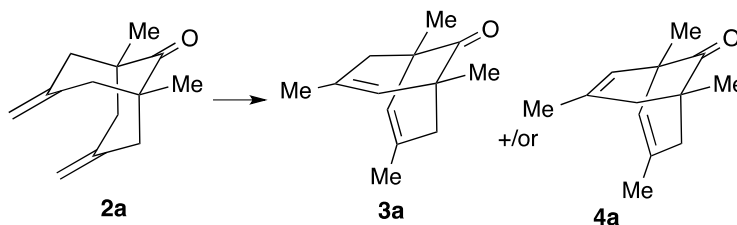


Figure 8.1. Structure of rugulosone.

The double rearrangement of this substrate **2a** to the C₂ isomer **3a** rather than the C_S isomer **4a** (Scheme 8.1) would be required to give the natural product. We believed that **3a** would be more stable than **4a** due to the steric nonbonded interaction of the indicated hydrogens in **4a** (Figure 8.2).

Scheme 8.1. Isomerization of **2a** to give **3a** and/or **4a**.



Initial attempts to directly isomerize diene **2a** with transition-metal catalysts such as Wilkinson's or Crabtree's catalyst failed to yield either **3a** or **4a**; only starting material was recovered (Scheme 8.2). The uniquely strained and/or hindered structure of the bicyclic core may cause this lack of reactivity. Unable to directly isomerize the olefins, we examined a longer, more complicated process. Epoxidation of **2a** (DMDO, 23 °C, 3h) afforded the diepoxide **5** in 71% yield. All attempts at acid- or base-promoted ring-opening of these epoxides to give allylic alcohols failed, as did attempts to prepare the tertiary alcohols through various hydride reductions.

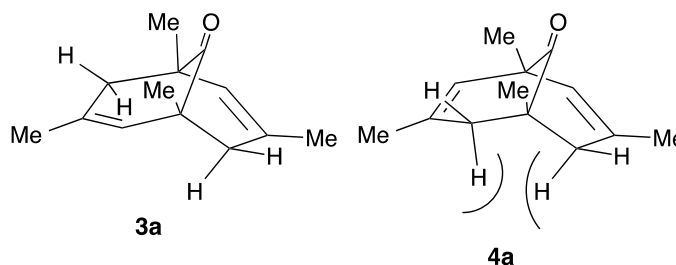
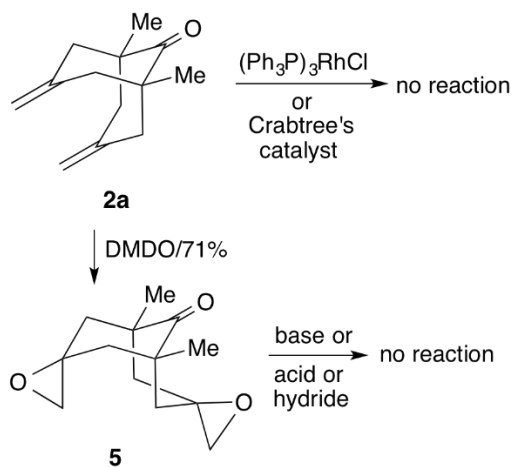


Figure 8.2. Structures of the C₂ and C_S dienes.

The desired isomerization was, however, effected by the use of an activated palladium catalyst mixed with hydrogen gas. Thus, treatment of **2a** in methanol with 4 mol% Pd/C under a balloon of hydrogen afforded the desired C₂ isomer **3a** along with the monoreduced isomerized product **6a** and the fully reduced material **7a** in a 68:28:4 ratio (by GCMS) (Scheme 8.3). A number of control experiments were conducted to demonstrate that hydrogen was required for this isomerization. The use of an argon atmosphere instead of hydrogen afforded no isomerization. Pretreating the catalyst with hydrogen gas to activate the palladium and then purging the flask with argon gave no isomerization. The addition of excess cyclohexene (to remove all the H₂ gas) before the addition of **2a** was also unsuccessful. The use of ammonium formate (transfer hydrogenation) also produced the expected isomerization. Thus, it seems that the reaction requires a small amount of hydrogen to initiate the isomerization.⁷

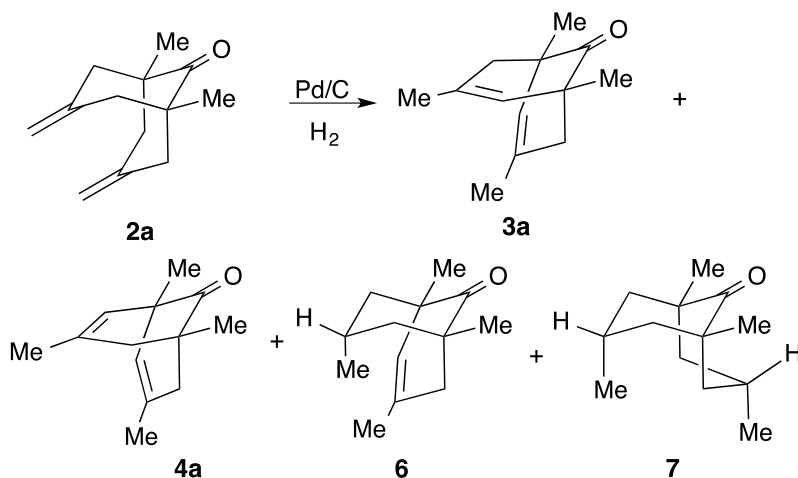
Scheme 8.2. Attempts to isomerize **2a**.



We postulated that alkene isomerization might be favored over reduction if the hydrogenation pathway could be slowed down, perhaps by a change in the solvent, since solvent effects on hydrogenation rates have been well studied.⁸ For that reason, various solvent systems were examined to see if solvent effects could improve the yield of isomerization (Table 8.1). Polar,

protic solvents, such as methanol and 2-propanol, gave large amounts of the monoreduced product **6a** and some of the fully reduced material **7a**. Reaction in ethyl acetate gave the desired C₂ product **3a** along with the first observation of the formation of the C_s isomer **4a** and the monoreduced product **6a**. Isomerization in other nonpolar solvents, e.g., hexane, gave similar results. Other aprotic polar solvents, e.g., acetone, dioxane and THF, also largely produced the desired C₂ product **3a** along with small amounts of the C_s isomer **4a** and the monoreduced compound **6a**.

Scheme 8.3. Isomerization of **2a** to give **3a** and other products.



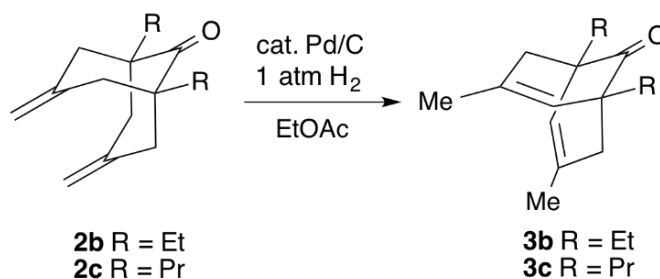
We explored whether the isomerization to the C₂ isomer in great preference to the C_s isomer was general. The additional di(exo)methylene compounds, **2b-c**, were prepared from the corresponding substituted ketones and the bis(chloromethyl)-ethylene. Treatment of both **2b** and **2c** under the conditions described above, namely Pd/C under an atmosphere of hydrogen gas, afforded predominately the C₂ products **3b** and **3c** in preference to the possible C_s product (Scheme 8.4). However, the diphenyl-substituted analogue gave only starting material under these conditions with no production of any isomeric or reduction products. Thus, this preference

for the C₂ product **3** rather than the C₅ product **4** occurs for all alkyl substituents at the bridgehead carbons.

Table 8.1. Effect of solvents on conversion of **2a** to **3a**, **4a**, **6a**, and **7a**.

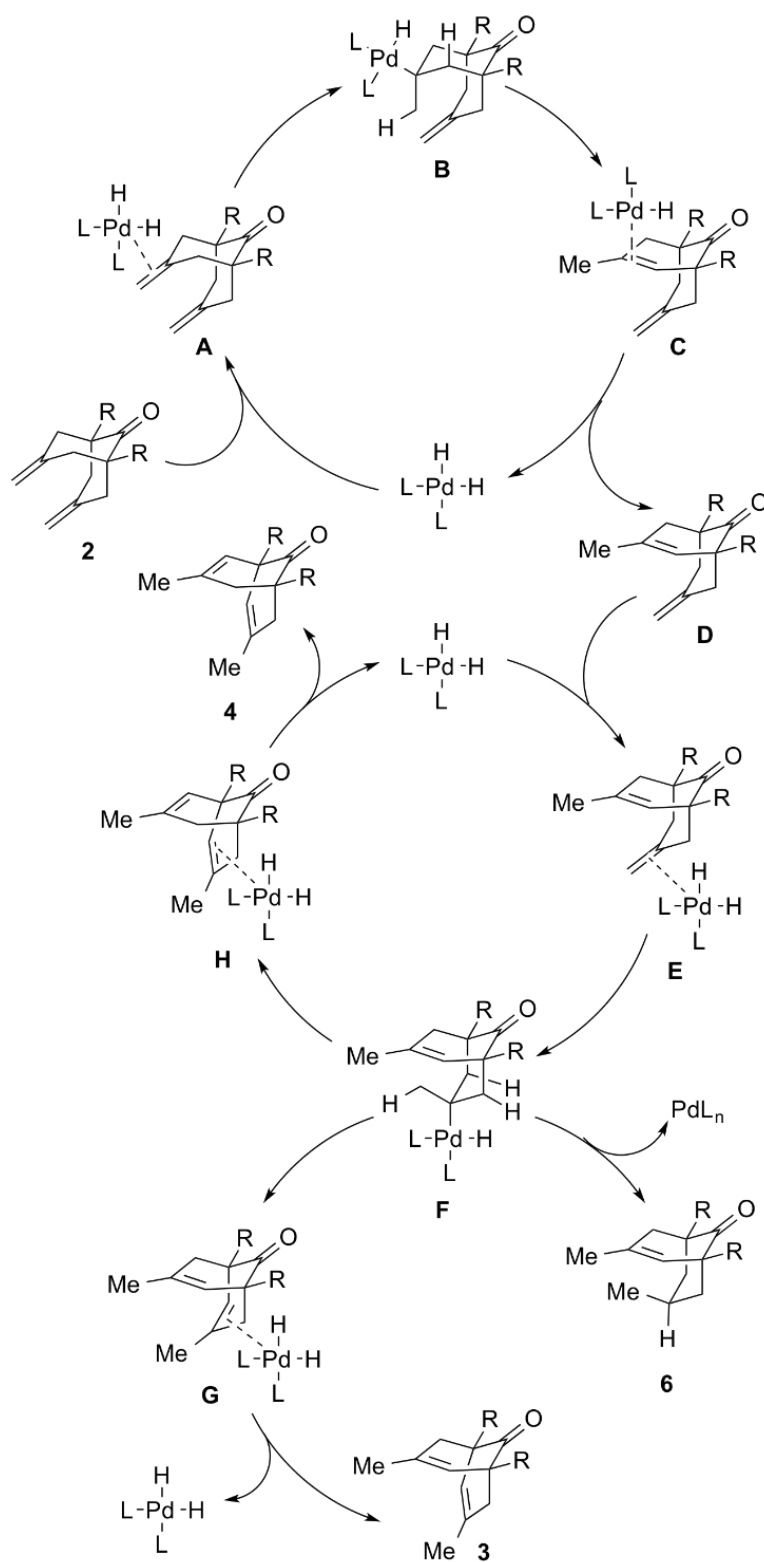
entry	solvent	time (h)	3a	4a	6a	7a	2a
1	MeOH	1	68	0	28	4	0
2	iPrOH	1	68	0	26	6	0
3	EtOAc	1	87	9	4	0	0
4	hexane	1	81	7	12	0	0
5	acetone	1	79	6	14	0	0
6	dioxane	1	64	6	11	0	19
7	THF	1	77	9	13	0	1

Scheme 8.4. Isomerization of alkenes **2bc**.



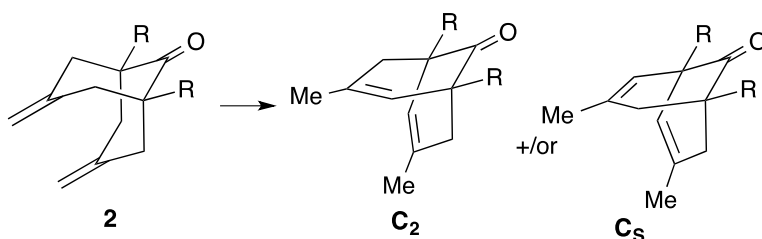
The proposed mechanism is shown in Scheme 8.5. Coordination of the di(exo)methylene **2** with palladium to give **A**, hydride addition to form **B**, β -hydride elimination to afford **C**, and then decomplexation converts **2** to the monoisomerized product **D**, which has never been observed. The same type of process can convert **D**, via the intermediates **E–H**, to either the C₂ isomer **3** or the C₅ isomer **4** and can interconvert these isomers as well. All processes are reversible, and the product ratio is most likely determined by thermodynamic stabilities.⁹

Scheme 8.5. Proposed Mechanism for the Isomerization of **2**.



In order to establish the energies of each of the isomers, we calculated the structure and energies of reactants, the monoisomerized species, and the isomeric di-isomerized species with density functional theory. Using Gaussian 09,¹⁰ optimizations were performed using B3LYP/6-31G(d),¹¹ followed by Mo6-2X/6-311+G(d,p) single-point calculations to account properly for dispersion effects.¹² The results are shown in Table 8.2. The parent unsubstituted system **2** (R = H) shows a 2.9 kcal/mol preference for the C₂ isomer over the C_s diene. All of the trisubstituted alkenes were significantly more stable than the disubstituted alkene starting materials. Methyl and larger alkyl substituents at the bridgehead carbons led to a greater preference for the C₂ isomer. This is in good agreement with the fact that under all conditions the C₂ diene **3** is the predominant product.

Table 8.2. Free Energy Calculations for Isomers.^a



R	Exo (SM)	C ₂	C _s	Difference
H	0.0	-8.0	-5.1	2.9
Me	0.0	-7.1	-3.8	3.3
Et	0.0	-9.0	-5.2	3.8
Pr	0.0	-8.7	-4.6	4.1
Ph	0.0	-9.2	-6.4	2.8

^a Gas phase calculations were carried out using Mo6-2X/6-311+G(d,p)//B3LYP/6-31G(d) and are quoted in kcal/mol.

We set out to investigate the source of the preference for the C₂ isomer. As mentioned before, the examination of molecular models revealed a possible unfavorable steric interaction

involving the two allylic hydrogen atoms in **4a** as shown in Figure 8.2. Inspection of the optimized geometries reveals that, although the decrease in H—H distance correlates well with an increase in stability across the isomers (Figure 8.3), a 2.28 Å distance is not sufficient to conclude that the 3–4 kcal/mol thermodynamic preference is dominated by steric repulsion. Interestingly, a twisting of the bicyclo[3.3.1]nonadienone core in **3a**, which is not observed in the less stable **4a**, points towards ring strain induced by nonbonding interactions as being another component of the energy difference. This slight rotation relieves some of the unfavorable eclipsing interactions and translates to an increase in the endo hydrogen distance.

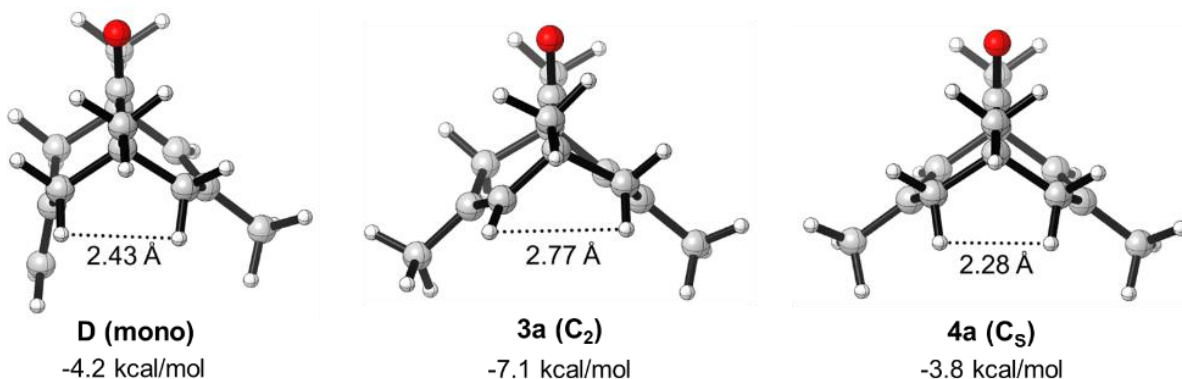


Figure 8.3. Monoisomerized and C₂ and C_s bis-isomerized optimized structures. Free energies calculated using Mo6-2X/6-311+G(d,p)//B3LYP/6-31G(d) are relative to **2a**.

In summary, the facile isomerization of the di(exo)methylene bicyclo[3.3.1]nonanone systems gives rise predominantly to the C₂ products rather than the possible C_s products. Theoretical calculations reveal that the origin of this preference stems from thermodynamic effects, involving transannular hydrogen—hydrogen interactions and ring strain induced by these interactions. Further calculations and the use of this procedure in the synthesis of rugulosone **1** are currently underway and will be reported in due course.

References

1. (a) Davies, S. G. *Organotransition Metal Chemistry. Applications to Organic Synthesis*; Pergamon Press: Oxford, 1982; pp 266–290. (b) Colquhoun, H. M.; Holton, J.; Thompson, D. J.; Twigg, M. V. *Isomerization of Alkenes. In New Pathways for Organic Synthesis*; Springer: New York, 1984; pp 173–193. (c) Casey, C. P.; Cyr, C. R. *J. Am. Chem. Soc.* **1973**, *95*, 2248.
2. (a) Whitesell, J. K. *Carbonyl Group Derivatization. In Comprehensive Organic Synthesis*; Trost, B. M., Fleming, I., Eds.; Pergamon Press: Oxford, 1991; Vol. 6, Chapter 4.1, pp 703–732. (b) Inoue, S.; Takaya, H.; Tani, K.; Otsuka, S.; Sato, T.; Noyori, R. *J. Am. Chem. Soc.* **1990**, *112*, 4897. (c) Otsuka, S.; Tani, K. *Synthesis* **1991**, 665. (d) Corey, E. J.; Suggs, J. W. *J. Org. Chem.* **1973**, *38*, 3224. (e) Cherkaoui, H.; Soufiaoui, M.; Gré'e, R. *Tetrahedron* **2001**, *57*, 2379. (f) Tanaka, K.; Fu, G. C. *J. Org. Chem.* **2001**, *66*, 8177.
3. (a) Danishefsky, S.; Uang, B. J.; Quallich, G. *J. Am. Chem. Soc.* **1985**, *107*, 1285. (b) Larsen, C. R.; Grotjahn, D. B. *J. Am. Chem. Soc.* **2012**, *134*, 10357; (Correction) **2012**, *134*, 15604. (c) Larsen, C. R.; Erdogen, G.; Grotjahn, D. B. *J. Am. Chem. Soc.* **2014**, *136*, 1226.
4. (a) Moses, J. E.; Baldwin, J. E.; Marquez, R.; Adlington, R. M.; Cowley, A. R. *Org. Lett.* **2002**, *4*, 3731. (b) Tan, E. H. P.; Lloyd-Jones, G. C.; Harvey, J. N.; Lennox, A. J. J.; Mills, B. M. *Angew. Chem., Int. Ed.* **2011**, *50*, 9602. (c) Chen, C.; Dugan, T. R.; Brennessel, W. W.; Weix, D. J.; Holland, P. L. *J. Am. Chem. Soc.* **2014**, *136*, 945.
5. (a) Tkach, V. S.; Suslov, D. S.; Gomboogin, M.; Ratovskii, G. V.; Shmidt, F. K. *Russ. J. Appl. Chem.* **2006**, *79*, 85. (b) Lim, H. J.; Smith, C. R.; RajanBabu, T. V. *J. Org. Chem.* **2009**, *74*, 4565. (c) Gauthier, D.; Lindhardt, A. T.; Olsen, E. P. K.; Overgaard, J.; Skrydstrup, T. *J. Am. Chem. Soc.* **2010**, *132*, 7998. (d) Mayer, M.; Welther, A.; von Wangelin, A. *J. ChemCatChem.* **2011**, *3*, 1567.
6. Moosophon, P.; Kanokmedhakul, S.; Kanokmedhakul, K.; Soyong, K. *J. Nat. Prod.* **2009**, *72*, 1442.
7. Shibuya, M.; Tomizawa, M.; Suzuki, I.; Iwabuchi, Y. *J. Am. Chem. Soc.* **2006**, *128*, 8412. See the Supporting Information (p. S12) of the original publication.
8. (a) Rajadhyaksha, R. A.; Karwa, S. L. *Chem. Eng. Sci.* **1986**, *41*, 1765. (b) Gamez, A.; Kóhler, J. U.; Bradley, J. S. *Catal. Lett.* **1998**, *55*, 73. (c) Martin, G.; Mañki-Arvela, P.; Murzin, D. Y.; Salmi, T. *Catal. Lett.* **2013**, *143*, 1051. (d) Bertero, N. M.; Trasarti, A. F.; Apesteguía, C. R.; Marchi, A. *J. Appl. Catal., A* **2011**, *394*, 228.
9. The opposite regiochemical addition of the palladium hydride species to the exomethylene unit of **2** would lead directly to a monoreduced product with no alkene isomerization.
10. Gaussian 09, Revision D.01: Frisch, M. J.; Trucks, G. W.; Schlegel, H. B.; Scuseria, G. E.; Robb, M. A.; Cheeseman, J. R.; Scalmani, G.; Barone, V.; Mennucci, B.; Petersson, G. A.; Nakatsuji, H.; Caricato, M.; Li, X.; Hratchian, H. P.; Izmaylov, A. F.; Bloino, J.; Zheng, G.; Sonnenberg, J. L.; Hada, M.; Ehara, M.; Toyota, K.; Fukuda, R.; Hasegawa, J.; Ishida, M.;

Nakajima, T.; Honda, Y.; Kitao, O.; Nakai, H.; Vreven, T.; Montgomery, J. A., Jr.; Peralta, J. E.; Ogliaro, F.; Bearpark, M.; Heyd, J. J.; Brothers, E.; Kudin, K. N.; Staroverov, V. N.; Kobayashi, R.; Normand, J.; Raghavachari, K.; Rendell, A.; Burant, J. C.; Iyengar, S. S.; Tomasi, J.; Cossi, M.; Rega, N.; Millam, N. J.; Klene, M.; Knox, J. E.; Cross, J. B.; Bakken, V.; Adamo, C.; Jaramillo, J.; Gomperts, R.; Stratmann, R. E.; Yazyev, O.; Austin, A. J.; Cammi, R.; Pomelli, C.; Ochterski, J. W.; Martin, R. L.; Morokuma, K.; Zakrzewski, V. G.; Voth, G. A.; Salvador, P.; Dannenberg, J. J.; Dapprich, S.; Daniels, A. D.; Farkas, O.; Foresman, J. B.; Ortiz, J. V.; Cioslowski, J.; Fox, D. J. Gaussian, Inc.: Wallingford, CT, 2009.

11. (a) Lee, C.; Yang, W.; Parr, R. G. *Phys. Rev. B* **1988**, *37*, 785. (b) Becke, A. D. *J. Chem. Phys.* **1993**, *98*, 5648. (c) Parr, R. G. *Annu. Rev. Phys. Chem.* **1995**, *46*, 701.
12. (a) Zhao, Y.; Truhlar, D. G. *Acc. Chem. Res.* **2008**, *41*, 157. (b) Zhao, Y.; Truhlar, D. G. *J. Phys. Chem. A* **2008**, *112*, 1095.

Chapter 9. Thermodynamics of Guest Exchange in Self-Folding Cavitands

Since Cram's discovery of supramolecular compounds in the early 1980s,^{1,2} the field of host–guest chemistry has been a quickly developing area of study. Cram defined several terms to describe the binding properties of newly created container molecules, one of which was a *cavitand*, a container-shaped molecule with a cavity capable of encapsulating a guest of complementary shape and size. Two types of binding, constrictive binding and intrinsic binding, were introduced to characterize different binding properties. Shown in the energy diagram in Figure 9.1, constrictive binding refers to the activation energy of the binding process, while intrinsic binding takes into account the free energy difference between the complex and the free host and guest molecules.³ Stronger (more negative) intrinsic binding results in more stable host–guest complexation. The intrinsic binding in host–guest complexes can be considered to arise from the aggregation of multiple noncovalent interactions.⁴

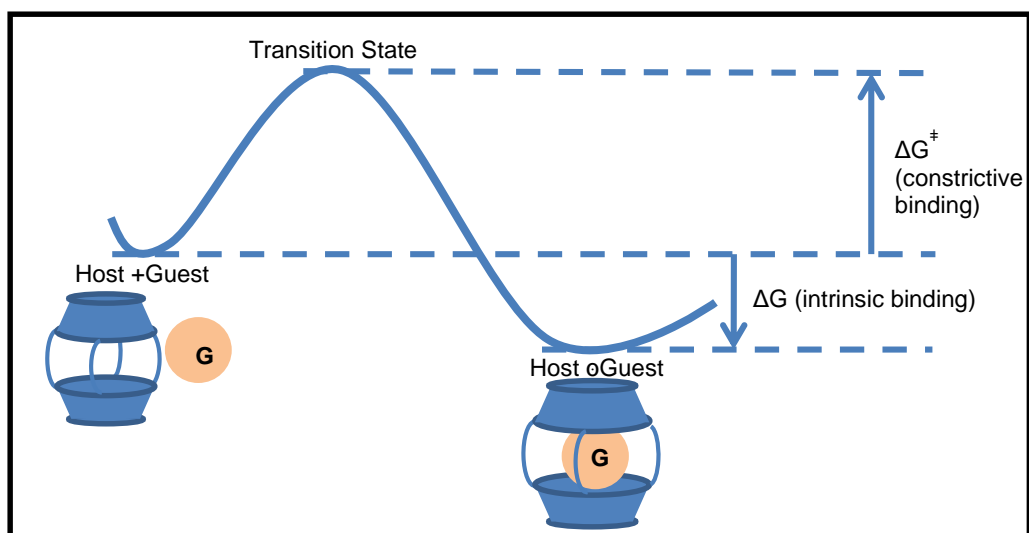


Figure 9.1. Representation of the reaction coordinate diagram of host–guest complexation.

Rebek's group has recently done experimental studies⁵ on self-folding cavitands that undergo conformational changes very similar to the Venus flytrap model of gating seen in proteins.⁶ The resorcinarene host **1** is a modification of the molecules originally synthesized by Cram (Figure 9.2a).⁷ The amide derivatives synthesized by Rebek adopt an open, kite-like conformation when they are empty and a closed, vase-like conformation when there is a bound guest inside (Figure 9.2b). Rebek proceeded to encapsulate various adamantane derivatives to study the steric and electronic effects of guest substitution on the binding energies of the formed complexes. By studying the energetics and mechanism of this cavitand in host-guest complexes, we will achieve a better understanding of this type of mechanical gating. We will also be able to develop efficient and robust techniques to accurately calculate binding affinities in host-guest complexes.

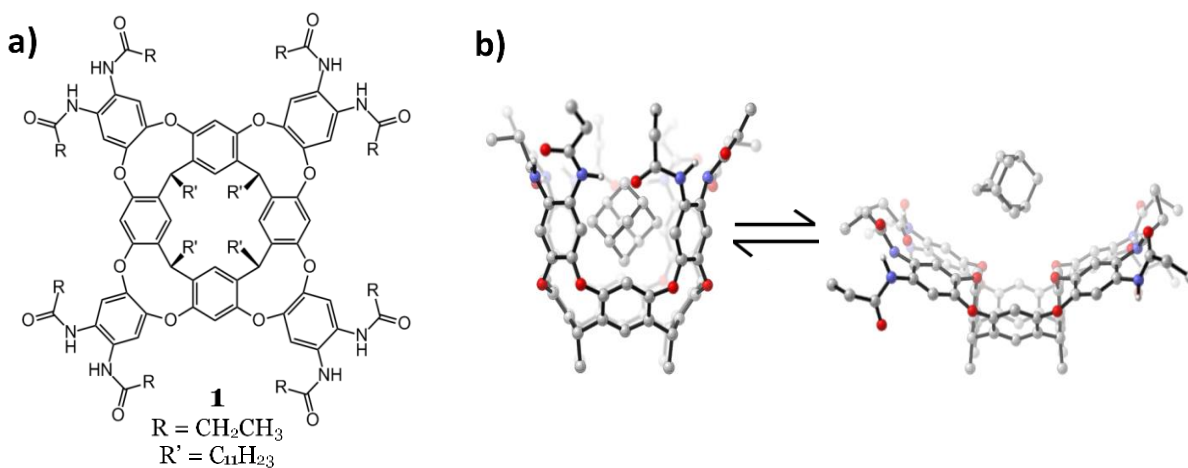


Figure 9.2. a) Structure of the resorcinarene-based cavitand **1**. **b)** Self-exchange process: Cavitand (host) with adamantane (guest) in the vase (left) and kite (right) conformations. Undecyl chains have been replaced with methyls; hydrogens have been removed for clarity.

Structures optimized with OPLS force field.

Computational Methods

All calculations were performed using the MACROMODEL⁸ module of Maestro 9.1, provided in the Schrodinger Suite package. Conformational searches were conducted with the OPLS_2005 and MMFFs force fields. Using the Torsional Monte Carlo Molecular Mechanics criteria (MCMM), 5000 conformers were generated and filtered and only unique (RMSD = 0.5 Å) and low-energy (within 1.2 kcal/mol of the global minimum) conformations were kept. The Generalized-Born/Solvent Accessible Surface Area (GB/SA) implicit solvation model of octanol and chloroform was utilized to simulate the mesitylene environment. Explicit solvent molecules were included when specified. The lowest energy conformation was then minimized using the same force field with stricter convergence criteria.

Results and Discussion

Quantum chemical calculations were conducted on these host-guest complexes using Rebek's experimental data as a source of comparison. Using the notion that the binding energies can be closely approximated from the difference in free energy between the host-guest complex and the individual components, we attempted to computationally replicate the binding constants of these cavitand hosts with adamantane-derivative guests. Thus, the free energy of binding can be given from the following equation:

$$\Delta G_{binding}^{solvated} = \Delta G_{host-guest}^{solvated} - (\Delta G_{host}^{solvated} + \Delta G_{guest}^{solvated})$$

Free energy values can be approximated by force field and GB/SA calculations through the following approximations:

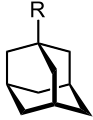
$$\Delta G_{binding}^{solvated} \approx (\Delta E^{FF} + \Delta E^{GB/SA})_{\text{host}\cdot\text{guest}} - [(\Delta E^{FF} + \Delta E^{GB/SA})_{\text{host}} + (\Delta E^{FF} + \Delta E^{GB/SA})_{\text{guest}}]$$

where ΔE^{FF} and $\Delta E^{GB/SA}$ are the potential energies of the force field and GB/SA solvent components, respectively, for the complex as well as the individual host and guest.

With the MMFFs and OPLS_2005 force fields, the binding energies were calculated for host **1** complexed with adamantane, 1-adamantanol, 1-chloroadamantane, and 1-cyanoadamantane. Because the GB/SA implicit solvent model for mesitylene was not available in the MACROMODEL program, both octanol and chloroform were employed as solvents in the study. In addition to implicit solvent, explicit solvent molecules were also added inside the empty host to model the occupation of the host cavity by solvent in the absence of a more suitable guest.

After assessing the two force fields using the various methods to account for solvent effects, the most promising results were found in octanol solvent with the incorporation of one explicit octanol molecule in the empty host. The results for both MMFFs and OPLS force fields are shown in Table 9.1. The MMFFs force field underestimates the favorable binding energy of the complexes and predicts no binding. There is also no observable qualitative trend seen in the calculated binding affinities, as compared to literature values. The OPLS_2005 force field does an adequate job of predicting the ΔG values with errors being within 1.5 kcal/mol, which is quite promising. However, from the data one can see that the deviation from experimental value increases as binding energy increases.

Table 9.1. Calculated binding energies of various adamantane derivatives with **1** in octanol using the MMFFs and OPLS_2005 force fields. GB/SA implicit solvent corrections were used, along with an explicit octanol molecule, to simulate solvent. All energies in kcal/mol.

Guest 	$\Delta G_{\text{binding}}$ (MMFFs)	$\Delta G_{\text{binding}}$ (OPLS_2005)	Experimental ΔG Value*
-H	2.0	-2.5	-2.4
-OH	0.6	-3.2	-3.5
-Cl	1.4	-5.4	-4.0
-CN	0.4	-6.4	-4.9

*Experimental values were reported as binding constants K_a (M^{-1}), which were converted to ΔG values.

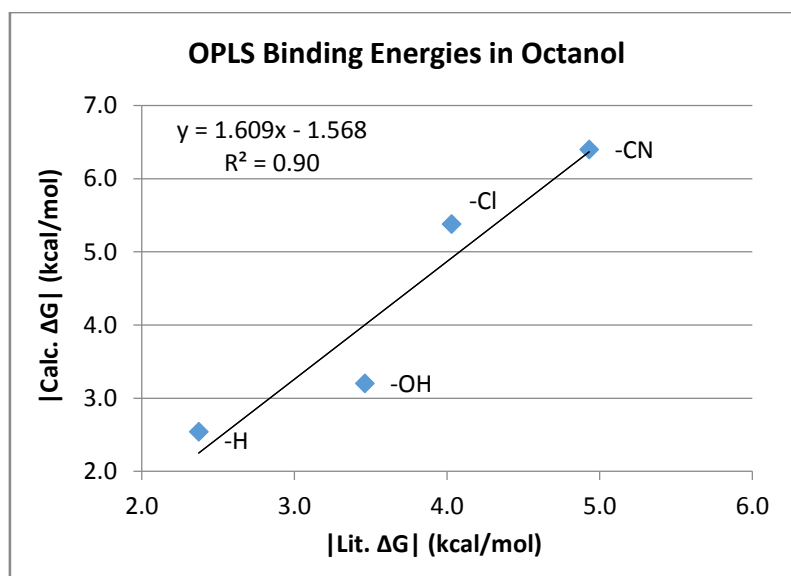


Figure 9.3. Plot of the OPLS binding energies. Absolute values of the calculated and literature ΔG values were used for clarity. Data taken from Table 9.1.

When the OPLS-computed values are plotted against Rebek's values measured through NMR experiments, a linear correlation can be seen (Figure 9.3, $R^2 = 0.90$). Although smaller binding energies were accurately predicted, a slope of 1.61 implies that larger magnitudes of ΔG will result in greater deviation. Fortunately, this method affords us an efficient and computationally feasible way to determine the likelihood of host-guest complexation with the added benefit of providing comparable binding energies.

To improve the assessment of binding affinities, free energy perturbation (FEP) methods⁹ with either the BOSS or the MCPro program,¹⁰ both developed in the Jorgensen lab at Yale, will be utilized. FEP is a more accurate, but more computationally intensive, method to compute binding free energy by calculating small changes along a multi-step pathway that connects the initial and final states. More specifically, FEP would start with the host-guest complex and systematically transmute the guest into a solvent molecule, simulating the occupied and empty forms of the cavitand, and calculating changes in ΔG at each step. Successful utilization of FEP to determine binding affinities can then be applied to other host-guest systems, and ultimately will be an invaluable tool in studying protein-ligand binding.

Conclusion

A preliminary assessment of binding affinity calculations has been carried out on resorcinarene-based cavitands containing adamantane-derivative guests synthesized by Rebek. Using OPLS and MMFFs force fields with implicit and explicit solvent, binding energies were computed and compared with experimental values to determine an efficient procedure for ascertaining the possibility of complexation. FEP methods will now be used to generate more accurate measurements of binding.

References

1. Cram, D. J. *Science*, **1983**, *219*, 1177–1183.
2. Cram, D. J. *Angew. Chem. Int. Ed.*, **1986**, *25*, 103–104.
3. Bryant, J. A.; Blanda, M. T.; Vincenti, M.; Cram, D. J. *J. Am. Chem. Soc.*, **1991**, *113*, 7717–7727.
4. Nakamura, K.; Sheu, C.; Keating, A. E.; Houk, K. N. *J. Am. Chem. Soc.*, **1997**, *119*, 4321–4322.
5. Hooley, R. J.; Shenoy, S. R.; Rebek, J., Jr. *Org. Lett.* **2008**, *10*, 5397–5400.
6. Mao, B.; Pear, M. R.; McCammon, J. A. *J. Biol. Chem.* **1982**, *257*, 1131–1133.
7. Moran, J. R.; Ericson, J. L.; Dalcinane, E.; Bryant, J. A.; Knobler, C. B.; Cram, D. J. *J. Am. Chem. Soc.* **1991**, *113*, 5707–5714.
8. MacroModel, version 9.5, Schrödinger, LLC, New York, NY, 2007.
9. Kollman, P. *Chem. Rev.* **1993**, *93*, 2395–2417.
10. Jorgensen, W. L.; Tirado-Rives, J. *J. Comput. Chem.* **2005**, *26*, 1689–1700.

Chapter 10. Hydrocarbon Binding by Proteins: Structures of Protein Binding Sites for $\geq C_{10}$ Linear Alkanes or Long-Chain Alkyl and Alkenyl Groups

Introduction

Long-chain alkyl or alkenyl groups are commonly found in nature; vital components of living organisms such as fatty acids, lipids, and biological surfactant molecules all contain long hydrocarbon moieties. Thus, the recognition of specific alkyl substrates by proteins is of utmost biological importance. For example, P450 enzymes containing a heme cofactor can catalyze the hydroxylation of long-chain alkanes under aerobic conditions,¹ drawing interest from both science and engineering disciplines due to their potential utility in biofuel production.² Intriguing examples of long-chain alkane recognition can also be found in microorganisms residing in deserted geographical regions such as swamps, marine sediment, and deep oil wells, where they have evolved to thrive under these harsh conditions by utilizing long-chain hydrocarbons as their carbon source.³ More recently, microbial genomic studies suggest the presence of enzymes capable of decomposing long-chain alkanes under anaerobic conditions;^{4,5} however, detailed structural information about the conformation of the bound substrate has yet to be determined.

The recognition of linear alkane motifs is of interest to biochemists as well as synthetic chemists. Because C–C bond activation has become an important research topic of synthetic chemistry, there is a growing interest in catalysts that are capable of promoting C–C bond activation with proper regio- and stereoselectivity.⁶ We envision *de novo*-designed enzymes capable of catalyzing the functionalization and cleavage of C–C bonds in long-chain alkanes.⁷ As a first step in the design process, scaffolds are sought upon which the catalytic groups required to effect the chemical reaction of interest can be installed. Further understanding of substrate–host interactions is necessary to optimize the substrate recognition capacity of these *de novo* enzymes, facilitating development of a regio- and stereoselective catalyst. These requirements motivated us

to collect and curate the structural information on proteins bound to long-chain alkanes. Specifically we aimed to answer the following questions: How do proteins recognize and bind long-chain alkyl and alkenyl motifs? What characteristics are shared by the binding pockets of these proteins? Can structural and functional characterization of these proteins lead to valuable insights useful for the development of C–C bond-cleaving enzymes?

In order to answer these questions, we selectively retrieved atomic-resolution protein structures with bound ligands containing long-chain alkyl functional groups (10 carbons or greater) from the Protein Data Bank (PDB).⁸ The selection criteria resulted in 874 hits in total, encompassing 194 unique ligands and 737 distinct proteins. We analyzed both the bound substrates and the protein binding sites, generating statistics based on the following data: the type and size distribution of ligands, the binding pocket amino acids and their secondary structures, the solvent-accessible surface area (SASA)⁹ buried upon ligand binding, surface complementarity of the ligand–protein interface, and the fraction of the binding pocket volume occupied by the ligand. Finally, we classified select PDB entries according to both the structural classification of proteins (SCOP)¹⁰ and functional categories based on UniProt.¹¹ We also discuss similarities to synthetic hosts capable of recognizing linear alkanes as guest molecules.

Results and Discussion

Searching for High Resolution Protein Structures Containing Long-Chain Alkanes

We searched for known protein structures deposited in the PDB and retrieved entries containing linear alkane motifs (Figure 10.1). Out of over 87,000 ligand-containing PDB structures, we filtered out any ligands having fewer than 10 carbon atoms in a linear chain or possessing a cyclic moiety. As summarized in Table 10.1, 874 PDB entries isolated with 194 unique ligands bound to proteins were identified (**set 1**). In the following sections, we present a statistical analysis on the nature of interactions between proteins and long-chain alkyl ligands.

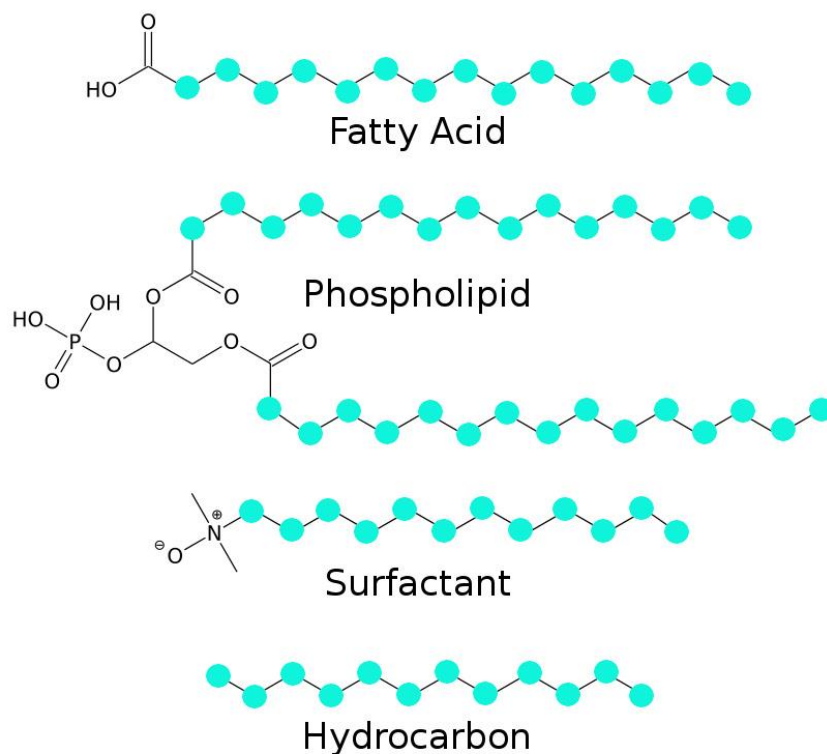


Figure 10.1: Selection of ligands having linear alkane motifs. Non-amino acid ligands such as fatty acids, phospholipids, surfactants, and hydrocarbons were selectively retrieved from the PDB database. Linear alkane motifs are highlighted in cyan.

We also considered two subsets of proteins which are especially significant to the understanding of long-chain alkane recognition in aqueous solutions. Out of the 874 PDB entries with ligands containing linear alkyl groups ≥ 10 carbons, 428 entries were soluble proteins (**set 2**). Furthermore, 28 of those soluble proteins were bound to pure hydrocarbons (**set 3**), which are listed in Table 10.2. As our motivation was to identify scaffolds for *de novo*-designed enzymes in aqueous media, we extended our statistical analysis to include the subsets of water-soluble proteins with ligands containing long-chain alkyl groups (**set 2**) and water-soluble proteins with hydrocarbon ligands (**set 3**).

Table 10.1: Description of the Different Protein–Ligand Complex Datasets.

Name	Selection criteria	No. of protein–ligand complexes	No. of distinct ligands
set 1	Contains ligand with ≥ 10 linear carbons	874	194
set 2	Subset of set 1 , containing water-soluble proteins only	428	143
set 3	Subset of set 2 , containing hydrocarbon ligands	28	9
CSAR¹²	A benchmark data set for ligand–protein docking studies	118	116

Table 10.2: PDB Entries of Soluble Proteins and Their Corresponding Ligands Containing Alkyl and Alkenyl Groups Larger than C₁₀.

PDB ID	Protein	Ligand Name	Formula
1EVY	Glycerol-3-phosphate dehydrogenase	Pentadecane	C ₁₅ H ₃₂
1EVZ	Glycerol-3-phosphate dehydrogenase	Pentadecane	C ₁₅ H ₃₂
1GKA	Beta-crustacyanin	Dodecane	C ₁₂ H ₂₆
1GZP	T-cell surface glycoprotein CD1b	Dodecane	C ₁₂ H ₂₆
1GZP	T-cell surface glycoprotein CD1b	Docosane	C ₂₂ H ₄₆
1GZQ	T-cell surface glycoprotein CD1b	Dodecane	C ₁₂ H ₂₆
1GZQ	T-cell surface glycoprotein CD1b	Docosane	C ₂₂ H ₄₆
1JDJ	Glycerol-3-phosphate dehydrogenase	Pentadecane	C ₁₅ H ₃₂
1TI1	Thiol:disulfide interchange protein DsbA	Dodecane	C ₁₂ H ₂₆
1Y9L	Lipoprotein MxiM	Undecane	C ₁₁ H ₂₄
1Z4A	Ferritin	Eicosane	C ₂₀ H ₄₂
1Z5L	T-cell surface glycoprotein CD1d antigen	Hexadecane	C ₁₆ H ₃₄
2CME	Protein 9b	Decane	C ₁₀ H ₂₂
2EUM	Glycolipid transfer protein	Decane	C ₁₀ H ₂₂
2EVS	Glycolipid transfer protein	Decane	C ₁₀ H ₂₂

2H4T	Carnitine ^K O-palmitoyltransferase 2 ^T	Decane	C ₁₀ H ₂₂
2ZYH	Lipase	Hexadecane	C ₁₆ H ₃₄
3ARB	Antigen-presenting glycoprotein CD1d1	Dodecane	C ₁₂ H ₂₆
3FE6	Pheromone binding protein ASP1	(20 <i>S</i>)-20-methyl-dotetracontane	C ₄₃ H ₈₈
3FE8	Pheromone binding protein ASP1	(20 <i>S</i>)-20-methyl-dotetracontane	C ₄₃ H ₈₈
3FE9	Pheromone binding protein ASP1	(20 <i>S</i>)-20-methyl-dotetracontane	C ₄₃ H ₈₈
3OAX	Rhodopsin	(4 <i>E</i> ,6 <i>E</i>)-hexadeca-1,4,6-triene	C ₁₆ H ₂₈
3OV6	T-cell surface glycoprotein CD1b	Dodecane	C ₁₂ H ₂₆
3R9B	Cytochrome P450 16A2	Dodecane	C ₁₂ H ₂₆
3TZV	T-cell receptor; glycoprotein CD1d	Dodecane	C ₁₂ H ₂₆
3UoP	Antigen-presenting glycoprotein CD1d	Undecane	C ₁₁ H ₂₄
4FXZ	Bacterial leucine transporter	Undecane	C ₁₁ H ₂₄

Statistics of Bound Ligands Containing Alkyl Groups $\geq C_{10}$

Figure 10.2 contains histograms portraying the abundance of the different types of ligands with alkyl groups longer than C₁₀ as well as the number of carbon atoms present in those ligands. As shown in Figure 10.2a, fatty acids are the most abundant type of ligand in **set 1**, followed by phospholipids, amine oxides, hydrocarbons, glycerides, and amides. Fatty acids remained the most common ligand once we limited our interest to only soluble proteins (**set 2**), whereas the abundance of other ligands significantly decreased; typical surfactants¹³ like phospholipids and amine oxides are associated with membrane-bound proteins, significantly reducing their presence in water-soluble proteins.

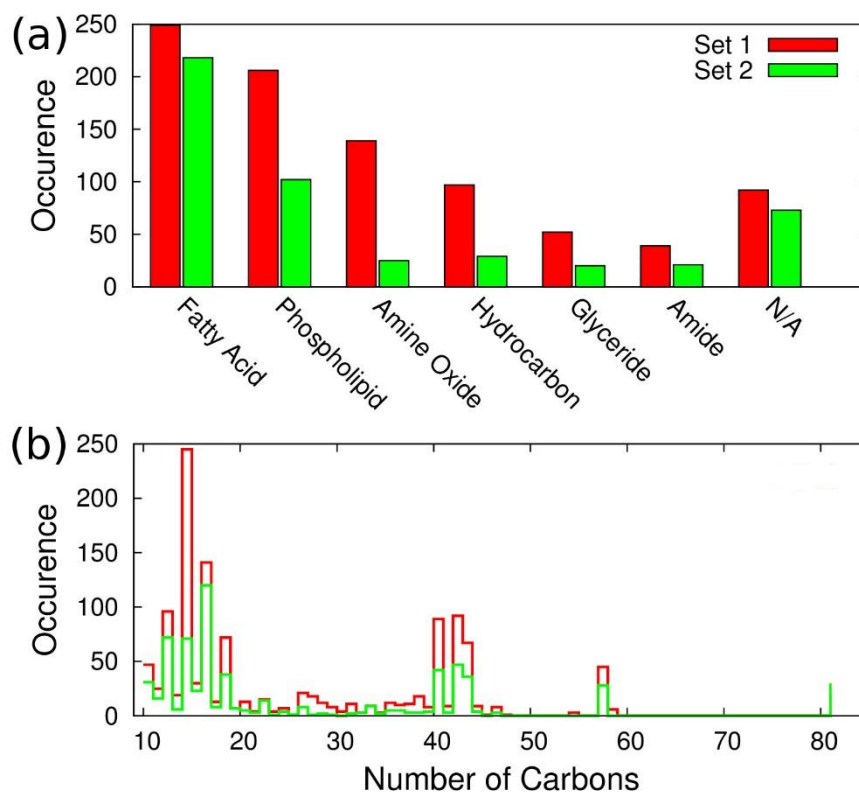


Figure 10.2. Functional classification and the size distribution of the ligands containing linear alkane motifs. (a) Ligands were classified according to the functional group attached to the linear alkane motif. (b) The distribution of the number of carbon atoms in each ligand. Ligands from all proteins are color-coded in red, whereas those from water-soluble proteins are in green.

We then considered the size of the bound ligands in Figure 10.2b. The number of carbon atoms was used as an index of ligand size. The histogram of **set 1** has its maximum at 14 carbon atoms, comprised of lauryl dimethylamine-*N*-oxide, myristic acid, (10*E*,12*Z*)-tetradeca-10,12-dien-1-ol, *S*-[2-(acetylamino)ethyl](3*R*)-3-hydroxydecanethioate, tetradecane, and (*R*)-3-hydroxytetradecanal (Figure 10.3). The largest entry found was cardiolipin (81 carbon atoms)¹⁴, a diphosphatidylglycerol molecule having four linear alkyl functional groups. The histogram of long-chain alkanes interacting with water-soluble proteins (**set 2**) was qualitatively similar to that

of **set 1**; ligands with 16 carbons were now the most common, whose members include 16-hydroxyhexadecanoic acid, (11*Z*,13*Z*)-hexadeca-11,13-dien-1-ol, (4*E*,6*E*)-hexadeca-1,4,6-triene, (2,2-Diphosphonoethyl)(dodecyl)dimethylphosphonium, (10*E*,12*Z*)-hexadeca-10,12-dienal, (10*E*)-hexadec-10-en-12-yn-1-ol, hexadeca-10,12-dien-1-ol, *N*-dodecyl-*N,N*-dimethylglycinate, decamethonium ion, 1-decyl-3-trifluoro ethyl-*sn*-glycero-2-phosphomethanol, 1-hexadecanesulfonic acid, 1-iodohexadecane, 10-oxohexadecanoic acid, hexadecan-1-ol, palmitic acid, and hexadecane. Once again, the largest ligand bound was cardiolipin.

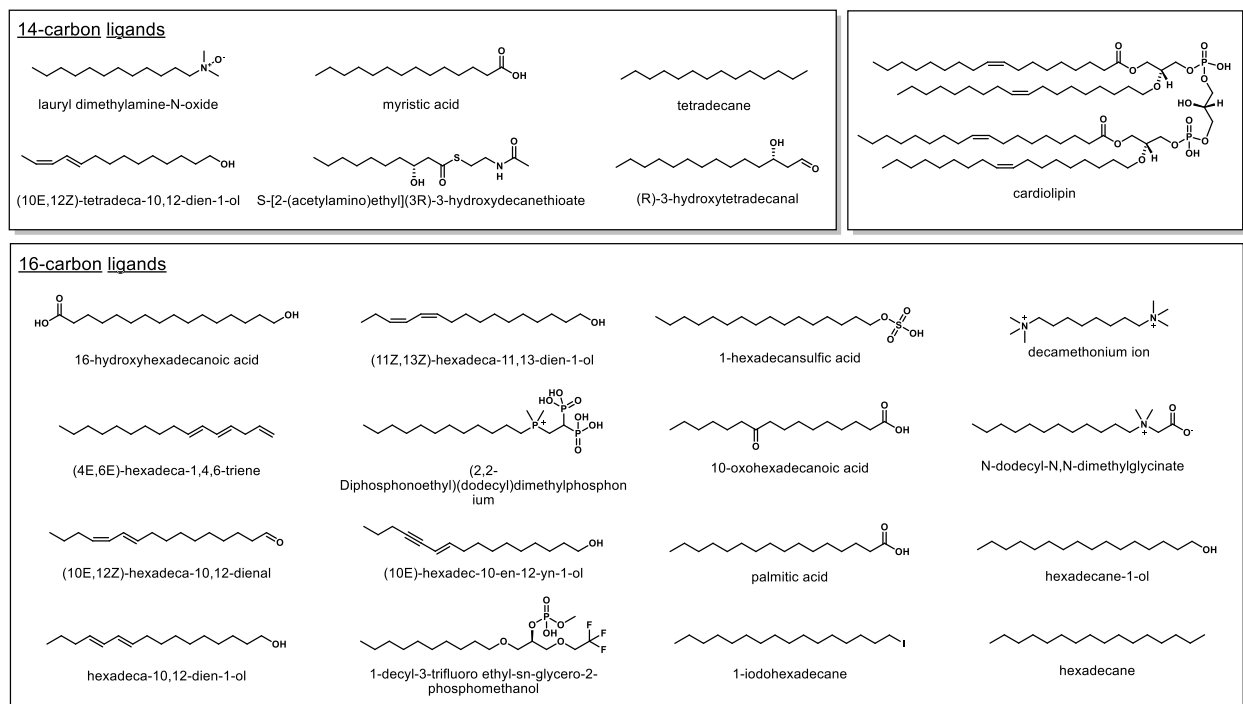


Figure 10.3. Structures of the 14-carbon ligands, 16-carbon ligands, and cardiolipin.

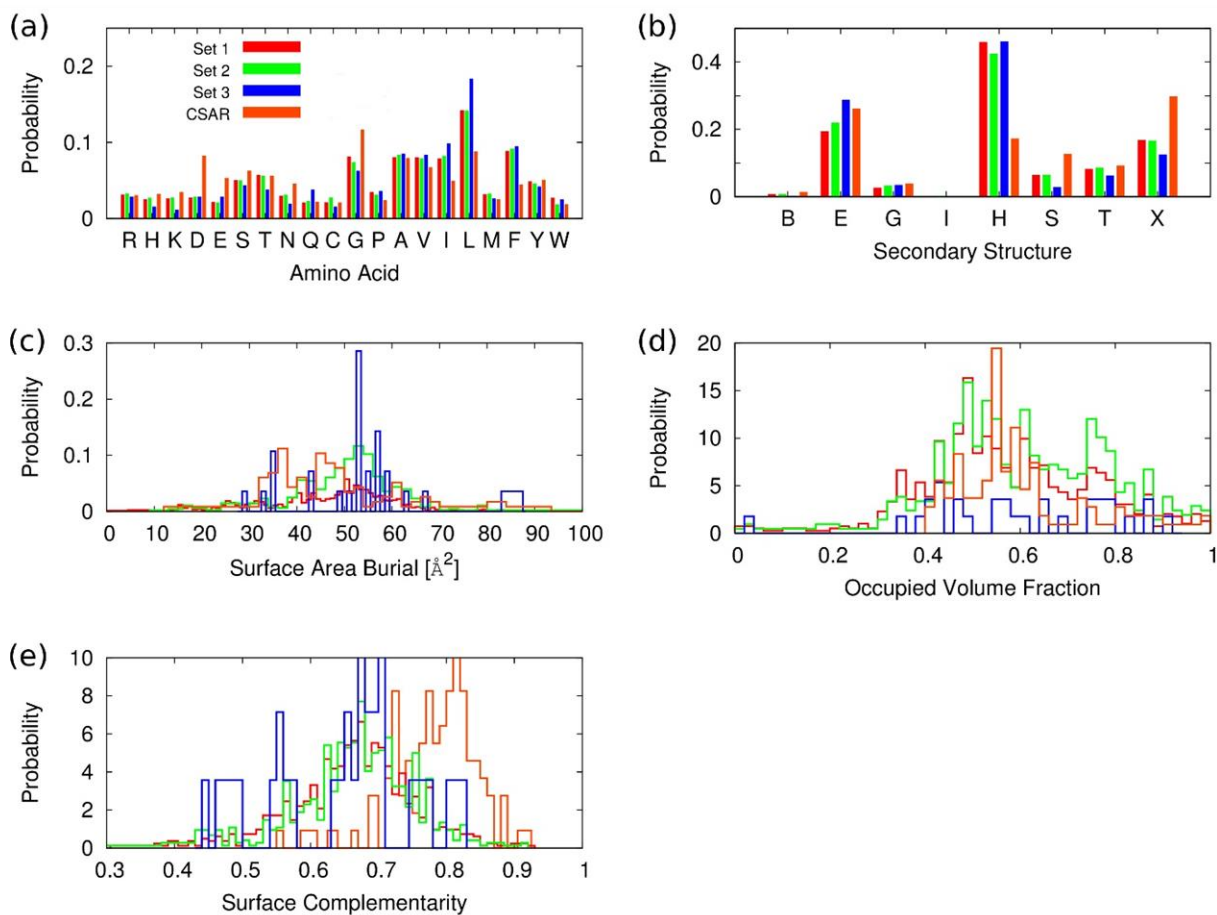


Figure 10.4. Statistics of the ligand-binding pockets: (a) population of amino acids, (b) backbone secondary structure distribution, (c) surface area burial per ligand-carbon atom, (d) occupied volume fraction of binding pocket by the ligand, and (e) surface complementarity between protein and ligand. Secondary structure abbreviations: B, β -bridge; E, β -sheet; G, turn; I, π -helix; H, α -helix; S, bend; T, hydrogen-bonded turn; X, unstructured.

Statistics on Amino Acids and Folds of Ligand Binding Pockets

Figure 10.4 portrays the frequency of amino acids defining the ligand-binding pocket. As detailed in the Methods, *Rosetta Interface Analyzer*¹⁵ was used to identify the binding pocket amino acids surrounding the bound ligand. The analysis of all long-chain alkane-binding proteins (**set 1**) resulted in the hydrophobic residues leucine (14%) and phenylalanine (9%) as two of the

most abundant amino acids. These became more abundant in water-soluble proteins (**set 2**) and hydrocarbon-bound soluble proteins (**set 3**). The binding pocket residues surrounding long-chain linear alkyl groups were then compared to those of drug–target proteins deposited in **CSAR**.¹² As drug-like molecules tend to include ring moieties and polar functional groups, this assessment could be beneficial for isolating unique features of ligand-binding pockets that specifically recognize alkyl groups that are linear, nonpolar, and hydrophobic. The comparison suggests that the populations of hydrophobic residues, including leucine, valine, and phenylalanine, are enriched in hydrocarbon-binding pockets relative to the binding pockets of drug molecules.

The secondary structures of the amino acids forming the protein backbone of the binding pocket were analyzed in Figure 10.4b using the DSSP software.¹⁶ The α -helices (H, 45%) and β -sheets (E, 20%) are the two most prevalent secondary structures found from the binding pocket residues of **set 1**. The higher frequency of α -helices lining the binding pocket is consistent in **sets 2** and **3**. An examination of the **CSAR** dataset (Figure 10.4b, orange) shows a dramatic decrease in α -helices relative to the other secondary structures. The population of unstructured secondary structures is doubled in reference to **set 3**. These findings strongly indicate that the binding of long-chain linear alkanes occurs at protein surfaces made of α -helices more often than any other secondary structure elements.

In Figure 10.4c, we plot the results of the computed surface area burial (SAB) per ligand-carbon atom upon formation of the protein–ligand complex. SAB provides a quantitative measure of how tightly a protein captures its ligand. On average, each carbon atom of the ligands in **set 1** buried $47 \pm 14 \text{ \AA}^2$ of the solvent accessible surface area (SASA) of the binding pocket. Water-soluble proteins bound to ligands containing long-chain alkanes (**set 2**) and to pure hydrocarbons (**set 3**) resulted in 50 ± 12 and $52 \pm 12 \text{ \AA}^2$ of the SAB, respectively. Although the average SAB is largest for **set 3**, the difference from **set 1** is within statistical uncertainty. The SAB of drug-

binding pockets ($49 \pm 22 \text{ \AA}^2$) is also comparable to that of the long-chain alkane-binding proteins. In short, the SAB per ligand-carbon atom of long-chain alkane-binding proteins is $47 - 52 \text{ \AA}^2$ on average and is similar to that of drug-target proteins.

In addition to surface area burial, we also analyzed the binding pocket volume occupied by the ligand (occupied volume fraction, OVF) in Figure 10.4d. Mecozzi and Rebek pointed out that 55% is an optimal OVF value, considering both the favorable enthalpic interactions between ligand and host as well as the entropic penalty associated with the limited conformational degrees of freedom imposed on the bound ligand.¹⁷ We computed the OVF of ligand binding pockets using POVME software.¹⁸ For both **set 1** and **set 2**, the OVF is close to the conjectured optimal value: 57 ± 18 and $61 \pm 17\%$, respectively. The same computation on the **CSAR** data set resulted in a similar observation: the OVF was $59 \pm 13\%$. The average OVF values of naturally occurring proteins bound to long-chain alkanes and of designed drug-like molecules are similar and are close to the optimal OVF value of 55%.

Finally we computed the surface complementarity¹⁹ (SC) between the binding pocket residues and the bound ligands. SC quantifies the congruency between two interacting molecular surfaces, where the SC of two perfectly complementary surfaces is 1 and that of two adjacent random shapes approaches 0. This quantity has been understood to be one of the fundamental descriptors of the compliance of two interacting molecules.²⁰ For the long-chain alkane-binding proteins, computed SC values are similar regardless of their solubility profile: 0.66 ± 0.08 , 0.66 ± 0.09 , 0.63 ± 0.09 for **set 1**, **set 2**, and **set 3**, respectively. On the other hand, the interfaces of drug-like molecules showed enhanced SC over that of the alkane-binding proteins: SC of the **CSAR** dataset is 0.78 ± 0.06 . SC is known to be correlated with the specificity of the interaction between a ligand and its binding pocket.²¹ The SC of interacting protein surfaces ranges from 0.70 to 0.76,¹⁹ resembling that of the **CSAR** dataset. Furthermore, drug molecules are optimized to achieve enhanced selectivity toward their targets, exploiting specific interactions such as

hydrogen bonding and electrostatic interactions. These tendencies are expected to result in higher SC values. In contrast, naturally occurring alkane-binding proteins stabilize their substrates through relatively weaker non-polar interactions, resulting in smaller SC values than the protein–protein or protein–drug interfaces.

Alkane Binding by Synthetic Hosts

Aside from the naturally occurring biomolecules we surveyed, synthetic supramolecular hosts have also been shown to bind diverse substrates. Cram pioneered the uses of carcerands, cavitands, and other molecular capsules as molecular containers and to catalyze reactions or stabilize reactive intermediates, garnering much interest in the scientific community.²² Of particular relevance, Rebek investigated the kinetics and thermodynamics of binding medium-chain alkanes with resorcinarene-based cavitands.^{23, 24} The host molecules dimerize, as shown in Figure 10.5, forming pill-shaped compartments capable of enclosing *n*-alkanes, from C₉ to C₁₄; shorter alkanes are bound in an extended straight-chain conformation, whereas longer chains adopt a folded and helical arrangement. Although the coiling of the longer alkanes results in unfavorable gauche conformations, the favorable C–H⋯ π interactions with the aromatic walls of the cavitand compensates for the increased torsional strain. The usual cutoff distance for C–H⋯ π interactions is considered to be approximately 3 Å, calculated from the respective van der Waals radii. Both computational²⁵ and crystallographic data²⁶ of encapsulated alkyl guests exhibit these interactions.

For guest molecules with narrow, extended conformations, the cavitand host deforms not only to increase C–H⋯ π interactions but also to attain more suitable packing coefficients. Rebek's dimeric host has a calculated volume of 425 Å³ and can bind guests that occupy about 55 ± 9% of the available volume, similar to the packing efficiency of most organic liquids.¹⁷ Guests that do not sufficiently fill the empty space suffer from the large entropic penalty of complexation; the

“empty” hosts prefer to be filled with solvent when the alkane is too small. In contrast, larger guests cause the binding site to be too crowded, thus experiencing steric repulsion. Other groups have shown that the general 55% parameter also applies to enzyme binding pockets.²⁷ The lack of observed complexes of the Rebek host cavitands with alkanes smaller than 9 carbons or longer than 14 carbons is a testament to the importance of size and shape complementarity when encapsulating substrates without any functional handles.

Through minor modifications of the cavitand molecules, formation of the dimer was suppressed, and hydrophilic “feet” were incorporated to create water-soluble supramolecules that were capable of binding medium-chain alcohols.²⁸ The polar hydroxyl group remains exposed to the aqueous environment, and the hydrophobic alkyl chain coils towards the inner cavity of the host, similar to the alkane conformations mentioned earlier. The alkane size and shape complementarity exhibited by these complexes bears some resemblance to the naturally occurring hydrocarbon-binding sites in proteins.

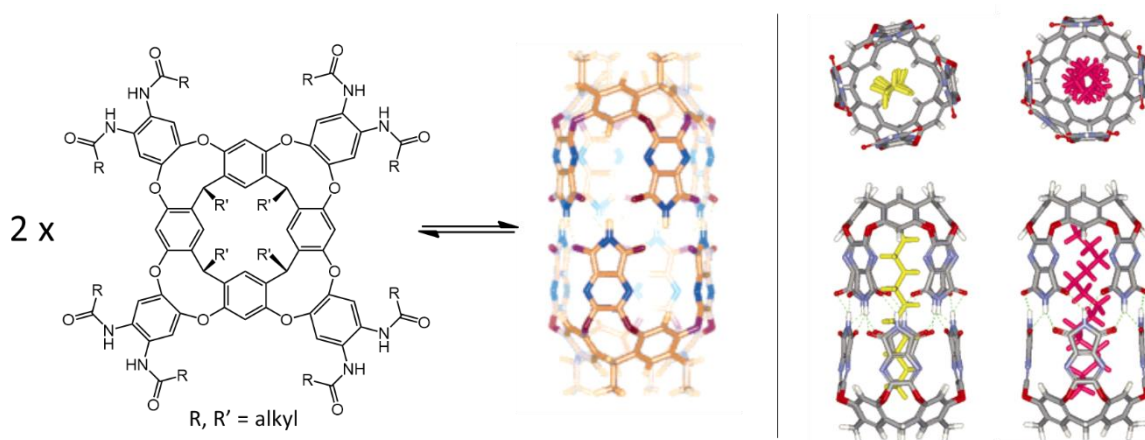


Figure 10.5. Left: A resorcinarene-based cavitand that can dimerize, creating a molecular capsule. **Right:** Top and side views of encapsulation of $n\text{-C}_{10}\text{H}_{22}$ in a straight-chain conformation (yellow) and $n\text{-C}_{14}\text{H}_{30}$ (red) in a helical arrangement. Images taken from Scarso, *et*

*al.*²³

Structural and Functional Classification of Long-Chain Alkane-Binding Proteins

We classified each hit from the selected PDB entries based on the structural classification of proteins (SCOP). In general, protein structure determination in the presence of a ligand is more difficult than that in its absence. This implies that high-resolution structures with bound ligands may represent only a subset of proteins having the potential to recognize linear alkanes. Fortunately, structurally similar proteins (homologues) share many functional similarities. Thus, one may establish the structures of proteins interacting with linear hydrocarbon motifs through homologue relationships. As of 2013, only 38222 PDB entries had SCOP classification IDs, from which we were able to classify 407 out of the 874 hits (Table 10.3). SCOP classifies proteins into several hierarchical levels, utilizing either their evolutionary relationships or structural similarities: the fold hierarchy of a protein reflects structural relationships with other proteins, whereas both family and superfamily hierarchies are based on evolutionary origin and functional similarity. We focused on the fold classification of proteins in the PDB search hits because we use this classification with the alkane-binding proteins to facilitate identification of protein design scaffolds sharing similar structural features. There are 72 distinct SCOP folds identified out of 407 proteins having SCOP IDs. For multidomain proteins, each domain in contact with the linear hydrocarbon ligand was analyzed separately. The most prevalent fold is the bacterial photosystem II reaction center, L and M subunits. Representative structures of the top six most frequently found SCOP folds are depicted in Figure 10.6a–f.

Table 10.3: SCOP Classification of the Selected PDB Entries Containing Linear Alkane Motifs

SCOP Fold Name	Number of Occurrences
Bacterial photosystem II reaction center, L and M subunits	53
Family A G protein-coupled receptor-like	35
Nucleoplasmin-like/VP (viral coat and capsid proteins)	21

Lipocalins	21
Cytochrome c oxidase subunit III-like	14
Serum albumin-like	13
Cytochrome c oxidase subunit I-like	12
Transmembrane beta-barrels	11
Single transmembrane helix	11
Phospholipase A2, PLA2	11
Nuclear receptor ligand-binding domain	11
Cupredoxin-like	11
Bifunctional inhibitor/lipid-transfer protein/seed storage 2S albumin	11
Thiolase-like	10
PRC-barrel domain	10
Immunoglobulin-like beta-sandwich	10
Ganglioside M2 (gm2) activator	10
alpha/beta-Hydrolases	8
Heme-binding four-helical bundle	7
Cytochrome P450	7
alpha/alpha toroid	7
Ribosomal protein S5 domain 2-like	6
a domain/subunit of cytochrome bc1 complex (Ubiquinol-cytochrome c reductase)	6
6-Phosphogluconate dehydrogenase C-terminal domain-like	6
Voltage-gated potassium channels	4
TIM beta/alpha-barrel	4
S-Adenosyl-L-methionine-dependent methyltransferases	4
Prealbumin-like	4
Cytochrome c	4
SCP-like	3
EF Hand-like	3
DAK1/DegV-like	3
alpha-alpha superhelix	3
Snake toxin-like	2

Rhomboid-like	2
MHC antigen-recognition domain	2
Lysozyme-like	2
Light-harvesting complex subunits	2
GroES-like	2
Glycolipid transfer protein, GLTP	2
Ferredoxin-like	2
beta-hairpin stack	2
Aha1/BPI domain-like	2
Acyl carrier protein-like	2
Thioredoxin fold	1
Thioesterase/thiol ester dehydrase-isomerase	1
TBP-like	1
SH3-like barrel	1
SARS ORF9b-like	1
Saposin-like	1
RuvA C-terminal domain-like	1
RRF/tRNA synthetase additional domain-like	1
Photosystem I subunits PsaA/PsaB	1
(Phosphotyrosine protein) phosphatases II	1
Ntn hydrolase-like	1
NAD(P)-binding Rossmann-fold domains	1
LuxS/MPP-like metallohydrolase	1
Long alpha-hairpin	1
Lipase/lipoxygenase domain (PLAT/LH2 domain)	1
Kringle-like	1
ISP domain	1
Gelsolin-like	1
FAD/NAD(P)-binding domain	1
Double-stranded beta-helix	1
DNA/RNA-binding 3-helical bundle	1
DhaL-like	1

Cystatin-like	1
Clc chloride channel	1
Class II aaRS and biotin synthetases	1
Chlorophyll a-b binding protein	1
Bromodomain-like	1
A DNA-binding domain in eukaryotic transcription factors	1

Next we considered functional attributes of the selected protein templates. Our specific interest was to identify alkane-binding proteins that have enzymatic activity. These proteins possess catalytic functional groups and/or bound cofactors that have more easily modifiable characteristics than nonenzymatic proteins. UniProt¹¹ is the central information repository of genomic sequence and functional information of proteins. Each entry in the PDB has one or more UniProt identification numbers, enabling us to annotate the functional role of each PDB structure containing ligands with a long-chain alkane motif. A subset of the selected PDB templates has enzymatic activity, which is identified by the enzyme commission (EC) number. On the basis of these functional descriptions of each entry from the UniProt database, we classified the 874 selected protein templates into functional categories. First, we identified enzymes having catalytic functionality with specific ligands (Table 10.4): there are 202 enzymes identified, catalyzing 89 distinct chemical reactions. The most frequently identified enzyme was cytochrome-c oxidase (UniProt ID: P00396, 17 entries) and the second was viral protease/RNA transferases (UniProt ID: P03300, 10 entries). There are also enzymes associated with biological reactions involving linear alkyl and alkenyl functional groups, such as 3-oxoacyl-[acyl-carrier-protein] synthase III (UniProt ID: P0A574), phospholipase A2 (UniProt ID: P00592) and cytochrome-P450 monooxygenase (UniProt ID: P14779).

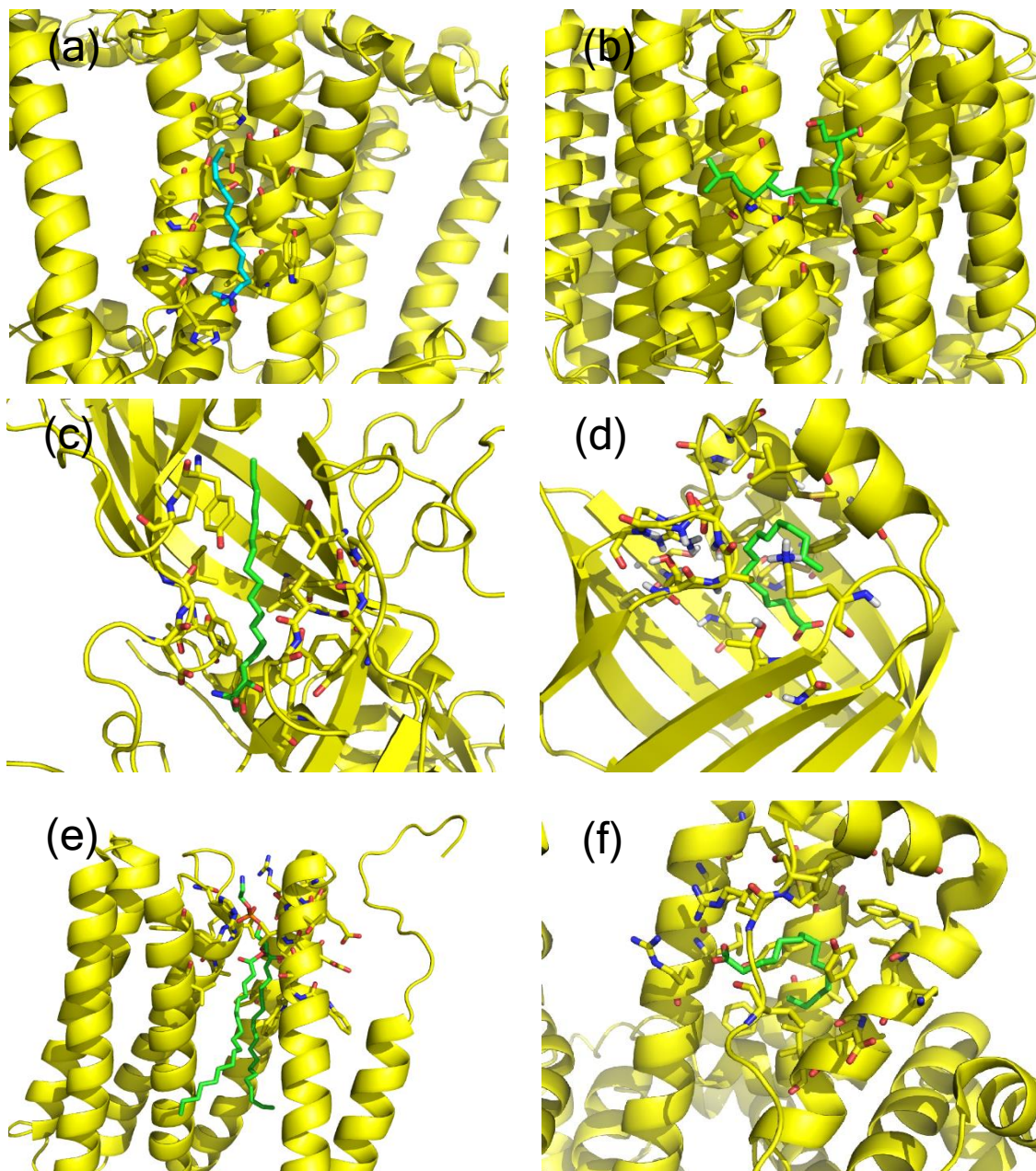


Figure 10.6: Frequently observed SCOP folds binding ligands with linear alkane motifs: (a) bacterial photosystem II reaction center protein (PDB ID: 1AIJ) bound to lauryl dimethylamine-N-oxide, (b) family A G protein-coupled receptor-like protein (PDB ID: 1BRR) bound to 3,7,11,15-tetramethyl-1-hexadecanol, (c) nucleoplasmin-like/VP protein (PDB ID: 1AL2) bound to sphingosine, (d) lipocalin (PDB ID: 1B56) bound to palmitic acid, (e) cytochrome C oxidase, subunit III (PDB ID: 1M56) bound to distearoyl-*sn*-phosphatidylethanolamine, and (f) serum albumin-like protein (PDB ID: 1H9Z) bound to myristic acid. PyMol was used for molecular visualization.¹⁸ Cartoon representations represent backbone arrangements of the protein, and bound ligands and binding pocket residues are shown using stick representations.

Finally, we questioned whether the binding sites of enzymes are significantly different from those of the nonenzymatic hydrocarbon-binding proteins, as enzyme catalysis usually requires the precise placement of substrates, leading to an enhanced binding specificity. However, statistics such as SC and OVF of the enzymes (0.68 ± 0.08 and 57 ± 13 %, respectively) are almost identical to those of long-chain alkane-binding proteins (**set 1**). The findings suggest that enzymatic proteins recognize their substrates based on the same chemical principles governing the binding of long-chain alkanes in nonenzymatic proteins.

Table 10.4: Subset of the Selected PDB Entries Having Enzymatic Activity.

UniProt ID	EC No.	Description
O33877	4.2.1.59	3-hydroxydecanoyl-[acyl-carrier-protein] dehydratase
PoA574	2.3.1.180	3-oxoacyl-[acyl-carrier-protein] synthase 3
P44783	3.4.21.10	5 Rhomboid protease GlpG
P09391	3.4.21.10	5 Rhomboid protease GlpG
P04058	3.1.1.7	Acetylcholinesterase
P21836	3.1.1.7	Acetylcholinesterase
Q6SLM2	3.1.1.4	Acidic phospholipase A2 1
PoAGG2	3.1.2.-	Acyl-CoA thioesterase 2
Q9NPJ3	3.1.2.-	Acyl-coenzyme A thioesterase 13
Q9I194	3.5.1.97	Acyl-homoserine lactone acylase PvdQ
P11766	1.1.1.1	Alcohol dehydrogenase class-3
O96759	2.5.1.26	Alkyldihydroxyacetonephosphate synthase
P97275	2.5.1.26	Alkyldihydroxyacetonephosphate synthase, peroxisomal
Q7D8I1	2.3.1.-	Alpha-pyrone synthesis polyketide synthase-like Pks18
P21397	1.4.3.4	Amine oxidase [flavin-containing] A
P27338	1.4.3.4	Amine oxidase [flavin-containing] B
P06653	3.5.1.28	Autolysin
B2IZD3	3.6.5.5	Bacterial dynamin-like protein
P59071	3.1.1.4	Basic phospholipase A2 VRV-PL-VIIIa

P14779	1.14.14.1	Bifunctional P-450/NADPH-P450 reductase
P00918	4.2.1.1	Carbonic anhydrase 2
P18886	2.3.1.21	Carnitine O-palmitoyltransferase 2, mitochondrial
P07773	1.13.11.1	Catechol 1,2-dioxygenase
P11451	1.13.11.-	Chlorocatechol 1,2-dioxygenase
P00590	3.1.1.74	Cutinase 1
P0C5C2	2.1.1.79	Cyclopropane mycolic acid synthase 1
P0A5P0	2.1.1.79	Cyclopropane mycolic acid synthase 2
Q79FX6	2.1.1.79	Cyclopropane mycolic acid synthase MmaA2
P08067	1.10.2.2	Cytochrome b-c1 complex subunit Rieske, mitochondrial
P98005	1.9.3.1	Cytochrome c oxidase polypeptide I+III
P00396	1.9.3.1	Cytochrome c oxidase subunit 1
P33517	1.9.3.1	Cytochrome c oxidase subunit 1
P08306	1.9.3.1	Cytochrome c oxidase subunit 2
P10632	1.14.14.1	Cytochrome P450 2C8
Q9H227	3.2.1.21	Cytosolic beta-glucosidase
Q02127	1.3.5.2	Dihydroorotate dehydrogenase (quinone), mitochondrial
Q08210	1.3.5.2	Dihydroorotate dehydrogenase (quinone), mitochondrial
P45510	2.7.1.29	Dihydroxyacetone kinase
Q9R1E6	3.1.4.39	Ectonucleotide pyrophosphatase/phosphodiesterase family member 2
P0A5Y6	1.3.1.9	Enoyl-[acyl-carrier-protein] reductase [NADH]
P97612	3.5.1.99	Fatty-acid amide hydrolase 1
P03368	3.4.23.16	Gag-Pol polyprotein
P03369	3.4.23.16	Gag-Pol polyprotein
P80035	3.1.1.3	Gastric triacylglycerol lipase
O91734	3.4.22.29	Genome polyprotein
P03300	3.4.22.29	Genome polyprotein
P04936	3.4.22.29	Genome polyprotein
P12915	3.4.22.29	Genome polyprotein
Q66282	3.4.22.29	Genome polyprotein
Q66479	3.4.22.29	Genome polyprotein

Q82122	3.4.22.29	Genome polyprotein
Q12051	2.5.1.-	Geranylgeranyl pyrophosphate synthase
O35000	3.5.99.6	Glucosamine-6-phosphate deaminase 1
P90551	1.1.1.8	Glycerol-3-phosphate dehydrogenase [NAD(+)], glycosomal
P48449	5.4.99.7	Lanosterol synthase
O59952	3.1.1.3	Lipase
P32947	3.1.1.3	Lipase 3
P41365	3.1.1.3	Lipase B
P37001	2.3.1.-	Lipid A palmitoyltransferase PagP
P23141	3.1.1.1	Liver carboxylesterase
P00698	3.2.1.17	Lysozyme C
Q9I596	3.5.1.23	Neutral ceramidase
Q6UEH2	2.3.1.221	Noranthrone synthase
Q10404	2.3.1.181	Octanoyltransferase
P52708	4.1.2.11	P-(S)-hydroxymandelonitrile lyase
P16233	3.1.1.3	Pancreatic triacylglycerol lipase
P07872	1.3.3.6	Peroxisomal acyl-coenzyme A oxidase 1
POA921	3.1.1.32	Phospholipase A1
P00593	3.1.1.4	Phospholipase A2
P00592	3.1.1.4	Phospholipase A2, major isoenzyme
P14555	3.1.1.4	Phospholipase A2, membrane associated
POA405	1.97.1.12	Photosystem I P700 chlorophyll a apoprotein A1
DoVWR8	1.10.3.9	Photosystem II D2 protein
P51765	1.10.3.9	Photosystem Q(B) protein
P50264	1.5.3.17	Polyamine oxidase FMS1
Q05769	1.14.99.1	Prostaglandin G/H synthase 2
P41222	5.3.99.2	Prostaglandin-H2 D-isomerase
P25043	3.4.25.1	Proteasome subunit beta type-2
Q02293	2.5.1.58	Protein farnesyltransferase subunit beta
Q04631	2.5.1.58	Protein farnesyltransferase/geranylgeranyltransferase type-1 subunit alpha
P00735	3.4.21.5	Prothrombin

P0A516	1.14.-.-	Putative cytochrome P450 124
P96416	1.-.-.-	R2-like ligand binding oxidase
P04191	3.6.3.8	Sarcoplasmic/endoplasmic reticulum calcium ATPase 1
P33247	4.2.1.129	Squalene--hopene cyclase
Q5EGY4	2.3.1.-	Synaptobrevin homolog YKT6
P96086	3.4.21.-	Tricorn protease
P00520	2.7.10.2	Tyrosine-protein kinase ABL1
Q06124	3.1.3.48	Tyrosine-protein phosphatase non-receptor type 11
O67648	3.5.1.-	UDP-3-O-[3-hydroxymyristoyl] N-acetylglucosamine deacetylase
P0CD76	2.3.1.-	UDP-3-O-acylglucosamine N-acyltransferase

Conclusion

We have surveyed proteins capable of recognizing long-chain hydrocarbons and long-chain alkyl groups and have considered various factors that influence this binding. Hydrophobic amino acids forming α -helical secondary structures are frequently a major component of the binding sites. The surface complementarity of the ligand–protein interfaces in alkane-binding proteins is lower than that of drug-binding proteins which typically have more polar substrates. However, the occupied volume fraction and the surface area burial by the ligand–protein interfaces are both comparable to those of drug-binding sites. The volume fraction occupied by the substrates is close to the ideal value of 55%, suggesting substrate recognition mechanisms similar to those of synthetic host molecules. Moreover, structural and functional classifications of the long-chain alkane-binding proteins will aid future efforts in searching for potential protein scaffolds. The protein structures and the analyzed binding-site characteristics should guide the design of new enzymes that can selectively recognize large alkyl substrates and catalyze their functionalization.

Methods

PDB Database Search

PDB entries containing one or more ligands with 10 or more carbons were selected using the PDB web-search interface. A Python programming library (OEChem²⁹) was used to postprocess the initial hits, ruling out any entry possessing rings. OEChem was also used to identify functional motifs in the identified ligands, leading to the classification of each ligand.

Analysis of Ligand Binding Pockets

The amino acids located in the binding pockets were identified using the Interface Analyzer module in the Rosetta software package.¹⁵ The surface area burial upon binding of the ligand was computed using the same package. The DSSP program was used to define the backbone secondary structure of the binding pocket amino acids.¹⁶ We used POVME software to calculate the binding pocket volume and the occupied volume fraction.¹⁸ For each statistic provided here, standard deviations were used as a measure of statistical uncertainty.

References

1. Timmis, K. N. *Handbook of Hydrocarbon and Lipid Microbiology*. Springer-Verlag: Berlin, 2010.
2. Yang, Y.; Liu, J.; Li, Z. *Angew. Chem. Int. Ed.* **2014**, *53*, 3120–3124.
3. Singh, S. N. *Microbial Degradation of Xenobiotics*; Springer: Berlin, 2012.
4. Callaghan, A. V. *Front. Microbiol.* **2013**, *4*, 89.
5. (a) Feng, L.; Wang, W.; Cheng, J.; Ren, Y.; Zhao, G.; Gao, C.; Tang, Y.; Liu, X.; Han, W.; Peng, X.; Liu, R.; Wang, L. *Proc Natl Acad Sci U.S.A.* **2007**, *104*, 5602–5607; (b) Li, L.; Liu, X.; Yang, W.; Xu, F.; Wang, W.; Feng, L.; Bartlam, M.; Wang, L.; Rao, Z. *J. Mol. Biol.* **2008**, *376*, 453–465.
6. Cramer, N.; Dermenci, A.; Dong, G.; Douglas, C. J.; Dreis, A. M.; Fu, X.-F.; Gao, Y.; Jones, W. D.; Jun, C.-H.; Kingsbury, J. S.; Moebius, D. C.; Nakao, Y.; Park, J.-W.; Parker, E.; Rendina, V. L.; Souillart, L.; Xu, T.; Yu, Z.-X., *C–C Bond Activation*; Springer: Berlin, 2014.
7. Kiss, G.; Çelebi-Ölçüm, N.; Moretti, R.; Baker, D.; Houk, K. N. *Angew. Chem. Int. Ed.* **2013**, *52*, 5700–5725.
8. Berman, H. M.; Westbrook, J.; Feng, Z.; Gilliland, G.; Bhat, T. N.; Weissig, H.; Shindyalov, I. N.; Bourne, P. E. *Nucleic Acids Res.* **2000**, *28*, 235–242.
9. Lee, B.; Richards, F. M. *J. Mol. Biol.* **1971**, *55*, 379–400.
10. (a) Andreeva, A.; Howorth, D.; Brenner, S. E.; Hubbard, T. J.; Chothia, C.; Murzin, A. G. *Nucleic Acids Res.* **2004**, *32*, D226–D229; (b) Hubbard, T. J.; Murzin, A. G.; Brenner, S. E.; Chothia, C. *Nucleic Acids Res.* **1997**, *25*, 236–239.
11. UniProt Consortium *Nucleic Acids Res.* **2014**, *42*, D191–D198.
12. Dunbar, J. B.; Smith, R. D.; Damm-Ganamet, K. L.; Ahmed, A.; Esposito, E. X.; Delproposto, J.; Chinnaswamy, K.; Kang, Y. N.; Kubish, G.; Gestwicki, J. E.; Stuckey, J. A.; Carlson, H. A. *J. Chem. Inf. Model* **2013**, *53*, 1842–1852.
13. Sanderson, H.; Tibazarwa, C.; Greggs, W.; Versteeg, D. J.; Kasai, Y.; Stanton, K.; Sedlak, R. I. *Risk Anal.* **2009**, *29*, 857–867.
14. Paradies, G.; Paradies, V.; De Benedictis, V.; Ruggiero, F. M.; Petrosillo, G. *Biochim. Biophys. Acta* **2014**, *1837*, 408–417.
15. Lewis, S. M.; Kuhlman, B. A. *PLoS One* **2011**, *6*, e20872.
16. Kabsch, W.; Sander, C. *Biopolymers* **1983**, *22*, 2577–2637.
17. Mecozzi, S.; Rebek, J. J. *Chem. Eur. J.* **1998**, *4*, 1016–1022.

18. Durrant, J. D.; de Oliveira, C. A.; McCammon, J. A. *J. Mol. Graphics Modell.* **2011**, *29*, 773–776.
19. Lawrence, M. C.; Colman, P. M. *J. Mol. Biol.* **1993**, *234*, 946–950.
20. Shoichet, B. K.; Kuntz, I. D. *J. Mol. Biol.* **1991**, *221*, 327–346.
21. Tinberg, C. E.; Khare, S. D.; Dou, J.; Doyle, L.; Nelson, J. W.; Schena, A.; Jankowski, W.; Kalodimos, C. G.; Johnsson, K.; Stoddard, B. L.; Baker, D. *Nature* **2013**, *501*, 212–216.
22. (a) Liu, F.; Wang, H.; Houk, K. N. *Curr. Org. Chem.* **2013**, *17*, 1470–1480; (b) Warmuth, R.; Yoon, J. *Acc Chem Res* **2001**, *34*, 95–105; (c) Stoddart, J. F. *Annu. Rep. Prog. Chem., Sect. B: Org. Chem.* **1988**, *85*, 353–386; (d) Cram, D. J.; Cram, J. M. *Container Molecules and Their Guests*; Royal Society of Chemistry: Cambridge, 1994.
23. Scarso, A.; Trembleau, L.; Rebek, J. *J. Am. Chem. Soc.* **2004**, *126*, 13512–13518.
24. Jiang, W.; Ajami, D.; Rebek, J. *J. Am. Chem. Soc.* **2012**, *134*, 8070–8073.
25. Ruan, Y.; Peterson, P. W.; Hadad, C. M.; Badjić, J. D. *Chem. Commun.* **2014**, *50*, 9086–9089.
26. Nishio, M.; Umezawa, Y.; Honda, K.; Tsuboyama, S.; Suezawa, H. *CrystEngComm* **2009**, *11*, 1757–1788.
27. (a) Zürcher, M.; Gottschalk, T.; Meyer, S.; Bur, D.; Diederich, F. *ChemMedChem* **2008**, *3*, 237–240; (b) Kawasaki, Y.; Chufan, E. E.; Lafont, V.; Hidaka, K.; Kiso, Y.; Mario Amzel, L.; Freire, E. *Chem. Biol. Drug. Des.* **2010**, *75*, 143–151; (c) Zürcher, M.; Diederich, F. *J. Org. Chem.* **2008**, *73*, 4345–4361; (d) Morellato-Castillo, L.; Acharya, P.; Combes, O.; Michiels, J.; Descours, A.; Ramos, O. H.; Yang, Y.; Vanham, G.; Ariën, K. K.; Kwong, P. D.; Martin, L.; Kessler, P. *J. Med. Chem.* **2013**, *56*, 5033–5047.
28. Zhang, K. D.; Ajami, D.; Gavette, J. V.; Rebek, J. *J. Am. Chem. Soc.* **2014**, *136*, 5264–5266.
29. Marcou, G.; Rognan, D. *J. Chem. Inf. Model.* **2007**, *47*, 195–207.